Numerical investigations into the mechanism of graben formation

Mithen, D. P.

NUMERICAL INVESTIGATIONS INTO THE MECHANISM OF GRABEN FORMATION

BY

D.P. MITHEN

A thesis presented for the degree of
Doctor of Philosophy in the
University of Durham

Graduate Society

October 1980

ABSTRACT

The formation of a graben has been investigated using finite element analysis. A new method of modelling faults has been developed which is based on calculating the shear stresses on the fault and, if they exceed the frictional strength, applying forces which cause frictional sliding. Both Newtonian visco-elastic and power law creep rheologies have been used for the lower lithosphere. The deformation patterns seen in the models are relatively insensitive to which one is used.

Stress amplification is shown to result in normal faulting in the upper, brittle layer as a result of relatively small stresses of about 20 MPa being applied throughout the depth of the lithosphere. When a fault is introduced into the model the stresses adjacent to the fault are re-orientated and secondary faulting is predicted. The bending profile associated with the fault deformation results in a weakness where the stresses are most greatly modified. A second normal fault may form here. If the fault movement is confined to the upper part of the brittle layer then the predicted graben width is between 5 and 15 km. For deeper fault movement and an underlying fluid the predicted width increases to 50 - 55 km. A more realistic rheology for the underlying material is visco-elasticity. In this case the predicted width is about 25 km. The fault throw increases as the visco-elastic material relaxes but no significant change is seen in the width.

The subsidence of a 50 km wide graben wedge has been examined. For applied stresses of about 50 MPa and coefficients of friction of less than about 0.1, subsidence of about 1 km is predicted. This does not include sediment infilling. The subsiding wedge causes large compressive

stresses in the underlying material which may be long-lasting. The subsidence is controlled by the boundary faults and causes bending of the block which may result in internal deformation.

ACKNOWLEDGEMENTS

I would like to thank all my colleagues in the Department of Geological Sciences for the interesting discussions that I have had with them during my time at Durham University. In particular, I wish to thank Professor M.H.P. Bott, who has supervised this research, and Mr. M.J.M. Park. I have also had useful discussions of the finite element method with Mr. R.C.A. Hindmarsh.

I also wish to thank Mr. B.R. Lander of the Computer Unit for the allocation of computing resources.

This work was undertaken whilst I was in receipt of a research studentship from the Natural Environment Research Council, to whom I am grateful.

CONTENTS

Page

CHAPTER 1

AN INTRODUCTION TO GRABEN STRUCTURES

1.1 Introduction

The basic geometry of a graben is of a downthrown block between two normal faults, although one fault only may be present. They are typically much longer (measured along the strike) than they are wide. These structures can be seen on many different scales and their importance to geodynamic studies results not only from an interest in the mechanics of their formation, but also their significance in rift valley systems, continental splitting, and as initiating mechanisms for sedimentary basin development.

The occurrence and physical characteristics of graben structures will be described briefly in this chapter, together with a review of current theories of their formation.

1.2 Occurrence and Physical Characteristics of Graben

1.2.1 Occurrence

Graben occur at all scales within continental plates. The large-scale continental graben are very long and have widths of up to 80 km. Some of these underlie major sedimentary basins, such as the North Sea (Kent, 1975; Ziegler, 1975), the Michigan basin and the Chad basin (Burke, 1976b), and may have acted as depressions for early sedimentation which have subsequently led to flexure and major basin formation (Beaumont and Sweeney, 1978; Beaumont, 1978). Other major graben, in particular the Rhinegraben, Lake Baikal and the East African rift

system, are situated on uplifted areas and are amenable to geological and geophysical study. The Basin and Range province of North America is characterised by many graben of typical width between 10 and 20 km (Wright and Troxel, 1973; Stewart, 1978). It is the possible mechanism of formation of these large, continental graben that will be investigated in this thesis.

On a smaller scale, graben with widths of several hundred metres and occurring at regular intervals are seen in the Canyonlands National Park, Utah (McGill and Stromquist, 1979), and graben of only a few metres in width can form as a result of an instantaneous tectonic event, such as the Alaskan earthquake of 1964 (Voight, 1974).

Graben also occur at passive plate margins. These are often relic graben and half-graben structures associated with ocean opening. Examples of these are seen around the margins of the Atlantic Ocean (Burke, 1976a). These may be reactivated, and new graben formed, as a result of subsidence and sedimentation on the continental shelf (Bott, 1971; Sheridan, 1976).

1.2.2 Surface features of major continental graben

Continental rift zones are very long and composed of many graben of different dimensions. The Baikal rift extends for 2,500 km in a SW - NE direction and the East African rift zone covers a distance of 4,000 km. The largest graben in the Baikal area is the South Baikal depression which is over 400 km long and up to 60 km wide and was the site of the earliest rifting in this area, in Middle Eocene times (Logatchev and Florensov, 1978). The largest graben in the East African system is the Gregory rift with a width of 60 to 70 km, situated in the central part of the Kenya rift (Baker and Wohlenberg, 1971). The Rhinegraben has a length of 300 km and a mean width of 36 km and started

subsiding in Middle Eocene times (Illies, 1970). Widths of between 30 and 70 km seem to be typical for major graben structures - the North Sea graben have widths in this range and the Oslo graben has a width of 40 km (Ramberg, 1972).

The typical structure of these graben is of a downthrown block, heavily faulted with tilted fault blocks, between normal faults of dip 55° to 80°, most frequently 60° to 65°. The shoulders form steep escarpments towards the graben and dip gently outwards at 1° to 3° (Illies, 1970). A striking feature of graben structures is the parallel nature of the boundary fault zones. The maximum shoulder uplift for all three major structures that have been discussed varies from 2 to 2.5 km (Illies, 1970; Kolmogorov and Kolmogorova, 1978; Baker and Wohlenberg, 1971). The Rhinegraben has a maximum sedimentary fill of 3.4 km (Illies, 1970). The boundary faults in the Baikal area have throws less than 1 km with the exception of the Obruchev fault which forms the western boundary of the South Baikal depression which has a throw of at least 6 km (Sherman, 1978). The throw on the boundary faults of the Gregory rift is 3 to 4 km (Baker and Wohlenberg, 1971). Figure 1.1 is a block diagram of the Rhinegraben and illustrates the typical graben structure discussed above.

The amount of extension undergone can be estimated by palinspastic reconstruction of the fault blocks. This method gives 4.8 km extension in the Rhinegraben (Illies, 1970). Extension in the Baikal area is, in general, a few kilometres, possibly exceeding 10 km in the South Baikal depression (Logatchev and Florensov, 1978), and in the East African rift zone is between 5 and 10 km (Baker and Wohlenberg, 1971).

The major rift zones are generally characterised by domal uplifts which preceded the initial stages of rifting (Kiselev et al., 1978;

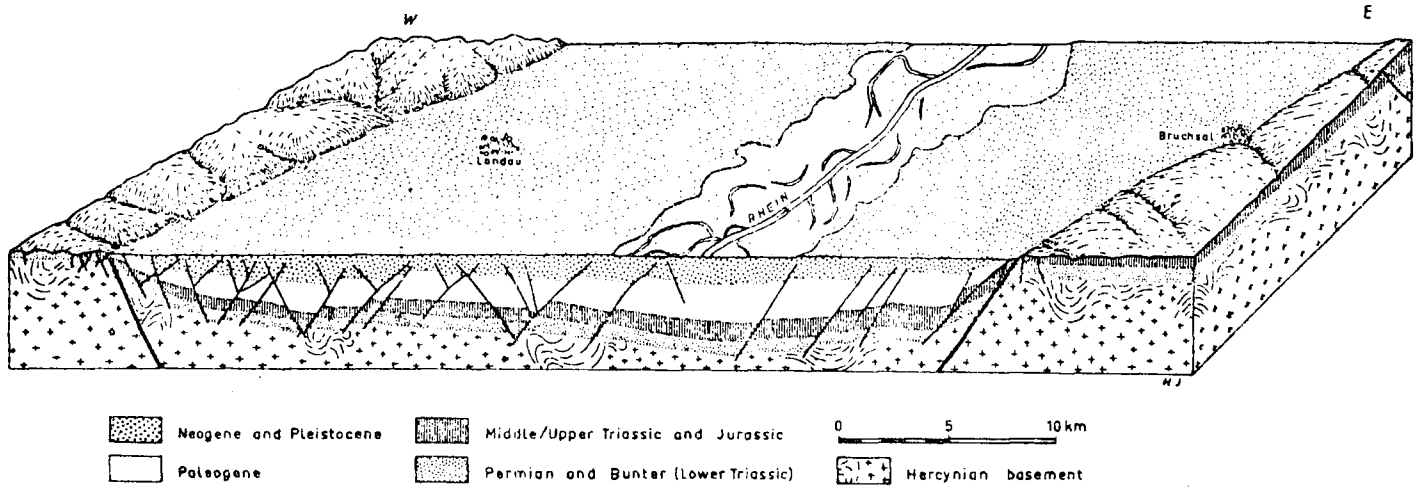

Fig. 1.1: Block diagram of the Rhinegraben north of Karlsruhe (after Illies, 1970)

Davidson and Rex, 1980). They are also characterised by a two stage evolution pattern, consisting of an early period of weak, tectonic movements and shallow, proto-rift basin formation, followed by a later stage of rapid activity with faulting and further uplift (Logatchev et al., 1972; Illies, 1975; Logatchev and Florensov, 1978). Volcanism is associated with these areas, although the amount varies. The Baikal area has approximately 5,000 km^3 of volcanics compared with 500,000 km^3 in East Africa. Basaltic lavas are the typical volcanics, particularly in the alkaline and intermediate range of composition (Logatchev et al., 1972; Kiselev et al., 1978). It has been pointed out that for the Rhinegraben, East Africa and the Baikal rift volcanism occurred earlier than graben formation and was associated with the doming rather than the future graben fault zones (Logatchev et al., 1972; Illies, 1977; Logatchev and Florensov, 1978).

1.2.3 Deep structure of major continental graben

The initial development of rift valley graben was probably controlled by pre-existing lines of weakness in the basement. The Rhinegraben follows Hercynian and Caledonian basement faults (Illies, 1977) and the South Baikal depression overlies a suture between the Precambrian Siberian platform and the Sayan-Baikal fold belt (Logatchev and Florensov, 1978). Younger graben developed after the initial faulting show less dependence and may cut across the structural grain of the area; for instance the northern part of the Baikal rift zone diverges from the ancient line of suture into the Sayan-Baikal fold belt (Zamarayev and Ruzhich, 1978).

Seismic refraction experiments over continental rift valleys typically demonstrate an upwarping of the Mohorovicic discontinuity

beneath the graben. Griffiths et al. (1971) in a refraction survey over the northern part of the Gregory Rift found a 20 km thick layer with P-wave velocity 6.4 km s^{-1} overlying material with a velocity of 7.5 km s^{-1}, which was interpreted as anomalous, low velocity mantle. Delays from teleseismic P-wave arrivals suggested a minimum thickness of 100 km for this material, assuming the velocity contrast remained the same. Long et al. (1973) pointed out that this low velocity mantle is confined to the axis of the Gregory rift, and Long and Backhouse (1976) concluded that the anomalous mantle thins not only westwards, away from the rift axis, but also northwards where the rift dies out in northern Kenya.

The Moho beneath the Baikal area also seems to be upwarped beneath the major graben to a depth of 35 km, compared with 42 to 46 km away from the rift. The morphology of this boundary is, however, a complicated surface which is irregular along the rift zone strike (Puzyrev et al., 1978). A low velocity layer in the crust, with a contrast of 0.2 to 0.3 km s^{-1}, at approximately 12 km has been detected by Puzyrev et al. (1978) who also suggested that anomalous, low velocity mantle of 7.6 to 7.8 km s^{-1} underlies the Moho with an average thickness of 17 km. This was thought to be underlain by normal mantle some tens of kilometres thick, although they suggested a narrow vertical connection between the anomalous layer and the deeper, low velocity zone located along the rift axis. The area of the anomalous mantle was thought to be 2 to 3 times wider than the Baikal rift zone as defined from surface geology. From a study of the delays associated with teleseismic P-wave arrivals Zorin and Rogozhina (1978) found that the upper boundary of the low velocity mantle rises up to the base of the crust only under the rift zone proper and dips away from this area.

Assuming a constant velocity differential of 0.3 km s^{-1}, the lower boundary was calculated as being 400 km deep beneath the greater part of the rift zone. This structure seems more reasonable than the 17 km thick layer proposed by Puzyrev et al. (1978) and has obvious similarities to the anomalous mantle beneath the Gregory rift.

Refraction studies by Meissner et al. (1970) and Ansorge et al. (1970) suggested that a 'cushion' of low velocity mantle (7.5 to 7.7 km s^{-1}) with a width of about 180 km existed at the base of the crust beneath the Rhinegraben at a depth of 25 km. However, this conclusion was shown to be incorrect by later reversed profiles (Rhinegraben Research Group for Explosion Seismology, 1974) which showed this boundary to be an 8.1 km s^{-1} refractor, consistent with 'normal' mantle. A joint interpretation of all seismic refraction profiles in the southern Rhinegraben area, using time-term analysis, by Edel et al. (1975) demonstrated an elevation of the crust-mantle boundary forming an arch with a span of 150 to 180 km and reaching a depth of 25 km beneath the flanks of the graben. Beneath the graben proper, a transition zone was found to be present with a thickness of 4 km and the strongest velocity gradient at a depth of 21 km. This zone was regarded as a region of crust-mantle interaction. Away from the Rhinegraben the Moho is at a depth of 30 to 35 km. Figure 1.2 shows the Moho topography and its relationship to the surface features. A low velocity layer at a depth of 10 km below the graben proper was found in the crust, extending to about 19 km. Between 19 and 25 km a laminated, transition structure was assumed on the basis of the striate character of the observed deep reflections (Mueller and Rybach, 1974) with, possibly, a thin low velocity layer at the base of the crust.

The Bouguer gravity anomaly over the Gregory rift in East Africa

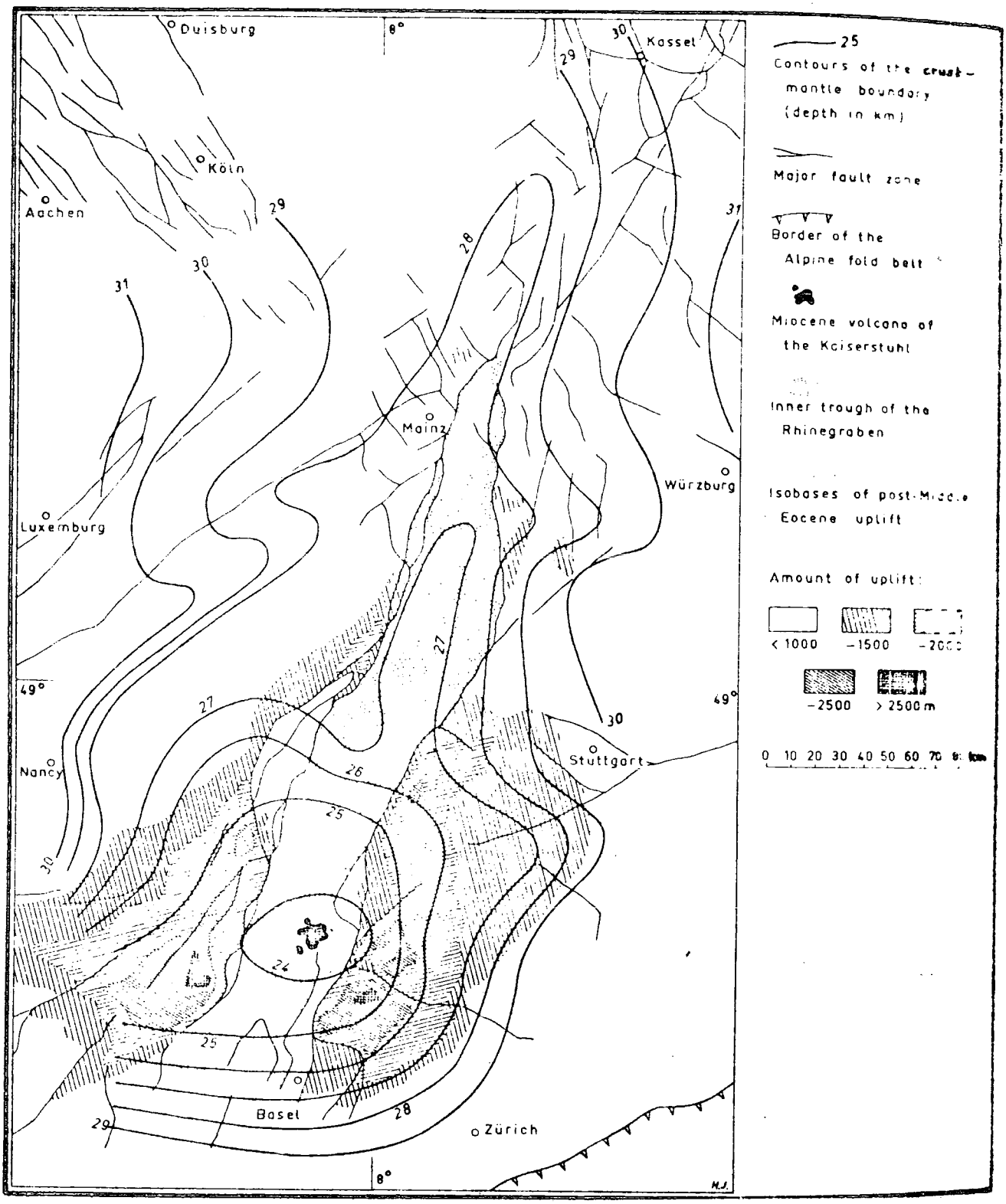

Fig. 1.2: The relationship between Moho topography and surface features for the Rhinegraben. (after Illies, 1977)

shows a long wavelength negative anomaly, 1000 km wide, with an amplitude of up to -150 mgal, together with a superimposed positive anomaly over the rift axis of 40 to 80 km width with an amplitude of +30 to +60 mgal (Fairhead and Girdler, 1972). The small gradients associated with the negative anomaly suggest that the cause is at considerable depth and the anomaly has been interpreted as being due to low density asthenosphere replacing the upper mantle part of the lithosphere. The axial positive anomaly is considered to be due to the presence of a mantle-derived, intrusive zone reaching to within 2 km of the rift surface. Various models have been proposed to fit this interpretation and have been summarised by Forth (1975).

Gravity anomalies in the Baikal region show weak, negative, regional isostatic anomalies with an extremely deep minimum coinciding with the Baikal Lake valley (Artemjev and Artyushkov, 1971). Negative anomalies of lower intensity correspond to other rift valleys in this area. After correcting for the sediments, and excluding the local minimum, the Baikal region is characterised by a wide relative maximum in the Bouguer anomalies. This is consistent with an upwarping of the Mohorovicic discontinuity. The local minimum over Lake Baikal cannot be completely removed by assuming that the isostatic balancing of the sediments and water filling the valley is total. This is interpreted by Artemjev and Artyushkov (1971) as being due to either an incomplete knowledge of the shape and sediment fill of the valley, or a variation in crustal thickness under Lake Baikal, or a decrease in upper mantle density beneath Lake Baikal. The third alternative is consistent with the general negative regional, high heat flow data, and seismic velocity decrease in the upper mantle beneath the rift as described previously.

The Rhinegraben is characterised by an asymmetric negative gravity

anomaly of about 30 mgal. Most of the anomaly can be accounted for by the sedimentary fill. However, Mueller and Rybach (1974) have pointed out that the observed minimum in the gravity anomaly does not coincide with the minimum due to the sediment cover. They have interpreted this as an upward indentation of the sialic low velocity (and presumably low density) crustal layer into the overlying basement. The effect of the elevated crust-mantle boundary beneath the Rhinegraben is not seen in the Bouguer anomaly. Fuchs (1974) has suggested that this may be due to either a column of lower lithosphere heated by conduction (and therefore of lower density), or a heating effect as a result of mass transfer either as a diapiric rise from the base of the lithosphere or as a zone of low velocity material in the lower lithosphere. The smaller time constant required for mass transport would make this more likely than heating by conduction.

The Oslo graben has a broad positive gravity anomaly which has been interpreted by Ramberg (1972) as a shallowing of the Mohorovicic discontinuity beneath the graben by 7 to 12 km. This is shallower than was indicated by seismic refraction experiments (Sellevoll and Warrick, 1970), which suggests that the anomaly is partly due to a positive density contrast in the crust, possibly an intrusive zone. A large magnetic anomaly is present of the same width as the exposed graben which supports the idea of intrusion of igneous material.

Studies of the deep structure beneath these major graben thus support the idea of a slightly upwarped Moho. Anomalous mantle is seen beneath Baikal and East Africa and a consideration of the gravity anomaly over the Rhinegraben (Kahle and Werner, 1980) suggests that low density mantle must be present at depth. The existence of anomalous thermal conditions beneath these rifts is supported by high heat flow (e.g. Haenel, 1970)

and whilst they are not now thought to be present beneath the Permian Oslo graben, the possible presence of intrusive bodies in the crust suggests that these conditions may have existed at the time of active rifting.

1.3 Theories of the formation of graben structures

1.3.1 The stress regime associated with graben formation

There now seems little doubt that graben structures originate as a result of tensional stresses. Early suggestions (e.g. Bullard, 1936) that they form as a result of compression and are bounded by reverse faults were shown to be incorrect by geological studies which demonstrated that graben are bounded by normal faults. Also, calculated Bouguer anomalies for the Lake Albert rift valley by Girdler (1964) showed that a normal fault bounded graben gave an anomaly much closer to the observed gravity than a reverse fault bounded graben. The seismicity of continental rift zones is important for providing fault plane solutions which indicate the principal stress orientations. Some graben structures may not now be subject to the same stress regime in which they first formed and this must be considered when evaluating fault plane solutions. The Rhinegraben is now deforming by a predominantly left-lateral, strike-slip motion and probably ceased to be an active rift valley sometime in late Miocene to early Pliocene times (Illies, 1977). Horizontal stylolites, which form with their long axes parallel to the direction of maximum compression, have been observed in the Mesozoic strata of Europe and are consistent with compression parallel to the graben strike (Illies, 1977). Figure 1.3 illustrates the differences in stress orientations in the region of the Rhinegraben in Mesozoic times and the

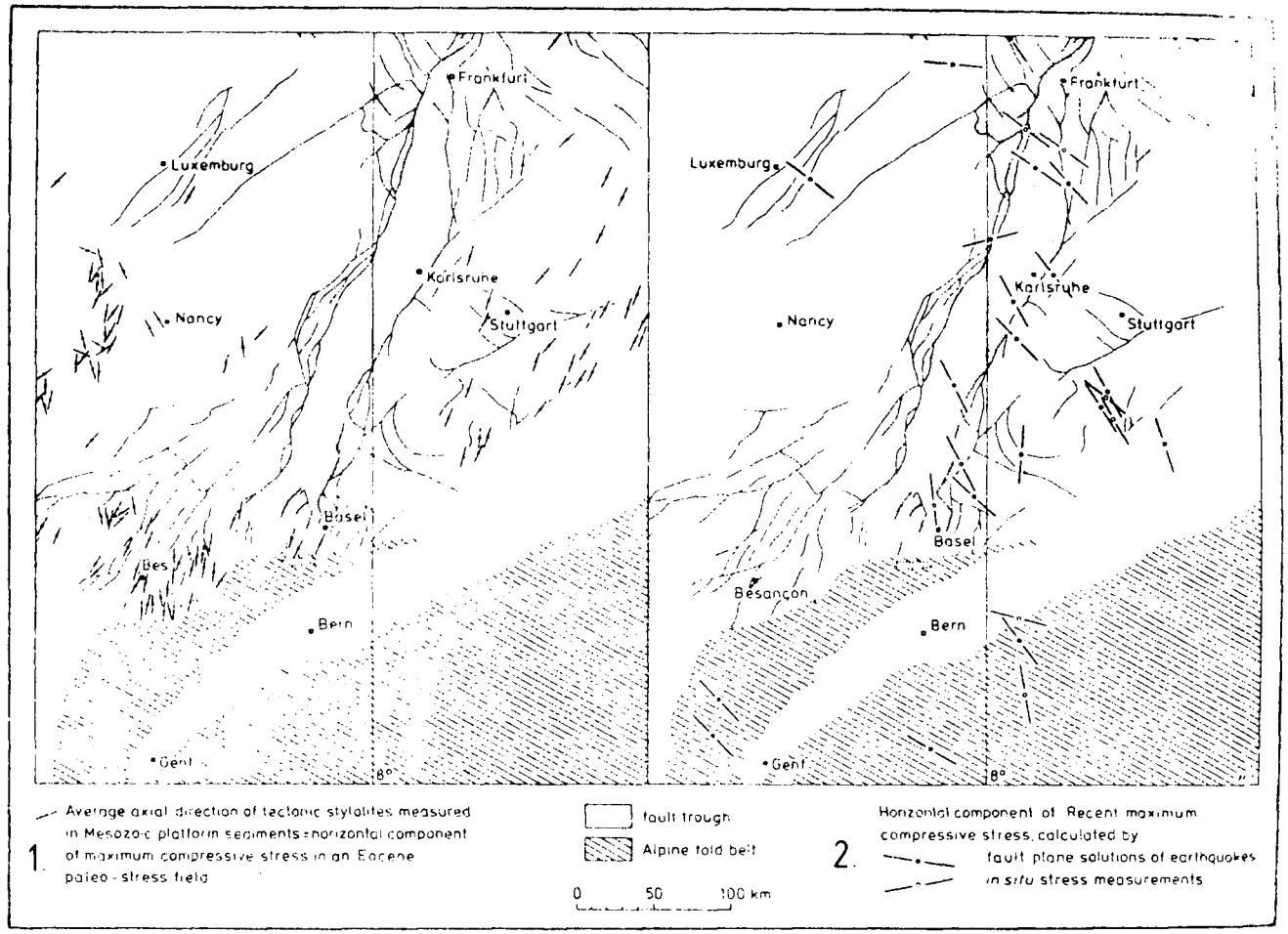

Fig. 1.3: Directions of the horizontal component of maximum compressive stress for the Rhinegraben in Eocene (1) and Recent (2) times. (after Illies, 1977)

present day. The Baikal rift zone is seismically very active and rifting is still taking place, with graben connected by strike-slip faults which are analogous to oceanic transform faults (Sherman, 1978). The maximum seismicity occurs in narrow belts which are unquestionably related to the major fault zones (Golonetsky and Misharina, 1978; Solonenko, 1978). The Baikal depression is actively widening as demonstrated by subsidence of crustal blocks associated with the large earthquakes of 1862 and 1959 (Solonenko, 1978). Normal faulting is observed to be consistently and overwhelmingly predominant (Golonetsky and Misharina, 1978) with compressional axes near-vertical and tensional axes near-horizontal and perpendicular to the strike of the surface structures (see Figure 1.4). The highest rates of recent crustal movement in the Baikal area are of 10 to 20 mm yr^{-1} and occur in the regions of highest topographic elevation differences (Kolmogorov and Kolmogorova, 1978). Fault plane solutions for earthquakes occurring in the East African rift system show either strike-slip or normal faulting with no evidence of compression (Fairhead and Girdler, 1972).

Studies in all areas confirm the asymmetry of graben structures, typically with one of the major fault zones being better developed, and an asymmetric sedimentary fill (e.g. Mueller, 1970; Girdler et al., 1969). All evidence points to periods of activity separated by quiet periods rather than slow progressive movements (e.g. Solonenko, 1978).

1.3.2 Sources of stress

The formation of graben structures perpendicular to tensional stress axes is strong evidence for a mechanism involving extension of the crust or lithosphere by tensile, lithospheric stresses. These stresses can have a magnitude of several tens of MPa and in some cases

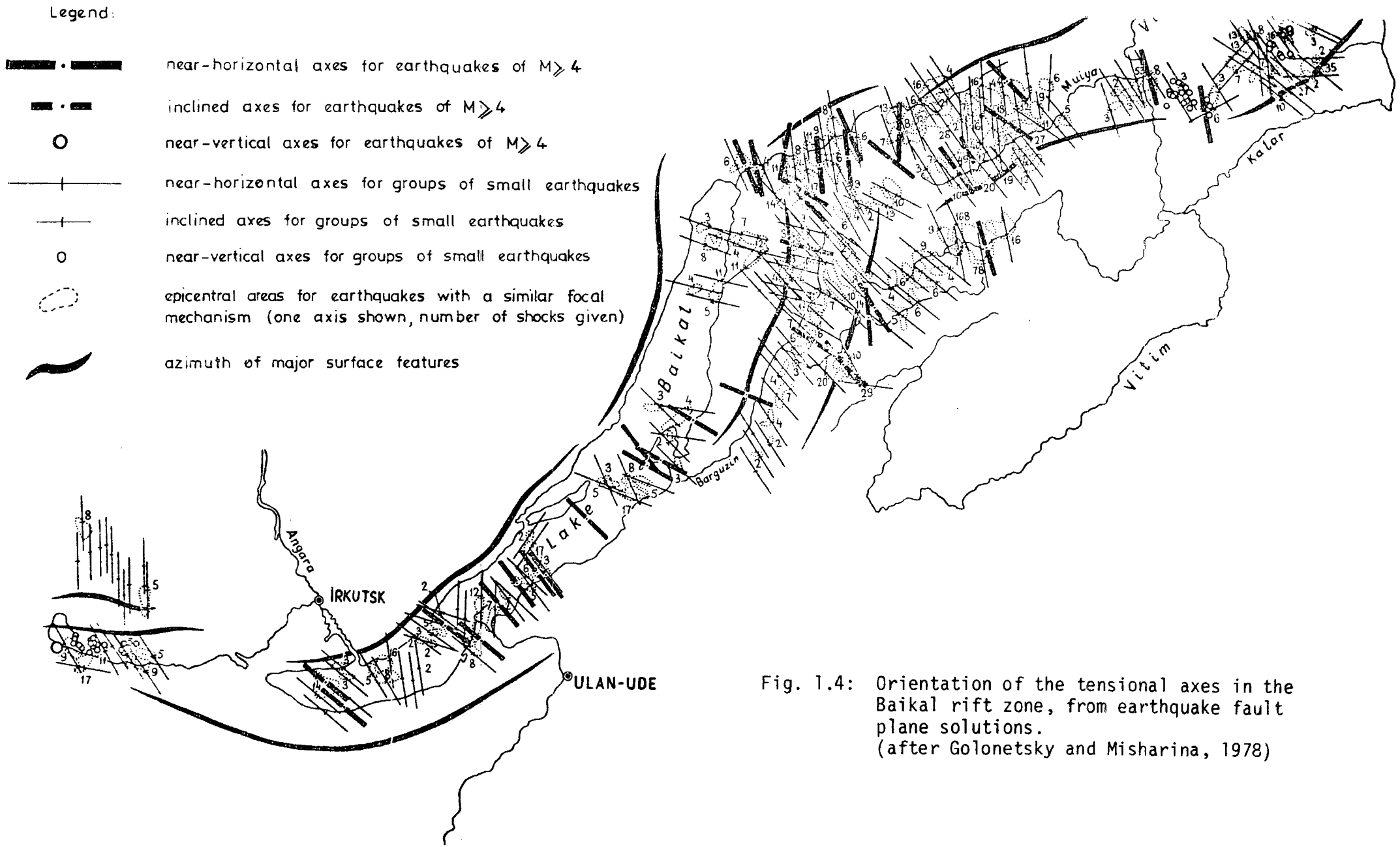

Fig. 1.4: Orientation of the tensional axes in the Baikal rift zone, from earthquake fault plane solutions.
(after Golonetsky and Misharina, 1978)

may exceed 100 MPa (Turcotte and Oxburgh, 1976; Murrell, 1977). The causes of stress in the lithosphere have been summarised by Turcotte and Oxburgh (1976) and can be divided into five classes:

1) Stresses due to the driving mechanism of plate tectonics. These include 'slab pull', 'ridge push' and traction forces occurring as a result of convection cells within the upper mantle. Particularly large stresses can accumulate at zones of plate interaction, such as continental collision zones and transform faults.
2) Thermal stresses as a result of temperature changes.
3) Membrane stresses caused by the movement of plates over the Earth's surface, which has the form of an oblate spheroid (Turcotte and Oxburgh, 1973; Turcotte, 1974).
4) Overburden stresses due to erosion or sedimentation.
5) Stresses due to variations in crustal thickness. These have been calculated analytically by Artyushkov (1973) and by finite element analysis for continental margins (Bott and Dean, 1972) and plateau uplifts (Bott and Kusznir, 1979).

Particular examples of stress sources have been suggested for some specific graben. Mantle plumes, which result in doming, have been cited as causes of the East African rift system (Burke and Whiteman, 1973) and the trilete systems of North Sea graben (Whiteman et al., 1975). Oxburgh and Turcotte (1974) have speculated that membrane tectonics have been responsible for the tensile stresses associated with the East African rift system (although this is inconsistent with the conclusion reached by Burke and Wilson (1972) that the African plate has been stationary for the last 25 M yrs). Molnar and Tapponier (1975, 1979) have suggested that the formation of the Baikal rift zone is linked to the very large strike-slip faults resulting from the collision between

India and Asia. For this to be the primary cause of rifting requires graben formation to commence in Miocene times rather than Eocene, and they suggest that the Eocene deposits seen are not related to the present style of rifting. Bott (1971) has used the stress differences due to the thickness variation across passive continental margins to account for hot creep of lower crustal material oceanwards and resultant graben formation in the brittle, upper crust. Neugebauer (1978) and Neugebauer and Braner (1978) have used finite element analysis to support their suggestion that the Rhinegraben formed as a result of rifting due to doming and later extension, caused by gravitational potential resulting from the uplift.

1.3.3 Mechanisms of graben formation

Illies (1970) suggested that the formation of fault zones along the axes of uplifted domes is a result of tension induced in the crust by the doming effect of low density mantle. He suggested that both master faults started from the same trace at the crust-mantle discontinuity. Whilst this is in agreement with the depth to the Moho at the time of initiation of rifting, which is consistent with observed depths outside the graben, it seems difficult to explain the faulting starting from the crust-mantle boundary. The increase in confining pressure and temperature (particularly in the presence of hot, rising mantle material) with depth suggests that deformation at depths of about 30 km will be by ductile flow rather than brittle fracture (see Chapter 2). A more fundamental objection to this mechanism, which was recognised by Illies (1970), is that the observed extension across major graben structures is too great to be explained by the tension generated along the crest of the rising dome. Artemjev and Artyushkov

(1971) demonstrated analytically that, for a plausible shaped dome, the extension caused will be of the order of hundreds of metres rather that the observed values of 4 to 10 km. This resulted in the suggestion that gravity sliding of the crustal blocks down the flanks of the domed uplift (Illies, 1970) could explain the extra extension. This has been challenged by Strobach (1974) who estimated the effective horizontal stress as a result of this mechanism to be about 0.5 MPa only. Voight (1974) suggested that gravity sliding over very weak sedimentary horizons is a feasible mechanism for small, thin-skinned graben such as those associated with the Alaskan earthquake of 1964, but rejected the hypothesis of gravity sliding for the Rhinegraben by consideration of the position of the 'toe' caused by the sliding block.

Vening Meinesz (1950) proposed a mechanism for graben formation which is illustrated in Figure 1.5. Extension of the crust results in a normal fault which makes an angle of 63° with the horizontal (Figure 1.5(a)). Isostatic considerations cause upbending of the block on the upthrown side (A) and sinking of the block on the downthrown side (B) (Figure 1.5(b)). Downward bending of the block B results in stretching of the upper part of the crust and the formation of a second normal fault where the maximum bending moment occurs. If this second fault is inclined towards the first fault a wedge-shaped block will be formed and will subside isostatically (Figure 1.5(c)). Elastic beam theory can be used to give values for the predicted width of the graben and the shape of the uplift at the flanks, assuming that the crust can be represented as an elastic beam overlying a fluid. The results only are quoted here but the theory is developed in Appendix 1. For a crustal thickness of 35 km and reasonable density values the predicted width of the graben is 65 km (Heiskanen and Vening Meinesz, 1958). The subsidence of the wedge is

860 m and the uplift of the flanks is 680 m. Two major objections make this theory unacceptable. Firstly, the formation of a graben predicts a crustal root as a result of subsidence of the wedge. This is nowhere observed. Indeed, the typical situation beneath a major graben is of an upwarped Moho and crustal thinning. Secondly, the downfaulted graben block is observed to be heavily faulted and composed of many tilted fault blocks. The mechanism by which this can occur has no explanation if the block is simply sinking into the underlying material.

The above objections have resulted in a modification of Vening Meinesz' theory. Mueller (1970) used the observed width of 36 km for the Rhinegraben to calculate a depth of 20 km for the fractured part of the crust. He correlates this depth with the top of the lamellar crustal layer which is separated from the upper crust by a low velocity layer. This mechanism was further developed by Artemjev and Artyushkov (1971) (Figure 1.6) who suggested that the observed upwarping of the Moho was a result of neck-shaped strains in the lower crust, analogous to those formed in rods and plates as a result of applied tension. Once a localised decrease in crustal thickness is present the necking process increases rapidly due to an increase in the flow velocity. In order for the upper, more viscous layer of the crust to stretch with the velocity of the lower layer the tensional stresses must concentrate there. Stress concentration of this type has been observed by Kusznir and Bott (1977) using finite element models. Once the stresses in the upper crust exceed the tensile strength a fault develops and necking of the lower layer increases rapidly. Owing to the high viscosity of the upper layer it is not able to go down with the same velocity as the neck forms and is further fractured into blocks. Fuchs (1974), applying this type of mechanism to the Rhinegraben, suggested that the necking occurred

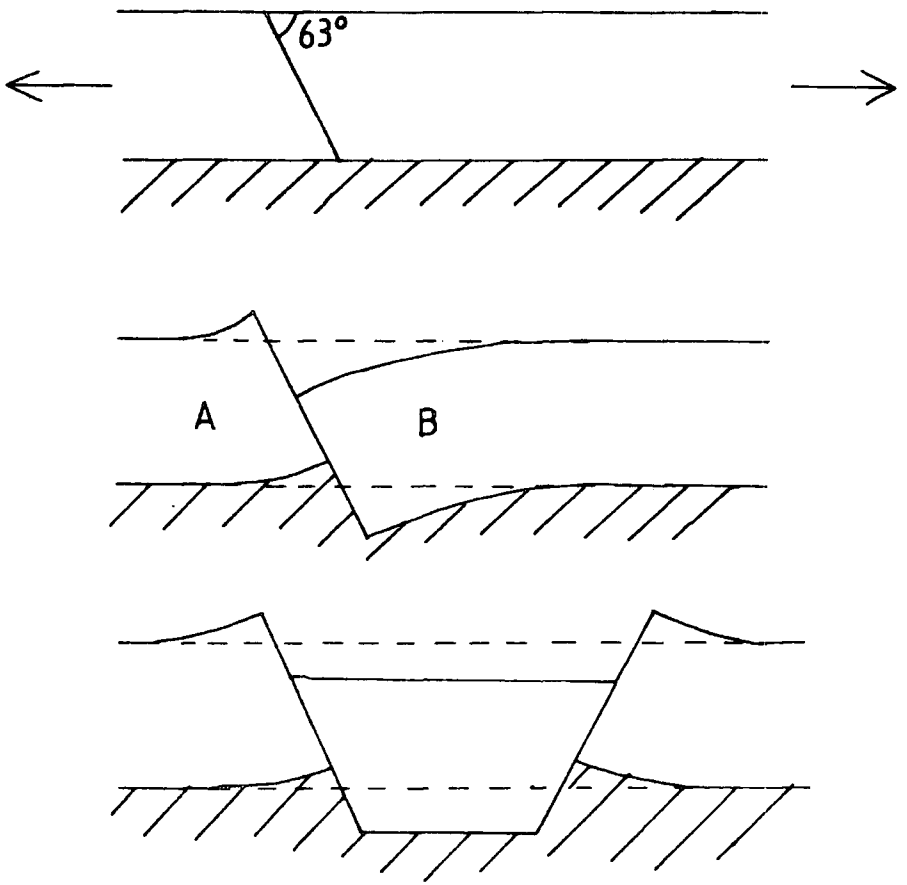

Fig. 1.5: Subsiding wedge theory of Vening Meinesz

crust
mantle
----- position of undisturbed crust

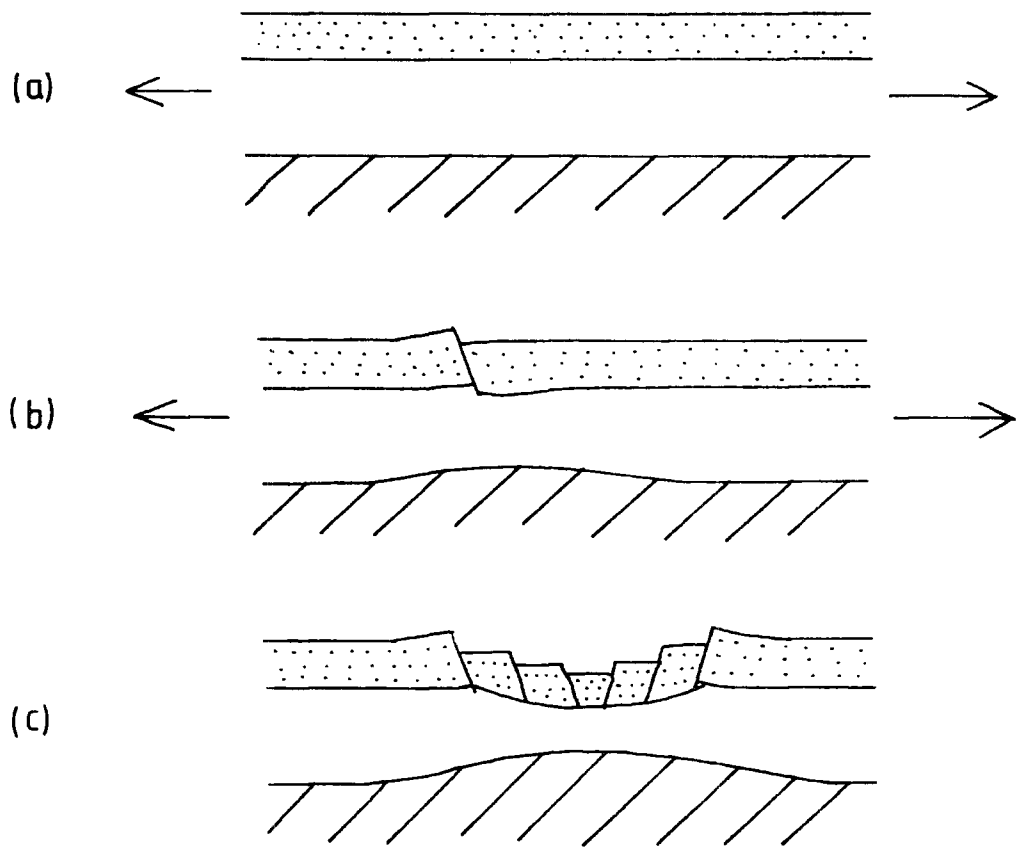

Fig. 1.6: Lower crustal necking mechanism of Artemjev and Artyushkov

high viscosity upper crust
low viscosity lower crust
mantle

in a low velocity crustal layer such as that observed beneath the Rhinegraben.

The most recent adaptation of this type of mechanism has been by Bott (1976), who applied the wedge subsidence theory of Vening Meinesz to the brittle upper layer of the crust and a stretching mechanism of the type suggested by Artemjev and Artyushkov to the lower crust. His proposed mechanism consists of a faulting stage, with an incremental drop in the tensile stress in the brittle layer and subsidence of the wedge, together with an immediate complementary increase in tension in the ductile layer resulting in a stretching stage. This increases the tensile stress in the brittle layer and may lead to the re-initiation of faulting. For a 10 km thick brittle layer and reasonable elastic moduli and densities a graben width of between 24 and 48 km is predicted using elastic beam theory (see Appendix 1), although the downward convergence of the normal faults and the widening due to subsidence may increase the surface width by up to 10 km. Bott also calculated the amount of subsidence that could occur by considering the energy budget available. This gave a value of over 5 km for a sediment filled graben of 30 to 40 km width, assuming that friction on the boundary faults was small.

1.3.4 Conclusions

Stresses act on the lithosphere as a result of various causes, and, if applied to a crust which consists of a brittle layer overlying ductile material, may result in the formation of graben structures similar to those observed in the field (Artemjev and Artyushkov, 1971; Bott, 1976). The effect of the anomalous thermal conditions, which seem to accompany rifting, is likely to be to increase the creep rate in the ductile material, with consequent concentration of stress in the

brittle layer, and cause graben formation in areas subject to these conditions. The initial stages of weak, tectonic movements and shallow basin formation may be a result of stretching of the anomalously hot, ductile, lower crust and the later stage of rapid fault movement and subsidence is probably due to the instability caused by normal faulting.

CHAPTER 2

BRITTLE FRACTURE AND DUCTILE FLOW IN THE CONTINENTAL LITHOSPHERE

2.1 Introduction

In this chapter the material properties of the continental lithosphere are discussed. The first part deals with the composition and rheological subdivision of the lithosphere. Later sections discuss faulting in the brittle layer and creep in the underlying ductile material. The physical properties and mode of deformation presented here form the basis of the finite element models used in later chapters to investigate the response of the continental lithosphere to applied stress systems.

2.2 Composition and elastic parameters

The continental lithosphere can be divided into upper crust, lower crust and lithospheric mantle. The upper crust has a mean composition approximately equivalent to granodiorite-diorite with a mean density of 2,750 kg m^{-3} to 2,800 kg m^{-3} and a P-wave velocity of 5.9 to 6.3 km s^{-1} (Bott, 1971; Wyllie, 1971). The Conrad discontinuity, where it is present, is sometimes considered to represent the boundary between the upper and lower crust. The lower crust has a mean density of about 2,900 kg m^{-3} (Bott, 1971) and P-wave velocities between 6.4 and 7.6 km s^{-1} with a typical value being 6.7 km s^{-1}. It used to be thought that the lower crust was of basaltic composition, but investigations of the stable mineral assemblages at lower crustal temperatures and pressures (Ringwood and Green, 1966; Green and Ringwood, 1967) together with the observed P-wave velocities seemed to rule out this idea. It now seems likely that the lower crust is composed of high pressure forms of granodiorite and

diorite or, if it is 'wet', of amphibolite (Bott, 1971). The Mohorovicic discontinuity, or Moho, represents the boundary between the lower crust and the mantle. A typical depth for this transition for continental lithosphere is 40 km, although older shield areas commonly have the Moho at a greater depth and warm regions often have a shallower Moho. The P-wave velocity just below the Moho is usually about 8.1 km s^{-1} which is interpreted as being associated with upper mantle material. Two common rock types have comparable P velocities - eclogite or an ultrabasic rock such as peridotite. Most evidence suggests that the Moho is a chemical discontinuity (for summaries see Wyllie, 1971; Bott, 1971) and the mantle is composed of an ultrabasic rock such as peridotite. Green and Ringwood (1963) proposed a ratio of 1 part basalt to 3 parts dunite which they called 'pyrolite'. This composition is similar to peridotite. The mean density of peridotite is about 3,300 kg m^{-3}.

In order to model elastic deformations in the lithosphere it is necessary to have values for Young's modulus and Poisson's ratio. These can be determined from the density and the P and S-wave velocities. S velocities are not as well known as P velocities and to avoid having to use them a value of 0.25 is assigned to Poisson's ratio. This is a geologically acceptable value. Substituting for Lamé's parameters (see Jaeger, 1969) in the equation for the P-wave velocity gives

$$V_p^2 = \frac{E(1-\nu)}{\rho(1+\nu)(1-2\nu)}$$

where V_p is the P-wave velocity, ρ is the density, E is Young's modulus and ν is Poisson's ratio. The calculated values of Young's modulus for the upper and lower crust and the lithospheric mantle are shown in

Table 2.1. It is generally assumed that these values, which are calculated from short period deformations, are extrapolatable to the much longer periods associated with elastic stress systems.

	V_p (km s^{-1})	ρ (kg m^{-3})	E (N m^{-2})
Upper crust	6.1	2,750	0.85×10^{11}
Lower crust	6.7	2,900	1.08×10^{11}
Mantle	8.1	3,300	1.80×10^{11}

Table 2.1: Values of Young's modulus assuming a Poisson's ratio of 0.25

2.3 Temperature regime and rheological subdivision

Mercier and Carter (1975) compared the mineral assemblages seen in xenoliths and Alpine-type peridotites with results of high temperature and pressure studies on mineral systems. On the basis of this work they proposed hyperbolic equations representing continental, low temperature oceanic, and high temperature oceanic geotherms. These geotherms correspond fairly well with the theoretical geotherms of Clark and Ringwood (1964) and geotherms for the Canadian shield and the Basin and Range province proposed by Herrin (1972). In order to investigate the mechanism of graben formation, it is necessary to have a geotherm that represents the temperature regime at the onset of faulting. The evidence cited in Chapter 1 suggests that doming and volcanism precede major graben formation indicating higher temperatures than for a cool, stable, continental lithosphere such as is represented by the continental geotherm of Mercier and Carter. On the other hand, it is unlikely that

the temperature regime at those times was as high as is observed at present day continental rifts, which satisfy the high temperature oceanic geotherm. Consequently, the most reasonable geotherm to use seems to be the low temperature oceanic geotherm of Mercier and Carter which has the form

$$T = 4.34(P + 8.6) - \frac{11840}{(P + 8.6)} + 1340$$

where P is the pressure in kilobars and T is the temperature in degrees centigrade. For a lithosphere thickness of 100 km, a reasonable value for a warm continent, this geotherm gives a temperature at the base of about 1200°C.

The traditional treatment of the lithosphere as a rheologically homogeneous body is now recognised to be an oversimplification. A more realistic model is of a strong elastic layer overlying ductile material and the evidence for this division can be summarised in a number of points:

1) Laboratory experiments of Griggs et al. (1960) showed that at low temperatures and relatively low pressures rocks deform by brittle fracture whereas at 500 MPa confining pressure and temperatures of 500 to 800°C the mode of deformation is a flow mechanism. Results of this type have been confirmed by more recent experiments (see sections 2.5 and 2.8).
2) Intraplate earthquakes are restricted to the upper part of the lithosphere. The maximum depth of earthquakes along the Calaveras fault zone of the San Andreas fault system is 15 km (Bufe et al., 1977) whereas for older, cooler zones, such as shield areas,

seismicity extends to depths of 30 to 40 km and in the Russian platform fault zones extend to about 60 km (Sollogub,Guterch cited in Vetter and Meissner, 1979). Vetter and Meissner (1979) suggested a correlation between the temperature regime and the maximum depth of seismicity with brittle behaviour extending to 15 to 20 km for a warm lithosphere and 50 to 60 km for a cold lithosphere.

3) Studies of lithospheric flexure as a result of surface loading, by Walcott (1970), showed that the effective thickness of the elastic lithosphere decreases with increasing time scales of loading. He calculated a value of 20 km for the thickness of the elastic lithosphere in the Basin and Range province. Calculations by Murrell (1976) based on published values of flexural rigidity also suggested a thickness of 20 km for the elastic lithosphere for warm continental regions. Similar calculations on the flexure of the oceanic lithosphere (Watts, 1978) suggested an elastic layer thickness of 20 to 30 km for the Pacific oceanic lithosphere.

It therefore seems reasonable to divide the lithosphere into a 20 km thick elastic layer overlying 80 km of ductile material. It also seems not unreasonable to equate the elastic layer with the upper crust. Figure 2.1 illustrates the lithosphere model that has been arrived at in this and the preceding section.

2.4 Theories of Brittle Fracture

2.4.1 The Coulomb criterion

Coulomb's criterion for shear failure in a plane is

$$|\tau| = S_0 + \mu\sigma_n \qquad 2.1$$

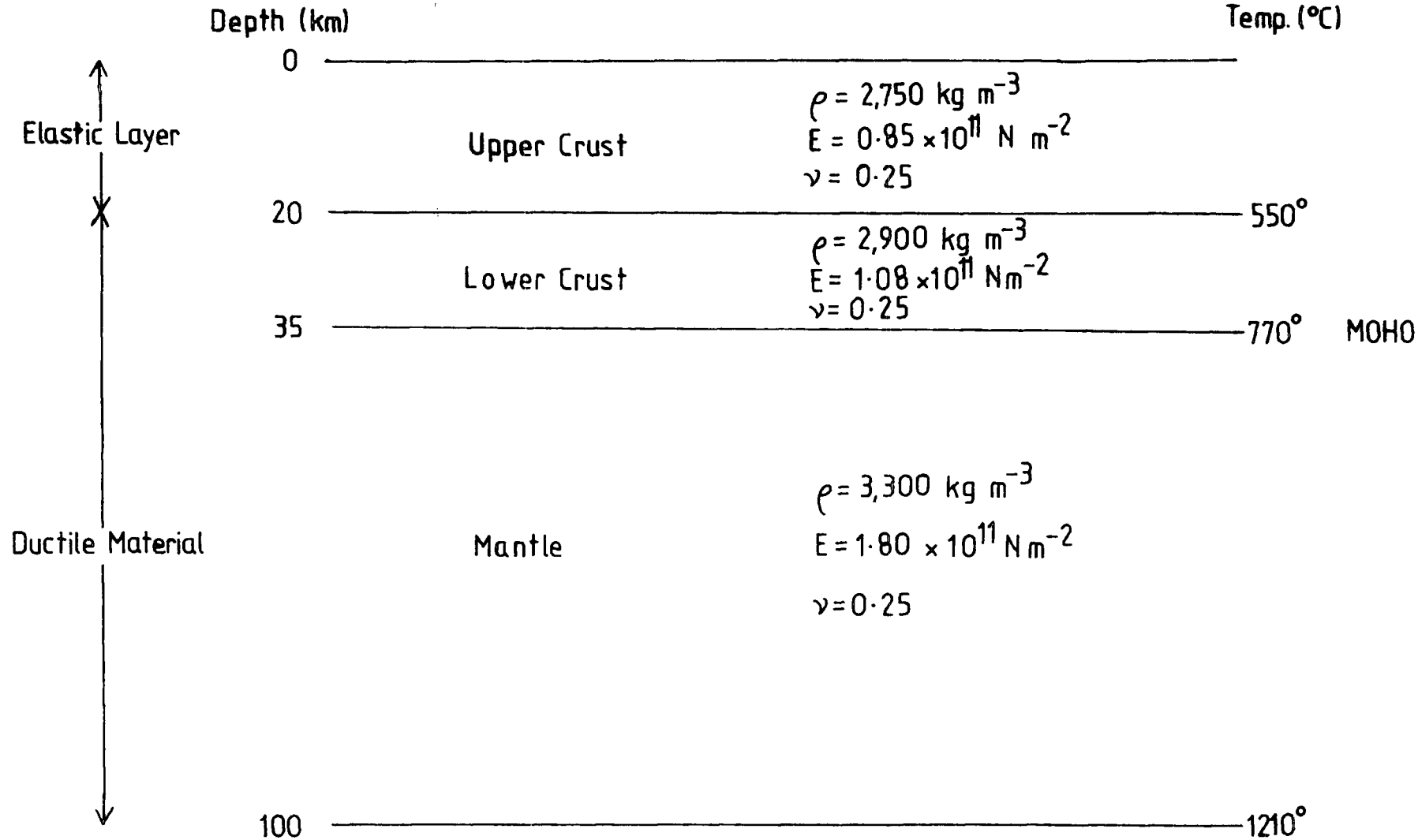

Fig. 2.1: Model of the lithosphere

where τ is the shear stress, σ_n is the normal stress, S_0 is the shear strength or cohesion and μ is the coefficient of internal friction. This can also be written

$$|\tau| = S_0 + \sigma_n \tan\phi \qquad 2.2$$

where ϕ is the angle of internal friction. By expressing τ and σ_n in terms of principal stresses and the angle of the fracture plane, θ', the following expression can be obtained

$$\theta' = \frac{\pi}{4} - \frac{1}{2}\phi \qquad 2.3$$

The sign of θ' can be changed without affecting the analysis which leads to the important conclusion that there are two possible conjugate planes of fracture passing through the direction of the intermediate principal stress and making angles of less than 45° with the direction of the maximum principal stress. For a more complete description of the Coulomb criterion the reader is referred to Jaeger and Cook (1976).

2.4.2 Mohr's hypothesis

Mohr proposed that when shear failure takes place across a plane, the normal stress, σ_n, and the shear stress, τ, across the plane are related by a functional relation characteristic of the material:

$$|\tau| = f(\sigma_n) \qquad 2.4$$

Equation 2.4 can be plotted in $\tau - \sigma_n$ space and Mohr circles can be plotted on the diagram for any stress system. If a Mohr circle touches the curve

given by equation 2.4 then failure will occur for that particular stress system. This hypothesis assumes that the value of the intermediate principal stress, σ_2, does not affect failure of the material.

The functional relation 2.4 is normally obtained experimentally as the envelope of Mohr circles corresponding to failure under a variety of conditions, and is consequently known as the Mohr envelope. The Mohr envelope for the Coulomb criterion is a straight line and is shown in Figure 2.2. This example and other types of envelope are discussed by Jaeger and Cook (1976).

2.4.3 The Modified Griffith Theory

Griffith developed a theory of brittle fracture which assumed that fracture is caused by stress concentrations at the tips of small Griffith cracks which are present throughout the material. This theory has been further modified by McLintock and Walsh (1962) to include the situation where the Griffith cracks close under sufficiently high compressive stresses and frictional forces become important. Griffith theory was developed by studying the variation of the tangential stress on the surface of a flat elliptical crack. Several good treatments exist in press (e.g. Murrell, 1964a,b; Jaeger and Cook, 1976) and the mathematics will not be covered here.

The original theory allowed for two types of failure: tensional failure and open crack shear failure. The work of McLintock and Walsh introduced a third regime of closed crack failure. In general, however, the limits of the open crack and closed crack regimes do not coincide. This is apparent when the Mohr envelope is constructed (Figure 2.3). In this thesis, the author has chosen to define a transitional regime between open and closed crack shear failure, which is shown in Figure 2.3.

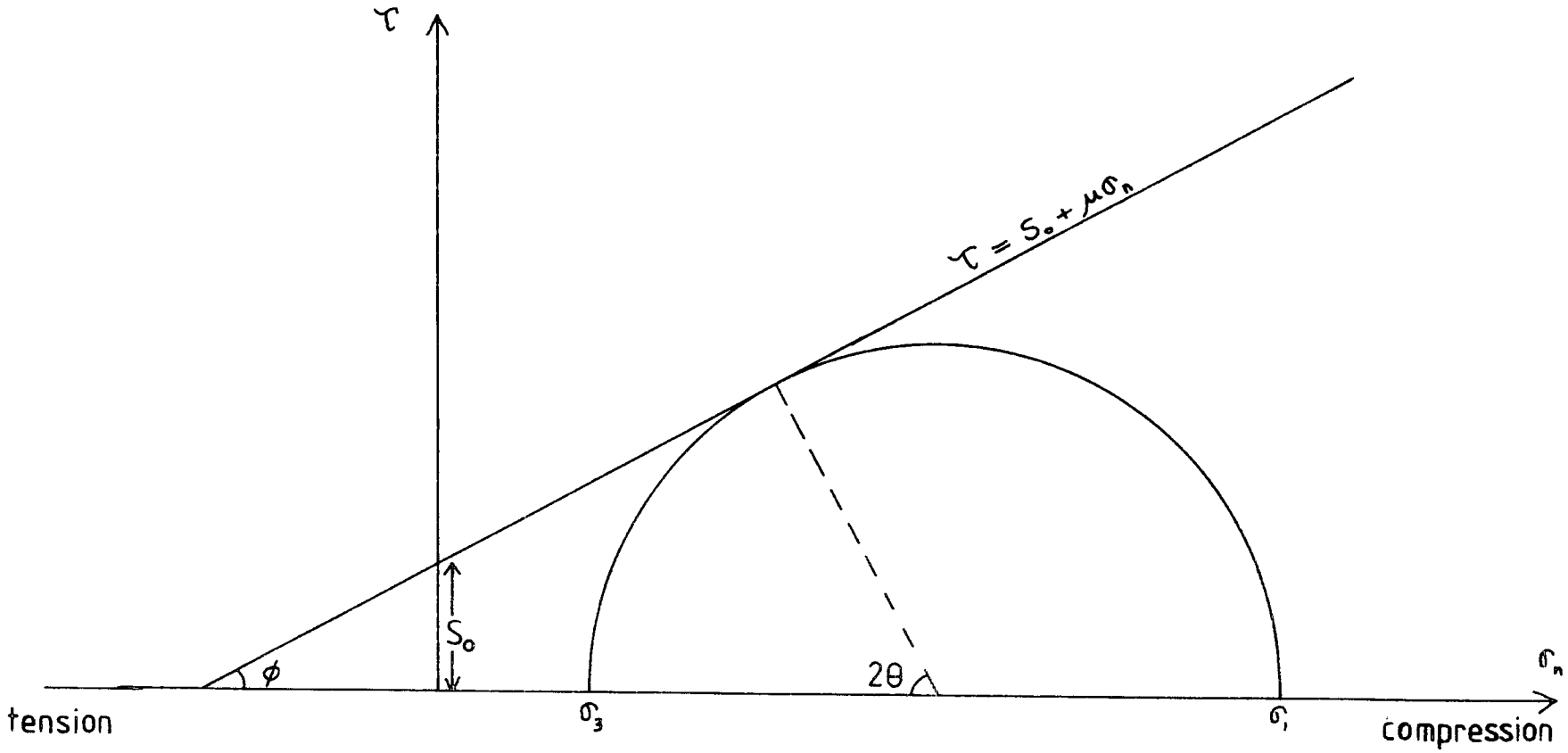

Fig. 2.2: Mohr envelope for the Coulomb criterion.

The criteria for failure are often quoted in terms of maximum and minimum principal stress (with compression positive). Here they are described in terms of maximum shear stress and mean stress, representing the radius and centre of the Mohr circle respectively, with tension positive, in line with their use in the subroutine ELFAIL of the finite element library FELIB (see Appendix 2). The following symbols are used:

T - the tensile strength

μ_F - the coefficient of friction on closed Griffith cracks

σ_c - the compressive stress necessary to close the cracks

θ - the angle between the fracture plane and the maximum stress (most tensile stress)

σ_m - the mean stress, $\frac{\sigma_1 + \sigma_2}{2}$

τ_m - the maximum shear stress, $\left|\frac{\sigma_1 - \sigma_2}{2}\right|$

The four failure criteria are

1) Tensional failure:

If $2\sigma_m + \tau_m \geqslant 0$,

then failure occurs if $\tau_m \geqslant T - \sigma_m$

with $\theta = 90°$

2) Open crack shear failure:

If $2\sigma_m + \tau_m < 0$

and $\sigma_m > \sigma_c - 2T$

then failure occurs if $\tau_m^2 \geqslant -4T\sigma_m$

with $\theta = \frac{1}{2}\cos^{-1}\left(\frac{\tau_m}{2\sigma_m}\right)$

3) Transitional regime failure:

If $2\sigma_m + \tau_m < 0$

and $\sigma_m < \sigma_c - 2T$

and $\sigma_m > \sigma_c - 2\mu_F\, T(1 - \frac{\sigma_c}{T})^{\frac{1}{2}}$

then failure occurs if $\tau_m^2 \geqslant 4T^2(1 - \frac{\sigma_c}{T}) + (\sigma_c - \sigma_m)^2$

with $\theta = \frac{1}{2}\tan^{-1}\dfrac{(2T(1 - \sigma_c/T)^{\frac{1}{2}})}{\sigma_c - \sigma_m}$

4) Closed crack shear failure:

If $2\sigma_m + \tau_m < 0$

and $\sigma_m < \sigma_c - 2\mu_F\, T(1 - \frac{\sigma_c}{T})^{\frac{1}{2}}$

then failure occurs if $\tau_m \geqslant \dfrac{2T}{(\mu_F^2 + 1)^{\frac{1}{2}}} \cdot (1 - \frac{\sigma_c}{T})^{\frac{1}{2}} + \dfrac{\mu_F}{(\mu_F^2 + 1)^{\frac{1}{2}}} \cdot (\sigma_c - \sigma_m)$

with $\theta = \frac{1}{2}\tan^{-1}\left(\frac{1}{\mu_F}\right)$

The Mohr envelope for open crack failure is a parabola

$$\tau^2 = 4T(T - \sigma_n) \qquad 2.5$$

and for closed cracks is a straight line

$$\tau = 2T(1 + \frac{\sigma_c}{T})^{\frac{1}{2}} - \mu\sigma_c + \mu\sigma_n \qquad 2.6$$

The transitional regime represents all Mohr circles which touch the envelope at the intersection of the two envelopes. The full envelope for the Modified Griffith Theory is illustrated in Figure 2.3.

2.4.4 Effect of pore pressure on failure criteria

A porous solid will have an internal pore pressure if the pores are filled with a fluid. The effect of this pore pressure has been incorporated into rock mechanics studies using the concept of effective stress, which was originally introduced for use with saturated soils.

If p is the pore pressure and σ_1, σ_2, σ_3 are the total principal stresses, then the effective stresses are

$$\sigma_i^e = \sigma_i - p, \qquad i = 1, 3 \tag{2.7}$$

Studies of rock deformation with pore pressures present (summarised in Jaeger and Cook, 1976) are in general agreement with this effective stress law.

The Coulomb criterion then becomes

$$|\tau| = S_0 + \mu(\sigma_n - p) \tag{2.8}$$

and the effective mean stress in the Modified Griffith Theory becomes

$$\sigma_m^e = \sigma_m - p \tag{2.9}$$

Consequently, for the Mohr envelope representation of a failure criterion, the shear stress, τ, is not altered by a pore pressure but the normal stress, σ_n, is reduced. The effect of this is to move the Mohr circles towards the origin without affecting their radii. Thus

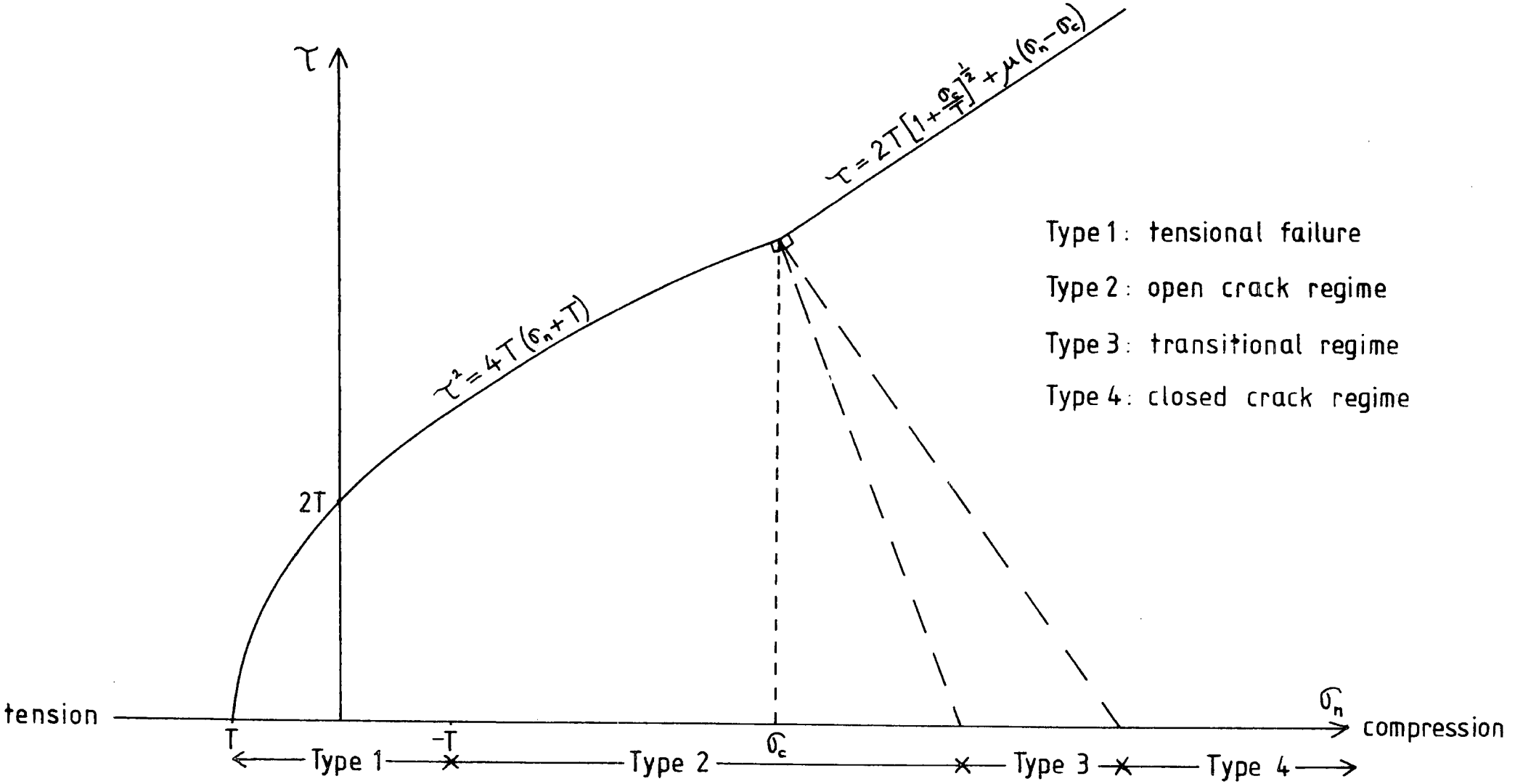

Fig. 2.3: Mohr envelope for the Modified Griffith Theory.

failure will be more likely if pore pressure is present or if the pore pressure is increased.

This concept of effective stress has been used by Hubbert and Rubey (1959) as a means of explaining how overthrust faulting can occur.

2.5 Experimental results on the brittle fracture of rocks

Fractures in rocks can be divided into two classes: extension fractures involving separation of a body across a surface normal to the direction of maximum tensile stress, and faults with an offset parallel to the direction of the fracture plane and inclined at an angle to the principal stress axes (Griggs and Handin, 1960). Extension fractures require an absolute tensile stress and, consequently, are not common in geological situations because of the compressive horizontal component of the overburden pressure. Faults are seen on all scales and can be divided into normal, reverse (or thrust) and transcurrent faults depending on the relative magnitudes of the principal stresses (Anderson, 1951), as illustrated in Figure 2.4.

Early work on fracture was usually interpreted using the Coulomb criterion. The angle between the shear plane and the direction of maximum principal stress (most compressive) is given by

$$\theta = \frac{\pi}{4} - \frac{1}{2}\phi \qquad \text{(equation 2.3)}$$

Measured values of ϕ were typically about 36°, though covering a wide span (summarised in Heiskanen and Vening Meinesz, 1958), giving an angle of 27° between the shear plane and the direction of maximum stress. This is in good agreement with the observation that many normal faults dip at angles of about 63°.

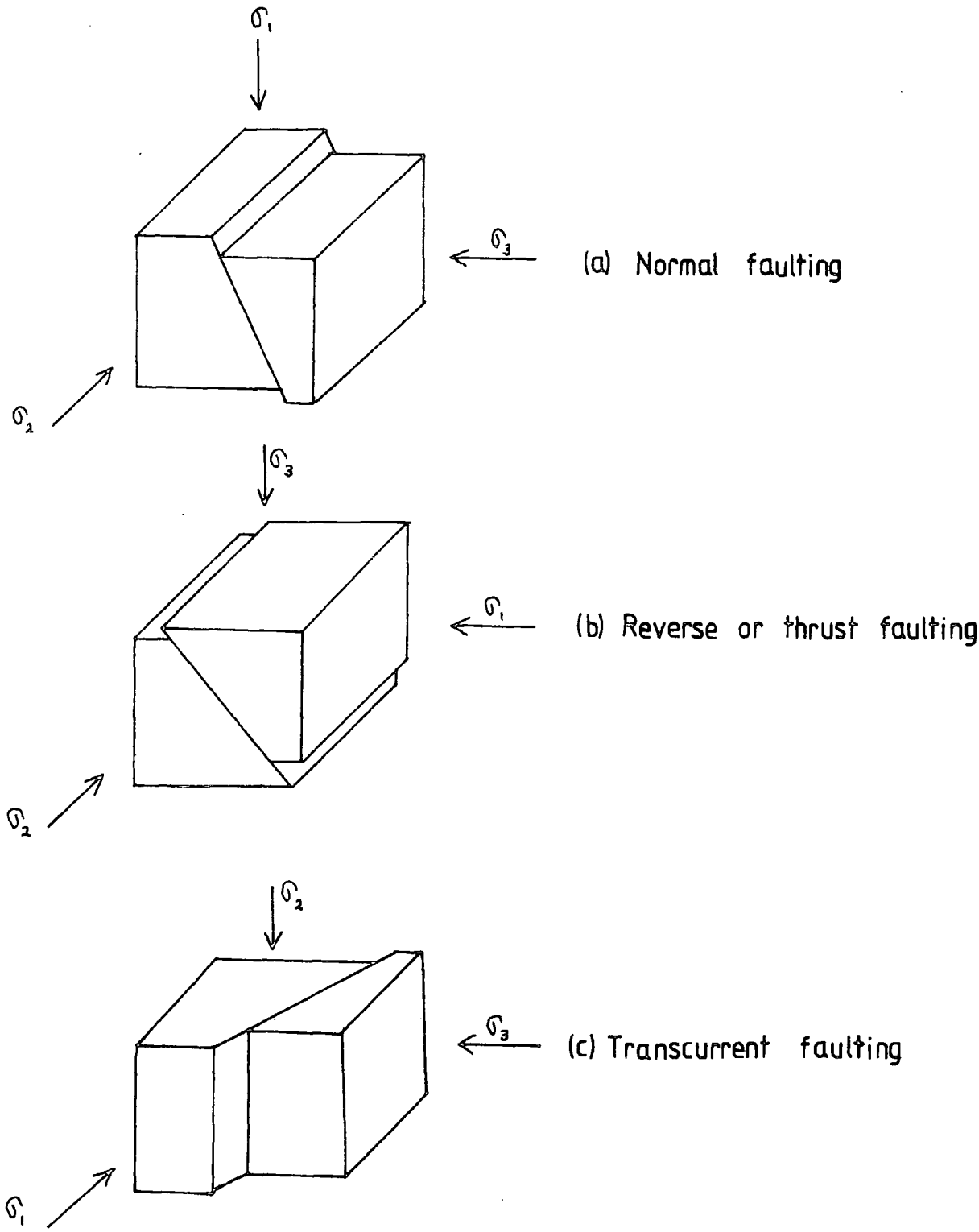

Fig. 2.4: Classification of faulting

σ_1 = maximum principal stress (most compressive)

σ_2 = intermediate principal stress

σ_3 = minimum principal stress

More recent work has shown that Mohr envelopes constructed from failure tests on rocks are generally characterised by straight line envelopes apart from a low pressure region where the envelope is concave (Brace, 1964; Mogi, 1974). This is in agreement with the envelope obtained from the Modified Griffith Theory (Figure 2.3). The two-dimensional theory used here is a reasonable approximation as the value of the intermediate principal stress has only a small effect on the fracture (Brace, 1964; Handin, 1969). Further support for the Modified Griffith Theory is that it is believed to be approximately correct for other brittle material, such as glass (Griffith, 1921). Also, the microscopic study of partially fractured material suggests that the fractures start at grain boundaries which, in the absence of larger scale features, are interpreted as being Griffith cracks (Brace, 1964).

Although the Griffith theory is generally accepted there are certain areas in which considerable problems exist. The predicted and observed tensile strengths of rocks do not agree closely, probably due to large uncertainties in the theoretical parameters and a large range of grain diameters (Brace, 1964), and the ratio of compressive strength to tensile strength is in poor agreement with the theory. The angles of the failure planes predicted by the theory may be different from those observed. This is because a crack in a field of compression does not propagate in its own plane but curves towards the direction of the compression and dies out (Bombolakis and Brace, 1963; Brace and Byerlee, 1967). The development of compressional fractures is probably caused by en echelon cracks joining up (Brace, 1964) and, consequently, a crack array will develop an instant before the fault forms. The effect of neighbouring cracks on the stress concentration at crack tips is obviously an important factor, but at the present time little is known

of this effect.

Despite these difficulties the Modified Griffith Theory seems to be the most reasonable set of failure criteria available and it is used later in this thesis. In order to use this theory it is necessary to select values for the tensile strength, T, the coefficient of friction between the crack faces, μ_F, and the stress necessary to close the cracks. σ_C. Table 2.2 shows a compilation of tensile strengths that have been determined for igneous rocks. A reasonable value for a hard, crystalline rock would seem to be 12 MPa. McLintock and Walsh (1962) compared experimental data with the theory for μ_F equal to 0, 0.5 and 1 and σ_C equal to 0, -3T and -15T and found a reasonable fit for $\mu_F = 1$, $\sigma_C = -3T$. Brace (1964) found that experimental data coincided with the Modified Griffith theory for values of μ_F between 0.9 and 1.5 and suggested that a value of 1 was probably not unreasonable. Murrell (1965) suggested, from analytical work, values of $\mu_F = 1.09$ and $\sigma_C = -4.19T$. A value of 1 for μ_F thus seems to be a reasonable choice. This value is larger than has been observed in rock-on-rock sliding experiments (see section 2.6) and it has been suggested by Ashby and Verrall (1978) that this may be because the crack faces are serrated and key together when under compression. A value of approximately -4T for σ_C, however, seems to be very small since for T = 12MPa the closure stress is only 48 MPa. Digby and Murrell (1976) showed that a value of $\sigma_C = -10T$ is better and this is in agreement with some experimental observations (Murrell, 1977). Recent work by Wang and Simmons (1978) showed that gabbro at a depth of approximately 5.3 km in the Michigan basin had few open microcracks. Core samples brought to the surface gave a closure pressure of 145 MPa, approximately equal to the in situ vertical stress. This value, supposing that the tensile strength lay between

Sample	Tensile Strength (MPa)	Reference
Granite	21.0 12.0 12.0	Brace[1], 1964
Trachyte	13.7 12.0 24.1 25.2	Jaeger and Cook[2], 1976
Granite	14.0 11.4 12.5	Goldsmith, Sackman and Ewert[3], 1975

Table 2.2: Tensile strengths of igneous rocks

1 Range of confining pressure from 30 MPa to 159 MPa

2 Results refer to different types of test; data from Jaeger and Hoskins (1966)

3 Results for 3 different directions under dynamic tension test. Average for 3 directions is 12.6 MPa

10 and 20 MPa, is in agreement with $\sigma_c = -10T$, which is the value used in this thesis.

2.6 Friction on faults

The frictional strength of a rock can be defined as the shear stress necessary to cause sliding on a pre-existing fracture or fault under specified conditions of confining pressure (normal stress), temperature, pore pressure and loading rate. It has been found by experimental studies that the frictional strength is, to within ± 10 to 15%, independent of mineralogy, temperature and loading rate and the dominant parameter is the normal stress (Stesky, 1978).

The frictional strength is usually defined as (Byerlee, 1978)

$$\tau = \mu\sigma_n$$

$$\text{or} \quad \tau = A + B\sigma_n \text{ where } \mu = B + \frac{A}{\sigma_n}$$

although other, more complex, relationships have been proposed (e.g. Murrell, 1965).

Experiments on rock-on-rock sliding reveal two dominant mechanisms of slip; stick slip and stable sliding (Byerlee, 1967; Johnson, 1975). Stick slip movement is characterised by intermittent rapid displacements accompanied by elastic radiation and has been considered to be the mechanism of earthquake generation on faults (Brace and Byerlee, 1967), whereas stable sliding is a steady, uniform movement and may be analogous to aseismic fault creep. The conditions that determine the type of sliding are complex, but in general stick slip is enhanced by high normal stresses, low temperatures, the presence of strong brittle

minerals such as quartz and feldspar, the absence of fault gouge, and low surface roughness (Stesky, 1978).

Figure 2.5 is a graph of shear stress against normal stress at the onset of sliding for a variety of rock types and is taken from Byerlee (1978). The data were best fitted by two equations:

$$\tau = 0.85\ \sigma_n \qquad \sigma_n < 2\ \text{kb} \qquad (1\ \text{kb} = 100\ \text{MPa})$$

$$\tau = 0.5 + 0.6\ \sigma_n \qquad 2\ \text{kb} < \sigma_n < 20\ \text{kb}$$

giving coefficients of friction

$$\mu = 0.85 \qquad \sigma_n < 2\ \text{kb}$$

and $$\mu = 0.6 + \frac{0.5}{\sigma_n} \qquad 2\ \text{kb} < \sigma_n < 20\ \text{kb}$$

Clearly, at high normal stresses

$$\mu \simeq 0.6$$

Values of between 0.6 and 0.85 are typical for rock-on rock sliding experiments.

A coefficient of friction of 0.6 will require very high shear stresses at depth for fault movement to occur because of the high normal stresses. For movement at 15 km we can consider the normal stress to be of the order of 500 MPa (due to the overburden). So for slip to occur

$$\tau = 0.6 \times 500 = 300\ \text{MPa}$$

If this is the maximum shear stress (the least favourable consideration

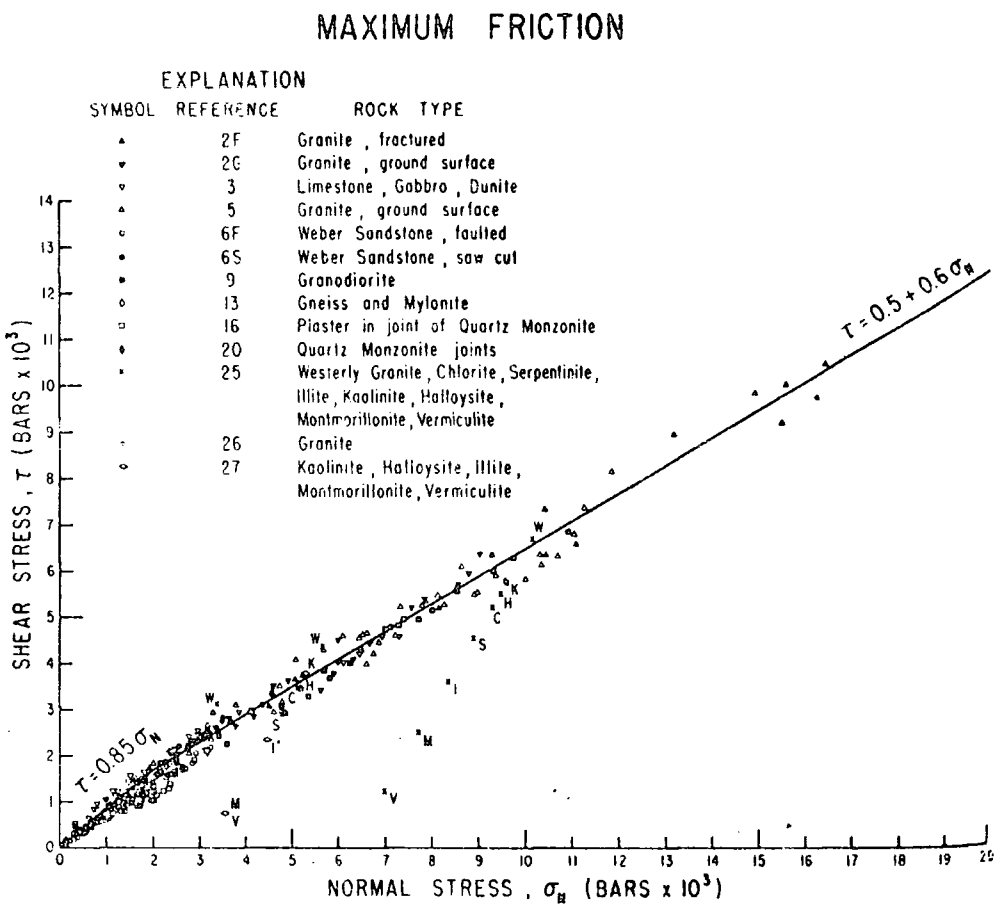

Fig. 2.5: Shear stress plotted as a function of normal stress, at the maximum friction, for a variety of rock types. (after Byerlee, 1978)

for this discussion) then the stress difference is

$$\sigma_D = 2\tau = 600 \text{ MPa}$$

and this is probably an unrealistically high value. The absence of a clear heat flow anomaly across the San Andreas fault has been interpreted to indicate a shear stress on the faults of no more than 20 MPa (Brune et al., 1969). Considerations of the energy budget available for normal faulting by Bott (1976) also suggested that the effective coefficient of friction must be considerably lower than 0.6 for fault movement to occur.

Consequently, it is necessary to propose a method of reducing the friction coefficient for in situ faults. There are two mechanisms available for this. Firstly, if a pore pressure is present the friction law must be modified to deal with the effective normal stress,

$$\tau = \mu(\sigma_n - p)$$

where p is the pore pressure. This will obviously result in a lower frictional strength. The second method of reducing the friction coefficient is the presence, and nature, of fault gouge. The points on Figure 2.5 marked M,V and I, referring to montmorillonite, vermiculite and illite, are seen to lie some distance below the best-fit line. Clearly for these clay minerals the effective coefficient of friction is much less than 0.6. Recent experiments by Wang and Mao (1979) on shearing of saturated clays in rock joints at high confining pressure found that the shear stress required to initiate sliding increases linearly with effective normal stress, the slope (the coefficient of friction) being 0.08 for montmorillonite, 0.12 for chlorite, 0.15 for kaolinite and 0.22 for illite. Thus the coefficient of friction for a

fault containing a saturated clay gouge is likely to be of the order of 0.1. Evidence that clay gouge can exist in fault zones at significant depths has been discussed by Wu (1978) and can be summarised in four points:

1) Pressure / temperature studies suggest that clays are stable at depth within the upper crust.
2) Clays of the types investigated above have been found in deep mines and tunnels.
3) Seismic and gravity studies of the San Andreas fault zone are compatible with laboratory data on clay gouges and suggest that gouge may exist down to a depth of 10 or 15 km (Wang et al., 1978).
4) Clays have been found to be capable of undergoing sudden earthquake-like displacements (Summers and Byerlee, 1977).

2.7 Creep mechanisms

The typical creep behaviour of a material undergoing constant stress at a constant pressure and temperature is shown in Figure 2.6. There is an instantaneous elastic strain (ε_0) followed by a period of transient creep (region I) during which the strain rate decreases. The change in the strain rate is due to changes in one or more of the parameters which affect the creep process, such as the dislocation density or dislocation structure. As these parameters become stable a period of steady state creep (region II) ensues in which the strain rate is constant. Finally, the strain rate may increase again prior to failure giving a period of tertiary creep (region III). Any of these major regions of the creep curve may be suppressed or enhanced depending on the material and physical conditions. At a given confining pressure an increase in the stress difference or the temperature enhances the rates of transient and steady state creep and favours the steady state (Carter and Kirby, 1978).

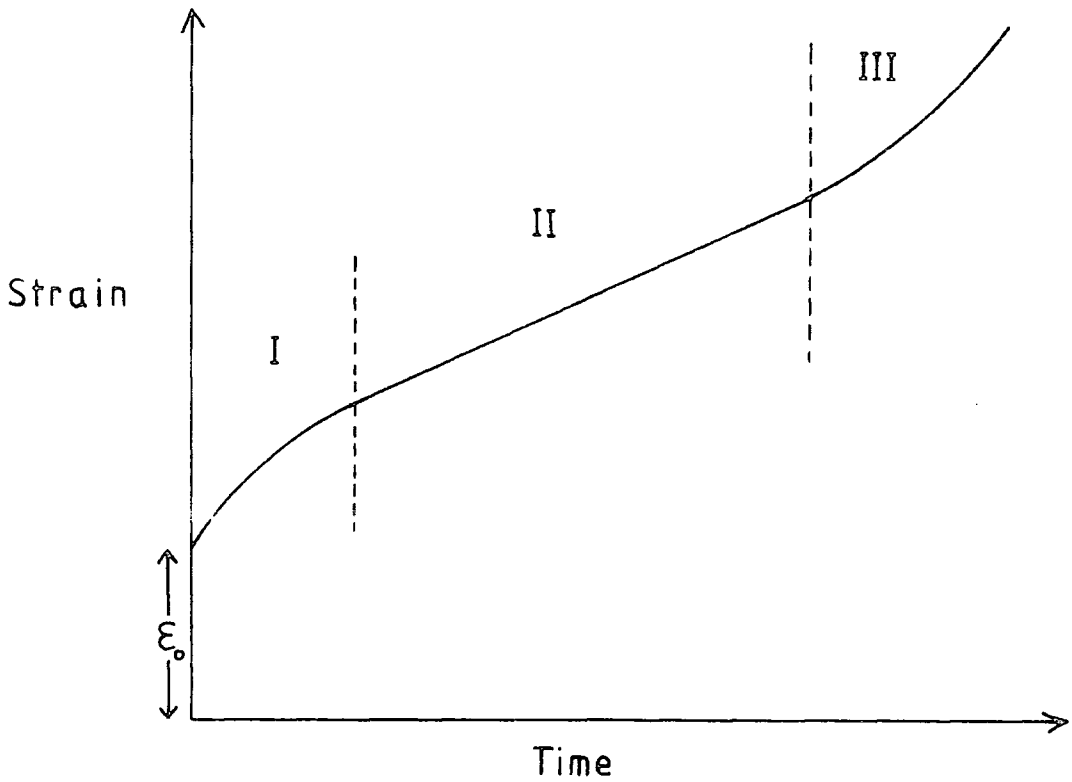

Fig. 2.6: A typical strain-time curve for a creep test.

ε_0 initial elastic strain
I transient creep region
II steady state creep region
III tertiary creep region

Tertiary creep is favoured in a situation where one or more of the principal stresses is tensile due to accelerated creep processes associated with voids (Misra and Murrell, 1965). This is consistent with the observation that an increase in confining pressure inhibits the tertiary stage (Carter and Kirby, 1978). Consequently, tertiary creep would not be expected to be an important factor in deformation in the lower lithosphere where the stress regime will, in general, be compressive due to the overburden.

Transient creep has been described by two empirical laws (Weertman and Weertman, 1975; Murrell, 1976). The first of these is a logarithmic law applicable for small strains and temperatures less than $0.2T_m$, where T_m is the melting temperature, and has the form

$$\varepsilon = \alpha_0 \log (1 + vt) \qquad 2.10$$

where α_0 and v are constants and other symbols in this section are listed in Table 2.3. The second empirical law, which applies at higher temperatures, is of the form

$$\varepsilon = Bt^m \qquad 2.11$$

where the power index m lies in the range 1/3 (giving Andrade's law) to 1/2 (Murrell and Chakravarty, 1973). B is a function of stress and temperature and has been described by Murrell (1976), based on experimental work, as

$$B = B_0 \left(\frac{\sigma_s}{G}\right)^n \exp\left(-\frac{E}{kT}\right) \qquad 2.12$$

where B_0 is a constant.

The transition to steady state creep occurs when the transient

Symbol	Material Property
ε	strain
$\dot{\varepsilon}$	strain rate
t	time
T	temperature in °K
T_m	melting temperature
k	Boltzmann's constant
σ_s	shear stress, $\frac{\sigma_1 - \sigma_3}{2}$
σ_D	differential stress, $\sigma_1 - \sigma_3$
G	shear modulus
E	activation energy for transient creep
Q	activation energy for steady state creep
V	activation volume
P	pressure
Ω	atomic volume
d	grain diameter
δ	thickness of grain boundary diffusion path
b	Burger's vector
D	diffusion coefficient
D_0	pre-exponential diffusion constant
D_V	volume diffusion coefficient
D_B	grain boundary diffusion coefficient

Table 2.3: Symbols used in creep laws

creep rate falls to the value of the steady state creep rate. This situation has been seen to occur after strains of about 10^{-2} (Goetze and Brace, 1972; Durham and Goetze, 1977).

The two most important mechanisms for steady state creep are diffusional flow and dislocation creep. Diffusional flow involves the mass transport of atoms by diffusional processes from one grain boundary to another. An account of the mechanics of this process, and of others mentioned here, is given in Nicolas and Poirier (1976). Diffusion of atoms through grains (lattice diffusion) is known as Nabarro-Herring creep after early investigators of this mechanism. The steady state equation is (Weertman and Weertman, 1975)

$$\dot{\varepsilon} = \frac{\alpha D \Omega}{d^2 kT} \cdot \sigma_s \qquad 2.13$$

where α is a constant. Temperature and pressure affect the creep rate primarily through the diffusion coefficient, D, which is given by (Weertman and Weertman, 1975)

$$D = D_0 \exp\left(-\frac{Q + PV}{kT}\right) \qquad 2.14$$

where D_0 is a constant. Mass transport can also take place along grain boundaries, through grain boundary diffusion. This is called Coble creep and its effect can be incorporated in equation 2.13 by replacing the diffusion coefficient, D, by an effective diffusion coefficient, D_{eff} (Stocker and Ashby, 1973; Ashby and Verrall, 1978), giving

$$\dot{\varepsilon} = 42 \frac{D_{eff}\, \Omega}{d^2 kT} \cdot \sigma_s \qquad 2.15$$

where $D_{eff} = D_V \left[1 + \frac{\pi\delta}{d} \frac{(D_B)}{(D_V)} \right]$ 2.16

Since the strain rate depends linearly on the stress this mechanism is essentially Newtonian and can be simplified to

$$\dot{\varepsilon} = \frac{1.\sigma_s}{2\eta} \qquad 2.17$$

where the viscosity, η, is a function of temperature and pressure:

$$\eta = \eta(T,P) \qquad 2.18$$

Dislocation creep is controlled by the movement of dislocations and is generally divided into dislocation glide and dislocation climb depending on the nature of the movement (Weertman and Weertman, 1975; Nicolas and Poirier, 1976). The mechanisms predict a steady state creep equation of the same basic form

$$\dot{\varepsilon} = A' \frac{DGb}{kT} .\left(\frac{\sigma_s}{G}\right)^n \qquad 2.19$$

where A' is a constant. If the cells between which the dislocations move are thought of as small grains, then dislocation creep can be interpreted as a kind of diffusional flow. Since the cell size depends on stress the creep is no longer Newtonian. Observations on metals show that the cell size, d, is given by

$$\frac{d}{b} \simeq \frac{G}{\sigma_s} \qquad 2.20$$

Inserting this into equation 2.13 for diffusional flow, and using the relationship

$$\Omega \simeq b^3 \qquad 2.21$$

gives equation 2.19 for dislocation creep (Ashby and Verrall, 1978). The power index, n, can be estimated for olivine by substituting for the parameters in equation 2.19. n has the value of $\sim$3 for climb-

controlled creep and ~ 5 for glide-controlled creep, which occurs at higher stresses. The constant A' is also different for these two mechanisms.

Since the strain rate for these processes depends on some power of the applied stress, these mechanisms are often referred to as power law creep and expressed in a simplified form of equation 2.19

$$\dot{\varepsilon} = A \exp \left(\frac{-Q + PV}{kT}\right) \sigma_s^{\,n} \qquad 2.22$$

2.8 Experimental results on creep of rocks

Transient creep parameters for crystalline rocks deformed to strains less than 10^{-2} have been determined by Misra and Murrell (1965), Goetze (1971), Goetze and Brace (1972) and Murrell and Chakravarty (1973) and a useful summary of their results is given in Carter and Kirby (1978). Transient creep is not used in this thesis (see section 2.9) and their values are consequently not quoted here.

High temperature, steady state creep in olivine and olivine-rich rocks has been investigated by many workers. In general their results have supported a power law creep mechanism and have been interpreted in the form

$$\dot{\varepsilon} = A \exp \left(\frac{-Q}{kT}\right) \sigma_D^{\,n} \qquad 2.23$$

where σ_D is the differential stress. Their results are summarised in Table 2.4. In order to make references to the original papers easier, the values are quoted in the traditional units. Equation 2.23 differs from the previous equation in that the pressure effect is not included in the exponential term. The activation volume, V, is poorly-known and experiments are usually performed at a constant confining pressure.

Dry single crystal olivine, $F_{0_{92}}$		125 ± 15	3 ± 1	0.01	1150 - 1650	0.1 - 1.5	Kohlstedt et al. 1976.
Dry single crystal olivine, $F_{0_{92}}$	5.3×10^{11}	125	3.6 ± 0.3	0.01	1150 - 1650	0.1 - 1.8	Durham & Goetze[6] 1977
Synthetic $F_{0_{100}}$	3×10^{7}	159 ± 6	2.85 ± 0.16	0.01	1480 - 1750	0.015-0.378	Durham et al. 1979

Table 2.4: Experimentally derived steady-state creep parameters

1. Results are interpreted in terms of the differential stress, $\sigma_D = (\sigma_1 - \sigma_3)$
2. Results originally interpreted in terms of effective shear stress. A has been adjusted for differential stress; $\sigma_D = 2\sigma_s$
3. Re-interpretation of data of Carter and Ave'Lallemant (1970).
4. Interpreted from data of Heard and Carter (1968).
5. First value from collapse of dislocation loops by annealing; second value from climb of dislocations.
6. Values of A and n observed to be slightly dependent on crystal orientation.
7. 1 kcal mol^{-1} = 4.186 kJ mol^{-1}

Weertman (1970) has suggested using the empirical relation

$$\exp\left(\frac{-Q + PV}{kT}\right) = \exp\left(\frac{-g\ T_m}{T}\right) \qquad 2.24$$

where g is a dimensionless constant and T_m is the melting temperature at pressure P. However the activation energy and volume must still be estimated in order to calculate g.

Experimental results together with theoretical calculations of strain rates based on the physical properties of a wide variety of materials enable deformation maps for olivine to be plotted (Stocker and Ashby, 1973; Ashby and Verrall, 1978). An example of these is shown in Figure 2.7, taken from Stocker and Ashby (1973) and also discussed by Goetze (1978).

2.9 Discussion of creep laws for the lower lithosphere

The importance of transient creep in the lithosphere is not well known. Surface loads, which usually cause small strains, may be relaxed by transient creep processes (Durham et al., 1979). This throws considerable doubt on steady state creep results obtained from isostatic rebound studies. Cathles (1975) has suggested that the Fennoscandia rebound data are inconsistent with a power law with n significantly greater than 1. The same data (with different assumptions) were used by Post and Griggs (1973) to support their power law with n equal to 3. Weertman (1978) has pointed out that the total strains during rebound are of the order of 10^{-3} and consequently should not be considered to be produced by steady state creep. Goetze and Brace (1972) have suggested that the extrapolation of transient creep data to the much lower strain rates observed under Fennoscandia is too great to be reasonable. Strains resulting from tectonic stresses acting on lithospheric plates may be associated with an initial transient period. The length of this transient

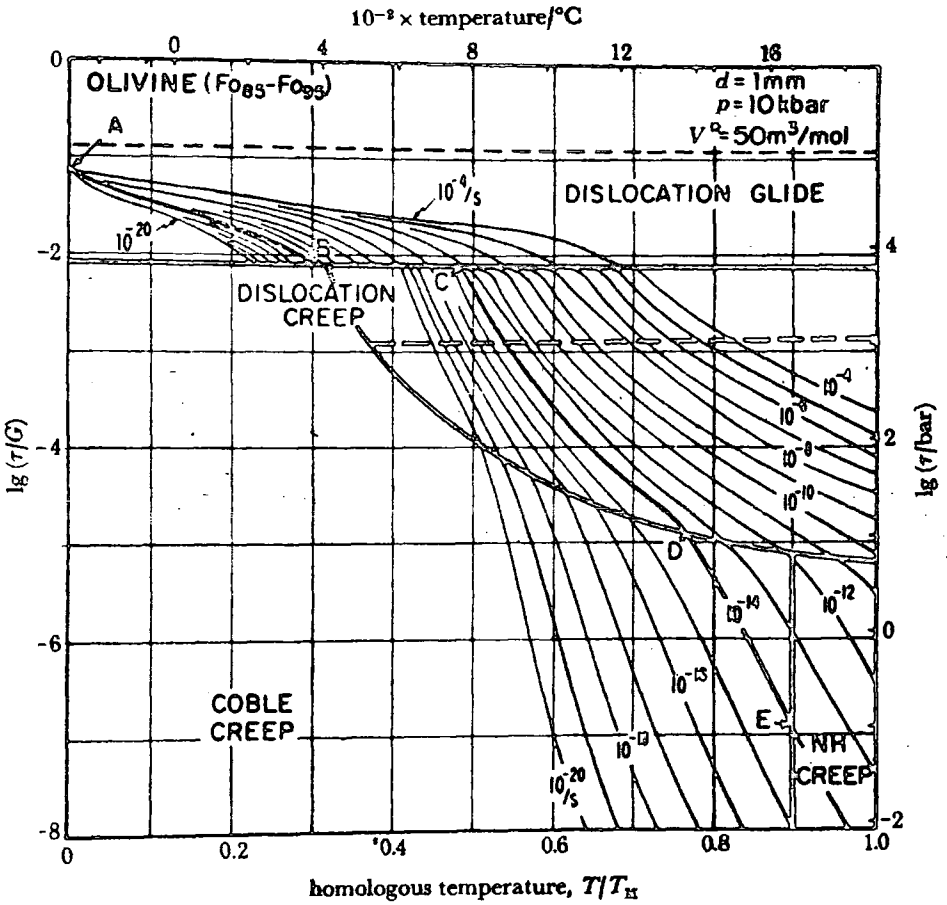

Fig. 2.7: Deformation map for olivine (after Stocker and Ashby, 1973)

will depend on factors such as the amount of pre-straining (Durham et al., 1979) and other physical conditions (Carter and Kirby, 1978). Because of this uncertainty, and because of the long term tectonic stresses considered to be acting on the lithosphere, transient creep will not be used in this thesis.

Two mechanisms of steady state creep will be considered. The first is Newtonian, and is expressed as

$$\dot{\varepsilon} = \frac{1}{2\eta} \cdot \sigma_s \qquad 2.25$$

where the viscosity, η, is regarded as a constant. The experimental evidence and the deformation map (Figure 2.7) both suggest that diffusional flow will not be the dominant mechanism in the lower lithosphere. Nevertheless, considerable numerical work has been done using a creep law of this form (e.g. Kusznir and Bott, 1977) and since it is the simplest it is useful for investigating the effect of viscosity contrasts between the lower crust and the upper mantle, which could be concealed by a more complex law.

The second mechanism that will be used in this thesis is power law creep of the form

$$\dot{\varepsilon} = A \exp(-\frac{Q}{kT}) (\sigma_s)^n \qquad 2.26$$

The deformation map of olivine (Figure 2.7) suggests that for the temperature and stress ranges applicable to the lower lithosphere, this is the most appropriate law. For use in the analysis, equation 2.26 must be written in tensor form (as must equation 2.25) and this is discussed in Chapter 3. The effect of leaving out the pressure term, $\exp(\frac{-PV}{kT})$,

in equation 2.26 is not significant for lower lithosphere pressures when compared to the accuracy of the other parameters. The effective viscosity can be defined as

$$\eta_{eff} = \frac{\sigma_s}{2\dot{\varepsilon}} \qquad 2.27$$

Two power laws will be used: one based on dry olivine for the upper mantle and the other based on quartzite for the lower crust. A value of 125 kcal mol^{-1} (523.25 kJ mol^{-1}) for the activation energy for olivine is considered to be a reasonable value (Goetze, 1978). A value of 3 for the exponent n is a common choice and agrees fairly well with the experimental data and with theoretical considerations. The value of the pre-exponential constant, A, is more difficult to select. Experiments can only be performed at strain rates greater than about 10^{-7}, so for their results to be applied to the mantle extrapolation of at least six orders of magnitude is necessary (Goetze, 1978). It is not known how sensitive this extrapolation is and, consequently, the method used here is simply to assume a value for A which gives realistic effective viscosities for the lower lithosphere and, in the case of the mantle, the asthenosphere. Taking a value of 10^9 s^{-1} kb^{-n} for A in the creep law for the mantle gives

$$\dot{\varepsilon} = 10^9 \exp\left(\frac{-125 \text{ kcal mol}^{-1}}{kT}\right) \sigma_s^3 \qquad 2.28$$

which is within the range of values given in Table 2.4. This equation is plotted in Figure 2.8 for a range of stresses between 1 MPa and 200 MPa (0.01 to 2 kb) and for temperatures applicable to the upper, central and lower parts of the lithospheric mantle. The enclosed portion

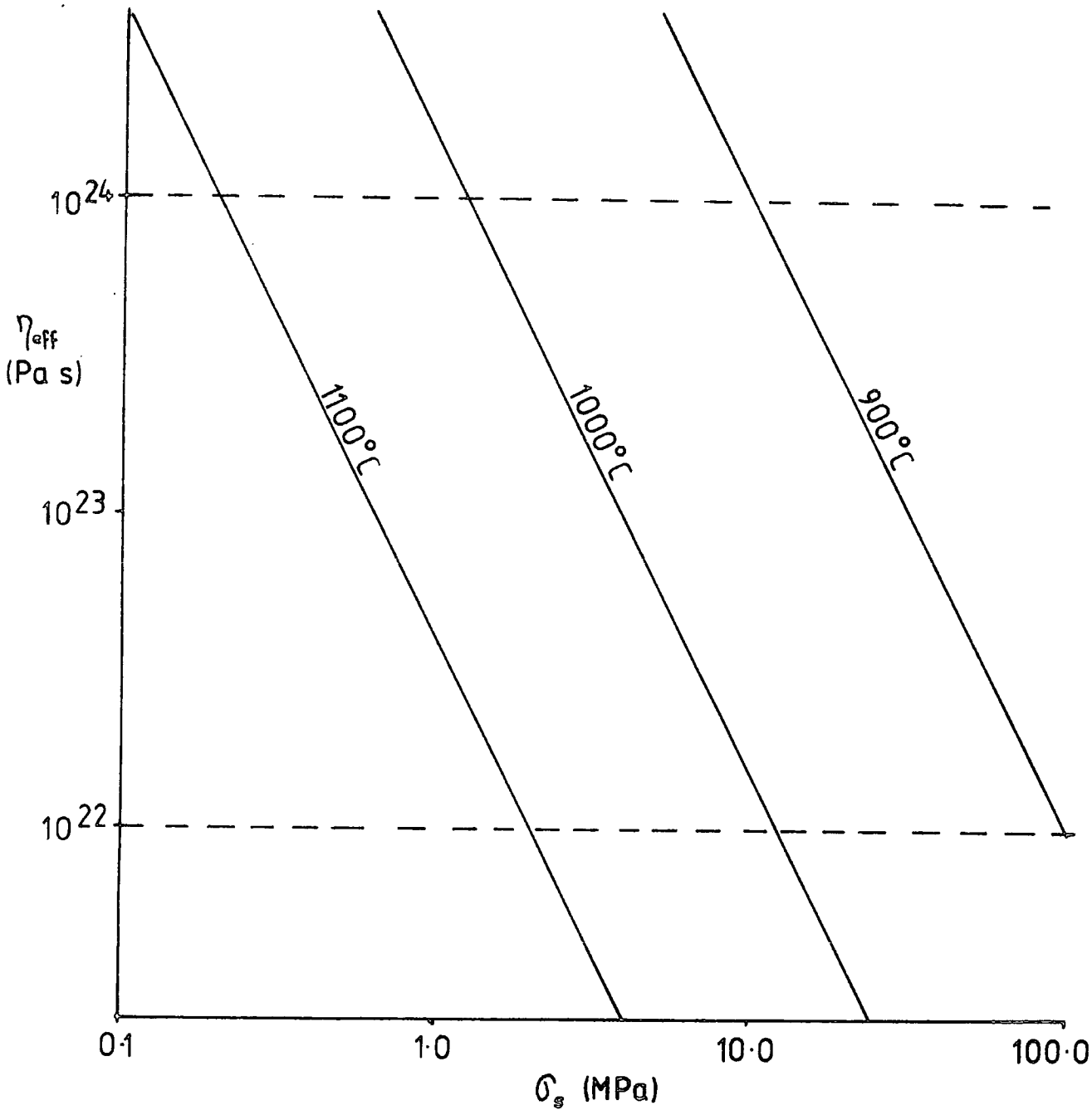

Fig. 2.8: Effective viscosities derived from the creep law for the lithospheric mantle.

of Figure 2.8 indicates the likeliest range of effective viscosities for the lithosphere (Walcott, 1970; Sleep and Snell, 1976) and the effective viscosity calculated from equation 2.28 in later models will be constrained to lie within the limits 10^{22} Pa s to 10^{24} Pa s. The value chosen for the pre-exponential constant agrees also with the range of effective viscosities thought to be representative of the asthenosphere. Taking the asthenosphere temperature to be 1300°C and the shear stress to be 1 MPa (0.01 kb), equation 2.28 gives an effective viscosity of 1.2×10^{20} Pa s and this is a typical value for the asthenosphere (Kirby and Raleigh, 1973).

Assigning values to creep parameters for lower crustal material is even more difficult. The only data come from Parrish et al. (1976) for quartzite, and here the wet quartzite data give effective viscosities that are much too low and the dry data give viscosities much too high. It also seems likely, from the value of the stress exponent, that the large stresses used in the experimental work on dry quartzite (Heard and Carter, 1968) has resulted in a creep mechanism of the type where n is equal to 5. A value of 64 kcal mol^{-1} (267.90 kJ mol^{-1}) is taken for the activation energy and 3 for the stress exponent. The constant A is assigned a value lying between the two values given in Table 2.4. It should be realised here that extremely large error bars are attached to the tabulated values (Parrish et al., 1976). The creep law is therefore

$$\dot{\varepsilon} = 10^2 \exp\left(\frac{-64 \text{ kcal mol}^{-1}}{kT}\right) \sigma_s^3 \qquad 2.29$$

This equation is plotted in Figure 2.9 for a range of suitable temperatures and stresses. This law gives values which lie between the wet and dry

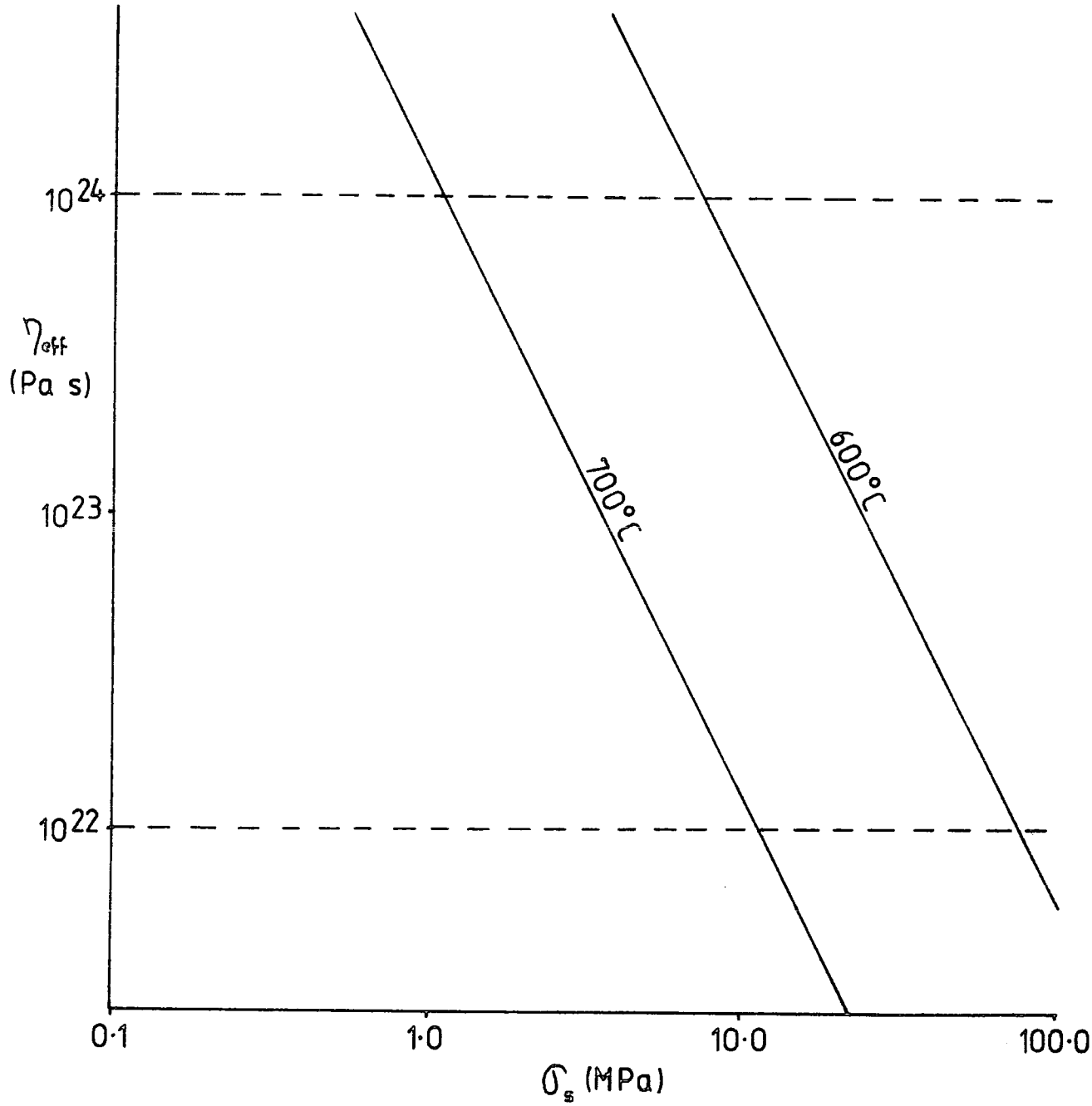

Fig. 2.9: Effective viscosities derived from the creep law for the lower crust.

quartzite laws of Table 2.4. Again, the effective viscosity is constrained to lie between 10^{22} Pa s and 10^{24} Pa s .

CHAPTER 3

FINITE ELEMENT ANALYSIS

3.1 Introduction

The analysis of stresses and displacements in a continuum involves the solution of differential equations with prescribed sets of boundary conditions. If the model is sufficiently simple these can be solved analytically. For geodynamic and geophysical problems the material properties of the continuum and the boundary conditions are often complex, with both lateral and vertical variations, and to solve the equations analytically usually involves unrealistic simplifications. For this reason it is necessary to use numerical solutions. One of the most useful techniques, which has been used extensively for engineering problems and, more recently, in the geological sciences, is the finite element method. This involves the construction of a set of simultaneous equations based on the differential equations and the boundary conditions of the problem, which are then solved using a digital computer. This chapter describes the use of finite element methods for elastic and visco-elastic analysis. Finite element programs to perform this type of analysis do exist at Durham University (Kusznir, 1976; Woodward, 1976), but the author has chosen to write his own program. This was done for two reasons. Firstly, it was felt desirable to have the program in the form of a subroutine library and a master calling program, which allows considerable flexibility and makes the addition of new subroutines straightforward. A program of this type was not available. Secondly, the programming of a finite element package results in considerable insight into the method. The subroutine library, FELIB, and the calling program, FEGEN, are listed

and described in Appendix 2 together with a test of the program.

3.2 Elastic finite element analysis

3.2.1 Theory

The application of the finite element method in this thesis involves the study of stress and strain distributions in two-dimensional elastic continua. This is described in detail by Zienkiewicz (1977) and his formulation is followed in this chapter. The plain strain approximation is used, whereby the strain in the direction perpendicular to the plane of the model is defined to be zero. This is a reasonable constraint for use with cross-sectional models through structures which are very long in the third dimension. The equations relating stress, strain and displacement in an elastic continuum are described in many texts (e.g. Housner and Vreeland, 1966; Jaeger and Cook, 1976) and will not be derived here.

If the displacement vector for any point in an elastic continuum is

$$\{f\} = \begin{Bmatrix} u \\ v \end{Bmatrix}$$

where u,v are the displacements in the two dimensions of the model (x,y), then the strain tensor $\{\varepsilon\}$ is defined as

$$\{\varepsilon\} = \begin{Bmatrix} \varepsilon_x \\ \varepsilon_y \\ \gamma_{xy} \end{Bmatrix} = \begin{Bmatrix} \dfrac{\partial u}{\partial x} \\ \dfrac{\partial V}{\partial y} \\ \dfrac{\partial u}{\partial y} + \dfrac{\partial V}{\partial x} \end{Bmatrix} \qquad 3.1$$

since for plane strain $\varepsilon_z = \gamma_{xz} = \gamma_{yz} = 0$

The stress tensor $\{\sigma\}$ is related to the strain tensor by the equation

$$\{\sigma\} = \begin{Bmatrix} \sigma_x \\ \sigma_y \\ \tau_{xy} \end{Bmatrix} = [D](\{\varepsilon\} - \{\varepsilon_0\}) + \{\sigma_0\} \qquad 3.2$$

where $\{\varepsilon_0\}$ is the initial strain tensor, $\{\sigma_0\}$ is the initial stress tensor, and $[D]$ is the elasticity matrix for plane strain given by

$$[D] = \frac{E(1 - \nu)}{(1+\nu)(1-2\nu)} \begin{bmatrix} 1 & \frac{\nu}{1-\nu} & 0 \\ \frac{\nu}{1-\nu} & 1 & 0 \\ 0 & 0 & \frac{1-2\nu}{2(1-\nu)} \end{bmatrix} \qquad 3.3$$

where E is Young's modulus and ν is Poisson's ratio. The stress necessary in the z-direction to maintain plane strain is

$$\sigma_z = \nu(\sigma_x + \sigma_y) \qquad 3.4$$

At one point in this thesis (Chapter 6), the plane stress approximation is also used, whereby the z-stress is constrained to be zero. In this case the elasticity matrix becomes

$$[D] = \frac{E}{1 - \nu^2} \begin{bmatrix} 1 & \nu & 0 \\ \nu & 1 & 0 \\ 0 & 0 & \frac{1-\nu}{2} \end{bmatrix}$$

If a system of forces is now applied to the continuum, consisting of distributed boundary forces, $\{q\}$, and distributed internal forces, $\{b\}$, then the governing equilibrium equations for the continuum can be obtained by minimising the total potential energy of the system with respect to the displacements caused by the loading. The variational approach to extremum problems of this type (Lanczos, 1949) is to consider the virtual quantities $\delta\{f\}$ and $\delta\{\varepsilon\}$:

then

$$\delta W = \int_V \delta\{f\}^T \{b\}\, dV + \int_A \delta\{f\}^T \{q\}\, dA \qquad 3.5$$

where W is the potential energy of the applied loads, and

$$\delta U = \int \delta\{\varepsilon\}^T \{\sigma\}\, dV$$

where U is the strain energy.

Substituting equation 3.2 into 3.5 gives

$$\delta U = \int_V \delta\{\varepsilon\}^T [D] \{\varepsilon\}\, dV - \int_V \delta\{\varepsilon\}^T [D] \{\varepsilon_0\}\, dV + \int_V \delta\{\varepsilon\}^T \{\sigma_0\}\, dV \qquad 3.6$$

From equations 3.5 and 3.6

$$W = \int_V \{f\}^T \{b\}\, dV + \int_A \{f\}^T \{q\}\, dA$$

$$U = \frac{1}{2} \int_V \{\varepsilon\}^T [D] \{\varepsilon\}\, dV - \int_V \{\varepsilon\}^T [D] \{\varepsilon_0\}\, dV + \int_V \{\varepsilon\}^T \{\sigma_0\}\, dV$$

and the total potential energy, π, is the sum of these,

$$\pi = \frac{1}{2}\int_V \{\varepsilon\}^T[D]\{\varepsilon\}dV - \int_V \{\varepsilon\}^T[D]\{\varepsilon_0\}dV + \int_V \{\varepsilon\}^T\{\sigma_0\}dV + \int_V \{f\}^T\{b\}dV + \int_A \{f\}^T\{q\}dA \qquad 3.7$$

This function must now be minimised with respect to the displacements,

$$\frac{\partial\pi}{\partial\{f\}} = 0 \qquad 3.8$$

For an elastic continuum this is not only a stationary value but is a true minimum.

In order to solve these equations it is necessary to constrain the displacement vector {f} to consist of a finite number of parameters. In the finite element method this is done by subdividing the continuum into a discrete number of elements which are interconnected at certain points on their boundaries, termed nodes. The solution of equation 3.8 in the context of nodal displacements will now be described. This is the displacement method and for a more complete description the reader is referred to Zienkiewicz (1977).

A typical triangular element, e, with nodes i,j,k at the corners is illustrated in Figure 3.1. Each node has displacement u in the x direction and v in the y-direction. If the nodal displacement vector is {d}, then

$\{f\}^e = [N]^e \{d\}^e$ where superscript e refers to element e

$$= \begin{bmatrix} N_i & 0 & N_j & 0 & N_k & 0 \\ 0 & N_i & 0 & N_j & 0 & N_k \end{bmatrix}^e \begin{Bmatrix} u_i \\ v_i \\ u_j \\ v_j \\ u_k \\ v_k \end{Bmatrix}^e \qquad 3.9$$

where $[N]^e$ is termed the element shape function and its components are prescribed functions of position within the element:

$$N_i = (a_i + b_i x + c_i y) / 2\Delta$$

$$\text{where } a_i = x_j y_k - x_k y_j \qquad 3.10$$

$$b_i = y_j - y_k$$

$$c_i = x_k - x_j$$

$$2\Delta = \begin{vmatrix} 1 & x_i & y_i \\ 1 & x_j & y_j \\ 1 & x_k & y_k \end{vmatrix} = 2 \times (\text{element area})$$

and N_j and N_k are obtained by cyclic permutation.

The strains at any point within the element are given by

$$\{\varepsilon\}^e = \begin{Bmatrix} \varepsilon_x \\ \varepsilon_y \\ \gamma_{xy} \end{Bmatrix}^e = \begin{bmatrix} \frac{\partial}{\partial x} & 0 \\ 0 & \frac{\partial}{\partial y} \\ \frac{\partial}{\partial y} & \frac{\partial}{\partial x} \end{bmatrix} \begin{Bmatrix} u \\ v \end{Bmatrix}^e = [L]\ \{f\}^e \qquad 3.11$$

So from 3.9

$$\{\varepsilon\}^e = [L]\ [N]^e\ \{d\}^e = [B]^e\ \{d\}^e \qquad 3.12$$

where $[B]^e$ is a matrix mapping nodal displacements into strains.

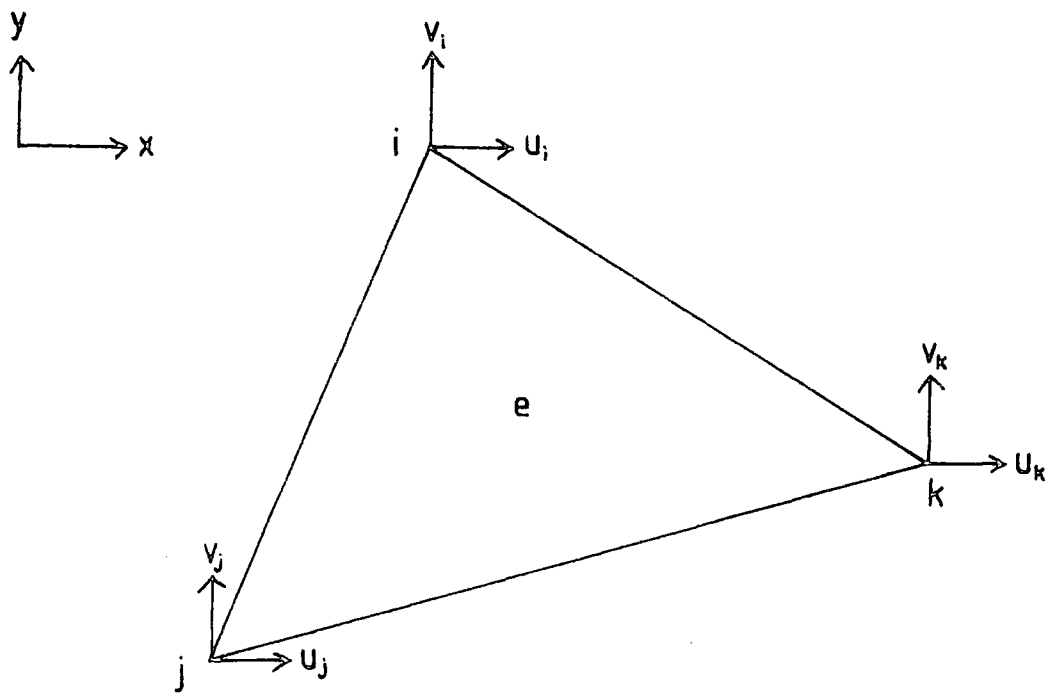

Fig. 3.1: Triangular element

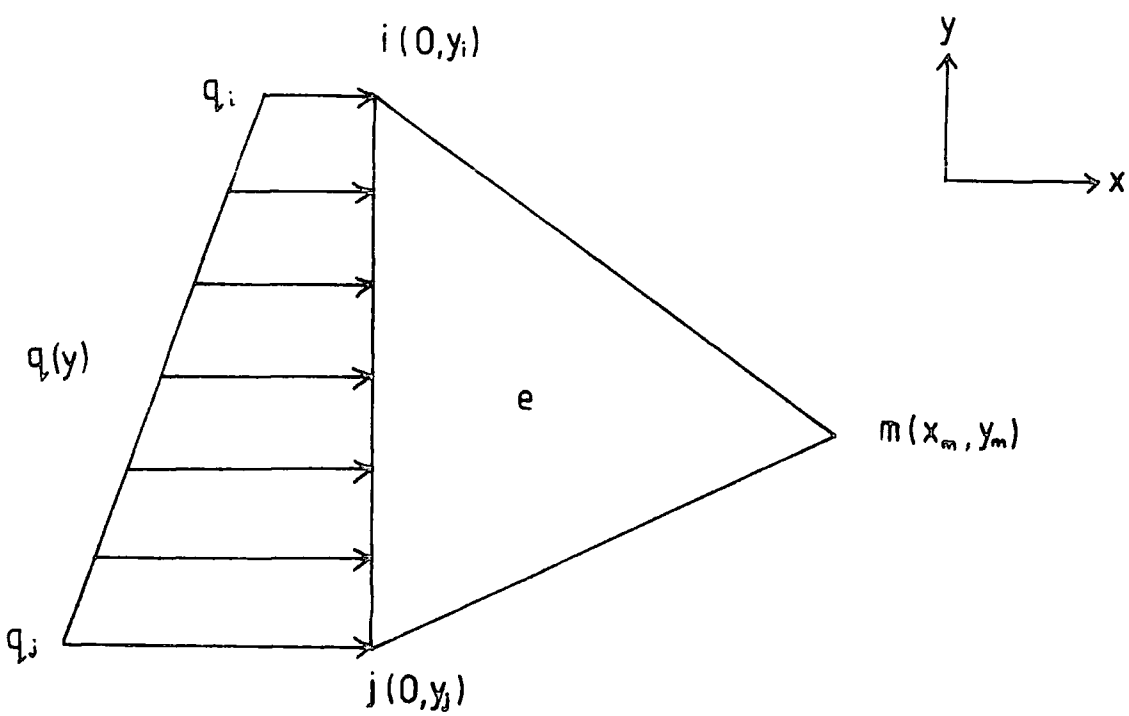

Fig. 3.2: Triangular element with one side subjected to a linearly varying pressure.

Evaluating [L] $[N]^e$ gives

$$[B]^e = \begin{bmatrix} b_i & 0 & b_j & 0 & b_k & 0 \\ 0 & c_i & 0 & c_j & 0 & c_k \\ c_i & b_i & c_j & b_j & c_k & b_k \end{bmatrix}^e \qquad 3.13$$

So the strain within the element does not depend on the position of the point considered, i.e. the element has a constant strain. This is a consequence of having a linear shape function (equations 3.10). Elements having mid-point nodes will have a quadratic shape function and will give rise to linear strain elements. These more advanced elements give more accurate solutions but require a considerable increase in computing time and numerical integration techniques.

The stresses at any point within the element are given by

$$\{\sigma\}^e = \begin{Bmatrix} \sigma_x \\ \sigma_y \\ \tau_{xy} \end{Bmatrix}^e = [D]^e \left(\{\varepsilon\}^e - \{\varepsilon_0\}^e\right) + \{\sigma_0\}^e$$

with $[D]^e$ as given in equation 3.3.

Substituting for $\{f\}$ and $\{\varepsilon\}$ in equation 3.7 and summing over all elements gives the total potential energy of the system

$$\pi = \frac{1}{2}\int_V \{d\}^T[B]^T[D][B]\{d\}dV - \int_V \{d\}^T[B]^T[D]\{\varepsilon_0\}dV + \int_V \{d\}^T[B]^T\{\sigma_0\}dV + \int_V \{d\}^T[N]^T\{b\}dV + \int_A \{d\}^T[N]^T\{q\}dA \qquad 3.14$$

and performing the differentiation of equation 3.8 gives

$$\int_V [B]^T[D][B]\{d\}dV - \int_V [B]^T[D]\{\varepsilon_0\}dV + \int_V [B]^T\{\sigma_0\}dV + \int_V [N]^T\{b\}dV +$$

$$\int_A [N]^T\{q\}dA = 0 \qquad 3.15$$

This can be simplified to the basic equation of the displacement method

$$[K]\ \{d\} = \{F\} \qquad 3.16$$

where

$$[K] = \int_V [B]^T[D][B]\ dV$$

$$\{F\} = \int_V [B]^T[D]\{\varepsilon_0\}dV - \int_V [B]^T\{\sigma_0\}dV - \int_V [N]^T\{b\}dV - \int_A [N]^T\{q\}dA$$

$$= \{F\}_{\varepsilon_0} - \{F\}_{\sigma_0} - \{F\}_b - \{F\}_q \qquad 3.17$$

[K] is known as the stiffness matrix.

3.2.2 Application

The use of constant strain triangular elements leads to certain simplifications in the expressions of equations 3.16 and 3.17. If $[K]^e$ is the stiffness matrix for element e, then

$$[K]^e = \int_V ([B]^e)^T\ [D]^e\ [B]^e\ dV$$

$$= \int_A ([B]^e)^T\ [D]^e\ [B]^e\ t\ dx\ dy$$

where t is the thickness of the element and the integration is over the

element area. If the model is considered to have unit thickness, then since [B] and [D] do not depend on position,

$$[K]^e = ([B]^e)^T \, [D]^e \, [B]^e \, \Delta \qquad 3.18$$

where Δ is the area of the element.

It is usual to form the element stiffness matrices as given by equation 3.18 and then add them into the global stiffness matrix, [K], in their correct positions as determined by their node numbers.

Similar considerations lead to a simplification of the element force vectors due to initial strains and stresses,

$$\begin{aligned} \{F\}^e_{\varepsilon_0} &= ([B]^e)^T \, [D]^e \, \{\varepsilon_0\}^e \, \Delta \\ \{F\}_{\sigma_0} &= ([B]^e)^T \, \{\sigma_0\}^e \, \Delta \end{aligned} \qquad 3.19$$

and these are added into the corresponding global force vectors.

Distributed internal forces usually take the form of gravitational body forces. In this situation

$\{b\} = \begin{Bmatrix} 0 \\ -\rho g \end{Bmatrix}$ where ρ is the density of the element and g is the acceleration due to gravity, and

$$\begin{aligned} \{F\}^e_b &= \int_V ([N]^e)^T \begin{Bmatrix} 0 \\ -\rho g \end{Bmatrix} dV \\ &= \int_A ([N]^e)^T \begin{Bmatrix} 0 \\ -\rho g \end{Bmatrix} dx \, dy \end{aligned}$$

Therefore, for node i

$$\{F_i\}^e_b = \begin{Bmatrix} 0 \\ -\rho g \end{Bmatrix} \int N_i \, dx \, dy \qquad 3.20$$

and from equation 3.10

$$\{F_i\}^e_b = \begin{Bmatrix} 0 \\ -\rho g \end{Bmatrix} \int_A (a_i + b_i x + c_i y)/2\Delta \, dx \, dy \qquad 3.21$$

Now defining the origin of the element co-ordinates at the centroid gives

$$\int_A x \, dx \, dy = \int_A y \, dx \, dy = 0$$

So from equation 3.21

$$\{F_i\}^e_b = \begin{Bmatrix} 0 \\ -\rho g \end{Bmatrix} \int_A \frac{a_i}{2\Delta} \, dx \, dy$$

$$= \begin{Bmatrix} 0 \\ -\rho g \end{Bmatrix} \frac{a_i}{2}$$

$$= \begin{Bmatrix} 0 \\ -\rho g \end{Bmatrix} \frac{\Delta}{3} \quad \text{since } a_i = a_j = a_k = \frac{2\Delta}{3} \qquad 3.22$$

and similarly for nodes j and k.

Therefore to apply forces due to gravity it is sufficient to apply one third of the weight of the element at each node,

$$\{F\}^e_b = \begin{Bmatrix} 0 \\ -\rho g/3 \\ 0 \\ -\rho g/3 \\ 0 \\ -\rho g/3 \end{Bmatrix} \Delta \qquad 3.23$$

The global body force vector is now formed by adding in all the element body force vectors.

The stiffness matrix [K] is symmetric, positive definite and banded. Consequently, it is not necessary to store the entire matrix. The finite element grid is drawn so that boundaries between different material properties correspond to element boundaries. The band-width of the matrix is dependent on the largest difference between any two nodes on any element. Careful numbering of the nodes enables the band-width to be kept as small as possible, which requires less computer storage. Various methods exist to solve equation 3.16 and can be found in most numerical analysis program libraries. The method used here is Gaussian elimination and the basis of this procedure is described in many texts (e.g. Kreyszig, 1972). The subroutine which performs the elimination is contained in the HARWELL scientific subroutine library (Hopper, 1973) and is very suitable for situations where many solutions from the same matrix are required.

3.2.3 Boundary conditions

In order to obtain a unique solution from equation 3.16 it is necessary to prevent rigid body rotations and translations. This is equivalent to ensuring that the stiffness matrix is non-singular. Rigid body translations are prevented by prescribing at least one fixed x and y displacement. In the event that these are both applied at the same node it is necessary to prescribe at least one other fixed displacement to prevent rotation. The best method of prescribing a fixed displacement to a nodal point is to set the diagonal element of the matrix [K] and the component of the force vector, {F}, corresponding to that node to a suitable value. The remainder of that row of [K] is set to zero. For instance, if the

x-displacement of the i th node is to be set to a, then the above operation replaces the original equation by

$$cd_{x_i} = ca \qquad \text{where c is a constant.}$$

The routine used in this thesis to solve equation 3.16 requires the whole band-width of the matrix to be stored. If only the semi-band-width is stored it is necessary to set the rest of the column to zero also and adjust the force vector in order to preserve the symmetry of the stiffness matrix (Hinton and Owen, 1977). The other type of boundary condition is boundary stresses, for instance a lithostatic pressure acting on the sides of the model. Then, in order to calculate the forces that have to be applied at the nodes it is necessary to perform the integration

$$\{F\}_q = \int_A [N]^T \{q\}\, dA \qquad \text{(from equation 3.17)}$$

Suppose a linearly varying pressure is to be applied along one side of an element, e, as shown in Figure 3.2. For this calculation the origin of the x-axis is defined to lie along the side ij in order to simplify the integration. The pressure along the side ij is a linear function of y and can be expressed as

$$q(y) = \frac{(q_j - q_i)}{(y_i - y_j)} \cdot (y_i - y) + q_i \qquad y_i \geqslant y \geqslant y_j$$

$$= \alpha y + \beta \qquad 3.24$$

where $\alpha = \dfrac{q_i - q_j}{y_i - y_j}$, $\beta = \dfrac{q_j y_i - q_i y_j}{y_i - y_j}$

Now the x-component of the force vector to be applied at node i is

$$F_i^x = \int_A N_i \, q(y) \, dA \qquad 3.25$$

Assuming the model has unit thickness and substituting equations 3.10 and 3.24 into 3.25 gives

$$F_i^x = \int_{y_j}^{y_i} [(a_i + b_i x + c_i y) / 2\Delta] \, (\alpha y + \beta) \, dy$$

Now x = 0 everywhere along side ij so the integral can be simplified to

$$F_i^x = \frac{1}{2\Delta} \int_{y_j}^{y_i} (c_i \alpha y^2 + (a_i \alpha + c_i \beta) y + a_i \beta) \, dy \qquad 3.26$$

$$= \frac{1}{2\Delta} \left[\frac{c_i \alpha}{3} (y_i^3 - y_j^3) + \frac{(a_i \alpha + c_i \beta)}{2} (y_i^2 - y_j^2) + a_i \beta (y_i - y_j) \right] \qquad 3.27$$

Now $a_i = x_j y_m - x_m y_j$

$= -x_m y_j$ since $x_j = 0$

and $c_i = x_m - x_j$

$= x_m$

Substituting for a_i, c_i, α and β in equation 3.27 gives

$$F_i^x = \frac{x_m}{12\Delta} (y_i - y_j)^2 . (2q_i + q_j)$$

and $x_m(y_i - y_j) = 2\Delta = 2 \times$ area of element

$$\therefore \quad F_i^x = \frac{(y_i - y_j)}{6} . (2q_i + q_j) \qquad 3.28$$

and similarly

$$F_j^x = \frac{(y_i - y_j)}{6} . (q_i + 2q_j)$$

So these equations give the forces necessary to apply to nodes i,j to represent the pressure q(y). It can be seen that F_i^x and F_j^x added together are equal to the total pressure applied on side ij, as is to be expected.

An important constraint on some models is the presence of an underlying fluid. In this situation it is necessary to have an isostatic compensation effect which dampens the displacements at that boundary (Dean, 1973). Suppose the base of the model is characterised by m nodes, b_1 ----b_m, where b_1 is the first node and b_m is the last node. Then, if the displacement of the i th base node in the y-direction is V_{b_i} and the density of the underlying fluid is ρ_m, the isostatic restoring force on that base node is

$$(F_I)_{b_i} = -A_{b_i} V_{b_i}$$

where A_{b_i} is given by

$$A_{b_i} = \begin{cases} \dfrac{\rho_m g(|x(b_i) - x(b_{i+1})|)}{2} & i = 1 \\ \dfrac{\rho_m g(|x(b_{i+1}) - x(b_i)| + |x(b_i) - x(b_{i-1})|)}{2} & 1 < i < m \\ \dfrac{\rho_m g(|x(b_i) - x(b_{i-1})|)}{2} & i = m \end{cases} \qquad 3.29$$

In matrix form this is

$$\{F\}_I = [A]\ \{d\} \qquad 3.30$$

where all components of [A] are zero apart from the diagonal elements

which refer to y-displacements of base nodes whose values are given by equation 3.29 . Incorporating this force vector into the total force vector in equation 3.16 gives

$$
\begin{aligned}
[K]\{d\} &= \{F\} + \{F\}_I \\
&= \{F\} - [A]\{d\} \\
\therefore \quad ([K] + [A])\{d\} &= \{F\}
\end{aligned}
\qquad 3.31
$$

So adding the matrix [A]into the stiffness matrix introduces the required isostatic forces. This addition also removes one set of linearly dependent equations from the matrix [K] making it no longer necessary to prescribe a y-displacement to prevent rigid body rotations and translations.

3.3 Visco-elastic finite element analysis

In Chapter 2 the importance of visco-elastic behaviour of lower crust and mantle material was discussed. A method of time-dependent finite element analysis will be discussed here, firstly for a simple Newtonian viscosity and then for a power law creep rheology.

An initial elastic solution enables the stress tensor in each element to be determined. If any deviatoric stresses exist,and the material is visco-elastic with viscosity η, then the creep strain rate components are

$$
\begin{aligned}
(\dot{\varepsilon}_x)_c &= \frac{1}{2\eta}\sigma_x' \\
(\dot{\varepsilon}_y)_c &= \frac{1}{2\eta}\sigma_y' \\
(\dot{\gamma}_{xy})_c &= \frac{1}{\eta}\tau_{xy}' \\
(\dot{\varepsilon}_z)_c &= \frac{1}{2\eta}\sigma_z'
\end{aligned}
\qquad 3.32
$$

where $\{\sigma'\}$ is the deviatoric stress tensor

$$\{\sigma'\} = \begin{Bmatrix} \sigma_x' \\ \sigma_y' \\ \tau_{xy}' \\ \sigma_z' \end{Bmatrix} = \begin{Bmatrix} \sigma_x - \sigma_m \\ \sigma_y - \sigma_m \\ \tau_{xy} \\ \sigma_z - \sigma_m \end{Bmatrix}; \ \sigma_m = \frac{1}{3}(\sigma_x + \sigma_y + \sigma_z)$$

The total creep strain occurring after a time step t is given by the simple integration

$$\{\varepsilon_c\} = \{\dot{\varepsilon}_c\}\ t \qquad 3.33$$

The method used in this thesis for visco-elastic analysis is the initial strain method (Zienkiewicz et al., 1968; Zienkiewicz, 1977) whereby the creep strains are treated as initial strains and the force vector corresponding to these strains, $\{F\}_{\varepsilon_0}$, is added into the total force vector and the equation solved again to give the new stresses.

$$\{\sigma\} = [D]\ (\{\varepsilon\} - \{\varepsilon_0\})$$

For the plane strain condition, the total strain ε_z must be zero. Since the presence of a deviatoric stress in the z-direction results in a creep strain $(\varepsilon_z)_c$ it is necessary to make the elastic strain $(\varepsilon_z)_{el}$ equal and opposite in sign to the creep strain so that

$$\varepsilon_z = (\varepsilon_z)_{el} + (\varepsilon_z)_c = 0$$

The initial strain method consists of the following steps:

1) Apply the load $\{F\}$ at time $t = 0$ and calculate the stresses $\{\sigma_0\}$ using elastic analysis.

2) Assume these stresses and the material properties remain unchanged during the first time step t_1. For each visco-elastic element calculate the creep strain $\{\varepsilon_c\}^e$ at the end of the time step using the equations 3.32 and 3.33.

3) Set $\{\varepsilon_0\}^e = \{\varepsilon_c\}^e$ and calculate the initial strain force vector for each element

$$\{F\}^e_{\varepsilon_0} = ([B]^e)^T [D]' \{\varepsilon_0\}^e \Delta$$

where

$$[D]' = \frac{E(1-\nu)}{(1+\nu)(1-2\nu)} \begin{bmatrix} 1 & \frac{\nu}{1-\nu} & \frac{\nu}{1-\nu} & 0 \\ \frac{\nu}{1-\nu} & 1 & \frac{\nu}{1-\nu} & 0 \\ 0 & 0 & 0 & \frac{1-2\nu}{2(1-\nu)} \end{bmatrix} .$$

Add in the element force vectors to the global force vector

$$\{F\}_{\varepsilon_0} = \sum_{\text{elems}} \{F\}^e_{\varepsilon_0}$$

and add this into the total force vector to give the new vector

$$\{F\}_1 = \{F\} + \{F\}_{\varepsilon_0}$$

4) Using this new force vector resolve the equation and calculate the strains at the end of the time step setting

$$(\varepsilon_z)_{el} = -(\varepsilon_z)_c$$

so that $\varepsilon_z = (\varepsilon_z)_{el} + (\varepsilon_z)_c = 0$

Calculate the stresses using

$$\{\sigma\}_1 = [D]'' (\{\varepsilon\} - \{\varepsilon_0\})$$

where

$$\{\sigma\}_1 = \begin{Bmatrix} \sigma_x \\ \sigma_y \\ \sigma_z \\ \tau_{xy} \end{Bmatrix} \quad \text{and} \quad [D]'' = \frac{E(1-\nu)}{(1+\nu)(1-2\nu)} \begin{bmatrix} 1 & \frac{\nu}{1-\nu} & \frac{\nu}{1-\nu} & 0 \\ \frac{\nu}{1-\nu} & 1 & \frac{\nu}{1-\nu} & 0 \\ \frac{\nu}{1-\nu} & \frac{\nu}{1-\nu} & 1 & 0 \\ 0 & 0 & 0 & \frac{1-2\nu}{2(1-\nu)} \end{bmatrix}$$

5) Calculate the mean stress during the time step by averaging the stress at the beginning (from 2)) and the stress at the end (from 4)). Use this to recalculate the creep strain during the time step. Repeat steps 2), 3), 4) and 5) until the mean stress converges to a reasonable value.
6) Assume these final stresses and the material properties remain unchanged at the start of the second time step, t_2, and continue as in step 2).
7) Repeat from step 2) for all remaining time steps.

If the time step, t, is too large then deviatoric stresses will not only be relaxed but will 'overflow' giving incorrect answers. Consequently, the creep of a time step must not exceed the deviatoric elastic strain. This condition enables a maximum length of time step to be calculated: the x-component of the deviatoric elastic strain is

$$(\varepsilon_x')_{el} = \frac{\sigma_x'}{E} - \frac{\nu\sigma_y'}{E} - \frac{\nu\sigma_z'}{E}$$

and the x-component of the creep strain is

$$(\varepsilon_x)_c = \frac{1}{2\eta}\sigma'_x t$$

Equating these gives

$$t = \frac{2\eta}{E} - \frac{2\eta\nu}{E}\frac{.\sigma'_y}{\sigma'_x} - \frac{2\eta\nu}{E}\frac{.\sigma'_z}{\sigma'_x}$$

and since the stresses are deviatoric,

$$\sigma'_z = -(\sigma'_x + \sigma'_y)$$

$$\therefore \quad t = \frac{2\eta}{E} + \frac{2\eta\nu}{E}$$

$$\therefore \quad t = \frac{2\eta(1+\nu)}{E}$$

Similarly the maximum time step calculated from the y- and z-components will also have this value.

For the xy-component,

$$(\gamma'_{xy})_{el} = \frac{2(1+\nu)}{E}\tau'_{xy}$$

$$(\gamma_{xy})_c = \frac{1}{\eta}\tau'_{xy}\ t$$

$$\therefore \quad t = \frac{2\eta(1+\nu)}{E} \quad \text{, as before.}$$

So a consideration of all the strain components shows that the maximum time step is

$$t = \frac{2\eta(1+\nu)}{E}$$

The initial strain method can also be applied for a power law creep rheology. The creep equation that will be used has been discussed in Chapter 2 and is of the form

$$\dot{\varepsilon} = A \exp\left(-\frac{Q}{kT}\right) \sigma_s^n$$

For use in the analysis the equation must be cast in tensor form and the individual components of strain rate and deviatoric stress must be related linearly ($\dot{\varepsilon}_{ij} \propto \sigma'_{ij}$ <u>not</u> $\dot{\varepsilon}_{ij} \propto (\sigma'_{ij})^n$) because steady state dislocation creep does not alter the volume of material (Stocker and Ashby, 1973). This is equivalent to saying that the rate of dilatation $\dot{\varepsilon}_{kk}$ (summation convention implied) is zero. The equation is expressed as

$$\dot{\varepsilon}'_{ij} = A \exp\left(-\frac{Q}{kT}\right) (\bar{\tau})^{n-1} \sigma'_{ij} \qquad 3.34$$

where $\bar{\tau}$ will be termed the effective deviatoric stress. It is necessary for $\bar{\tau}$ to be invariant so that the choice of axes does not affect the effective viscosity or strain rate. $\bar{\tau}$ is chosen to be the square root of the second invariant of the deviatoric stress tensor

$$\begin{aligned}
\bar{\tau} &= (J_2)^{\frac{1}{2}} \\
&= \left(\frac{1}{2} \sigma'_{ij} \sigma'_{ij}\right)^{\frac{1}{2}} \qquad \text{(summation convention implied)} \\
&= \left[\frac{1}{2} (\sigma'^2_x + \sigma'^2_y + \sigma'^2_z) + \tau^2_{xy} + \tau^2_{yz} + \tau^2_{xz}\right]^{\frac{1}{2}}
\end{aligned}$$

Referring to principal axes,

$$\bar{\tau} = \left[\frac{1}{2} (\sigma'^2_1 + \sigma'^2_2 + \sigma'^2_3)\right]^{\frac{1}{2}}$$

It can easily be seen that in the event of one of the deviatoric

stresses being zero, equation 3.34 gives the correct relation between the strain rate and the deviatoric stress.

Equation 3.34 gives the following creep strain rate components

$$
\begin{aligned}
(\dot{\varepsilon}_x)_c &= A \exp\left(\frac{-Q}{kT}\right) (\bar{\tau})^{n-1} \sigma'_x \\
(\dot{\varepsilon}_y)_c &= A \exp\left(\frac{-Q}{kT}\right) (\bar{\tau})^{n-1} \sigma'_y \\
(\dot{\gamma}_{xy})_c &= 2A \exp\left(\frac{-Q}{kT}\right) (\bar{\tau})^{n-1} \tau_{xy} \\
(\dot{\varepsilon}_z)_c &= A \exp\left(\frac{-Q}{kT}\right) (\bar{\tau})^{n-1} \sigma'_z
\end{aligned}
\qquad 3.35
$$

So by analogy with equation 3.32, the effective viscosity is

$$
\eta_{eff} = \frac{1}{2A} \exp\left(\frac{Q}{kT}\right) (\bar{\tau})^{1-n} \qquad 3.36
$$

The method proceeds as described earlier, except that for each iteration of each time increment the temperature of the element and the deviatoric stress tensor are used to calculate the effective viscosity of that element. As discussed in the previous chapter, this is constrained to lie within the limits 10^{22} Pa s (10^{23} P) and 10^{24} Pa s (10^{25} P) and, consequently, the maximum length of time increment that can be used, as calculated earlier, must correspond to a viscosity of 10^{22} Pa s .

3.4 Stress system re-creation

It is often useful in finite element analysis to be able to re-create a stress system that has been arrived at by visco-elastic analysis over a long period of time, by an instantaneous elastic solution. This is

particularly true in this thesis where the development of a graben is followed through a number of stages involving changes in the boundary conditions and also in the finite element grid (see Chapter 6).

Suppose a visco-elastic model has been run for some length of time, t, using the intial strain method as described in the last section. Then the total nodal force vector at the end of this time period is equal to the applied force vector plus the sum of the initial strain force vectors for all the the time increments,

$$\{F\}_{total} = \{F\}_{app} + \sum_{\substack{time \\ incs}} \{F\}_{\varepsilon_0}$$

This can be stored after the last time increment. Similarly, the total initial strain (or creep strain) tensor can be stored.

If an elastic analysis is now performed on the same model using the total force vector as the applied forces and subtracting the total initial strain tensor from the calculated strain tensor, then the system of stresses and elastic strains that existed after time t of the visco-elastic analysis will be re-created. The stress system will not be identical because of successive very small differences arising from the incremental nature of the original solution. However, it is very close to it, as is demonstrated in Chapter 6.

This method is discussed and illustrated, with reference to small alterations to the finite element grid, in Chapter 6.

CHAPTER 4

STRESS AMPLIFICATION AND THE DEVELOPMENT OF NORMAL FAULTING

4.1 Introduction

In this chapter finite element analysis is used with a model derived from Chapter 2 to investigate the response of the lithosphere to tensional stresses. The first part of the chapter discusses the application of body forces and the types of boundary conditions that can be used. The remainder of the chapter deals with the long term response of the lithosphere, using both Newtonian visco-elastic and power-law creep rheologies, to applied tensional stresses. The failure criterion discussed earlier is used to predict the onset of faulting, and the stress system present at the time of faulting will be carried through the thesis to Chapter 6 where it will be re-applied to a model containing a fault.

4.2 The finite element model

The finite element grid used in this chapter is illustrated in Figure 4.1. The model is divided into upper crust, lower crust and lithospheric mantle as discussed in Chapter 2. The physical properties of the model are summarised in Table 4.1.

The grid used is 4,000 km long, but most of the graphical output will refer to the central 400 km. In this thesis graben formation within plates rather than at their edges is being investigated and consequently it is necessary to have a very long grid so that the bending stresses and vertical displacements that occur at the edges of the plate in response to applied horizontal stresses (Kusznir and Bott, 1977) do not affect the

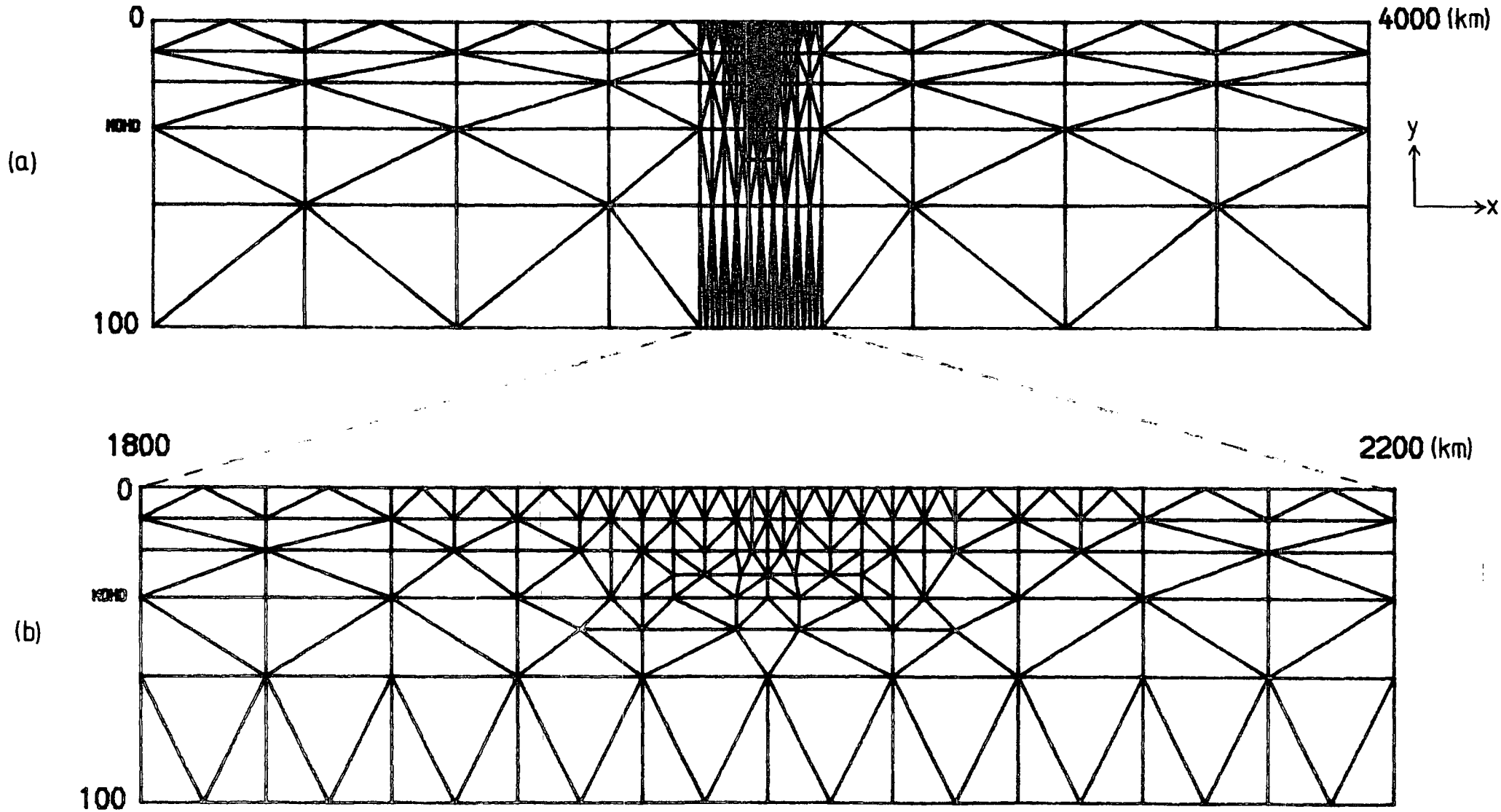

Fig. 4.1: Finite element grid

(a) Full grid

(b) Central 400 km section of grid

	Depth Range (km)	ρ (kg m^{-3})	ν	E (Nm^{-2})	Rheology
Upper crust	0 - 20	2,750	0.25	0.85×10^{11}	Elastic
Lower crust	20 - 35	2,900	0.25	1.08×10^{11}	Visco-elastic
Mantle	35 -100	3,300	0.25	1.80×10^{11}	Visco-elastic

Table 4.1: Physical properties of the finite element model.

centre of the model. The central section of the grid is fairly complex. This is so that a fault can be introduced into the grid, as will be seen in later chapters. The base of the model is assumed to be underlain by a fluid of density 3,300 kg m^{-3} and the boundary condition at the base is the isostatic compensation procedure discussed in Chapter 3. To prevent horizontal translation of the model, the central node on the base is fixed in the x-direction. Since this lies on an axis of symmetry, this prescribed displacement will not distort the results. The plane strain approximation is used in line with later chapters where the model will represent a section through a fault or graben which is long in the direction perpendicular to the plane of the model.

4.3 Body forces and the lithostatic stress assumption

The stresses present in the lithosphere can be divided into two types: stresses due to gravity and tectonic stresses. Residual stresses, caused by earlier tectonic events, will not be considered here. In this section the stresses present as a result of the body forces (i.e. gravity) will be discussed. For a horizontally layered model with a flat surface the state of stress at a given depth will be constant across the model.

It seems reasonable that one of the principal stresses will be vertical and be due to the overburden of material,

$$\sigma_y = \int_0^h \rho\, g\, dh \qquad \text{(y axis is vertical)}$$

where ρ is the density of the overlying material and g is the acceleration due to gravity. The lithostatic stress assumption is that the two horizontal principal stresses are also equal to this value.

$$\sigma_x = \sigma_z = \sigma_y = \int_0^h \rho\, g\, dh$$

Since this stress system is hydrostatic ($\sigma_x = \sigma_y = \sigma_z$) there are no deviatoric stresses. This assumption has been used by many workers on rock mechanics (Jaeger and Cook, 1976) and has been discussed by Collette (1976). It can be argued that over long periods of geological time, creep in the lithosphere will tend to result in this stress distribution as the deviatoric stresses relax. In situ stress measurements (Ranalli and Chandler, 1975) are of little use when discussing stresses due to gravity at depth because they can only be determined for depths to about 1 km and include stresses due to topography and residual stresses. Surface relief and lateral variations in density result in deviatoric stresses (Bott and Dean, 1972; Artyushkov, 1973; Bott and Kusznir, 1979) and in these situations the state of stress due to gravity will not be lithostatic. For the plane layered model of the lithosphere shown in Figure 2.1 and investigated by finite element analysis in this chapter, however, the lithostatic stress assumption is considered to be valid. Clearly, whilst using a horizontally layered model it is not necessary to incorporate the lithostatic stresses into the analysis since they can

be easily calculated and added into any stress system resulting from the applied tectonic forces. It is, however, interesting at this point to examine how a lithostatic stress distribution can be brought about by the application of body forces.

Figure 4.2(a) shows the principal stresses, plotted to scale and at their principal orientations, resulting from the body forces with the sides fixed in the horizontal (x) direction. For this plot, and all similar plots throughout this thesis, broken lines represent tensile stresses and full lines represent compressive stresses. The principal stresses are aligned approximately vertically and horizontally. Since the elements used are constant strain elements (and therefore also constant stress) the stresses shown are those acting throughout the elements. The vertical stresses are lithostatic for a point close to the centre of the element. The horizontal stresses, however, are only approximately one-third of the lithostatic stress. This situation is a result of the boundary conditions applied to the edges of the model. By fixing these in the x-direction the strain in that direction is constrained to be zero.

Therefore $$\varepsilon_x = 0 = \frac{\sigma_x}{E} - \frac{\nu\sigma_y}{E} - \frac{\nu\sigma_z}{E}$$

Now, for the plane strain condition

$$\sigma_z = \nu(\sigma_x + \sigma_y)$$

$$\therefore \quad (1 - \nu^2)\ \sigma_x = \nu(1 + \nu)\ \sigma_y$$

$$\therefore \quad \sigma_x = \frac{\nu}{1 - \nu}\ \sigma_y$$

and since $\nu = 0.25$

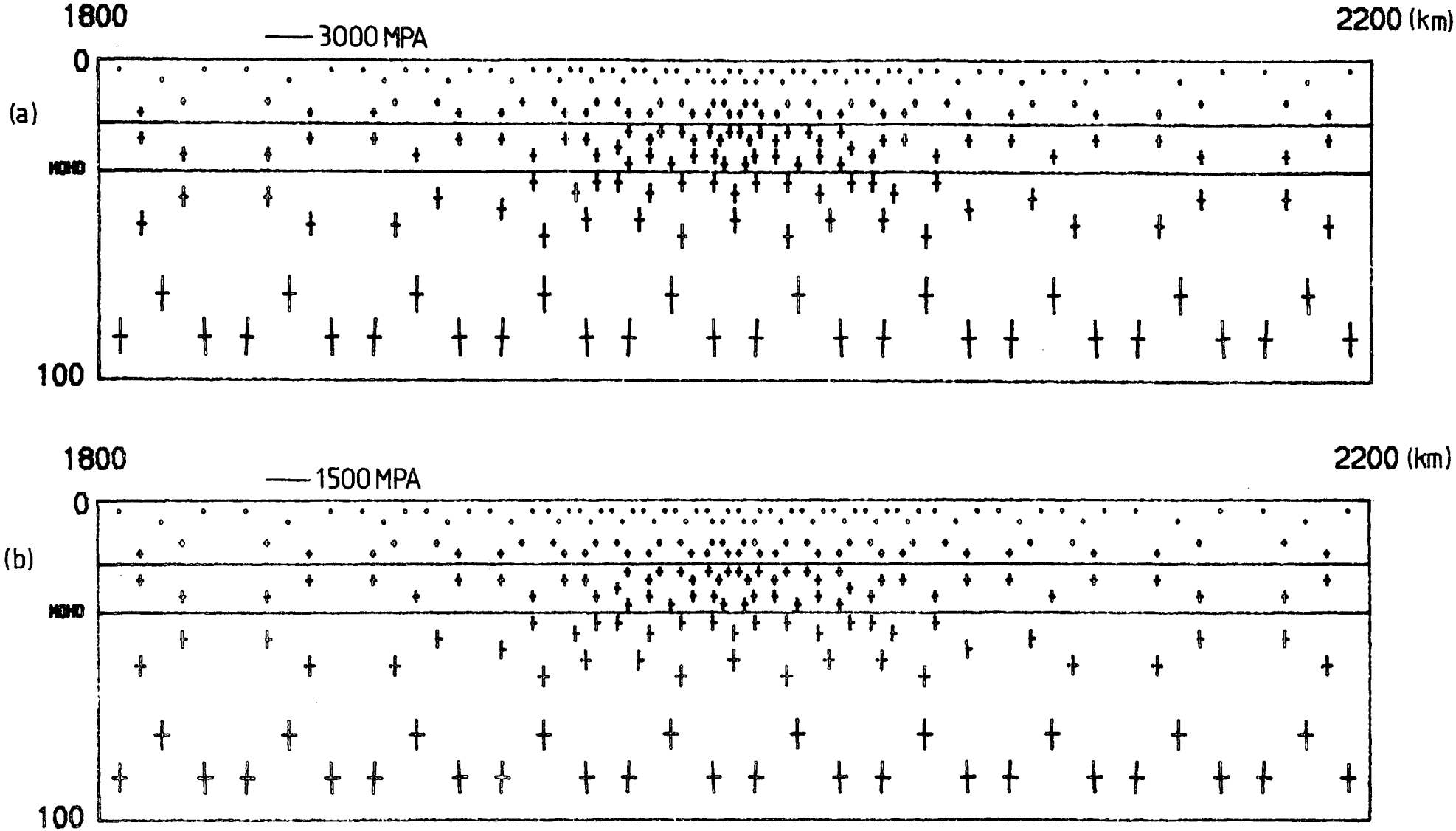

Fig. 4.2: Principal stresses for an elastic model with body forces applied and the sides fixed in the x-direction.

(a) Total stresses

(b) Deviatoric stresses

$$\sigma_x = \frac{1}{3}\sigma_y \qquad \text{as observed.}$$

This stress system is unreasonable because of the very large deviatoric stresses present near the base of the lithosphere (Figure 4.2(b)).

Figure 4.3(a) illustrates the stress system resulting from the body forces with horizontal lithostatic stresses applied at the edges. As can be seen, the in-plane principal stresses are more nearly equal, although considerable deviatoric stresses still exist near the base (Figure 4.3(b)). There is, however, a more serious objection to this approach. Suppose edge stresses were applied such that the in-plane stresses were equal,

$$\sigma_x = \sigma_y = \int_0^h \rho\, g\, dh$$

Then

$$\sigma_z = \nu(\sigma_x + \sigma_y) \qquad \text{(plane strain condition)}$$

$$= 2\nu \int_0^h \rho g\, dh$$

So, for $\nu = 0.25$

$$\sigma_z = \frac{1}{2}\int_0^h \rho\, g\, dh$$

Consequently, even if the in-plane stresses were equal, considerable deviatoric stresses would still exist because of the value of the z-stress necessary to maintain plane strain. Clearly, in this situation, the plane strain approximation is inadequate for an elastic model held by stresses at the edge. This is not surprising - the effect on a plate of uniform stresses around its perimeter would be expected to approximate

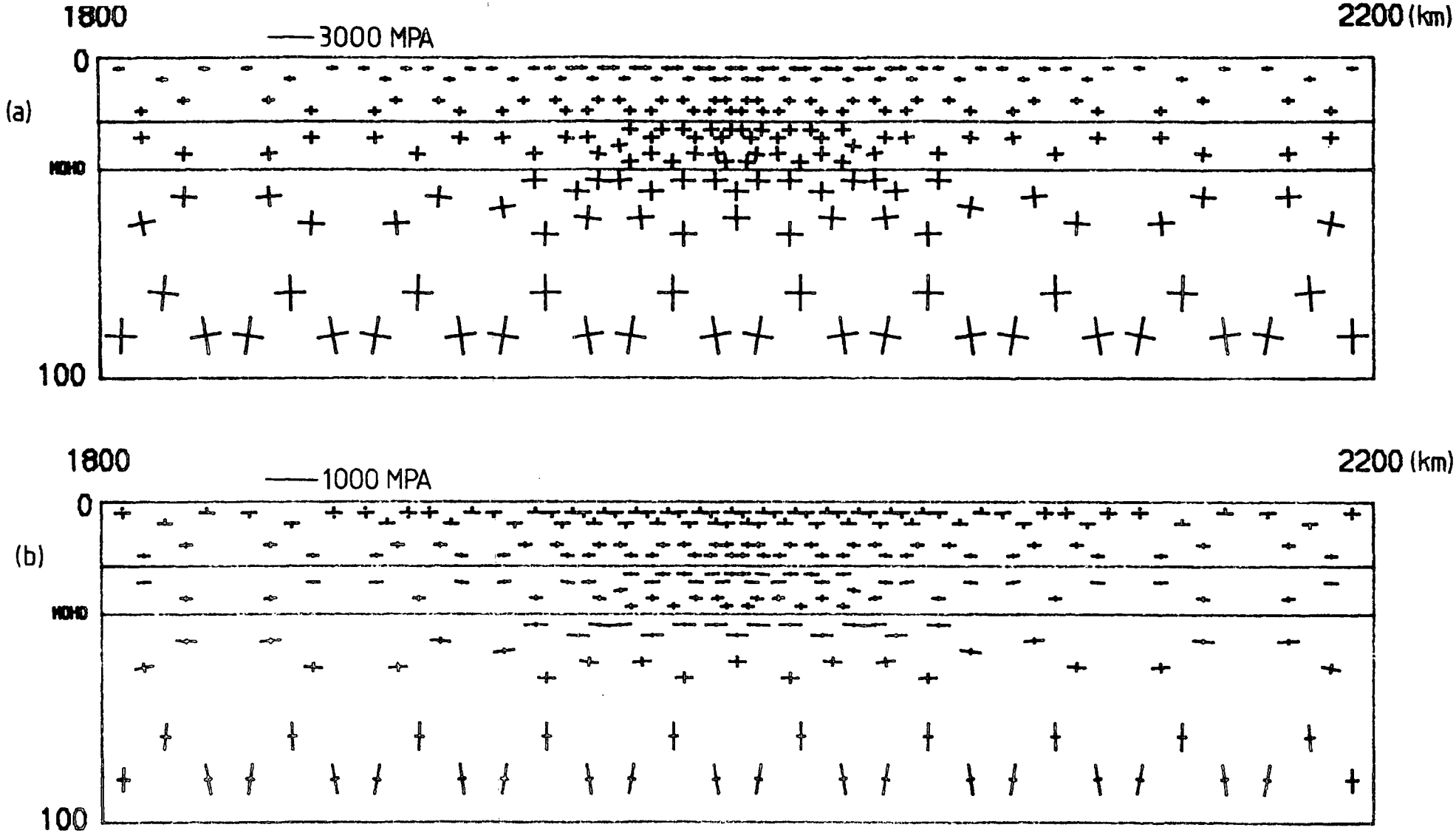

Fig. 4.3: Principal stresses for an elastic model with body forces and lithostatic stresses applied to the sides.

(a) Total stresses

(b) Deviatoric stresses

more closely to an axi-symmetric situation. Thus it is not apparent how an elastic solution that gives a lithostatic stress distribution can be obtained.

It should be pointed out, at this stage, that it is possible to get a lithostatic stress field by considering the whole model to be visco-elastic. This is done by using the first type of boundary condition (sides held) and allowing the model to relax so that the deviatoric stresses are dissipated by creep. Figure 4.4(a) shows the stress system resulting after 10 M yrs for a visco-elastic model with viscosity 10^{23} Pa s and body forces applied. The sides were fixed in the x-direction. The principal stresses are almost exactly lithostatic with values corresponding to the centres of the elements. As can be seen from Figure 4.4(b), the deviatoric stresses are very small, having largest magnitude of 0.6 MPa.

For the remainder of this thesis, body forces are not included in the models. Any errors that this may introduce will be discussed in the final chapter. The lithostatic stresses are explicitly added in to the calculated stresses for the purpose of determining whether an element will fail, since for failure mechanics the total stress system must be used.

4.4 Stress vs. displacement boundary conditions

Horizontal tensile stresses can be introduced into a finite element model of the lithosphere by two different types of edge constraint. The first of these is to prescribe displacements to the edges such that the model is strained in the horizontal direction. This is equivalent to an instantaneous deformation. The second type of boundary condition is to apply tensile stresses at the edges. The method of determining the nodal forces to be applied on the edge nodes has been described in Chapter 3. This type of constraint is equivalent to a constant stress over time.

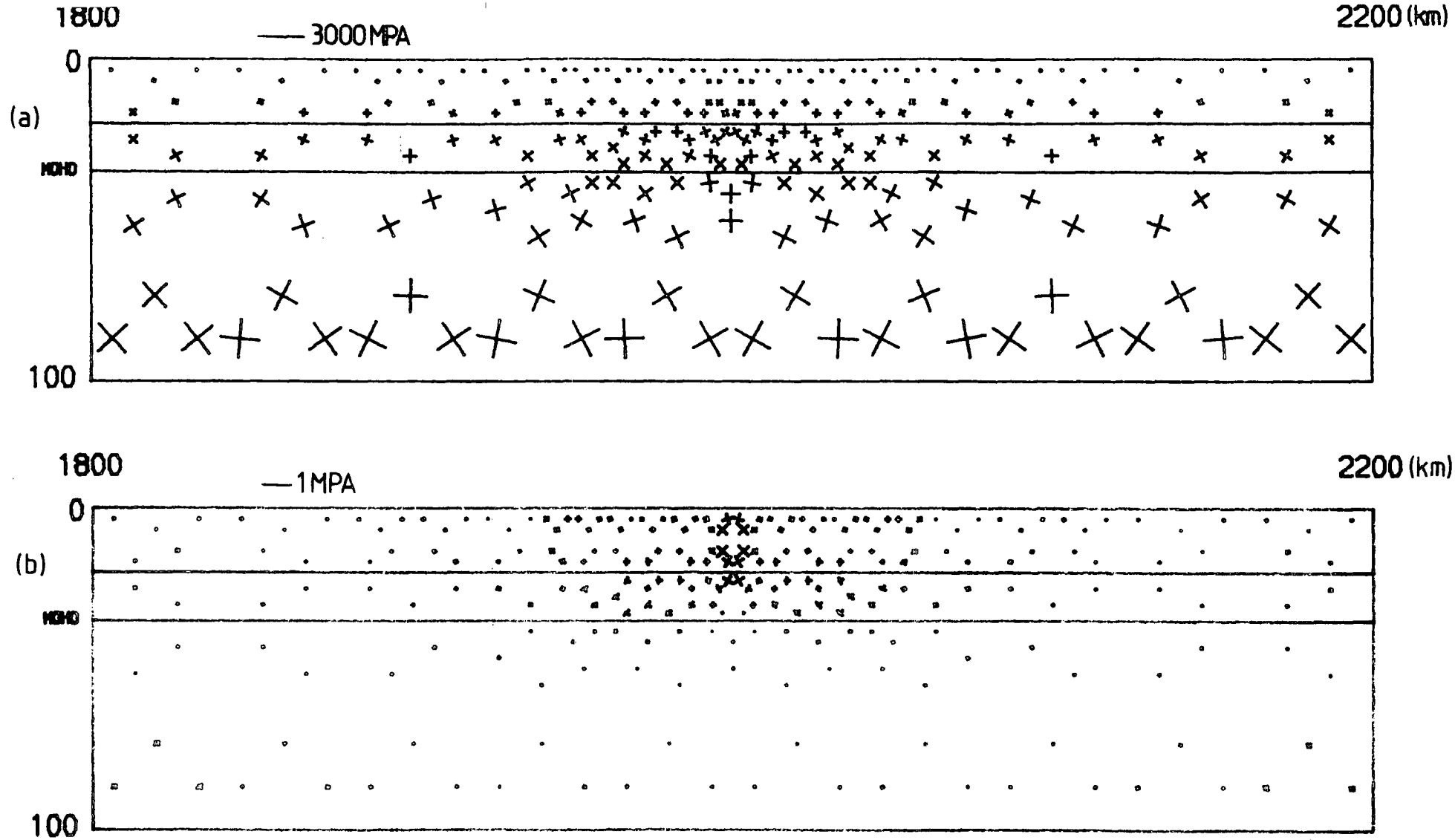

Fig. 4.4: Principal stresses for a visco-elastic model after 10 Myrs with body forces applied and the sides fixed in the x-direction.

(a) Total stresses

(b) Deviatoric stresses

These two types of boundary condition have a fundamentally different effect for the situation where the lithosphere consists of an elastic layer overlying ductile material, as has been pointed out by Kusznir and Bott (1977). If a tensile stress is introduced into the model by displacement boundary conditions (i.e. constant strain) and the visco-elastic material is allowed to relax over time, then no amplification of stresses in the elastic layer occurs. This is illustrated in Figure 4.5 for an applied strain of 0.5 millistrains and a viscosity for the lower crust and mantle of 10^{23} Pa s . However, if constant stress boundary conditions are used then relaxation of the stresses in the visco-elastic material results in amplification of the stresses in the elastic layer, as has been demonstrated by Kusznir and Bott (1977). It is this phenomenon which will be investigated in the remaining sections of this chapter.

Consequently, it is important to apply the type of boundary condition which is most suited to the situation being modelled. The sources of stress which may act on lithospheric plates have been discussed by Turcotte and Oxburgh (1976) and briefly described in Chapter 1. Of these, the most relevant in applying tectonic tensile stress are stresses due to the driving mechanism, stresses due to variations in crustal thickness and membrane stresses. Thermal stresses are important in the cooling of the oceanic lithosphere but are probably only a minor constituent of the stress field in the continental lithosphere, although they may be significant in the region of rift valleys where anomalously high thermal gradients are present.

Stresses due to the driving mechanism will result from some combination of 'slab pull' at subduction zones, 'ridge push' at mid-ocean ridges, and traction forces from convection cells in the asthenosphere (Turcotte and Oxburgh, 1976). Clearly these stresses are best modelled as

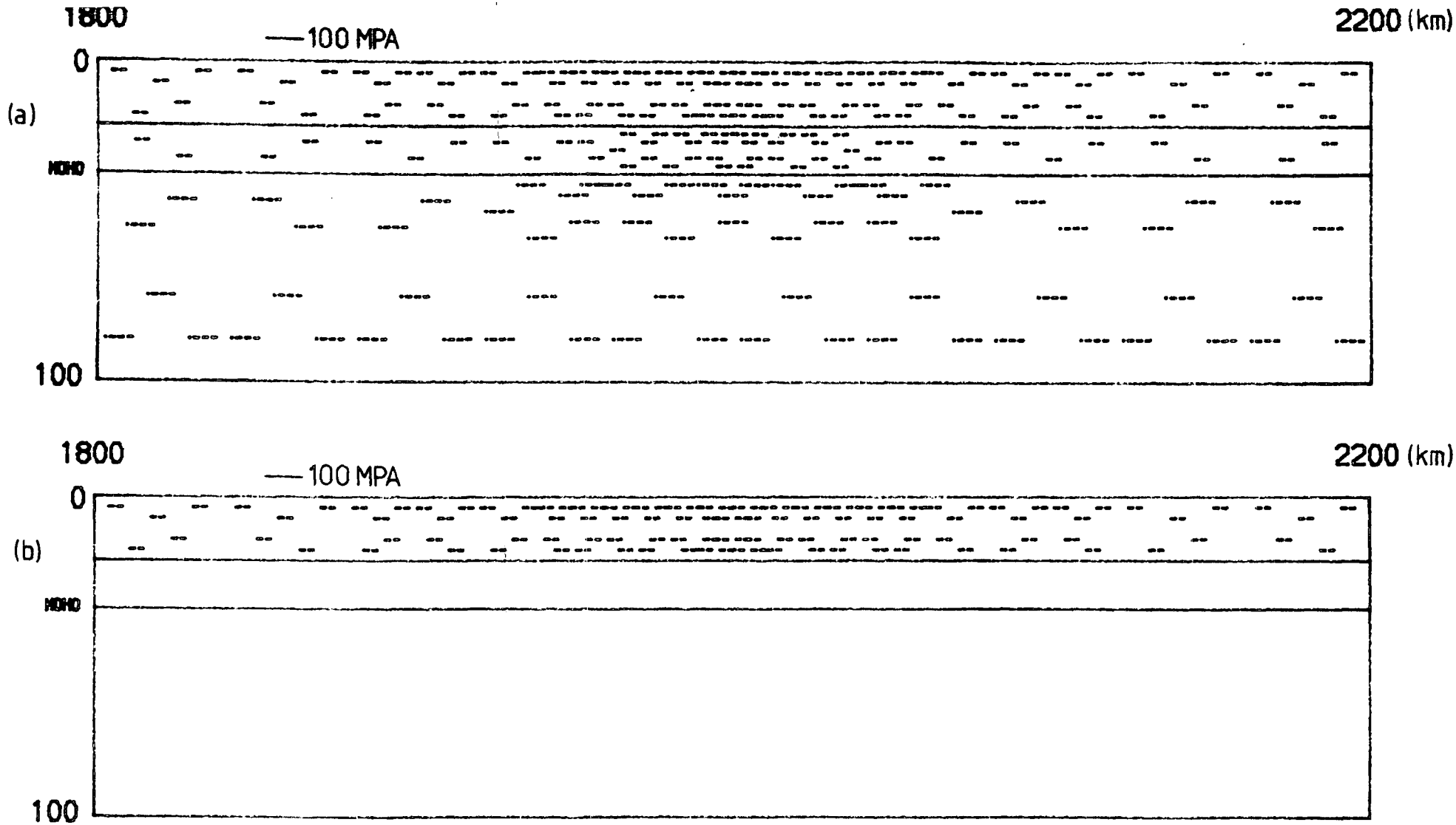

Fig. 4.5: Principal stresses for an applied strain of 0.5 millistrains.

(a) Elastic solution

(b) Solution after 1 Myrs with a viscosity of 10^{23} Pa s for the lower crust and mantle

a constant stress over time, i.e. by stress boundary conditions. It also seems likely that these stresses are applied over the whole depth of the lithosphere.

Stresses due to variations in crustal thickness have been shown to exist analytically by Artyushkov (1973) and by finite element analysis (Bott and Dean, 1972; Bott and Kusznir, 1979). Crustal thickness variations exist over long periods of time (as can be seen by the presence of very old mountain belts) and are thus also best represented by the stress boundary condition. These types of stresses are clearly not produced in the models used here since there are no lateral density variations. The depth of the lithosphere over which these stresses act depends on the isostatic compensation mechanism. If surface relief is compensated for by a crustal root, then the stresses will exist mainly in the crust. Compensation by low density mantle at some greater depth, however, will result in the stresses extending through a greater depth of the lithosphere.

The importance of membrane stresses to rifting is not clear. Oxburgh and Turcotte (1974) suggest that this source may be responsible for the East African rift system. Their calculations show a tensile stress of up to 60 MPa being produced as a result of northward movement of the African plate over the last 100 M yrs. Thus if these stresses are important, they also are best modelled as a constant stress over time rather than an instantaneous deformation.

Consequently, although the relative contributions of different stress sources to the tectonic stress system is not known, the boundary condition best suited to these sources is the stress boundary condition.

4.5 Stress amplification: Newtonian visco-elastic rheology

The concentration of stresses in an elastic layer as a result of plastic flow in underlying material has been commented on by Artemjev and Artyushkov (1971) in their discussion of the formation of the Baikal rift. More recently, Kusznir and Bott (1977) have used finite element analysis to demonstrate this phenomenon for a two layer model with uniform Young's modulus. In this section their work will be extended to a three layer model with different Young's moduli which is more realistic. The effect of a viscosity contrast between the lower crust and the upper mantle will be investigated. In all cases the prediction of faulting in the upper crust as a result of stress amplification will be studied since this can be considered to represent the first stage of graben formation.

Many major faults and graben are situated on previous zones of weakness. In Chapter 2 it was shown that the tensile strength of crystalline rocks probably lies with the range of 10 to 20 MPa. In this chapter the lower limit of 10 MPa will be used in order to simulate a weak zone in the centre of the model.

For a multi-layer model, the stresses in the layers, at sufficient distance from the edges, are related to the applied stress by the expression

$$\sigma_{APP} \cdot \ell = \sum_{i=1}^{n} \sigma_i \ell_i \qquad 4.1$$

where $\ell = \sum_{i=1}^{n} \ell_i$

and σ_{APP} is the applied stress, σ_i is the stress in the i th layer and ℓ_i is the thickness of the i th layer. The stresses in the lower crust

and mantle, which are visco-elastic, will decay exponentially to zero and the stress in the elastic upper crust will therefore increase towards the limit

$$\sigma_{uc} = \frac{\ell}{\ell_{uc}} \cdot \sigma_{APP} \qquad 4.2$$

where σ_{uc} is the stress in the upper crust and ℓ_{uc} is the thickness of the upper crust. If this value is greater than the stress necessary to cause failure, the amplification of stresses in the elastic layer will result in faulting after some period of time.

Figure 4.6 shows the time period for faulting to occur for a range of applied stresses from 20 to 150 MPa and a viscosity of 10^{23} Pa s for the lower crust and lithospheric mantle. If the viscosity is reduced by an order of magnitude, then the failure times are also reduced by an order of magnitude. The reverse is true for an increase in viscosity. For all values of the applied stress, open-crack shear failure is predicted to occur in the shallowest elements, by the Modified Griffith criteria, with a fault hade of approximately 30°. The centres of these shallowest elements is at 3.33 km, and the value of the horizontal stress in the upper crust when failure is predicted is about 86.5 MPa. This is in excellent agreement with a direct calculation made from the theory. For the open-crack regime, failure will occur if

$$\tau^2 \geqslant -4T\sigma_m$$

where τ is the maximum shear stress, $\frac{\sigma_{max} - \sigma_{min}}{2}$, σ_m is the mean stress, $\frac{\sigma_{max} + \sigma_{min}}{2}$, and T is the tensile strength. Note that the mean stress must include the lithostatic stress, which can be explicitly added in.

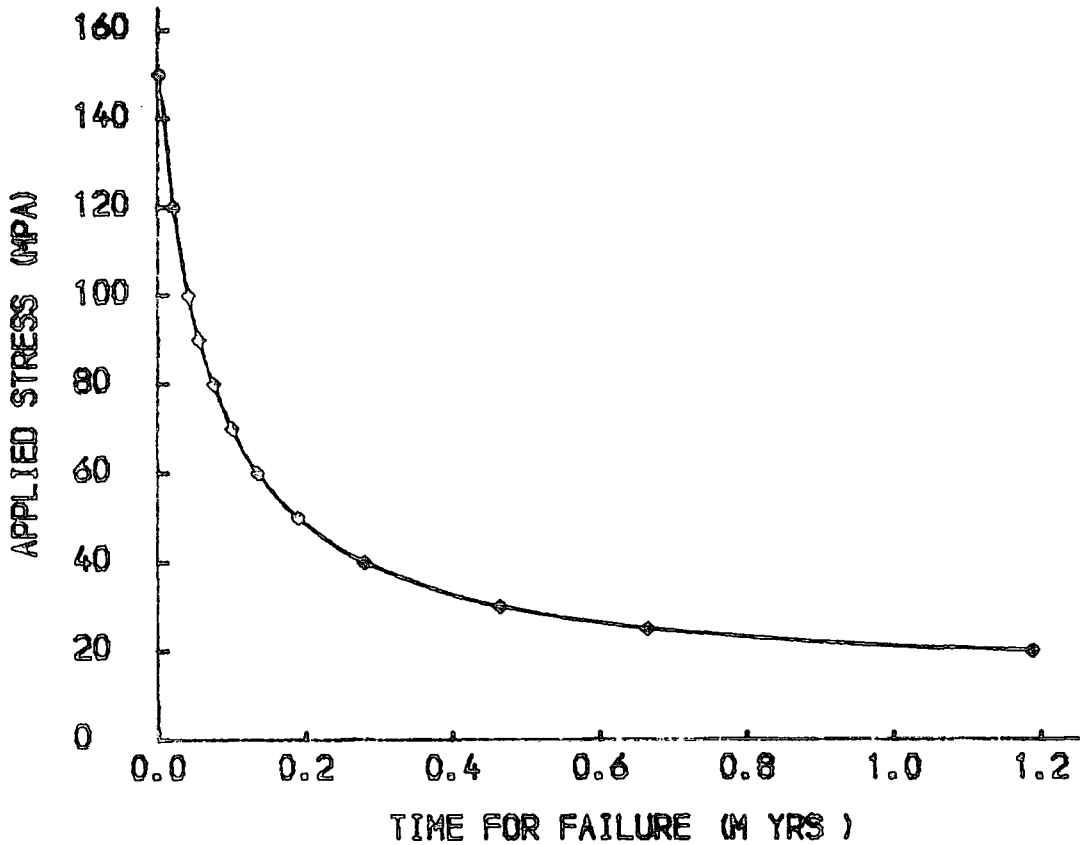

Fig. 4.6: Time period for faulting to occur for a range of applied stress and a viscosity of 10^{23} Pa s for the lower crust and mantle

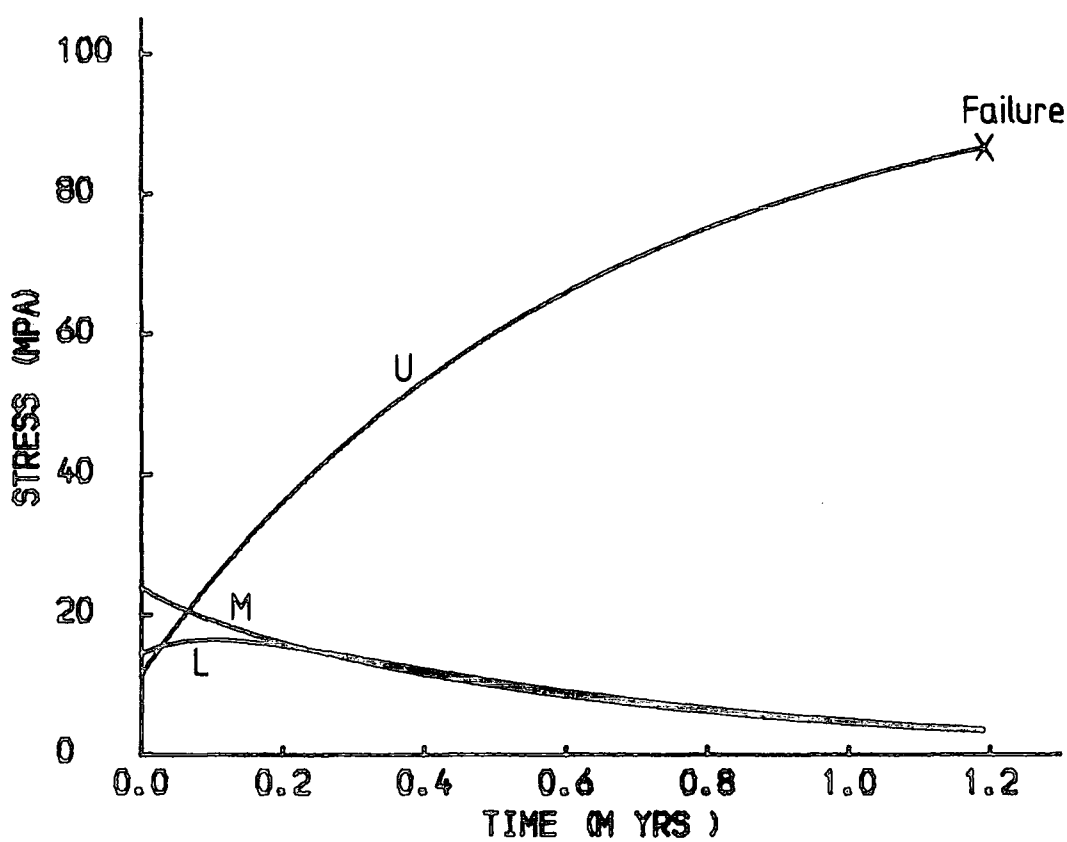

Fig. 4.7: Variation of stress with time for the upper crust (U), the lower crust (L) and the mantle (M) at the centre of the model for an applied stress of 20 MPa and a viscosity of 10^{23} Pa s for the lower crust and mantle.

Applying a tensile stress in the x-direction results in the x-stress being the largest. The y-stress can be considered to be negligibly small and the z-stress is the intermediate stress, which has no effect. Therefore,

$$\tau = \frac{\sigma_x}{2}$$

$$\sigma_m = \frac{\sigma_x}{2} + \int_0^h \rho\, g\, dh$$

For the shallowest elements, the lithostatic stress at the centre (3.33 km depth) is -89.9 MPa, so for a tensile strength of 10 MPa

$$\frac{\sigma_x^2}{4} = 40(89.9 - \frac{\sigma_x}{2})$$

$$\therefore \sigma_x^2 + 80\sigma_x - 14384 = 0$$

which gives

$$\sigma_x = 86.4 \text{ MPa}$$

For a thickness of the upper crust of 20 km and of the lithosphere of 100 km, as used in the finite element model, the minimum value of the applied stress for faulting to occur can be calculated from equation 4.2,

$$\sigma_{APP} = \frac{86.5}{5} = 17.3 \text{ MPa}$$

It is obvious from equation 4.2 that for a thinner elastic layer this minimum value for faulting will be less and the time for faulting to occur will also be less for all values of applied stress. The reverse is true for a thicker elastic layer. Consequently, faulting will be

more likely in areas of localised elastic layer thinning, such as the Basin and Range province, than in old shield areas with thick elastic layers. This was also noted by Kusznir and Bott (1977).

For the remainder of this chapter an applied tensile stress of 20 MPa will be used. This is within the stress levels thought to be caused by the stress sources discussed earlier (Bott and Dean, 1972; Artyushkov, 1973; Turcotte and Oxburgh, 1976; Bott and Kusznir, 1979).

Figure 4.7 shows the variation of stress with time in the three layers, at the centre of the model, for a viscosity of 10^{23}Pa s for the lower crust and mantle and an applied stress of 20 MPa. The instantaneous elastic stresses generated in the three layers are not equal. This is because the layers have different Young's moduli. The relationship between the stress in any layer and the applied stress, near the centre, is given by

$$\sigma_i = \frac{E_i}{\overline{E}} \cdot \sigma_{APP} \qquad 4.3$$

where σ_i and E_i are the horizontal stress and the Young's modulus for layer i respectively, and $\overline{E}$ is a weighted mean Young's modulus given by

$$\overline{E} = \frac{\sum_{i=1}^{n} E_i \ell_i}{\sum_{i=1}^{n} \ell_i} \qquad 4.4$$

where ℓ_i is the thickness of the i th layer. This relationship clearly satisfies equation 4.1. For the physical parameters used in the finite element model (listed in Table 4.1),

$$\bar{E} = 1.502 \times 10^{11} \mathrm{Nm}^{-2}$$

and the stresses near the centre are

$$\sigma_{UC} = 11.3 \text{ MPa}$$
$$\sigma_{LC} = 14.4 \text{ MPa}$$
$$\sigma_{M} = 24.0 \text{ MPa}$$

which are in exact agreement with the values calculated from the finite element analysis for the centre of the model and shown in Figures 4.7 and 4.8(a). This is the explanation of the fact that although a stress of 86.5 MPa in the elastic layer is sufficient to cause failure, an applied stress of 86.5 MPa would not cause instantaneous failure. The smallest value of the applied stress that would result in immediate failure can be calculated from equation 4.3,

$$\sigma_{APP} = \frac{\bar{E}}{E_{UC}} \times 86.5 \text{ MPa}$$
$$= 153 \text{ MPa}$$

This is in good agreement with Figure 4.6 where an applied stress of 150 MPa requires only 2,000 yrs for failure to occur.

The stresses in the central section of the model for an elastic solution are shown in Figure 4.8(a). Figure 4.8(b) shows the surface displacement of the whole model. The reason for using a long grid now becomes apparent. Because the upper layers have smaller Young's moduli than the lower layer, they are able to stretch more in response to the applied tension. This results in a downward bending of the model near

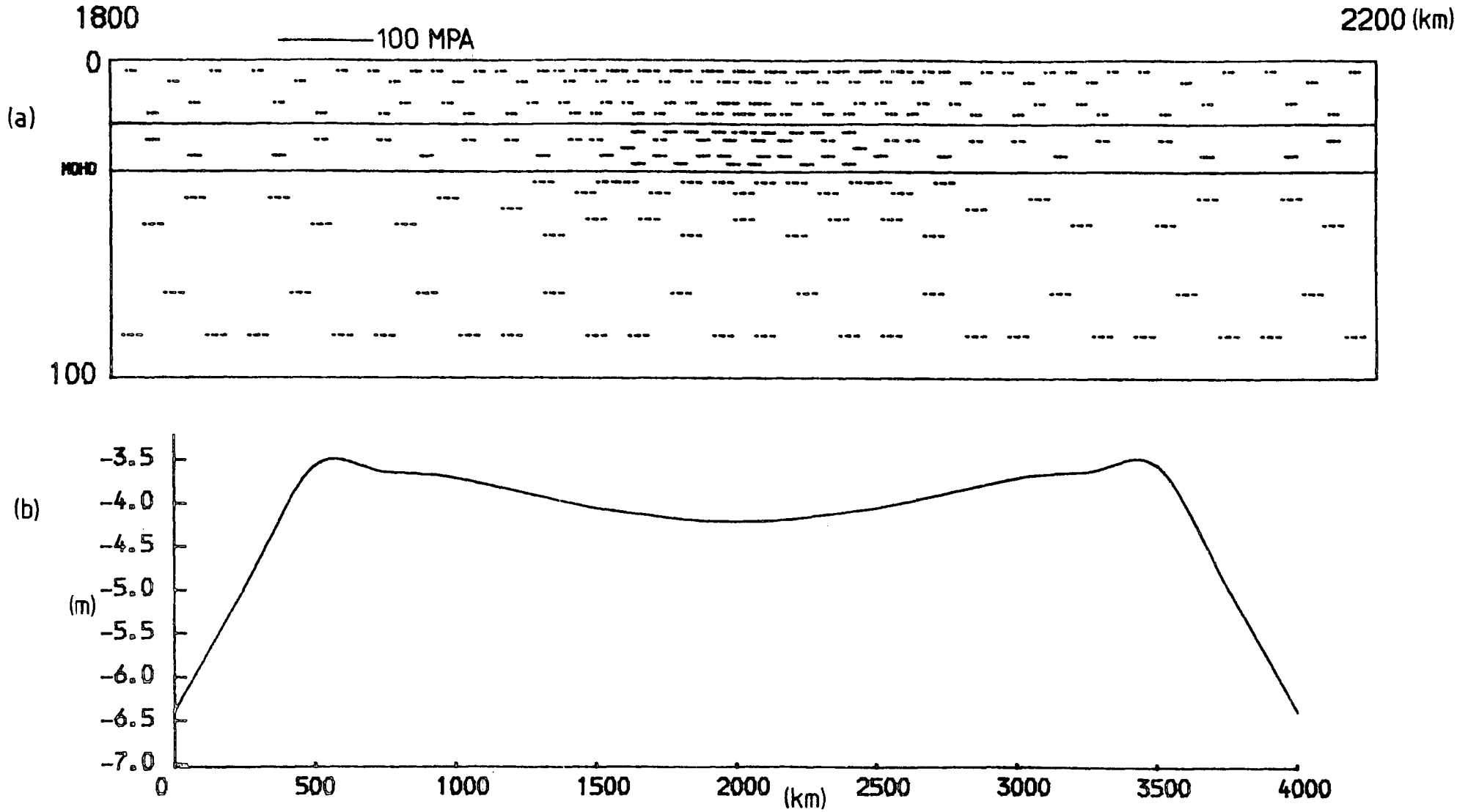

Fig. 4.8: Elastic solution for an applied stress of 20 MPa

(a) Principal stresses for central section of grid

(b) Surface displacements for whole model

the edges, which modifies the stresses slightly from the values given above for the centre of the model. This bending effect extends into the model for a distance of about 1700 km. The displacements have a maximum value of 6.4 m at the edges of the model. The central section, which is unaffected by the edge effects, subsides by 4.2 m.

Figure 4.7 shows that as the visco-elastic material relaxes, the stress in the upper crust increases until failure occurs after 1.19 M yrs. The stresses in the lower crust are initially slightly increased and then decrease at the same rate as the stresses in the mantle. The initial slight increase is because the instantaneous stresses in the mantle are greater than in the lower crust, and, consequently, the mantle initially relaxes more rapidly and causes a small amount of amplification in the lower crust until the stresses are approximately equal when they both relax at the same rate, as would be expected since they have the same viscosity.

The stresses at the time of failure, after 1.19 M yrs, are illustrated in Figure 4.9(a) where the result of the stress amplification can be clearly seen. The stresses in the upper crust have reached a value of 86.5 MPa whereas the stresses in the lower crust and mantle have values of 3.6 MPa and 3.3 MPa respectively. Figure 4.9(b) shows the surface flexure for the whole model after 1.19 M yrs. The edges of the model are now bent upwards. This is because the lower part of the model has been allowed to flow outwards, in response to the applied tension, and can deform more than the upper part which is elastic. The effect has been commented on by Kusznir and Bott (1977), who point out that it could be a significant source of vertical movement near plate boundaries. The edges have subsided by 68 m and the centre of the model, away from the edge effects, has subsided by 81 m. The maximum amount of subsidence

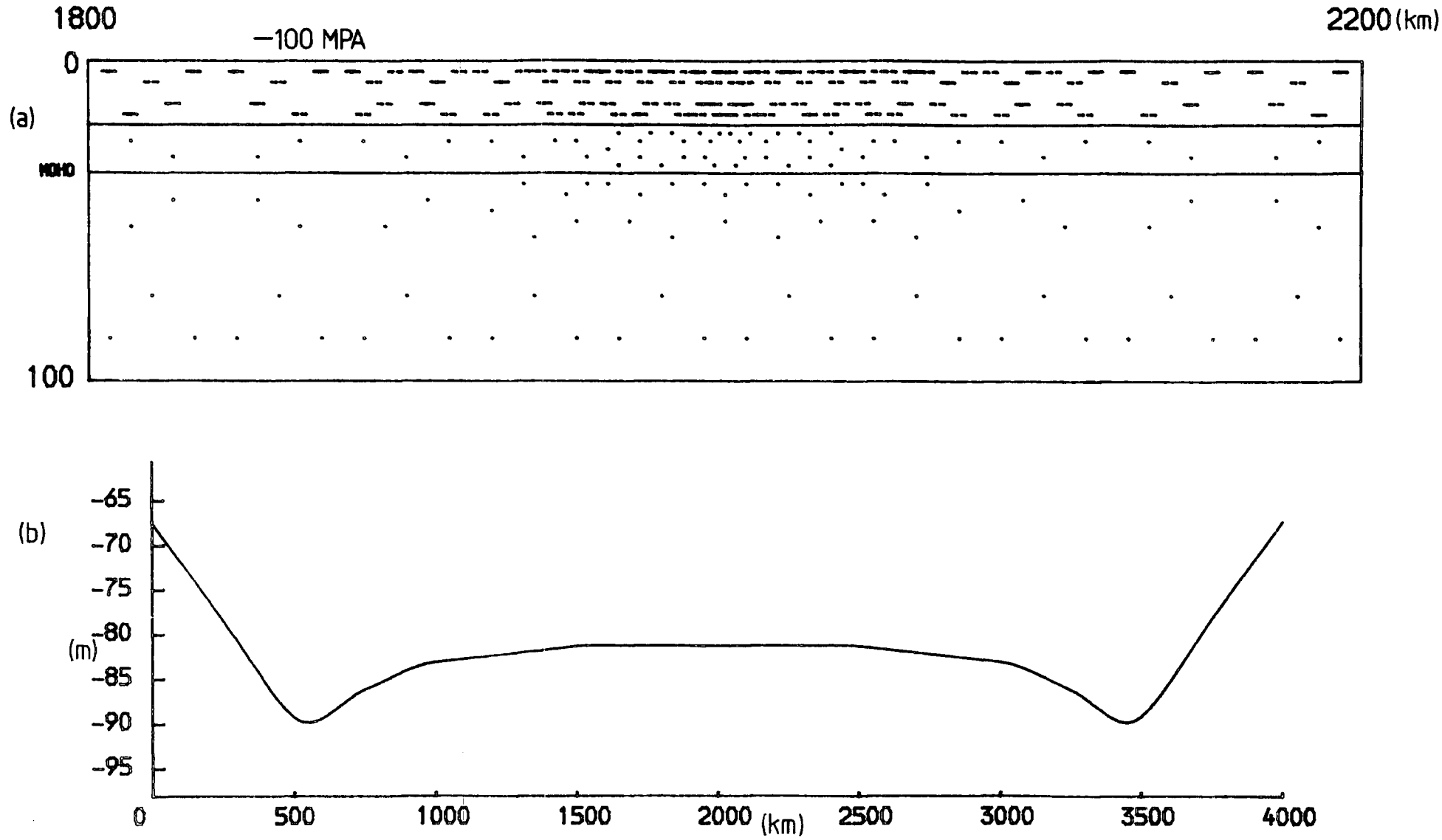

Fig. 4.9: Solution after 1.19 Myrs for an applied stress of 20 MPa and a viscosity of 10^{23} Pa s for the lower crust and mantle.

(a) Principal stresses for central section of grid

(b) Surface displacements for whole model

has occurred about 500 km in from the edges with value 90 m. The stress system illustrated in Figure 4.9(a) will be reapplied, in Chapter 6, to a model containing a fault.

It is interesting at this point to examine the effect of a viscosity contrast between the lower crust and the mantle. Figure 4.10 shows the variation of stress with time in the three layers, at the centre of the model, for an applied stress of 20 MPa and viscosities of 10^{23} Pa s for the mantle and 10^{22} Pa s for the lower crust. The initial elastic stresses are, of course, the same as those in Figures 4.7 and 4.8(a). The stresses in the lower crust relax very rapidly, because of its lower viscosity, and after only 50,000 yrs have fallen from 14.4 MPa to 4.5 MPa. The effect of this is to cause the stresses in the upper crust to increase more rapidly than in Figure 4.7 and also to amplify slightly the mantle stresses from an initial value of 24.0MPa to a maximum of 25.0 MPa. This effect is small because the thickness of the lower crust is considerably less than the thickness of the lithospheric mantle. Following this slight amplification, the stresses in the mantle relax at a similar rate to the constant viscosity case, as can be seen in Figure 4.12. Because of the more rapid amplification rate of stresses in the upper crust, failure occurs after a shorter time period. Failure is predicted after 0.99 M yrs, when the stress in the upper crust has a value of 86.5 MPa and the stresses in the lower crust and mantle have fallen to 0.4 MPa and 4.1 MPa respectively.

Figure 4.11 shows the variation of stress with time, at the centre of the model, for an applied stress of 20 MPa and viscosities of 10^{23} Pa s for the mantle and 10^{24} Pa s for the lower crust. The stresses in the mantle relax more rapidly than in the two previous cases, as can be seen in Figure 4.12, and in the process amplify both the lower crustal

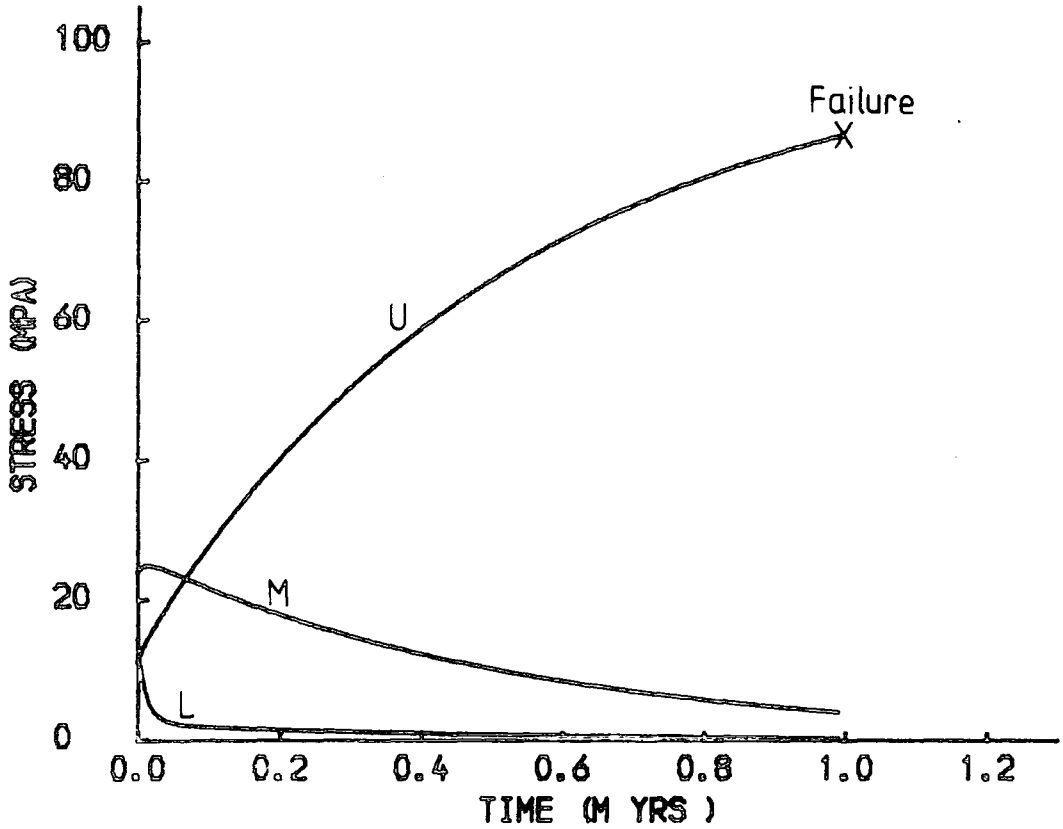

Fig. 4.10: Variation of stress with time for the upper crust (U), the lower crust (L) and the mantle (M) for an applied stress of 20 MPa and viscosities of 10^{23} Pa s for the mantle and 10^{22} Pa s for the lower crust.

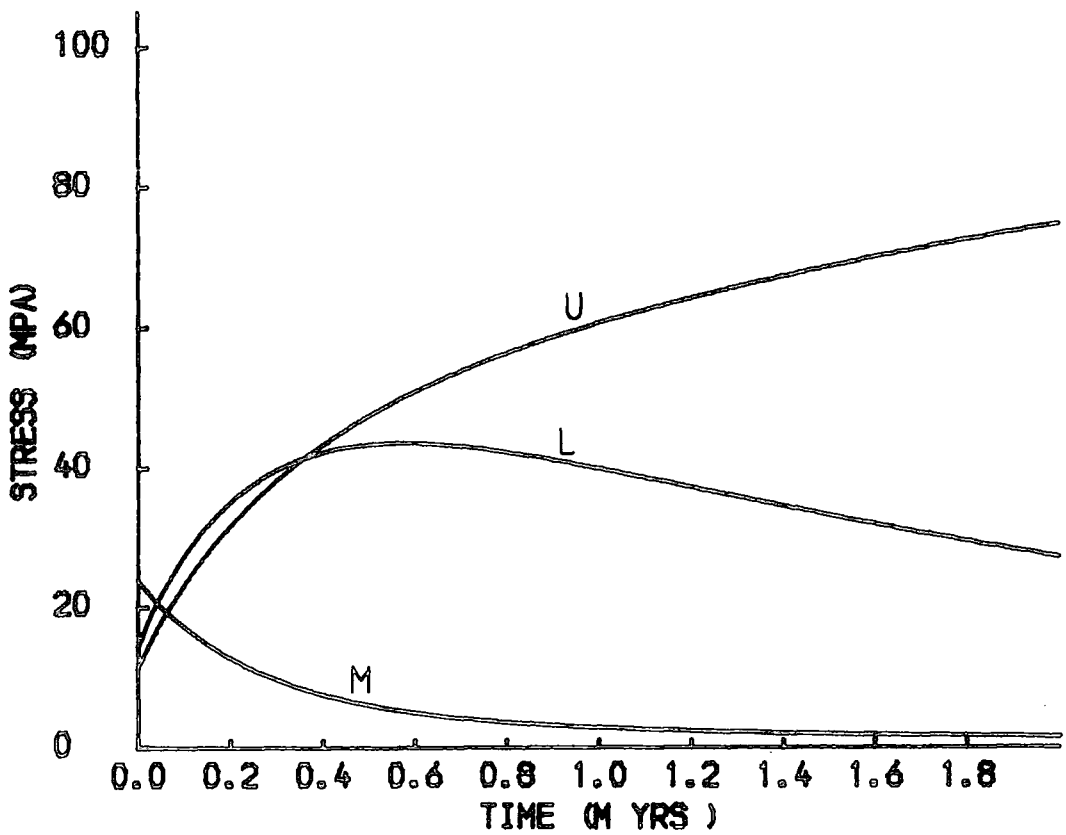

Fig. 4.11: Variation of stress with time for the upper crust (U), the lower crust (L) and the mantle (M) for an applied stress of 20 MPa and viscosities of 10^{23} Pa s for the mantle and 10^{24} Pa s for the lower crust.

and upper crustal stresses. Initially the stresses in the lower crust are amplified slightly more rapidly than in the upper crust. After about 0.57 M yrs, when the stresses in the mantle have fallen to 5.3 MPa, the lower crustal stresses reach their maximum of 43.6 MPa and start to decrease. The rate of decrease of the lower crustal stresses, and the corresponding rate of increase of the upper crustal stresses, is fairly small and even after 2 M yrs failure has not occurred. The stress in the upper crust after this time has a value of 74.6 MPa and is increasing only at the rate of 0.1 MPa in every 10,000 yrs. Thus to reach the failure value of 86.4 MPa will take at least another 1.18 M yrs. In fact it will probably take considerably longer than this because the amplification rate decreases with time.

In order to compare the stress - time curves for the three situations described above, Figures 4.7, 4.10 and 4.11 are plotted on the same diagram in Figure 4.12. It can be concluded from these diagrams that a lower viscosity lower crust results in a slightly shorter time for failure to occur than for the constant viscosity case, whereas a higher viscosity lower crust results in a much greater time for failure.

4.6 Stress amplification: power law creep rheology

In Chapter 3 the power law creep equation was defined as

$$\dot{\varepsilon}_{ij} = A \exp(-\frac{Q}{kT})(\bar{\tau})^{n-1}\sigma'_{ij}$$

and for each element the creep strain vector is calculated from the temperature and the stress tensor for the element. An important point here is the calculation of the temperature. If the temperature of each element is calculated, at its centre, from the pressure and the geotherm

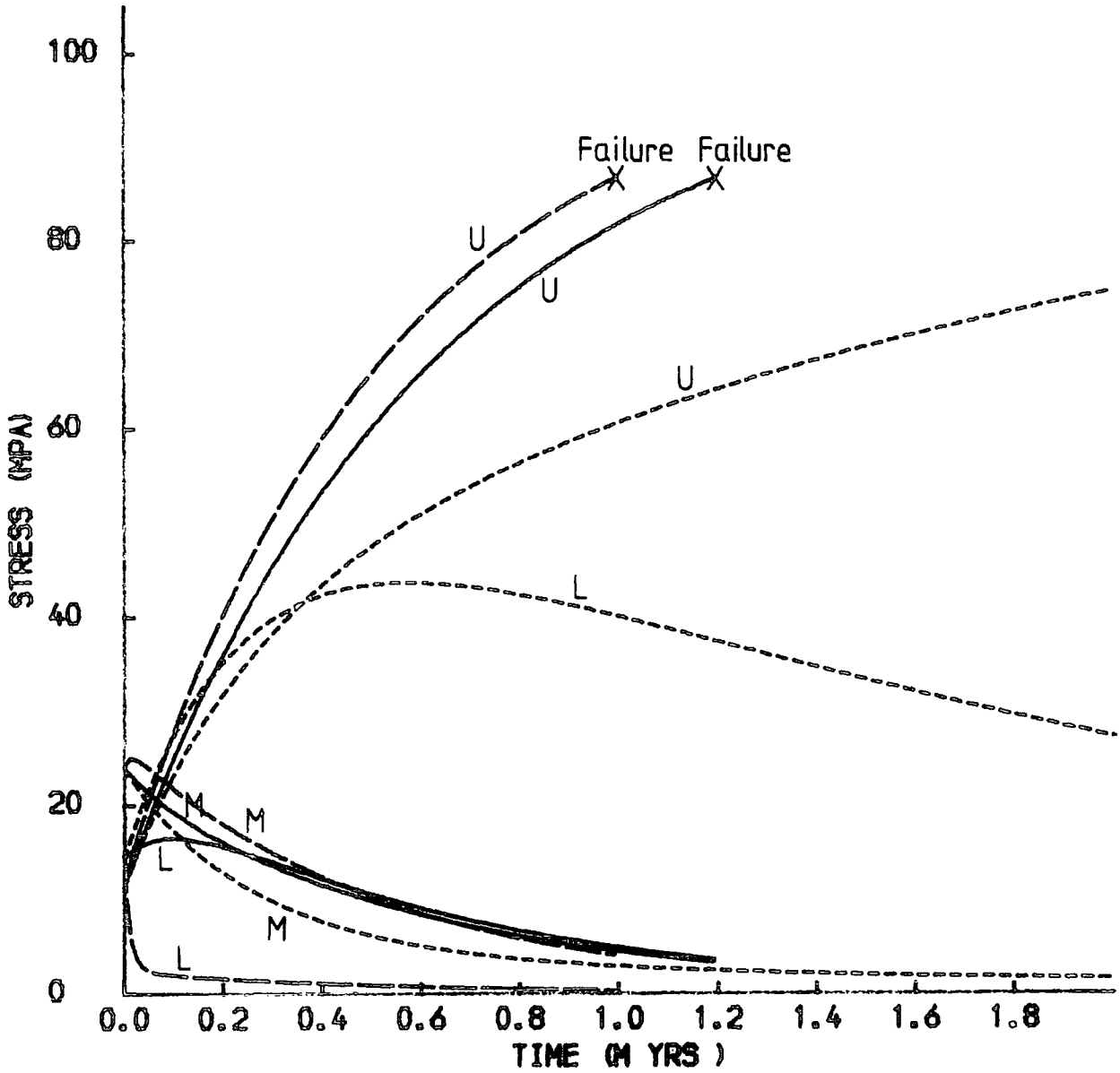

Fig. 4.12: Variation of stress with time for the upper crust (U), the lower crust (L) and the mantle (M) for an applied stress of 20 MPa and viscosities for the lower crust and mantle of:

——————— $\eta_{LC} = 10^{23}$ Pa s ; $\eta_M = 10^{23}$ Pa s

— — — — $\eta_{LC} = 10^{22}$ Pa s ; $\eta_M = 10^{23}$ Pa s

- - - - - - - - $\eta_{LC} = 10^{24}$ Pa s ; $\eta_M = 10^{23}$ Pa s

(Figure is composed of Figs. 4.7, 4.10, 4.11)

given in Chapter 2 and the analysis is run through time, then peculiar flexures occur throughout the model. These are illustrated in Figure 4.13. A long, regular grid has been used (Figure 4.13(a)) to show the simple nature of these displacements. This flexure is an artifact of the method and is caused by calculating the temperature of each element at its centre. Consider the section of grid illustrated in Figure 4.14. The effective viscosity on the vertical line a-a can be considered to be the same as that of the elements A and A' to which it belongs. Similarly, the effective viscosity on b-b is that of elements B and B'. Now the elements A,A' have their centres at different depth from B and B' and so their temperatures, calculated from the geotherm, will be different. Consequently, their viscosities will be different and so the effective viscosity of the line a-a will be different to that of b-b. The effect of this is to make some sections of the grid more resistant to creep than others. This causes the flexure seen in Figure 4.13(c). The 'highs' correspond to the vertical sections labelled α-α in Figure 4.14 and the 'lows' to sections β-β. This result is obviously physically incorrect. Since the stresses and temperatures, in the model used here, are constant at a given depth, the viscosities should also be constant at that depth. So the effective viscosities along lines a-a and b-b should be equal.

This artificial effect can be avoided by assigning a temperature to each horizontal layer. Then elements A,A',B and B' will all have the same viscosity (providing their stresses are equal) and the effective viscosities on the lines a-a and b-b will be equal. Returning to the grid that has been used for the chapter so far, and will continue to be used (Figure 4.1), there are three horizontal layers, in the ductile material, that extend across the model. It will be assumed that the

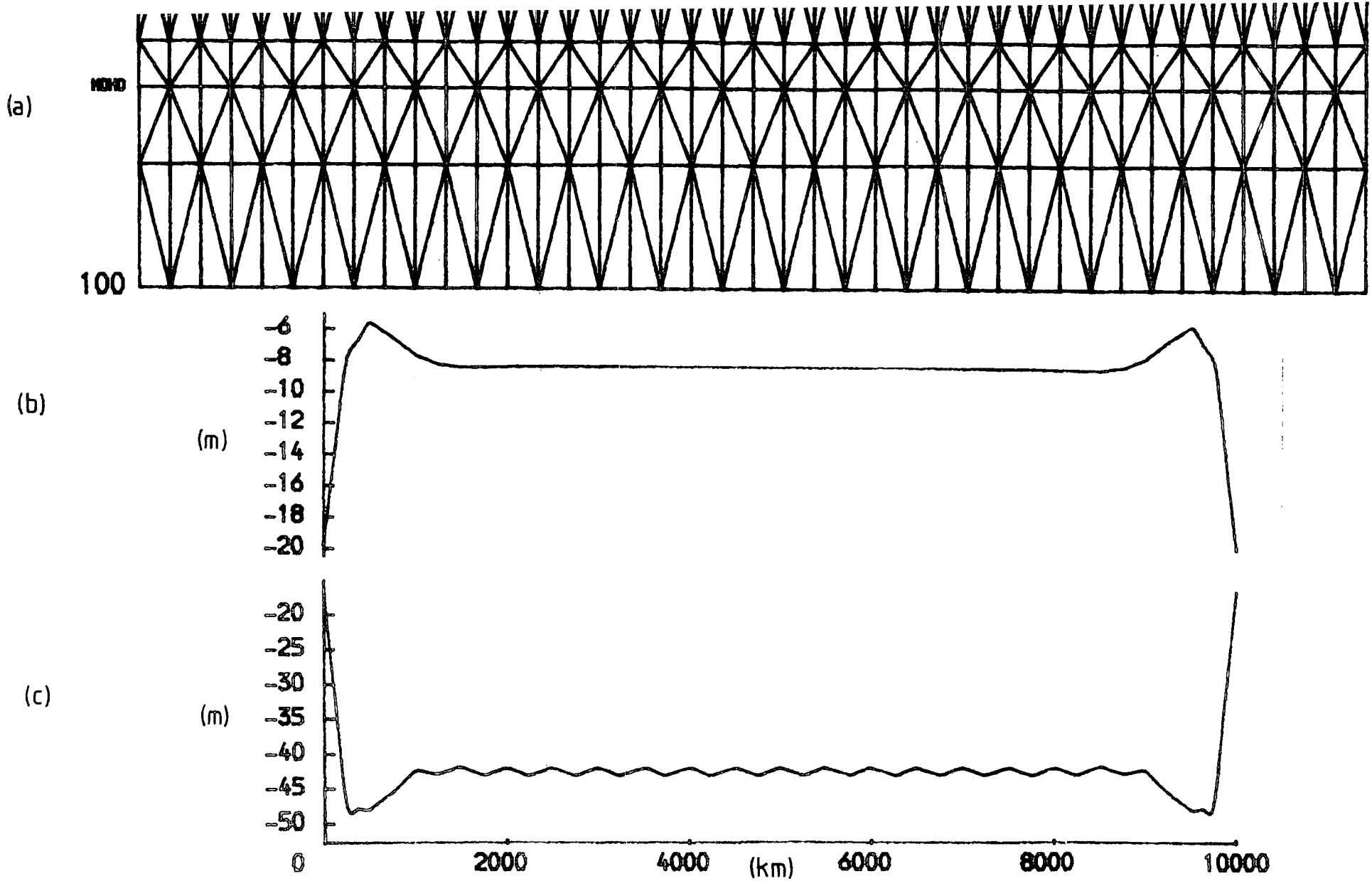

Fig. 4.13: (a) Finite element grid
(b) Elastic solution surface displacements for an applied stress of 20 MPa
(c) Visco-elastic solution surface displacements after 20,000 yrs using power law creep

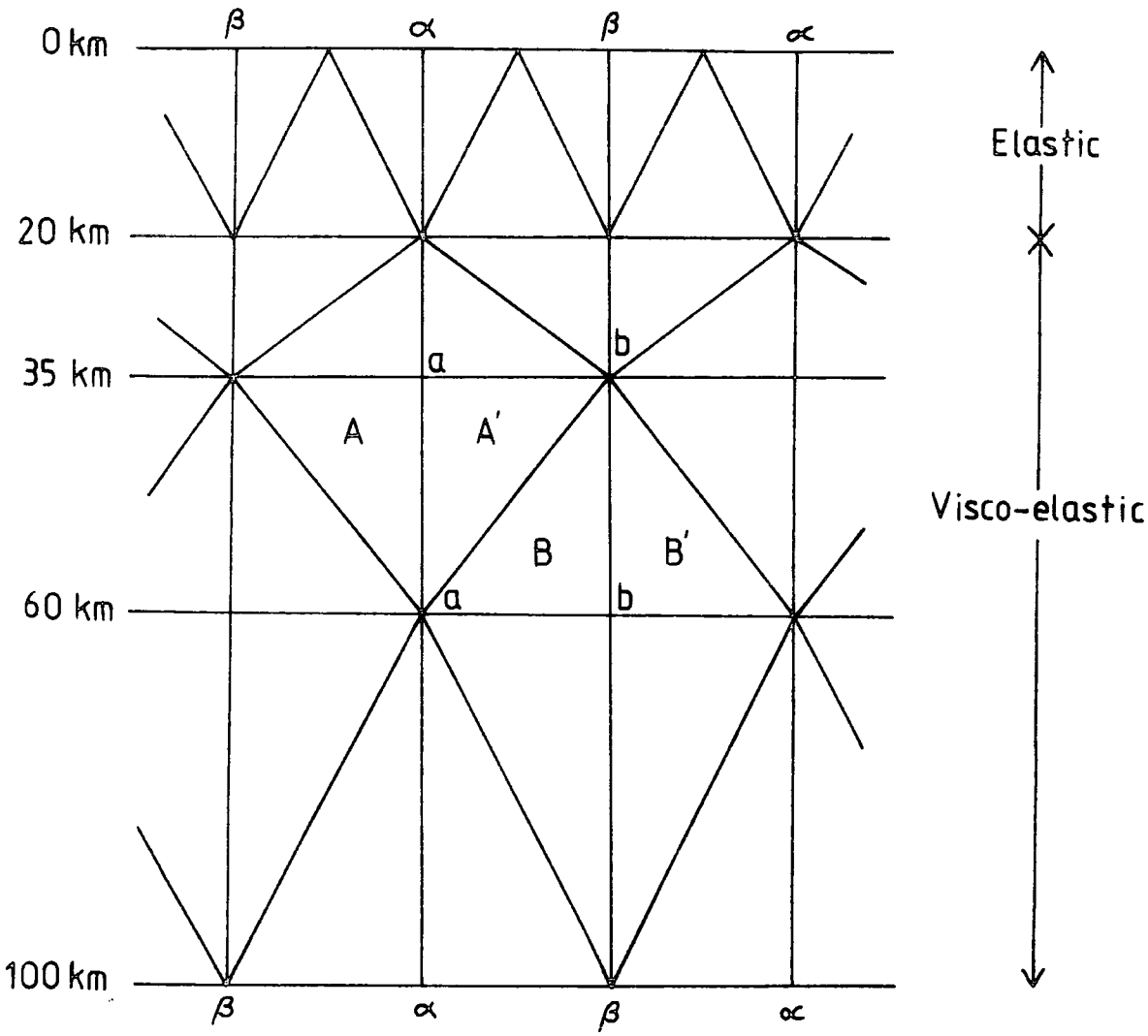

Fig. 4.14: Section of finite element grid shown in Figure 4.13(a).

temperature of all elements in any one layer is constant. This temperature is calculated at the centre of the layer using the geotherm given in Chapter 2 (Mercier and Carter, 1975). Table 4.2 lists the temperatures and depth ranges of these layers together with their creep parameters which have been discussed in Chapter 2.

Figure 4.15 shows the time period for faulting to occur for a range of applied stresses and a power law creep rheology for the lower crust and mantle. Comparing this plot with Figure 4.6 shows that

	Depth Range (km)	Temp (°C)	Q (kJ mol^{-1})	A ($MPa^{-3}s^{-1}$)	n
Lower crust	20 - 35	676	267.904	10^{-4}	3
Upper lithospheric mantle	35 - 60	906	523.250	10^{3}	3
Lower lithospheric mantle	60 - 100	1122	523.250	10^{3}	3

Table 4.2: Creep parameters for the lower lithosphere

at stresses above about 25 MPa the time period before failure occurs is greatly reduced. For an applied stress of 150 MPa it is only 200 yrs. For stresses below about 25 MPa it is greatly increased, and for 20 MPa it is 3.608 M yrs. This is to be expected with a stress-dependent viscosity where high stresses result in low viscosities and vice-versa.

Figure 4.16 shows the variation of stress with time for an applied stress of 20 MPa. There are now four distinct layers in the model corresponding to the elastic upper crust, the lower crust, the upper lithospheric mantle (35 to 60 km) and the lower lithospheric mantle

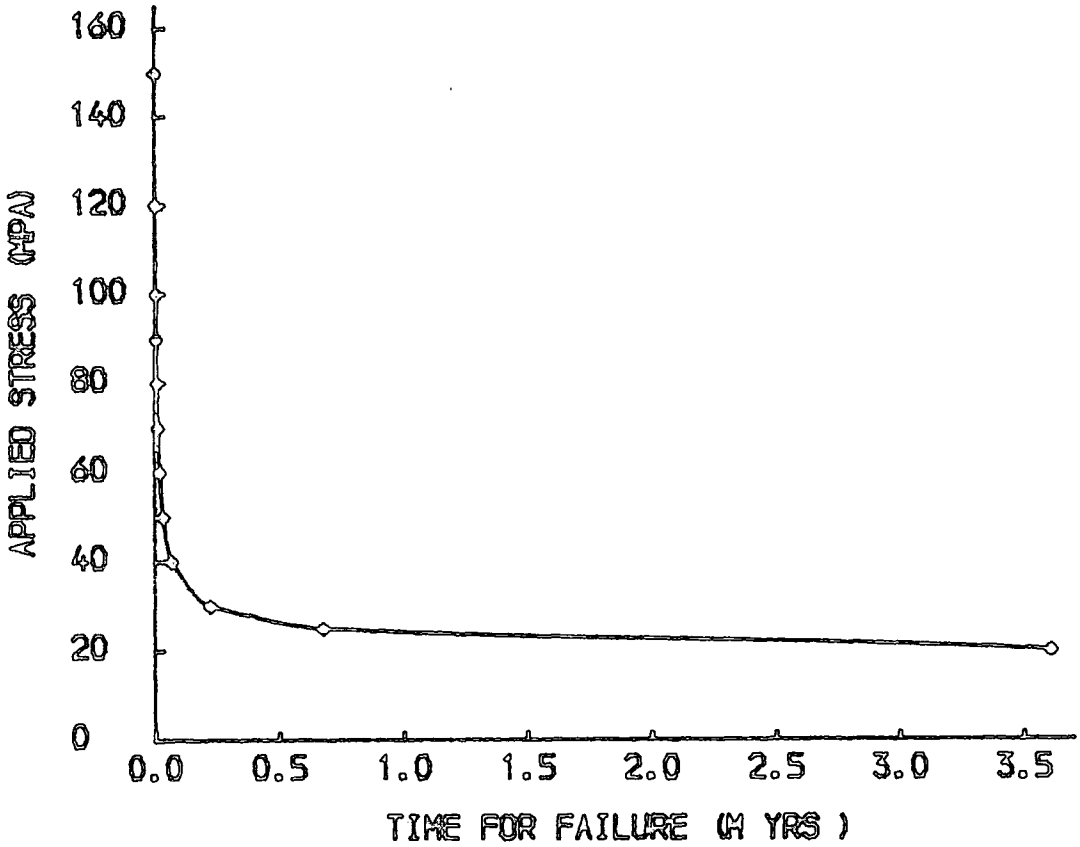

Fig. 4.15: Time period for faulting to occur for a range of applied stress and a power law creep rheology for the lower crust and mantle.

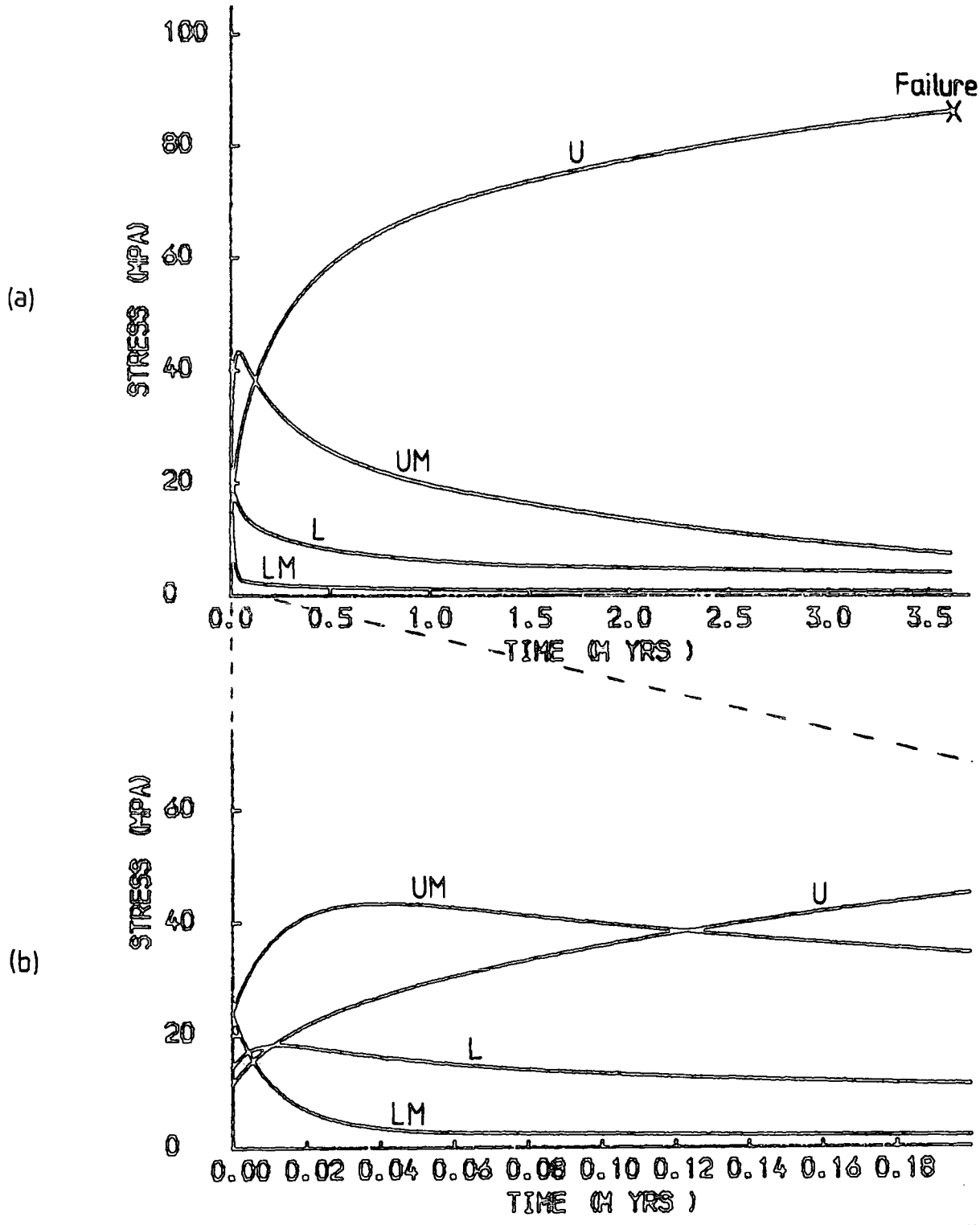

Fig. 4.16: (a) Variation of stress with time for the upper crust (U), the lower crust (L), the upper lithospheric mantle (UM) and the lower lithospheric mantle (LM) for an applied stress of 20 MPa and a power law creep rheology.

(b) Expanded version of (a) for the initial 200,000 yrs.

(60 to 100 km). The stresses for the initial 200,000 yrs are plotted on a larger time scale in Figure 4.16(b) so that their early variations can be better seen. The stresses in the upper crust increase in a similar manner to the previously discussed constant viscosity models up to a value of 86.5 MPa when faulting is predicted. The lower crustal stresses increase initially to a value of 18.3 MPa after 14,000 yrs and then decrease. The stresses in the upper part of the lithospheric mantle increase significantly to a maximum of 43.3 MPa after 40,000 yrs. The lower lithospheric mantle stresses decrease very rapidly at first, and then more slowly. Comparing these effects with those seen in earlier models suggests that the lower lithospheric mantle has the lowest viscosity, followed by the lower crust and then the upper lithospheric mantle. This is confirmed by Figure 4.17 which shows the variation of effective viscosity with time in these three layers. It must be remembered that the effective viscosity has been constrained to lie between 10^{22} Pa s and 10^{24} Pa s . After 3.608 M yrs, when failure is predicted in the upper crust, the stresses in the lower crust, upper lithospheric mantle and lower lithospheric mantle have fallen to 4.1, 7.5 and 0.8 MPa respectively.

It is interesting at this point to investigate the effect on stress amplification in the upper crust of a thermal anomaly in the lower lithosphere. Figure 4.18(a) shows the central section of the finite element grid with the region of anomalous temperature shaded. All the elements in this shaded region have their temperatures raised by 50°C. With this model faulting is predicted after only 828,000 yrs. This large decrease in failure time is due to the decreased viscosity in the central region, where the temperature is higher. Figure 4.18(b) shows the surface displacement of the central 400 km of the model at the time of faulting. For the constant temperature situation the subsidence was uniform (dashed

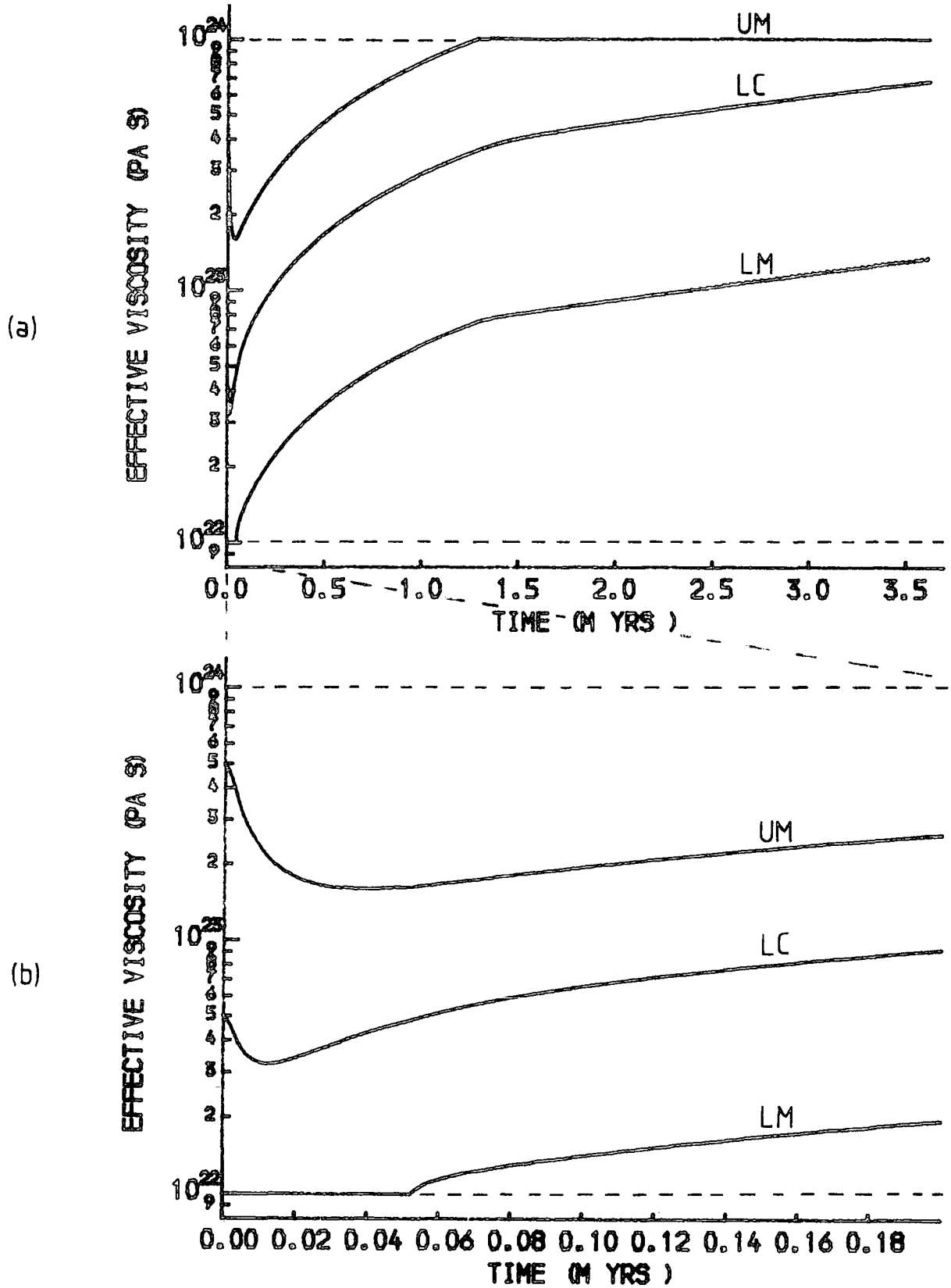

Fig. 4.17: (a) Variation of effective viscosity with time for the lower crust (LC), the upper lithospheric mantle (UM) and the lower lithospheric mantle (LM) for an applied stress of 20 MPa.

(b) Expanded version of (a) for the initial 200,000 yrs.

Note the constraint: $10^{22} \leqslant \eta_{eff} \leqslant 10^{24}$

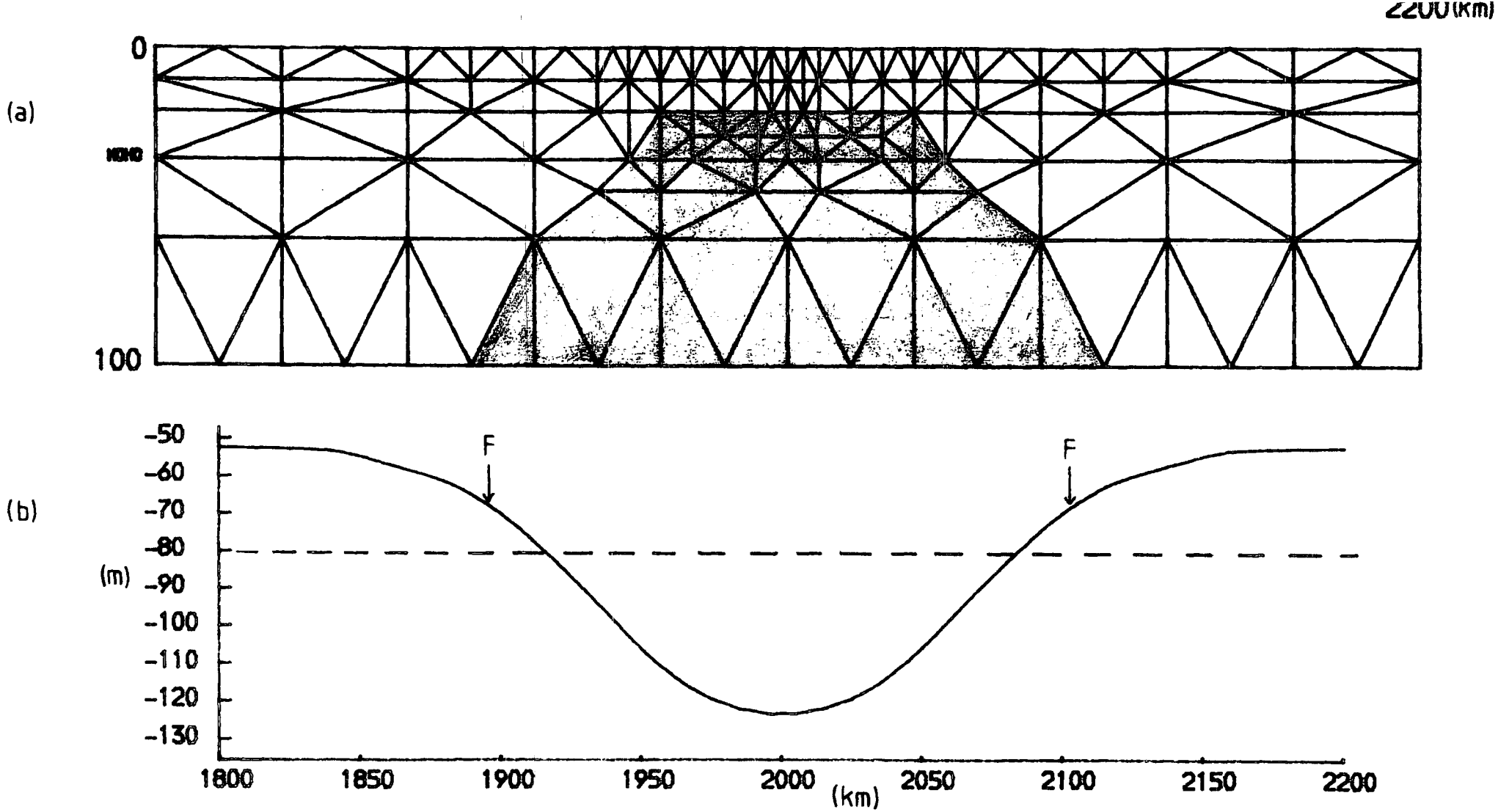

Fig. 4.18: (a) Central section of grid with anomalous temperature region shaded.
(b) ———— surface displacements at time of failure with anomaly present.
F position of predicted failure.
— — — — surface displacements at time of failure with no anomaly.

line in Figure 4.18(b)), whereas in this case there is a marked area of increased subsidence directly overlying the higher temperature material. This is a result of the decreased viscosity in that region. This flexure affects the stresses in the upper crust to a small degree. On the flanks of the subsided area the near-surface tensional stresses have been slightly increased because of the nature of the bending, whereas in the centre they have been slightly reduced. Consequently, faulting is predicted to occur on the flanks, at the positions marked 'F' in Figure 4.18(b).

It should be realised here that only the effect on the viscosity of the thermal anomaly has been considered. Other more important effects, particularly with regard to the flexure, will be due to thermal expansion and to density variations and the probable effect, if all the parameters are considered, will be for doming and plateau uplift to occur. The stress distribution that would be associated with uplift of this type has been investigated by Bott and Kusznir (1979). Nevertheless, the significant change in the time for failure to occur does suggest that faulting will happen preferentially in areas where anomalously high temperatures exist. This is in agreement with the observations noted in Chapter 1 that major graben development is often preceded by doming and volcanism.

4.7 Summary

The main conclusions of the work described in this chapter will now be summarised in point form:

1) Stress boundary conditions, which are the most realistic, result in amplification of upper crustal stresses as the lower crust and

lithospheric mantle relax. This was pointed out by Kusznir and Bott (1977). Provided the applied stresses are sufficiently large, which depends on the relative thicknesses of the layers, failure will eventually occur in the upper crust. For a tensional stress system the failure will take the form of normal faulting with a fault dip of about 60°.

2) If Young's modulus varies with depth, then different magnitude stresses are developed in the different layers by a uniform applied stress. A Young's modulus that increases with depth, which is supported by the increase in P-wave velocity with depth, results in lower stresses near the top of the lithosphere and higher stresses near the base. Consequently, an applied stress greater than the value necessary for faulting may not result in instantaneous failure.
3) The time period for faulting to occur depends on the viscosity of the ductile material and the magnitude of the applied stress.
4) If the elastic upper crust is locally thinned, then stress amplification will occur more rapidly in that region and failure can occur for a smaller value of applied stress. Consequently, faulting is more likely in areas of crustal thinning, such as the Basin and Range province, than in stable shield areas with thick crust.
5) If the viscosity of the lower crust is decreased by an order of magnitude, then the time to failure is slightly decreased. If its viscosity is increased by an order of magnitude then a large increase in the time to failure occurs. Some stress amplification in high viscosity material will occur initially as a result of the rapid relaxation of the low viscosity material.
6) A power law creep rheology for the lower lithosphere results in a similar pattern of stress amplification to that of a Newtonian

visco-elastic rheology. The time to failure depends greatly on the value of applied stress. High stresses, which result in low effective viscosities, lead to rapid failure. Low stresses give high viscosities and very long periods of time are necessary before faulting will occur.

7) The variation of stress with time in any layer is dependent on the effective viscosity of the layers. Layers with high viscosities have their stresses initially amplified as the low viscosity layer relaxes. This is consistent with the results obtained using a Newtonian visco-elastic rheology.

8) A thermal anomaly giving localised higher temperatures results in more rapid stress amplification in that region, because of the decreased effective viscosity, and hence a shorter time to failure. The lateral variation in viscosity leads to differential subsidence of the surface, and stresses associated with this flexure will lead to preferred positions for faulting to occur. Although there are other important effects due to the thermal anomaly, it seems likely that faulting will occur preferentially in areas where the geothermal gradient is anomalously high. This is supported by the observations that major graben formation is often preceded by doming and volcanism, for example in the Rhinegraben, the Baikal rift and East Africa (Illies, 1977; Logatchev and Florensov, 1978; Davidson and Rex, 1980).

CHAPTER 5

FAULT MODELLING USING FINITE ELEMENTS

5.1 Introduction

In order to continue investigating the development of graben structures it is necessary to have a method of modelling faults in the context of the finite element analysis used here. Deformation associated with faulting arises from two sources. The first of these is the difference in elastic properties between the fault zone and the surrounding material. This effect is incorporated into the stiffness matrix. The method of Goodman et al. (1968), with certain minor modifications, is used for developing the fault stiffness matrix. The second, and most important, source of fault movement is the result of frictional sliding on the fault caused by shear stresses exceeding the frictional strength. In this chapter a new method of modelling frictional sliding is described. The method allows the use of a variety of friction laws to determine the frictional strength. In the presence of deviatoric stresses, and particularly after long periods of time, fault movement as a result of shear stresses dominates the elastic effect of a weak fault zone.

The first section of this chapter is devoted to a brief discussion of previous methods of fault modelling using finite elements. The remaining sections describe in detail the proposed method, which will be used in Chapters 6, 7 and 8. The programming is performed in two subroutines, FORMKF and FSHEAR, of the finite element subroutine library FELIB and is listed in Appendix 2.

5.2 Previous methods of fault modelling

The representation of a fault as a discontinuity with the nodes across the fault joined by pin-ended straight members was suggested by Anderson and Dodd (1966). Normal compressive stress was transmitted across the fault in a satisfactory manner, but in the event of tensile stress the straight members had to be removed and the analysis performed again. Apart from the disadvantage of having to adjust the grid, possibly in the middle of a time-dependent solution, their method of modelling the fault offered no resistance to movement parallel to the fault. Service and Douglas (1973) suggested modelling a fault as a band of anisotropic elastic elements having weak elastic parameters in the direction of the fault plane. The major disadvantage in this method is that of deciding by how much to reduce the elastic parameters. Whilst the mechanism of fault movement is not well understood, there seems to be no justification for assuming that it can be simulated by making the fault behave as a weak elastic body. A secondary disadvantage is that the weak elements will deform rapidly, which may result in having to recalculate the stiffness matrix during time-dependent solutions. This operation results in a large increase in computing time and expense and should be avoided if possible. Despite these disadvantages this method has been used for studying lithospheric deformation (Neugebauer and Spohn, 1978). A similar approach has been used in time-dependent analysis whereby the fault is represented by elements having lower effective viscosities than the surrounding material (Bird, 1978; Neugebauer and Spohn, 1978).

A more sophisticated method for modelling a discontinuity was described by Goodman et al. (1968). They developed a stiffness matrix for a joint of zero width which involved only the length of the joint

and the unit normal and shear stiffnesses. The stiffness matrix derivation of Goodman et al. will be discussed in the next section. Their method has been used by Bischke (1974) to model a thrust fault at a convergent plate margin. In his work, the amount of fault movement was controlled by adjusting the normal and shear stiffnesses. This is equivalent to altering the elasticity of the fault zone. Consequently, this method still does not allow for the most important effect of fault slip due to high shear stresses which exceed the frictional strength. The modelling of joints has been further developed by Goodman (1976) to include iterative procedures for allowing opening, closing and sliding of the joints. A considerable amount of detailed input data is required which makes this method suitable for near-surface geological engineering studies, for which it was designed, since many of the properties can be measured in the laboratory. For the modelling of deep faults, extending to 20 km, say, there are problems with assigning values to the parameters. In particular, the shear stiffness is very important in Goodman's method because the shear stresses on the fault are calculated from it. For deep faults, which die out at depth, the shear stiffness is not known. Indeed, it cannot be accurately estimated since, in cases where it has been determined in the laboratory, it displays a strong scale effect (Barton, 1972). Consequently, an alternative method is developed here whereby the calculation of the shear stress on the fault is dependent on the stress levels in the surrounding material rather than the shear stiffness of the fault.

5.3 Proposed method

The fault is represented as a plane boundary between a number of element pairs and is characterised by 'dual nodes' which initially have

the same spatial co-ordinates, but belong to different elements and can move independently along the fault plane. Fault deformation can arise from two sources. These are the elastic properties of the fault, and frictional sliding due to large shear stresses. This is illustrated in Figure 5.1. A stiffness matrix is formulated for each section of the fault, based on the work of Goodman et al. (1968), and depends only on the normal and shear stiffnesses. Incorporating these matrices in the global stiffness matrix allows for the effect of the elastic strength of the fault. By assigning a high value of normal stiffness the fault can be constrained to remain closed. Frictional sliding is dependent on the shear stresses acting on the fault. The stresses in surrounding elements are calculated by an elastic solution of the finite element equations and the normal and shear stresses on the fault are calculated from these. The amount of shear stress that can be maintained on the fault plane without slip (the frictional strength) is determined from the normal stress on the fault and an appropriate friction law. The pore pressure in the fault can be included at this stage. If the shear stress on the fault plane exceeds the value of the frictional strength, then the excess shear stress is converted to forces which are applied at the nodes on the fault and the finite element equations are re-solved. An iterative procedure is followed until the shear stress on the fault falls to an acceptable value. A detailed description of how these operations are performed will now be given.

5.3.1 Fault representation

The fault is represented in the finite element model as a plane boundary between several element pairs, and is divided into sections between the nodes lying on this boundary (Figure 5:2). The nodes on the

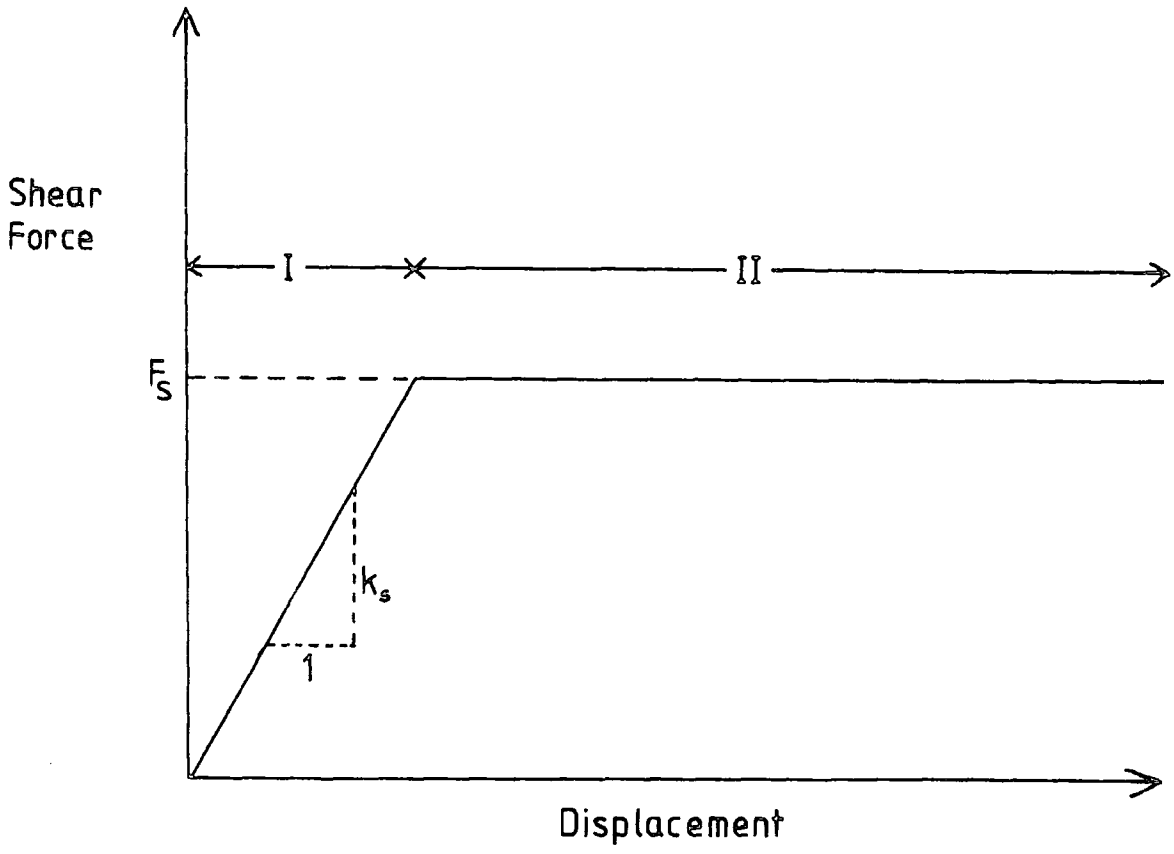

Fig. 5.1: Schematic diagram of the shear force - displacement characteristics of a fault.

k_s shear stiffness

F_s shear force corresponding to the frictional strength

I displacements resulting from the elastic strength

II displacements resulting from frictional sliding

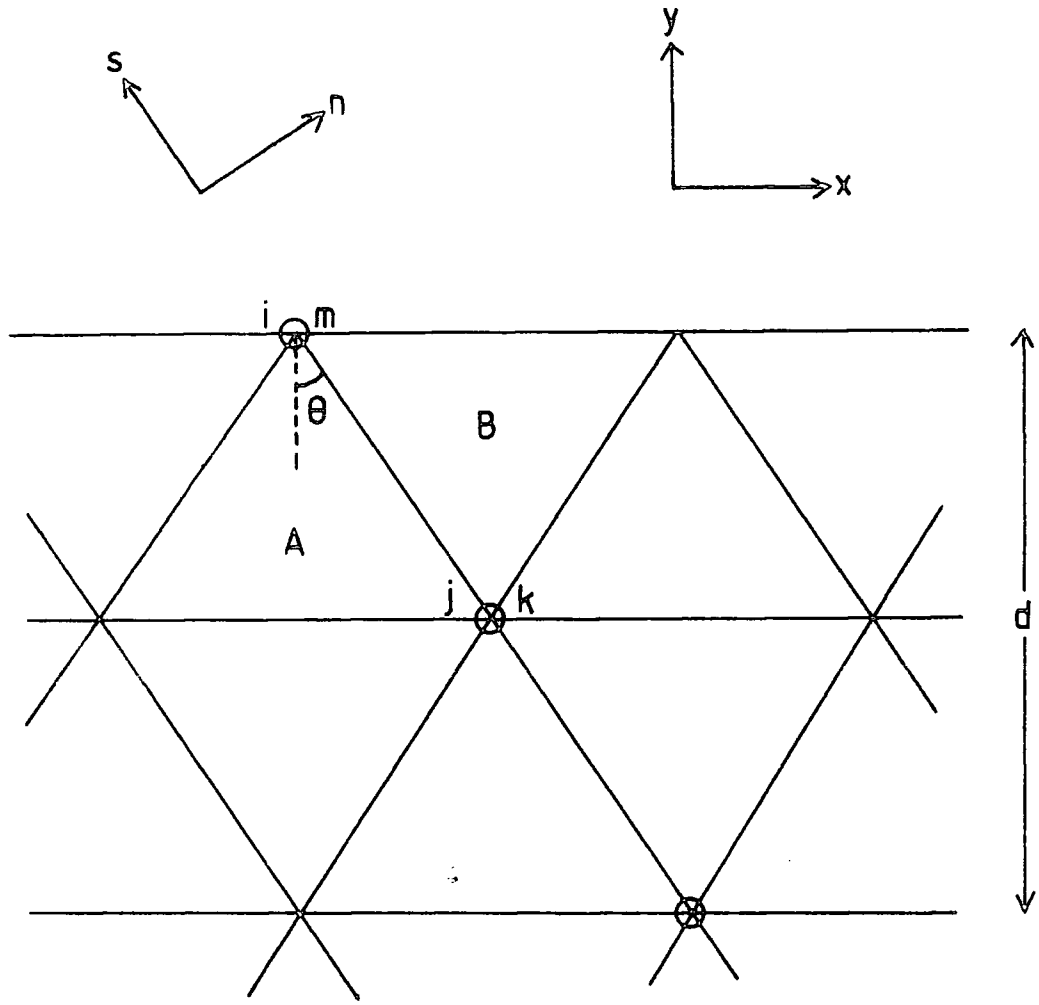

Fig. 5.2: Fault Representation

⊙ positions of dual nodes

d depth of fault

θ hade of fault

(x,y) global co-ordinate system

(s,n) local co-ordinate system

Nodes i,j belong to element A;

nodes k,m belong to element B.

fault are termed dual nodes because they have two node numbers assigned to them. The two node numbers belong to the elements on each side of the fault. In order to maintain the basic element geometry, the fault plane must be continued in the same direction beyond the base of the fault so that differential movement of the dual nodes at the fault base does not result in misshapen elements or 'holes' in the grid.

5.3.2 Stiffness matrix for a fault section

For each fault section it is necessary to construct a local stiffness matrix which is incorporated into the global stiffness matrix. This allows for the effect of the elastic properties of the fault. The usual method of calculating element stiffness matrices (Chapter 3) cannot be used since the fault sections have zero area in the plane of the model. The method used here is taken from the work of Goodman et al. (1968). However, there are certain differences in the derivation here which will be discussed where they occur. The local co-ordinate system for this section is different from that of Goodman et al., which results in a different ordering of the stiffness matrix from that given in their work.

Figure 5.3 shows a fault section of zero width in its local co-ordinate system. Using a variational approach, as in Chapter 3, and considering the virtual quantity $\delta\{w\}$,

$$\delta W = \int_A \delta\{w\}^T \{p\}\, dA \qquad 5.1$$

where W is the stored energy, $\{w\}$ is the relative displacement vector given by

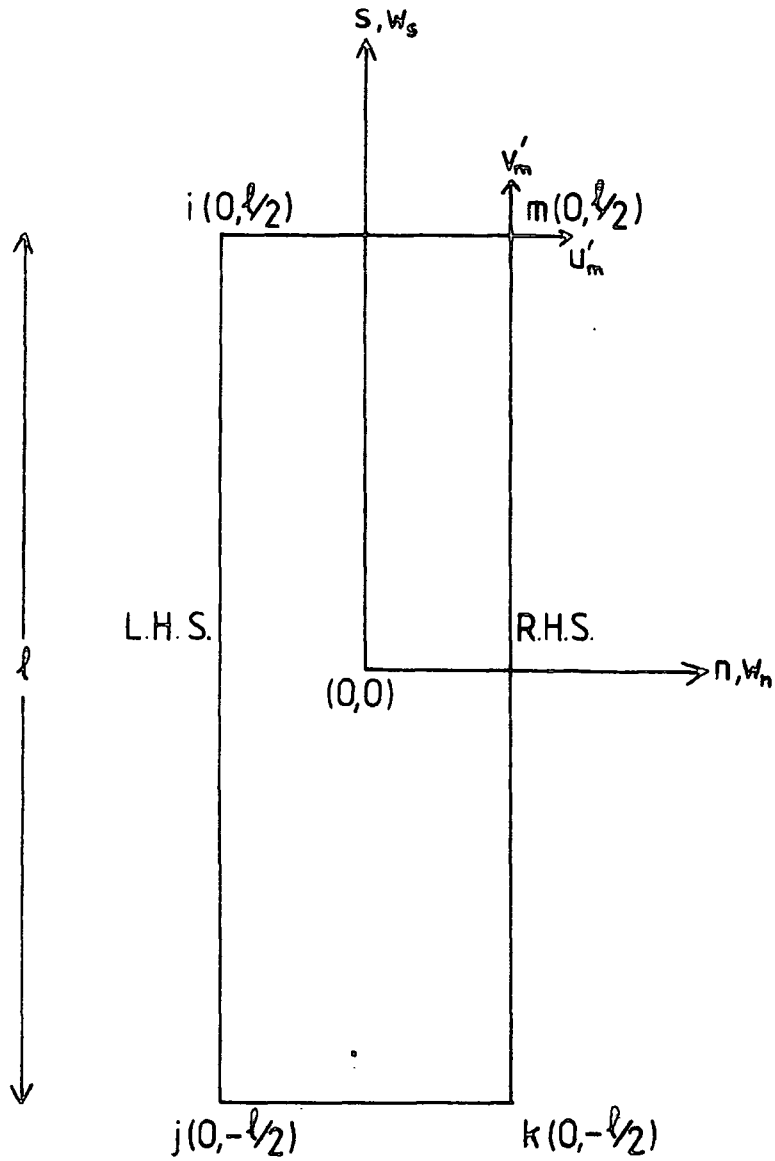

Fig. 5.3: Fault section of zero width in local co-ordinates.

$$\{w\} = \begin{Bmatrix} w_n(RHS) - w_n(LHS) \\ w_s(RHS) - w_s(LHS) \end{Bmatrix} \qquad 5.2$$

and $\{p\}$ is the force per unit area vector. This is equivalent to saying that the stored energy in the fault section is due to the applied forces acting through the displacements and summed over the fault section.

Now, since the finite element model has unit thickness, equation 5.1 can be written as

$$\delta W = \int_{-\ell/2}^{\ell/2} \delta\{w\}^T \{p\}\, ds \qquad 5.3$$

where $\{p\}$ is now the force per unit length vector given by

$$\{p\} = \begin{Bmatrix} p_n \\ p_s \end{Bmatrix} \qquad 5.4$$

$\{p\}$ has been expressed by Goodman et al. in the form

$$\{p\} = [k]\ \{w\} \qquad 5.5$$

where $$[k] = \begin{bmatrix} k_n & 0 \\ 0 & k_s \end{bmatrix} \qquad 5.6$$

They call k_n and k_s the unit normal and unit shear stiffnesses. An alternative way of expressing $\{p\}$ is

$$\{p\} = \frac{1}{\ell} [k] \{w\} \qquad 5.7$$

where

$$[k] = \begin{bmatrix} k_n & 0 \\ 0 & k_s \end{bmatrix} \qquad 5.8$$

and here k_n and k_s are the normal and shear stiffnesses for the fault section. These have the correct units for stiffness of force per unit length. This equation (5.7) will be used here and the differences in the stiffness matrix developed here from that of Goodman et al. will be discussed after the remainder of the analysis.

Substituting equation 5.7 in 5.3 gives

$$\delta W = \int_{-\ell/2}^{\ell/2} \frac{1}{\ell} . \delta\{w\}^T [k] \{w\} \, ds \qquad 5.9$$

and so

$$W = \frac{1}{2\ell} \int_{-\ell/2}^{\ell/2} \{w\}^T [k] \{w\} \, ds \qquad 5.10$$

If u_i' and v_i' are the displacements of node i in the s and n directions, then the displacements {w} may be expressed in terms of the nodal displacements by a linear interpolation formula,

$$\begin{Bmatrix} w_n \text{ (LHS)} \\ w_s \text{ (LHS)} \end{Bmatrix} = \frac{1}{2} \begin{bmatrix} 1 + \frac{2s}{\ell} & 0 & 1 - \frac{2s}{\ell} & 0 \\ 0 & 1 + \frac{2s}{\ell} & 0 & 1 - \frac{2s}{\ell} \end{bmatrix} \begin{Bmatrix} u_i' \\ v_i' \\ u_j' \\ v_j' \end{Bmatrix} \qquad 5.11$$

and

$$\begin{Bmatrix} w_n \ (RHS) \\ w_s \ (RHS) \end{Bmatrix} = \frac{1}{2} \begin{bmatrix} 1 - \frac{2s}{\ell} & 0 & 1 + \frac{2s}{\ell} & 0 \\ 0 & 1 - \frac{2s}{\ell} & 0 & 1 + \frac{2s}{\ell} \end{bmatrix} \begin{Bmatrix} u_k' \\ v_k' \\ u_m' \\ v_m' \end{Bmatrix} \qquad 5.12$$

Substituting these into equation 5.2 gives

$$\{w\} = \frac{1}{2} \begin{bmatrix} -A & 0 & -B & 0 & B & 0 & A & 0 \\ 0 & -A & 0 & -B & 0 & B & 0 & A \end{bmatrix} \begin{Bmatrix} u_i' \\ v_i' \\ u_j' \\ v_j' \\ u_k' \\ v_k' \\ u_m' \\ v_m' \end{Bmatrix} \qquad 5.13$$

where $A = 1 + \frac{2s}{\ell}, \quad B = 1 - \frac{2s}{\ell}$

This can be written as

$$\{w\} = \frac{1}{2} [L] \{d'\} \qquad 5.14$$

where [L] and {d'} are given by equation 5.13. [L] is equivalent to a shape function matrix and {d'} is the nodal displacement vector in the local co-ordinates s,n.

Substituting equation 5.14 into equation 5.10 gives

$$W = \frac{1}{2\ell} \int_{-\ell/2}^{\ell/2} \frac{1}{4} \{d'\}^T [L]^T [k] [L] \{d'\} ds \qquad 5.15$$

Now,

$$[L]^T [k] [L] = \begin{bmatrix} -A & 0 \\ 0 & -A \\ -B & 0 \\ 0 & -B \\ B & 0 \\ 0 & B \\ A & 0 \\ 0 & A \end{bmatrix} \begin{bmatrix} k_n & 0 \\ 0 & k_s \end{bmatrix} \begin{bmatrix} -A & 0 & -B & 0 & B & 0 & A & 0 \\ 0 & -A & 0 & -B & 0 & B & 0 & A \end{bmatrix} \qquad 5.16$$

$$= \begin{bmatrix} k_nA^2 & 0 & k_nAB & 0 & -k_nAB & 0 & -k_nA^2 & 0 \\ 0 & k_sA^2 & 0 & k_sAB & 0 & -k_sAB & 0 & -k_sA^2 \\ k_nAB & 0 & k_nB^2 & 0 & -k_nB^2 & 0 & -k_nAB & 0 \\ 0 & k_sAB & 0 & k_sB^2 & 0 & -k_sB^2 & 0 & -k_sAB \\ -k_nAB & 0 & -k_nB^2 & 0 & k_nB^2 & 0 & k_nAB & 0 \\ 0 & -k_sAB & 0 & -k_sB^2 & 0 & k_sB^2 & 0 & k_sAB \\ -k_nA^2 & 0 & -k_nAB & 0 & k_nAB & 0 & k_nA^2 & 0 \\ 0 & -k_sA^2 & 0 & -k_sAB & 0 & k_sAB & 0 & k_sA^2 \end{bmatrix} \qquad 5.17$$

The only terms in equation 5.15 that vary with s are A^2, AB and B^2, and these integrals can be evaluated:

$$\int_{-\ell/2}^{\ell/2} A^2\, ds = \int_{-\ell/2}^{\ell/2} \left(1 + \frac{2s}{\ell}\right)^2 ds = \frac{4\ell}{3}$$

$$\int_{-\ell/2}^{\ell/2} AB\, ds = \int_{-\ell/2}^{\ell/2} \left(1 - \frac{4s^2}{\ell^2}\right) ds = \frac{2\ell}{3} \qquad 5.18$$

$$\int_{-\ell/2}^{\ell/2} B^2\, ds = \int_{-\ell/2}^{\ell/2} \left(1 - \frac{2s}{\ell}\right)^2 ds = \frac{4\ell}{3}$$

Substituting equations 5.17 and 5.18 into 5.15 gives

$$W = \frac{1}{2} \{d'\}^T [K_F'] \{d'\} \qquad 5.19$$

where $[K_F']$ is the stiffness matrix for the fault section, in local co-ordinates, given by

$$[K_F'] = \frac{1}{6} \begin{bmatrix} 2k_n & 0 & k_n & 0 & -k_n & 0 & -2k_n & 0 \\ 0 & 2k_s & 0 & k_s & 0 & -k_s & 0 & -2k_s \\ k_n & 0 & 2k_n & 0 & -2k_n & 0 & -k_n & 0 \\ 0 & k_s & 0 & 2k_s & 0 & -2k_s & 0 & -k_s \\ -k_n & 0 & -2k_n & 0 & 2k_n & 0 & k_n & 0 \\ 0 & -k_s & 0 & -2k_s & 0 & 2k_s & 0 & k_s \\ -2k_n & 0 & -k_n & 0 & k_n & 0 & 2k_n & 0 \\ 0 & -2k_s & 0 & -k_s & 0 & k_s & 0 & 2k_s \end{bmatrix} \qquad 5.20$$

This matrix is different from that of Goodman et al. in two ways. Firstly, the row ordering is different. This is just the result of using a different local co-ordinate system. Secondly, their stiffness matrix is multiplied by ℓ, the length of the joint element (they call it a joint element rather than a fault section). This is because of the different definitions of k_n and k_s used here, which are stiffnesses rather than unit stiffnesses. It is felt that the matrix developed here is preferable to theirs for modelling deep faults. This is because normal and shear stiffnesses can be assigned to the whole fault and the stiffness matrix is then not dependent on the length of the fault sections. This is analogous to stiffness matrices for elastic continua which are unchanged by scaling the dimensions of the model if the elastic parameters are kept constant. To use their stiffness matrix and obtain a solution which does not depend on the number of fault sections requires a knowledge of the variation of unit stiffness with the length of section. This is not known for deep faults. However, for the results to be meaningful , the variation must be such that it cancels out the effect of the length in the stiffness matrix. By using total stiffness instead of unit stiffness this problem is overcome and gives a method that is consistent with the assigning of elastic parameters to finite element models of elastic continua.

Equation 5.19 can now be rotated to global co-ordinates (x,y) by using the rotation matrix [R] where,

$$[R] = \begin{bmatrix} \cos\theta & -\sin\theta & 0 & 0 & 0 & 0 & 0 & 0 \\ \sin\theta & \cos\theta & 0 & 0 & 0 & 0 & 0 & 0 \\ 0 & 0 & \cos\theta & -\sin\theta & 0 & 0 & 0 & 0 \\ 0 & 0 & \sin\theta & \cos\theta & 0 & 0 & 0 & 0 \\ 0 & 0 & 0 & 0 & \cos\theta & -\sin\theta & 0 & 0 \\ 0 & 0 & 0 & 0 & \sin\theta & \cos\theta & 0 & 0 \\ 0 & 0 & 0 & 0 & 0 & 0 & \cos\theta & -\sin\theta \\ 0 & 0 & 0 & 0 & 0 & 0 & \sin\theta & \cos\theta \end{bmatrix} \qquad 5.21$$

and θ is the hade of the fault measured anticlockwise from the y-axis (Figure 5.1).

This gives

$$W = \frac{1}{2}\{d\}^T [K_F] \{d\} \qquad 5.22$$

where

$$\{d\} = [R] \{d'\}$$

$$\{K_F\} = [R] [K_F'] [R]^T$$

Minimising the energy with respect to the nodal displacements, as in Chapter 3, gives

$$\frac{\partial W}{\partial\{d\}} = [K_F] \{d\} = 0 \qquad 5.23$$

and this must be added into the equations for the whole body (equation 3.16) giving

$$[K + K_F]\ \{d\} = \{F\} \qquad 5.24$$

So the stiffness matrix for each fault section is added into the global stiffness matrix in a similar manner to the element stiffness matrices.

5.3.3 Calculation of fault stresses

An elastic solution for the finite element model with the fault present gives the stresses and displacements throughout the model. These include the effect of the elasticity of the fault, since the stiffness matrices for the fault sections have been incorporated into the global stiffness matrix. However, they do not include any changes in the stresses and displacements caused by slip on the fault which occurs when the shear stress exceeds the frictional strength. In order to account for these it is necessary firstly to calculate the normal and shear stresses on the fault. The method proposed here involves calculating these from the stresses in the surrounding elements. This is considered to be preferable, for this situation, to the method of Goodman (1976) where the stresses on the fault are calculated from the normal and shear stiffnesses of the fault, since these are not known for deep faults which die out at depth. The elastic solution gives the stress tensor for each element. For the element pairs which form the sides of the fault, the stress tensors are rotated by the rotation matrix

$$[R] = \begin{bmatrix} \cos\theta & \sin\theta \\ -\sin\theta & \cos\theta \end{bmatrix}$$

where θ is the hade of the fault, to give the normal and shear stresses acting in the elements on a plane parallel to the fault plane. The stresses on the fault are now calculated from these. Unfortunately, displacement method approaches to finite element analysis have a discontinuous stress field at element boundaries. This is true for higher order strain elements as well as the constant strain elements used here (Hinton and Owen, 1977). Various methods of stress smoothing have been proposed (e.g. Hinton and Campbell, 1974), but the most economical and simple method of calculating stresses at boundaries is to average the stresses in the adjoining elements. If these elements are of approximately the same size this method works well for the type of plane strain analysis used here. Consequently, the normal and shear stresses in each pair of elements across the fault are averaged to give the stresses on the fault (Figure 5.4).

The fault is likely to be percolated by fluids which will give rise to a pore pressure. This is subtracted from the normal stress on the fault in line with the effective stress law which was discussed in Chapter 2. Of course, the pore pressure has no effect on the shear stress.

5.3.4 Calculation of excess shear stress on the fault

The excess shear stress on the fault is defined here as the total shear stress on the fault minus the frictional strength. The frictional strength is calculated from the normal stress across the fault and an appropriate friction law. Nur (1978) has shown that the main first-order features of active faulting can be explained by spatial variation in the frictional strength, and one advantage of the method proposed here is that different sections of the fault can each have different friction laws or coefficients of friction if required.

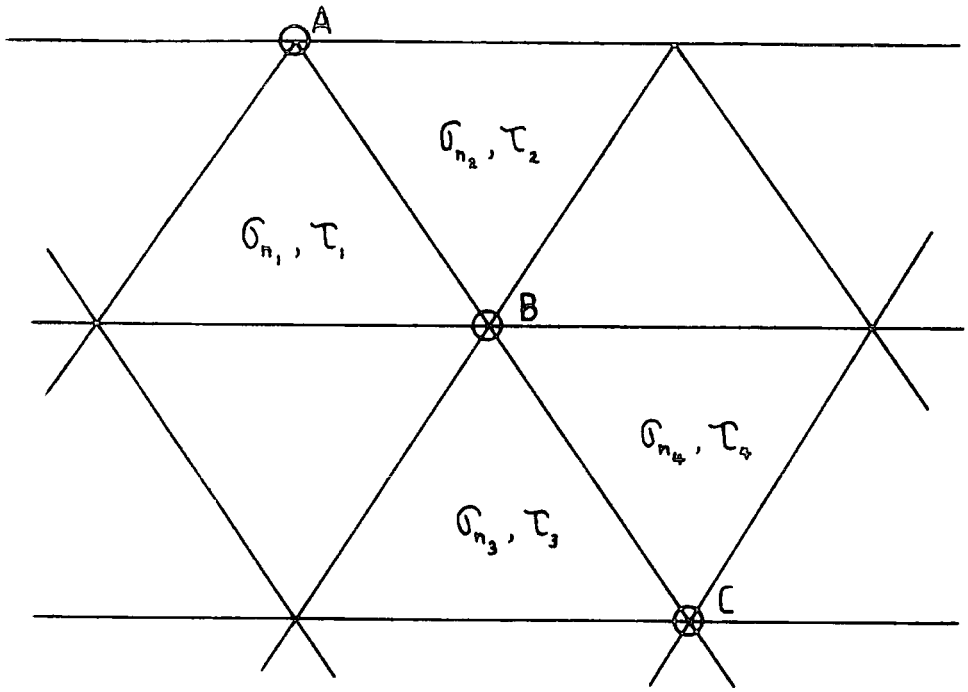

Fig. 5.4: Averaging of rotated element stresses to give fault plane stresses

$$\tau(AB) = \frac{\tau_1 + \tau_2}{2}$$

$$\tau(BC) = \frac{\tau_3 + \tau_4}{2}$$

and similarly for the normal stresses.

Frictional relationships between normal and shear stresses for rock-on-rock sliding have been summarised by Byerlee (1978) and were discussed in Chapter 2. The simplest of these is

$$\tau_F = \mu\sigma_n$$

where μ is the coefficient of friction, σ_n is the normal stress across the fault, and τ_F is the frictional strength. For each fault section the frictional strength is calculated from the normal stress and the coefficient of friction for that section. The excess shear stress on that section, which will result in slip, is then given by subtracting the frictional strength from the value of the shear stress given by the analysis,

$$\tau_{XS} = \tau_{FE} - \tau_F$$

where τ_{XS} is the excess shear stress and τ_{FE} is the shear stress calculated from the finite element solution. Clearly, if the frictional strength is larger than the calculated shear stress there is no excess shear stress and slip will not occur. This operation is performed for each fault section.

5.3.5 Conversion of excess shear stress to nodal forces

The excess shear stress on each section of the fault can be converted to a force by multiplying by the area of the fault section. Since two-dimensional finite element models have unit thickness, this is equivalent to multiplying the excess shear stress by the length of the fault section,

$$F = \tau_{xs} \cdot \ell$$

where F is the force and ℓ is the length of the fault section. This gives the force acting on one side of the fault. It will, of course, act in the direction of the fault plane. The other side of the fault is acted on by a force of equal magnitude but opposite sign. The sign of the forces is determined by the sign of the shear stress. For the convention used here of tension positive, negative shear stress is dextral shear and positive shear stress is sinistral shear. This force is divided equally between the nodes at the top and the base of the fault section, as illustrated in Figure 5.5. This is repeated for each fault section. Consequently, nodes in the central part of the fault will have two contributions to their forces; one from the section above them and one from the section below. The forces to be applied to the fault nodes are now rotated to global co-ordinates and added into the global force vector.

5.3.6 Iterative procedure

The finite element equations are now solved again using the modified force vector. The stresses on the fault, the excess shear stress, and the nodal force vector are recalculated as described above. The forces due to the fault are added into the global force vector and the equations re-solved. This iterative procedure is continued until the excess shear stress on the fault falls to an acceptable value. A suitable criterion is when the shear stress for each section of the fault approaches sufficiently close to the frictional strength for that section. The limiting value for this approach is taken to be 0.1 MPa in this thesis. After each iteration the convergence criterion described above is tested.

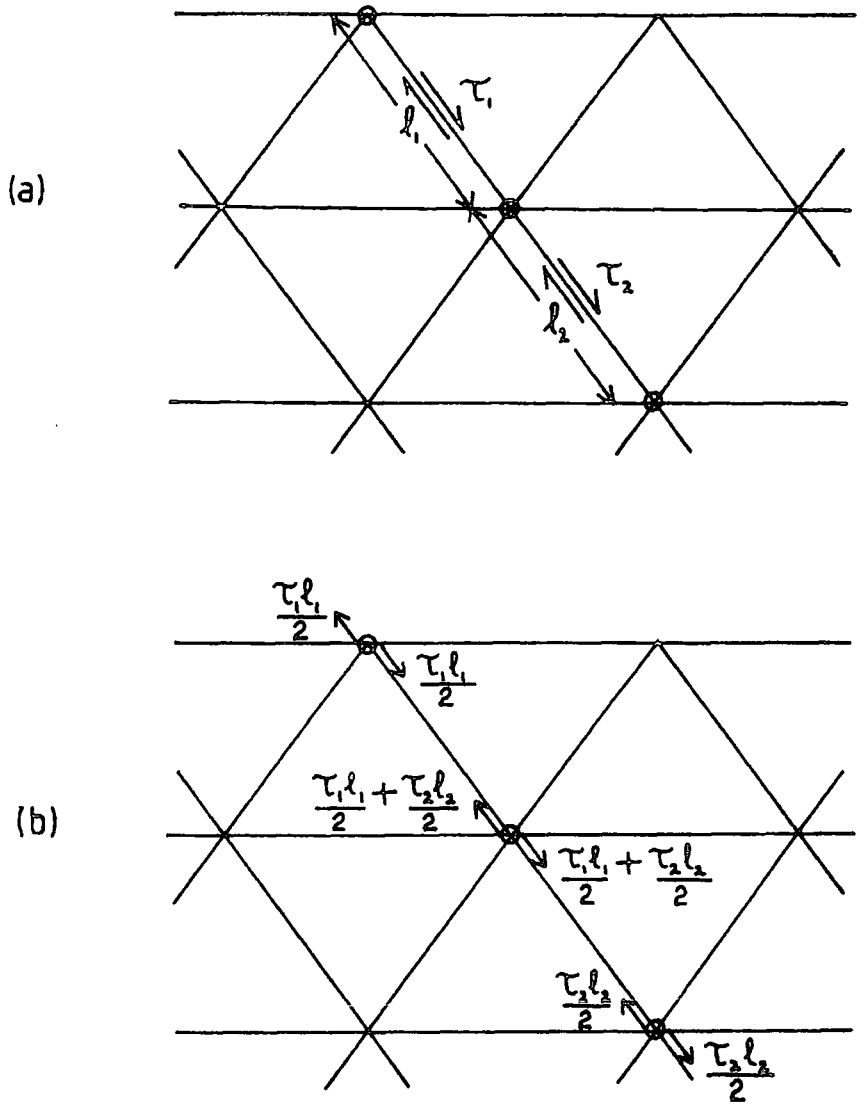

Fig. 5.5: Conversion of excess shear stress on the fault to nodal forces.

(a) Excess shear stress on the fault

(b) Nodal force distribution

The method has been found to converge for all situations that have been tried. Clearly, the number of iterations necessary before the convergence criterion is satisfied will depend on how resistant the fault is to movement. This, in turn, depends on the shear stiffness of the fault. It has been found that the number of iterations can be greatly reduced by multiplying the force vector for the fault nodes by some factor, f. This factor is dependent on the shear stiffness of the fault. An explicit relationship between f and the shear stiffness, k_s, has not been found, but the factor can be estimated on a simple 'trial-and-error' basis for an elastic model. This value of f can then be used for all further solutions using that particular value of k_s.

5.4 Application to time-dependent analysis

The lithosphere is often considered, in deformation problems, as consisting of a brittle upper layer overlying ductile material (e.g. Bott and Kusznir, 1979). This is, of course, the situation in this thesis. The modelling of faults in the upper layer can be easily incorporated into a time-dependent model where the underlying material deforms by a flow mechanism. The method described above is followed for each time increment of the analysis, such that at the start of the next increment the fault has no excess shear stress acting on it. Using the factor, f, described in the last section, it has been found that the procedure is not prohibitive from the viewpoint of computing time and cost.

The only modification that may be necessary, in the case of a large amount of fault slip, is in the averaging of stresses in adjacent elements to determine the stresses on the fault plane. At the start of any time increment the fault may already have moved considerably with respect to the length of its individual sections, such that what were

originally dual nodes now occupy significantly different spatial positions. The average shear stresses between nodes on the fault are calculated as before and the average shear stress for each section (i.e. the part of the fault forming the edge of an element) is now calculated by weighting these values by the appropriate fault lengths between nodes. This is illustrated in Figure 5.6. If reasonable sized elements are used it has been found unnecessary to use this modification. Indeed, it can be argued that if this weighting is necessary then the amount of fault movement that has occurred ought to make it necessary for the global stiffness matrix to be recalculated, and this is usually cost and time prohibitive.

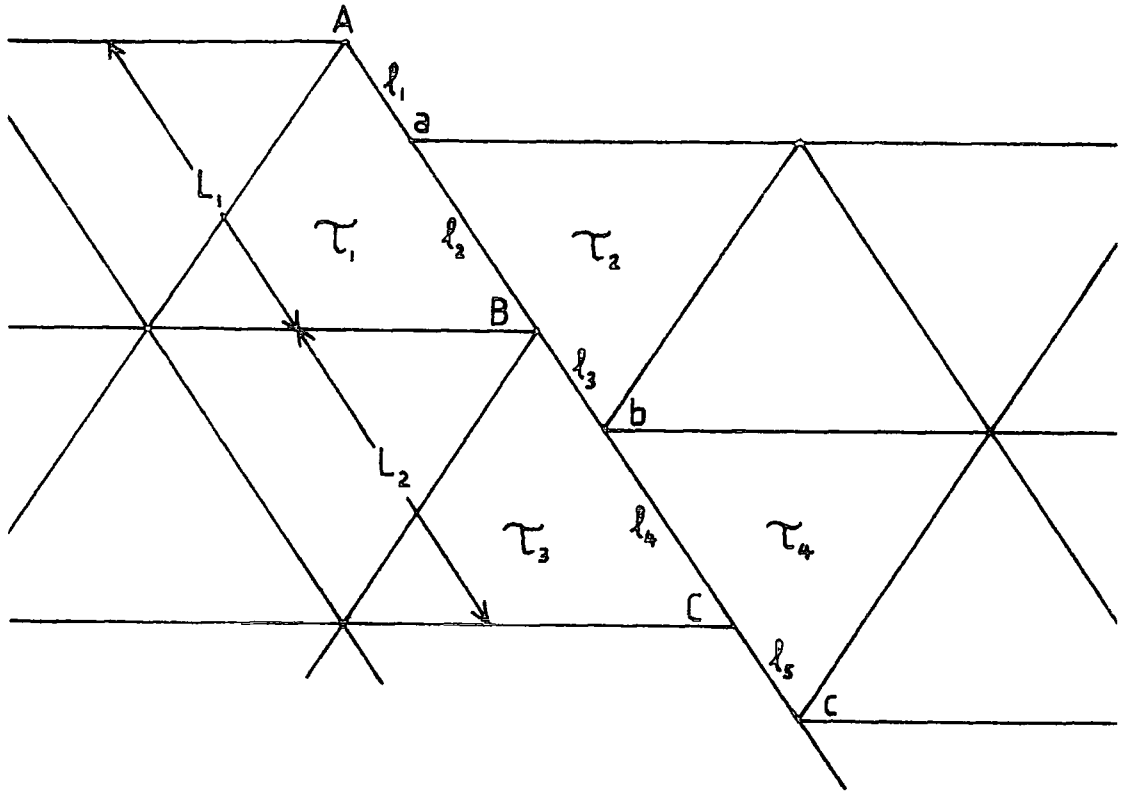

Fig. 5.6: Averaging of rotated element stresses after significant movement has occurred.

$$\tau(AB) = \tau(Aa) + \tau(aB)$$

$$= 0 + \frac{\tau_1 + \tau_2}{2} \cdot \frac{\ell_2}{L_1} \qquad \text{(Aa is a free surface)}$$

$$\tau(BC) = \tau(Bb) + \tau(bC)$$

$$= \frac{\tau_2 + \tau_3}{2} \cdot \frac{\ell_3}{L_2} + \frac{\tau_3 + \tau_4}{2} \cdot \frac{\ell_4}{L_2}$$

and similarly for $\tau(ab)$, $\tau(bc)$ and for the normal stresses.

CHAPTER 6

NORMAL FAULT DEFORMATION AND THE DEVELOPMENT OF ASSOCIATED FAULTING

6.1 Introduction

In this chapter a fault will be introduced into the finite element model using the method described in the previous chapter. The stresses and displacements associated with the fault will be examined by finite element analysis and the Modified Griffith criteria will be used to predict the occurrence of further faulting. In the first part of the chapter a simple model of the elastic layer underlain by a fluid will be used. This enables the results from the finite element analysis to be compared with theoretical work based on elastic beam theory. For the second part, the full lithosphere model described in Chapter 4 will be used. The stress system at the time of faulting will be reapplied to the model, with a fault present, and the analysis continued through time using both Newtonian visco-elastic and power law creep rheologies.

6.2 Finite element model of the elastic layer

In this section the deformation resulting from a fault in the elastic layer will be investigated. The elastic layer is assumed to be underlain by a fluid. Although this assumption is geologically naïve, it means that the model predictions can be compared with earlier analytical work based on elastic beam theory (Heiskanen and Vening Meinesz, 1958; Bott, 1976).

6.2.1 Comparison of bending with elastic beam theory

Before comparing the deformation resulting from the fault with predicted results from beam theory, it is necessary to show that simple bending of a finite element model of an elastic continuum agrees reasonably with elastic beam theory. The finite element model and parameters used for this are shown in Figure 6.1. Results from this model can be compared with elastic beam theory for a downward force, P, applied at the origin of a continuous beam. The full equations of elastic beam analysis are developed in Appendix 1. The relevant equation for this situation is

$$v = \frac{P}{2\alpha\rho_m g} \cdot \exp\left(-\frac{x}{\alpha}\right).\left(\cos\frac{x}{\alpha} + \sin\frac{x}{\alpha}\right)$$

where v is the vertical displacement, x is the horizontal distance, α is the flexural parameter (defined in Figure 6.1), ρ_m is the density of the underlying fluid and g is the acceleration due to gravity. The theory assumes that the beam is underlain by a fluid, and this is taken into account in the finite element model by using the isostatic compensation procedure, described in Chapter 3, at the base.

The displacement profile given by the above equation is plotted in Figure 6.2, together with the finite element solutions for plane stress and plane strain. These solutions refer to the central line of the model, labelled N-N in Figure 6.1, which represents the neutral fibre. Beam theory implies plane stress, but the models used in this thesis are best suited to plane strain. Consequently, the model has been tested for both situations. In fact, it can be seen from Figure 6.2 that the plane stress and plane strain solutions are very similar, and they both agree well with the theoretical solution. Figure 6.3 shows the plane

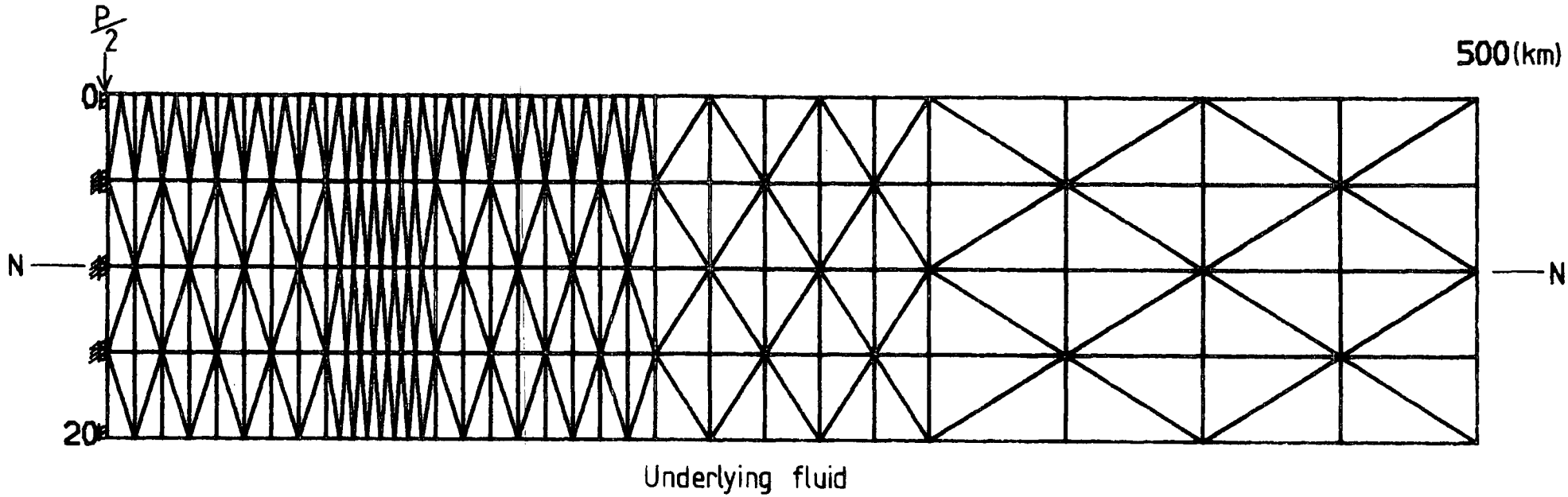

$P = 2.0 \times 10^{12}$ N
$E = 0.85 \times 10^{11} \mathrm{Nm}^{-2}$
$T = 2.0 \times 10^{4}$ m
$\rho_m = 2.9 \times 10^{3}$ kg m^{-3}
$g = 9.81$ m s^{2}
$\nu = 0.25$

Flexural rigidity $= D = \dfrac{ET^3}{12(1-\nu^2)} = 6.04 \times 10^{22}$ Nm

Flexural parameter $= \left(\dfrac{4D}{\rho_m g}\right)^{\frac{1}{4}} = 5.4 \times 10^{4}$ m

Fig. 6.1: Finite element model and parameters used for comparing displacements resulting from a simple bending model with elastic beam theory.

N—N position of neutral fibre

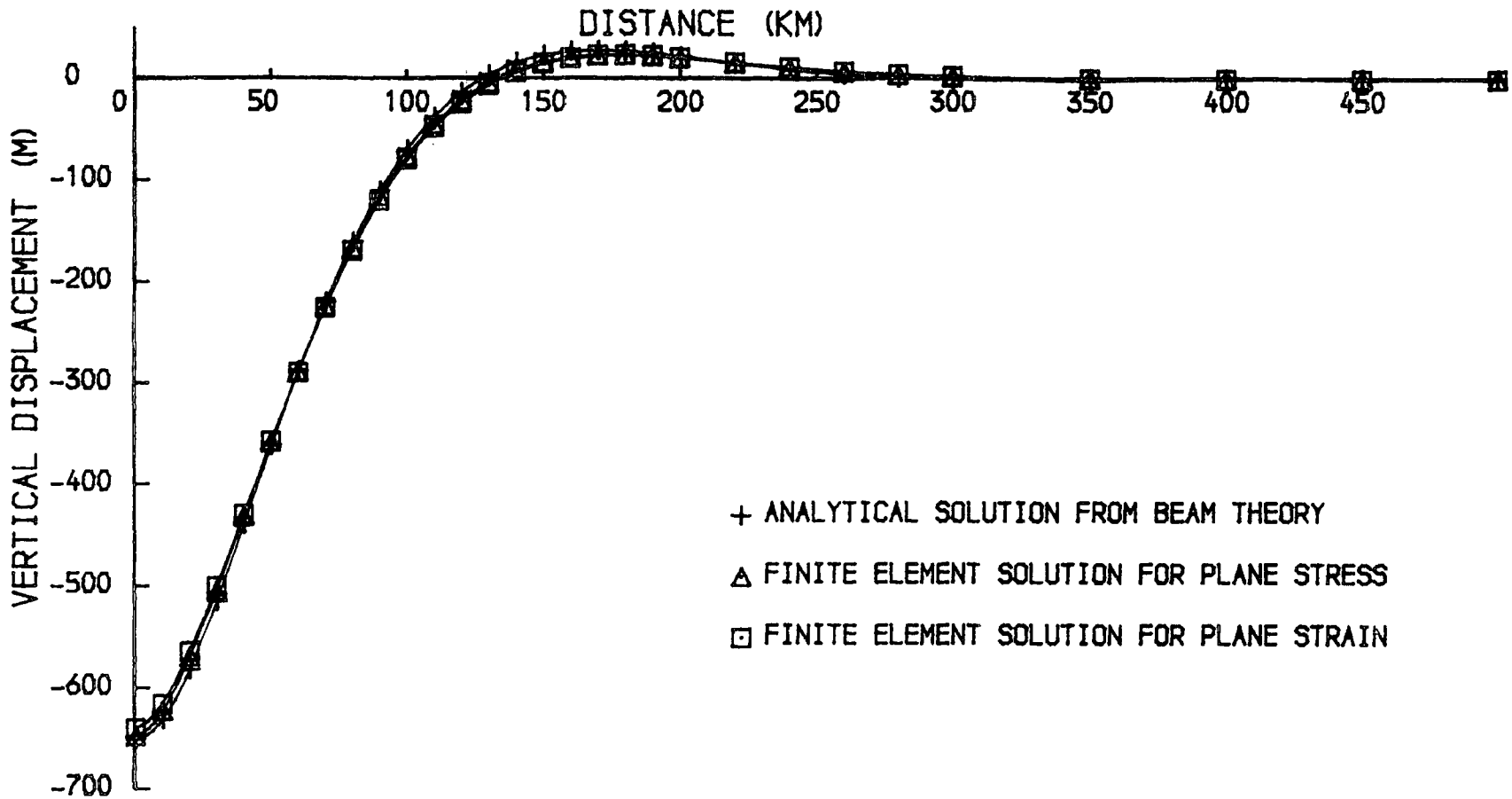

Fig. 6.2: Comparison of finite element results using the model shown in Figure 6.1 with the elastic beam theory solution.

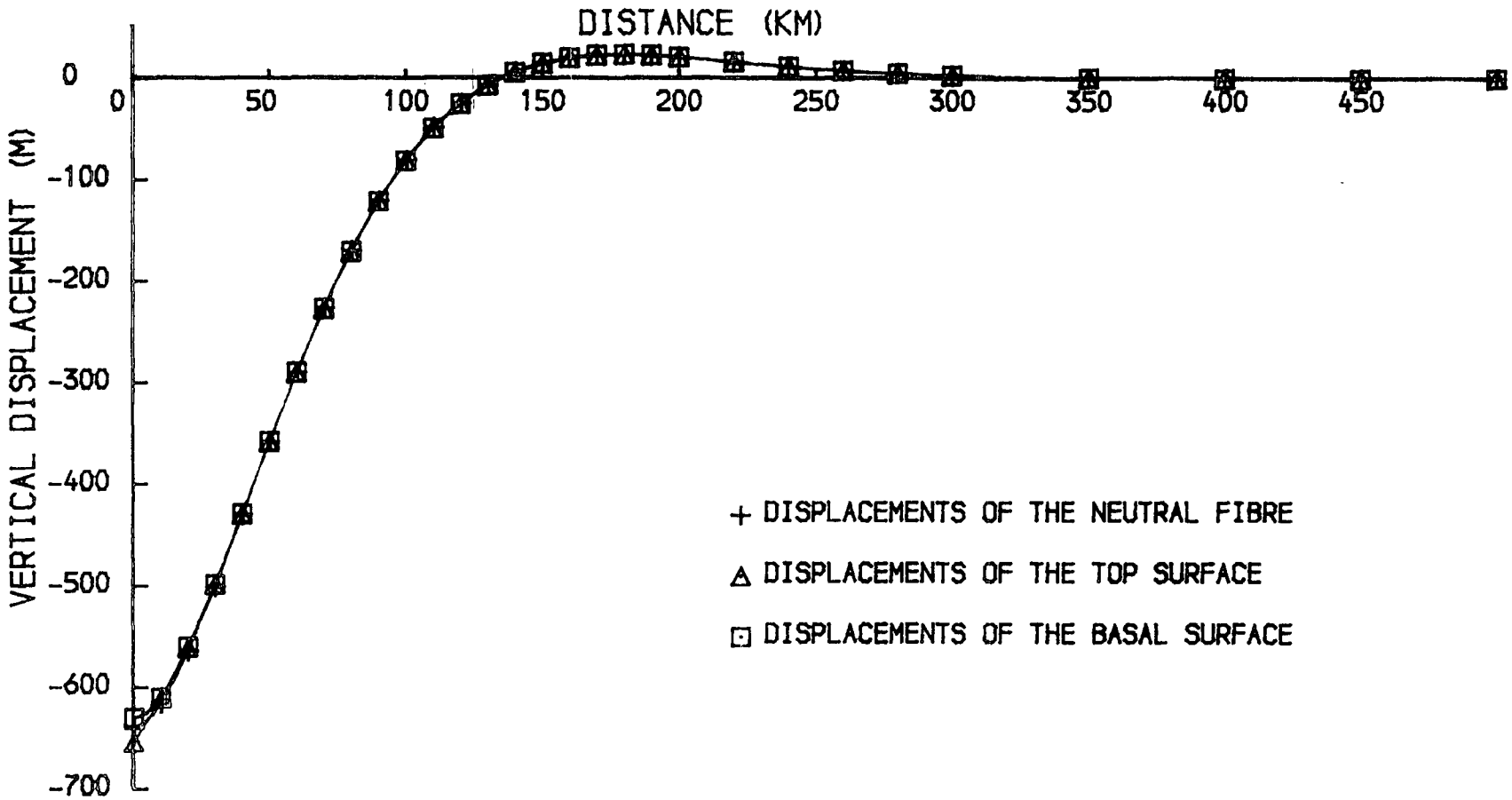

Fig. 6.3: Comparison of finite element plane strain results for the neutral fibre, the top surface and the base of the model shown in Figure 6.1.

strain solutions for the neutral fibre, the top surface of the model and the base of the model. These are in excellent agreement except in the immediate vicinity of the load. It is felt that the agreement between the finite element analysis and the beam theory equations is sufficiently close to permit the comparison of the finite element results with beam theory calculations.

6.2.2 Model parameters

The finite element grid used in this section is shown in Figure 6.4. The grid represents a 1,000 km long section of the elastic layer. The parameters for the elastic layer are the same as have been used previously: its thickness is 20 km, Young's modulus is 0.85×10^{11} Nm^{-2}, Poisson's ratio is 0.25, and the density is 2,750 kg m^{-3}. The elastic layer is assumed to be underlain by a fluid of density 2,900 kg m^{-3} and the isostatic compensation procedure is taken to be the boundary condition at the base. The right-hand edge of the model is constrained to have zero horizontal displacement to ensure uniqueness of the solution. Although this implies an axis of symmetry, it is sufficiently far from the centre of the model to have no effect. Different values of tensile stress are applied to the left-hand edge of the model. Since the model is completely elastic and has uniform elastic parameters, there are no edge effects of the type discussed in Chapter 4 and, consequently, it is not necessary to use such a long grid.

In Chapter 4 it was shown that a tectonic, tensile stress regime will eventually cause faulting, provided that the stresses can attain a suitably high value. The dip of the fault plane predicted by the Modified Griffith theory was about 60°. The fault used in this finite element grid extends throughout the layer and has a dip of 63.43°. This

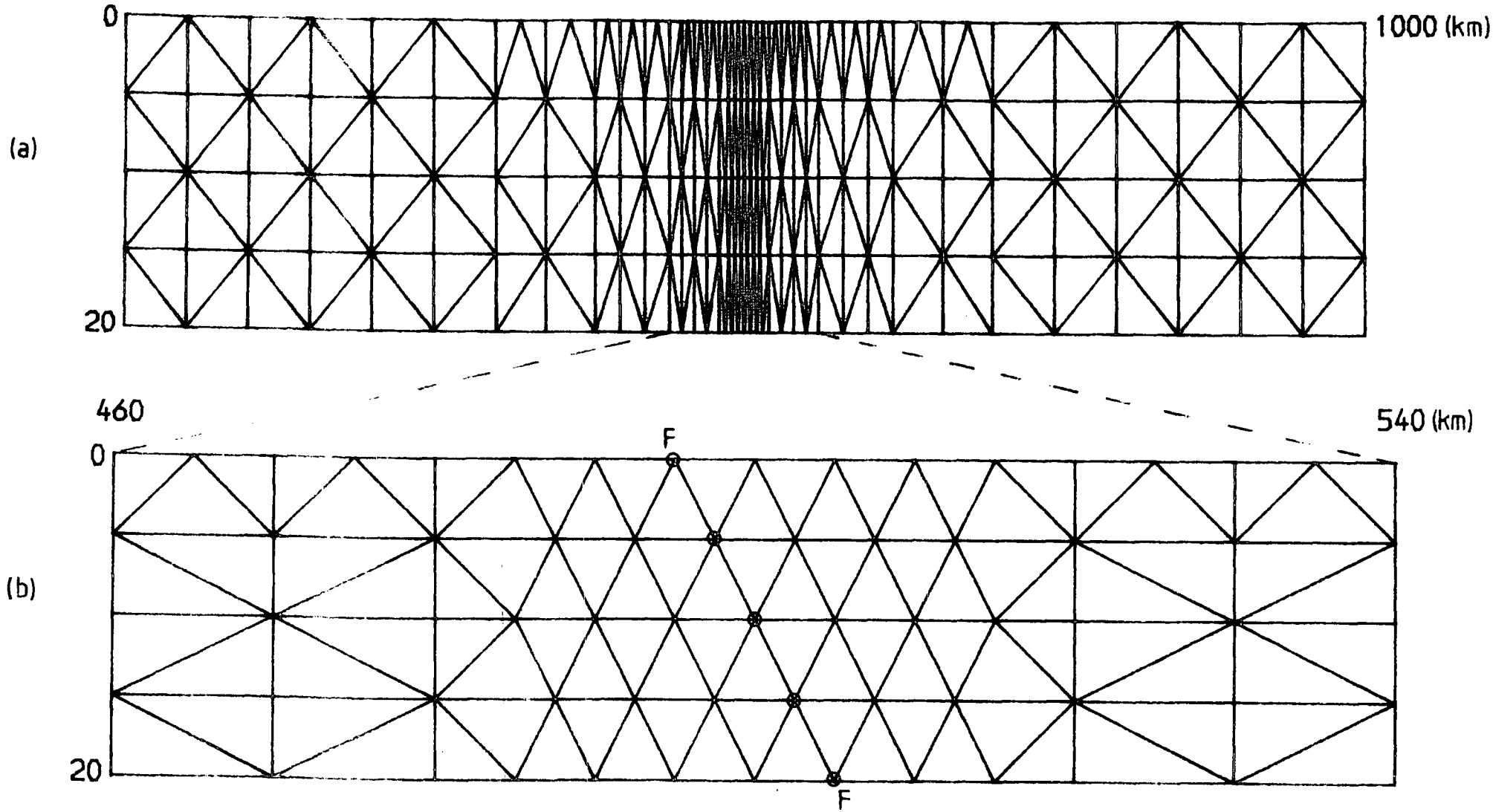

Fig. 6.4: Finite element grid for an elastic layer containing a fault
(a) Full grid
(b) Central 80 km section of grid
F —— F position of fault; ⊙ position of dual node.

value agrees well with the previous prediction and with observations of naturally occurring normal faults (e.g. Illies, 1970), many of which are observed to have dips of between 60 and 65 degrees. The exact value of 63.43 degrees is chosen because the tangent of this angle is 2. This makes the construction of the finite element grid straightforward.

The local stiffness matrix for each fault section, described in the previous chapter, depends on the normal and shear stiffnesses. It is not possible to obtain experimental values for these for faults of the size used here. Consequently, it is necessary to assign values to these parameters. It is considered reasonable that the initial value for the shear stiffness of a fault is similar to the stiffness of the surrounding material. This is because the fault will initially be locked by asperities (Goodman, 1976; Byerlee, 1978). The shear stiffness will probably decrease with time, as the fault moves, due to the grinding away of these asperities. This effect is ignored in this thesis because it necessitates recalculation of the stiffness matrix. This is not a significant omission, as will be shown later in this chapter, because the deformation resulting from the shear stiffness is very much less than that resulting from frictional sliding, which is independent of shear stiffness in the method used here and developed in Chapter 5. Examination of the global stiffness matrix reveals that the stiffness terms for the surrounding elastic material are of the same order of magnitude as the Young's modulus, i.e. about 10^{11} Nm^{-2}. Consequently, the shear stiffness is assigned a value similar to this. Figure 6.5 shows the surface displacement of the finite element model for an applied stress of 50 MPa and a range of values of the shear stiffness. These displacements are only those resulting from elastic deformation of the fault - displacements caused by frictional sliding are not included. It can be seen from this

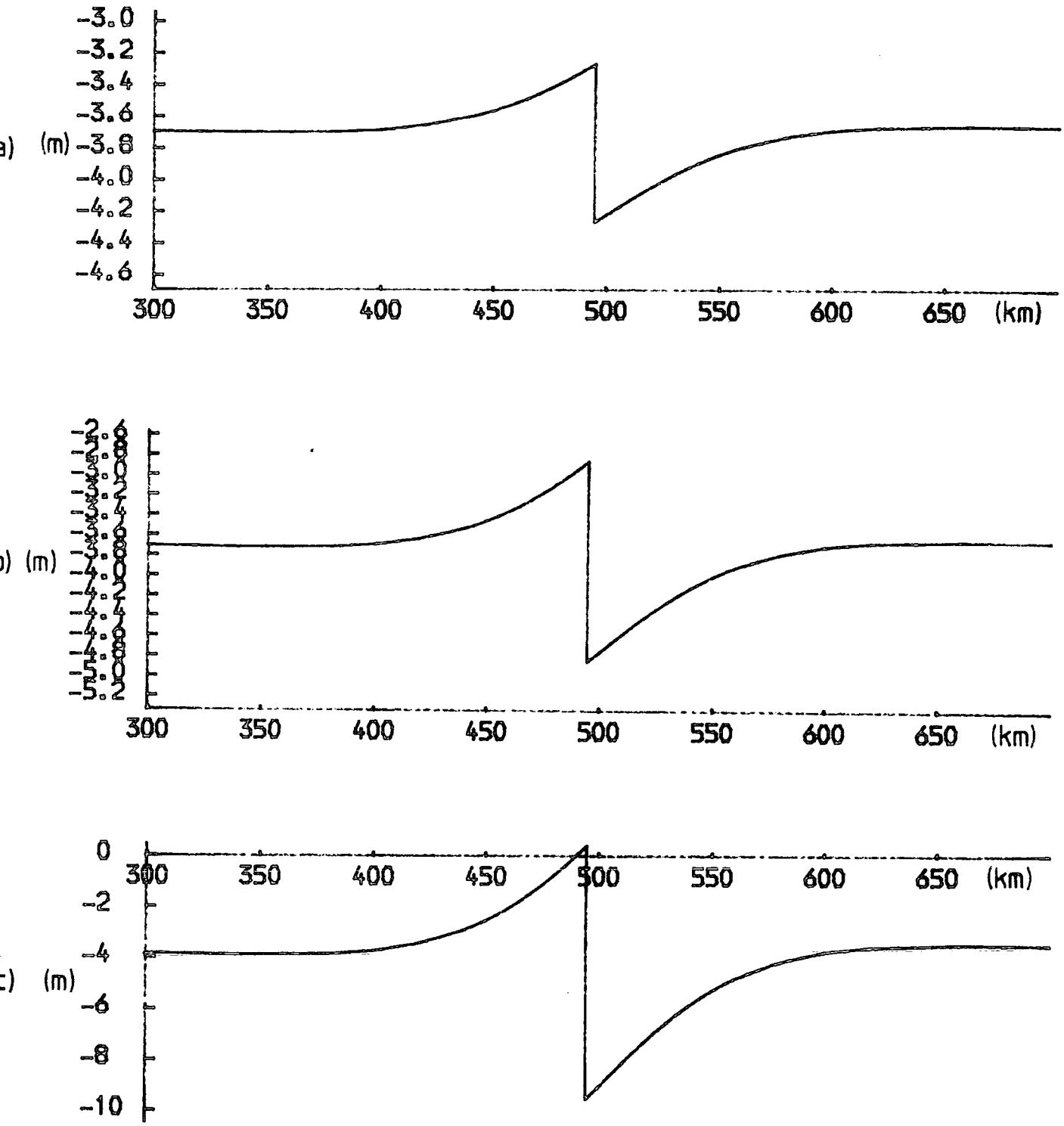

Fig. 6.5: Surface displacements resulting only from the elasticity of the fault for an applied stress of 50 MPa.

(a) $k_s = 10^{11}\ \mathrm{N\,m^{-1}}$

(b) $k_s = 5 \times 10^{10}\ \mathrm{N\,m^{-1}}$

(c) $k_s = 10^{10}\ \mathrm{N\,m^{-1}}$

figure that the displacements are small, ranging from 9 m for a stiffness of 10^{10} Nm^{-1} to 1 m for a stiffness of 10^{11} Nm^{-1}. When these are compared with total displacements, which include those due to frictional sliding (Figure 6.9), these are seen to be very small indeed. Consequently, the choice of shear stiffness is not important. A value of 5×10^{10} Nm^{-1} will be used in this thesis. The normal stiffness is taken to be 10^{15} Nm^{-1}. This very high value ensures that the fault remains closed. This is desirable since shear faults are not extensional fractures and will be closed at all depths, except possibly the top few hundred metres, because of the lithostatic pressure.

In order to model the deformation caused by large shear stresses on the fault, it is necessary to know the frictional strength. The frictional relationship used here is

$$\tau_F = \mu\sigma_n$$

A value of 0.1 is taken for μ, the coefficient of friction, based on the work of Wang and Mao (1979). This assumes that wet fault gouge containing clay minerals is present. Friction laws and coefficients of friction have been discussed in Chapter 2. Throughout this thesis, a lithostatic stress distribution has been assumed to exist in the model as a result of the body forces. This is justifiable because there are no lateral density contrasts. Consequently, body forces have not been included in the finite element force vector. It is therefore necessary to add the lithostatic stress into the normal stress when calculating the frictional strength. It is likely that the fault plane is percolated by water, which will give rise to a pore pressure. It is assumed here that the pore pressure on a fault section is equal to the overburden pressure of

the water. This pore pressure is subtracted from the normal stress, as described in Chapter 5.

6.2.3 Fault deformation and subsequent failure

Figures 6.6 to 6.10 show the deformation of the model in response to increasing applied stress. In each of these figures, diagram (a) shows the principal stress vectors plotted at their principal orientations, at the centres of the elements, for the central 80 km of the grid. Dashed lines represent tensile stresses and full lines represent compressive stresses. These plots do not include the lithostatic stresses. Diagram (b) shows the surface displacements for the central 400 km of the model. It should be realised that the disparity in the horizontal and vertical scales in these displacement diagrams results in an apparent vertical displacement where the fault intersects the surface of the model. In fact, the displacement is along the fault plane, which dips at approximately 63°. The position of the element closest to failure, determined using the Modified Griffith Theory, is also marked on these diagrams.

Some generalisations on the deformation can be made from a study of these figures. Firstly, the displacement plots show that the fault is indeed a normal fault. Note that this was not assumed in the method since the sense of the fault movement is dependent on the sign of the shear stress. Normal faulting is, of course, what would be expected with horizontal, deviatoric tension (Anderson, 1951). Secondly, deformation on the fault results in changes of the stress distributions in the material immediately adjacent to the fault. The principal stresses become aligned approximately parallel and perpendicular to the fault plane. This is a result of the low frictional strength of the fault and is a well-known phenomenon (Anderson, 1951; Ramsay, 1967). For all applied stresses

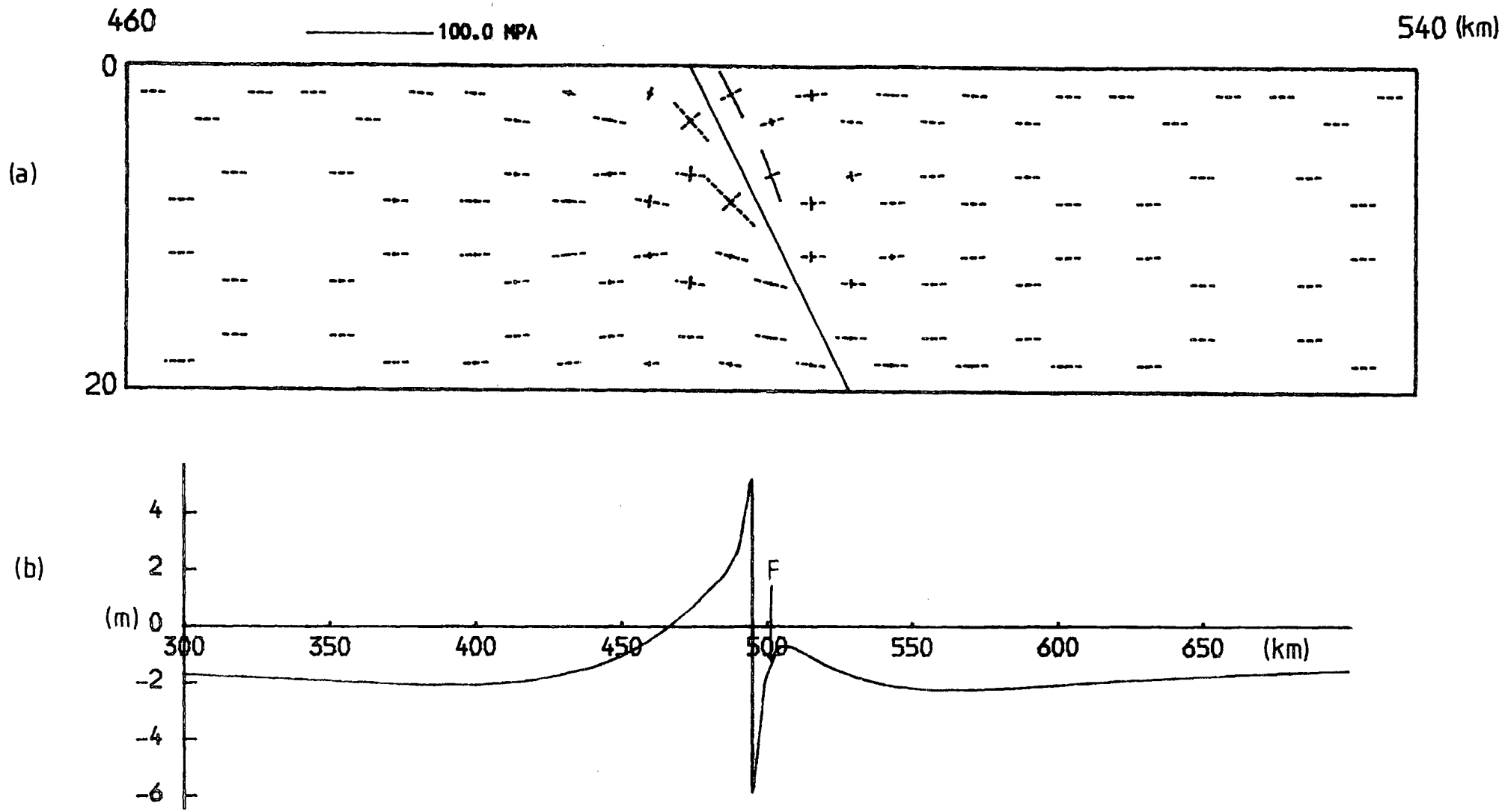

Fig. 6.6: Deformation of the model for an applied stress of 20 MPa
(a) Principal stresses around the fault
(b) Surface displacement profile
F position of weakest element

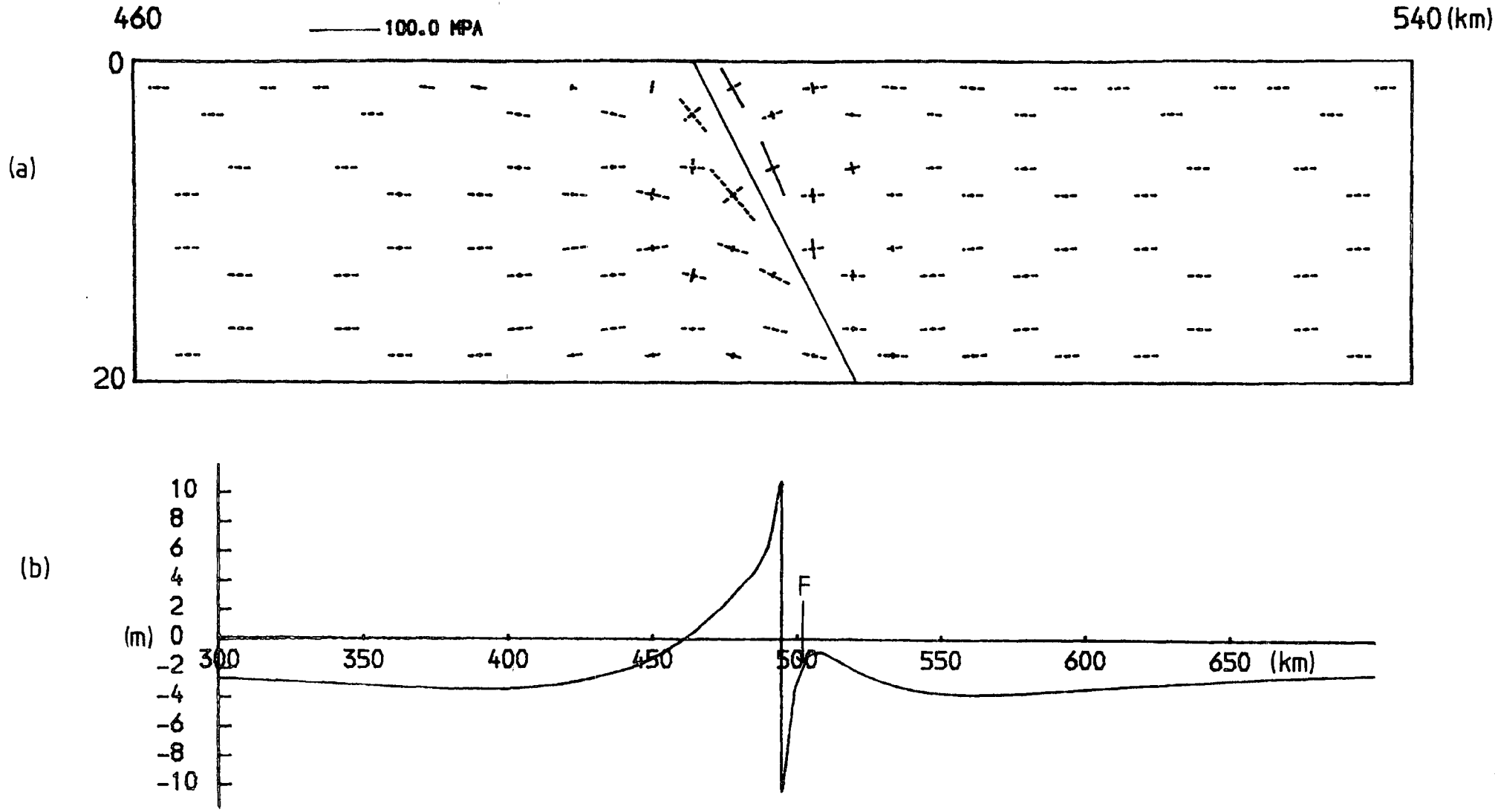

Fig. 6.7: Deformation of the model for an applied stress of 30 MPa
(a) Principal stresses around the fault
(b) Surface displacement profile
F position of weakest element

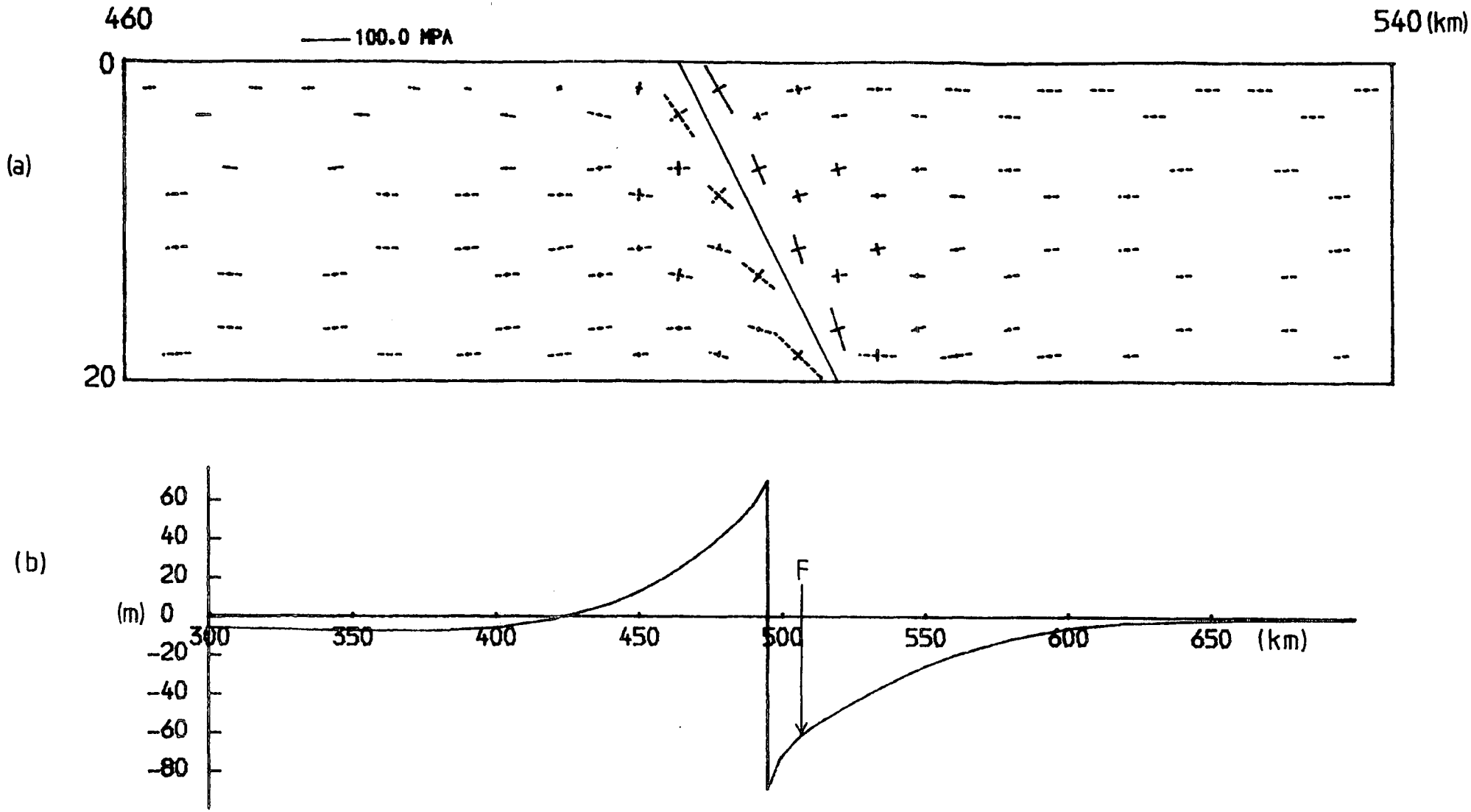

Fig. 6.8: Deformation of the model for an applied stress of 40 MPa
(a) Principal stresses around the fault
(b) Surface displacement profile
F position of weakest element

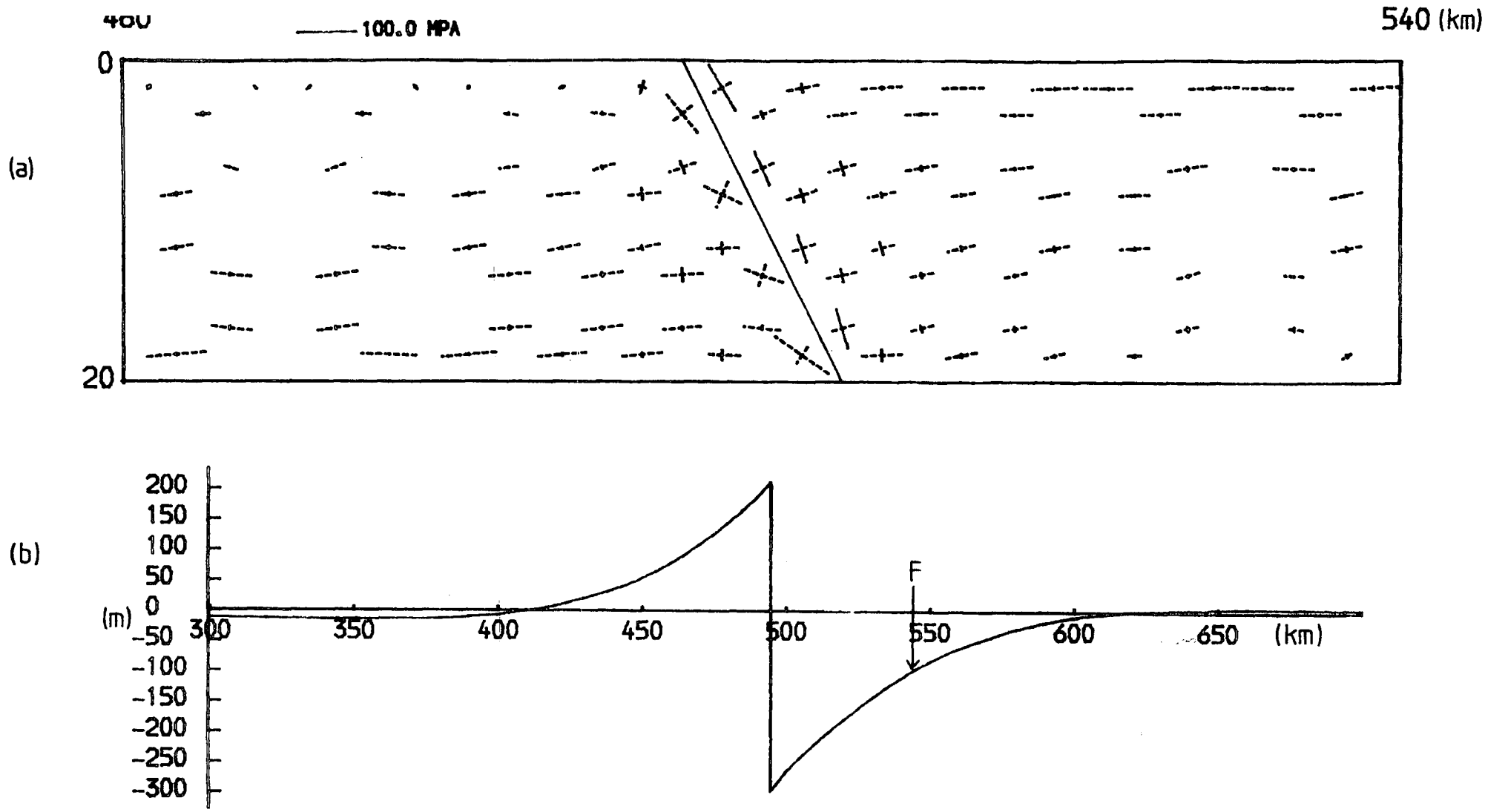

Fig. 6.9: Deformation of the model for an applied stress of 50 MPa
(a) Principal stresses around the fault
(b) Surface displacement profile
F position of weakest element

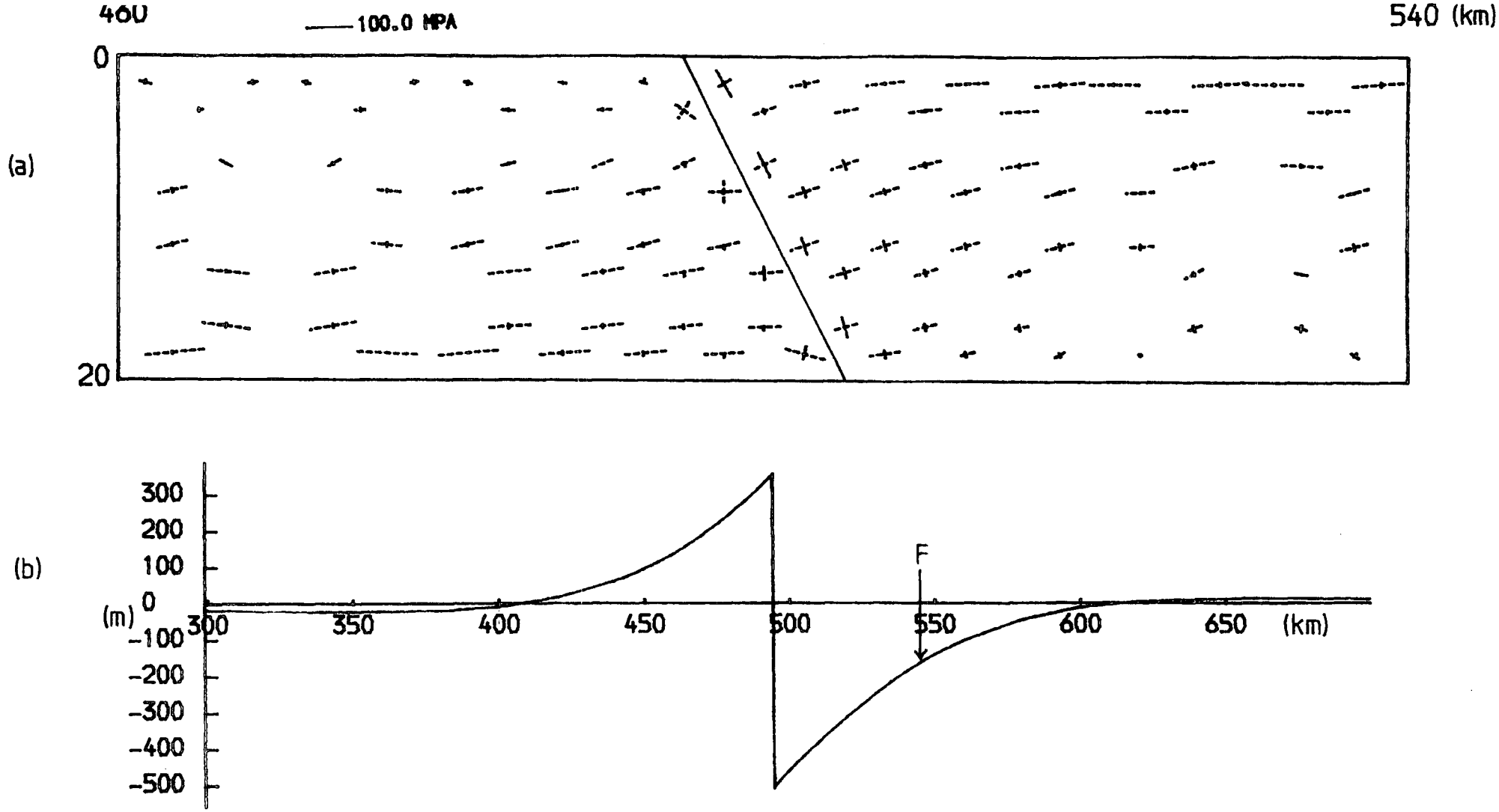

Fig. 6.10: Deformation of the model for an applied stress of 60 MPa
(a) Principal stresses around the fault
(b) Surface displacement profile
F position of weakest element

the model predicts compression parallel to the fault on the downthrown side and tension on the upthrown side. Thirdly, as the applied stress is increased the frictional strength is exceeded at successively greater depths on the fault. For an applied stress of 20 MPa (Figure 6.6) the frictional strength is exceeded only on the upper 5 km of the fault. Between about 30 and 40 MPa the depth of frictional sliding increases to 10 km, and from 40 to 60 MPa it reaches 15 km. At stresses greater than about 60 MPa the frictional strength is exceeded throughout the depth of the fault. The large increases in the throw of the fault which are associated with this propagation of fault slip are apparent in Figures 6.6 to 6.10. The throw ranges from 11 m for an applied stress of 20 MPa to about 870 m for an applied stress of 60 MPa. Also associated with this is a fundamental change in the shape of the displacement profile on the downthrown side of the fault. This will be discussed later.

For all applied stresses up to 40 MPa the element closest to failure is the one adjacent to the fault on the downthrown side (Figures 6.6 to 6.8). The development of subsidiary fault systems along the margins of a major fault is known as secondary faulting and has been discussed by Ramsay (1967) and King (1978). McKinstry (1953), Moody and Hill (1956) and Chinnery (1966) have all performed calculations on wrench faults which show that secondary faulting will occur, although they are not in agreement about the mechanism. For a tensile strength of 12 MPa (see Chapter 2) open crack shear failure has been predicted in this element. One of the two conjugate fault planes for this new fault is predicted to dip towards the master fault at an angle of about 85°. This is the fault plane that is considered most likely to develop and agrees well with possible second order faults deduced by Ramsay (1967) from the stress trajectories around a major fault. This secondary faulting will

intersect the major fault plane close to the surface and its effect on the deformation pattern is likely to be very localised. Consequently, no attempt is made to model the secondary faulting.

As the applied stress is increased, the near-surface stresses at some distance from the fault are modified by the fault movement. These stresses are approximately horizontal, but the tensile stresses on the upthrown side are reduced and those on the downthrown side are increased. This is a result of the bending, which compresses the upthrown side and stretches the downthrown side. For applied stresses greater than 40 MPa the element closest to failure shifts to a distance of 50 to 55 km from the original fault. For a tensile strength of 12 MPa, open crack shear failure is predicted with a new fault plane dipping at about 70°. Although this faulting is a result of movement on the major fault, it is not strictly secondary faulting, since it is a considerable distance away. The stress system here is one of horizontal deviatoric tension, which has been increased by the bending, and, consequently, another normal fault will be formed. The new fault plane will either dip towards the existing fault or be approximately parallel to it. In the former case a graben will be formed, and in the latter case a tilted fault block will result. These two possibilities are illustrated in Figure 6.11.

In this thesis, the former situation will be considered to occur and a graben of width 50 to 55 km will be formed.

Earlier in this section, the change of displacement profile with applied stress was mentioned. This will now be discussed in detail. For low applied stresses, the downthrown side is characterised by a 'bulge' situated about 10 km from the fault. As the applied stress is increased the shape of the bulge changes slightly and becomes relatively smoother. At high applied stress the profile becomes much smoother and more

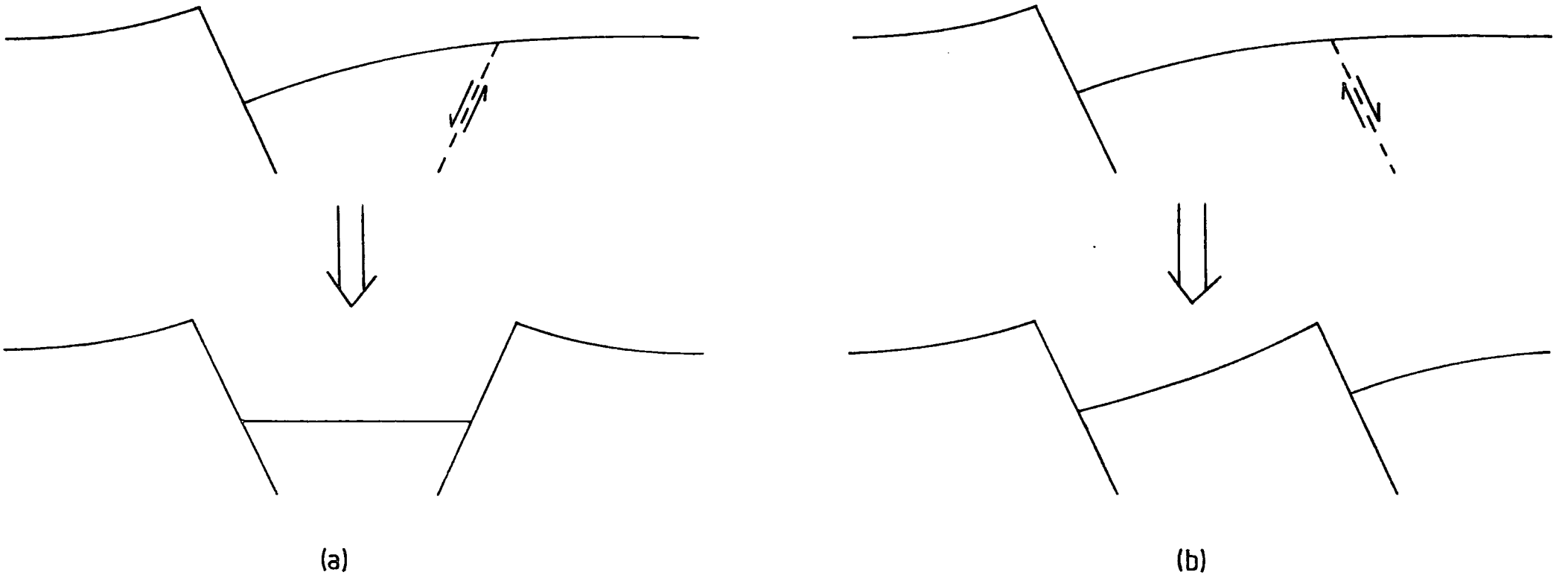

Fig. 6.11: Types of structure that can occur as a result of the formation of a second normal fault.
(a) Graben wedge
(b) Tilted fault block

similar to flexure associated with bending. It would be expected that the tensile stresses at the top of the bulge would be increased because of the severe curvature in that region. The results for the models illustrated in Figures 6.6 to 6.10 have been examined and this is found to be the case. The position of the element closest to failure changes as the bulge becomes smoother. For applied stresses up to about 30 MPa the weakest element is situated 5 to 10 km from the fault. Note that the weakest element refers to the one closest to failure; all elements have the same tensile strength. For applied stresses of about 40 MPa the weakest element is 10 to 15 km from the fault, and for stresses greater than 45 MPa it is 50 to 55 km from the fault. In this discussion, failure in the element adjacent to the fault is not considered since, as was discussed earlier, this is secondary faulting resulting from the re-orientation of the principal stresses in the immediate vicinity of the fault. The tensile strength seems important, therefore, for determining the position of failure. Low values will give failure at 5 to 15 km from the fault and higher values will give failure at 50 to 55 km from the fault. It is very interesting that elements between 15 to 50 km and further away than 55 km are never the closest ones to failure. There seems to be a definite transition from failure in the range of 5 to 15 km to failure at about 50 km. These two positions for failure to occur correspond to the two different types of displacement profile. The weak elements at 5 to 15 km are connected with the bulge that occurs at low applied stress, and the weakness at about 50 km is connected with the smooth bending profile seen at high applied stress. An explanation for these results will now be proposed.

For low applied stresses, the frictional strength has only been exceeded for the upper part of the fault. Consequently, the situation

is not one where the fault movement is opposed by an isostatic restoring force. Instead, the shape of the flexure is determined by the elastic response of the underlying material. This will be termed the elastic restoring force. At an applied stress of 40 MPa the fault movement extends to 10 to 15 km and there is, consequently, a smaller thickness of elastic material beneath the active part of the fault as well as larger forces acting along the fault plane. At this point, movement into the fluid becomes significant. Now a more recognisable type of bending profile is seen (Figure 6.8), although there is still a slight bulge at about 10 km from the fault. This is due to the elastic restoring forces. At applied stresses greater than 50 MPa (Figures 6.9 and 6.10) the fault movement extends to 15 km and, eventually, through the complete depth of the elastic layer. For these situations the movement into the fluid completely dominates the bending and a smooth bending profile, with the weakest element at 50 to 55 km, is seen.

If the above explanation is correct, then the thickness of the elastic layer will determine at what values of applied stress the displacement profile becomes smooth. A thicker layer will require higher applied stresses before fault movement will occur throughout the layer. The reverse will be true for a thinner layer. This hypothesis has been tested by varying the thickness of the elastic layer, and has been found to be correct. The position of the weakest element is shown in Table 6.1 for different values of the layer thickness and the applied stress. For a 10 km thick layer all applied stresses of about 30 MPa and greater give a smooth bending profile and the weakest element again at 50 to 55 km. Consequently, even low values of the tensile strength predict faulting at this distance. For a 30 km thick layer, applied stresses of about 80 MPa are necessary before a smooth profile is obtained. The weakest

Elastic layer thickness (km)	Applied stress (MPa)	Depth of fault movement[1] (km)	Distance of weakest element from fault[2] (km)
	10	2.5	5 - 10
	20	5.0	10 - 15
10	30	7.5	50 - 55
	40	10.0	50 - 55
	50	10.0	50 - 55
	20	5.0	5 - 10
	30	10.0	5 - 10
	40	10.0	10 - 15
20	45	15.0	50 - 55
	50	15.0	50 - 55
	60	15.0	50 - 55
	70	20.0	50 - 55
	80	20.0	50 - 55
	20	7.5	5 - 10
	40	7.5	5 - 10
	60	15.0	10 - 15
30	70	15.0	10 - 15
	80	22.5	50 - 55
	100	30.0	50 - 55
	140	30.0	50 - 55

Table 6.1: Depth of fault movement and position of weakest element for a range of elastic layer thicknesses and applied stresses.

1. Defined as the depth to the base of the deepest fault section on which the frictional strength is exceeded.

2. Not including possible secondary faulting adjacent to the original fault.

element is, surprisingly, once more at 50 to 55 km from the original fault. In this case, high tensile strengths are necessary to obtain faulting at this distance.

6.2.4 Discussion of results

Assuming that the approximations of beam theory are not too severe, the predicted width of a graben can be calculated theoretically to lie between two values, representing situations of maximum and minimum constraint at the fault. The theory is given in Appendix 1. The limits are

$$\frac{\pi\alpha}{4} \leqslant \text{width} \leqslant \frac{\pi\alpha}{2}$$

where α is the flexural parameter. The calculated values for different thicknesses of the elastic layer and the elastic parameters used in the model are given in Table 6.2.

Elastic layer thickness (km)	Flexural parameter (km)	Predicted width, w (km)
10	32.1	$25.2 \leqslant w \leqslant 50.4$
20	54.0	$42.4 \leqslant w \leqslant 84.8$
30	73.2	$57.5 \leqslant w \leqslant 115.0$

Table 6.2 Predicted graben widths from beam theory for varying elastic layer thicknesses.

For the finite element models that have been described above, situations where the predicted width (the distance of the weakest element

from the fault) is obviously the result of elastic restoring forces are clearly not applicable to beam theory. This leaves the cases where there are smooth bending profiles. For all thicknesses of the elastic layer these have given graben widths of 50 to 55 km. This result is very surprising and is at variance with the beam theory results given above. It is not clear why this is. The finite element models are sufficiently long for the boundary conditions at the edges not to affect the results, as can be seen in the diagrams. One possible reason for the discrepancy is that bending problems are not adequately modelled by the finite element technique used here, and the reasonable fit for a 20 km thick beam, shown in Figure 6.2, is coincidental. To show that this is not the case, simple bending models with the same elastic parameters as the earlier model have been run for thicknesses of 10 and 30 km. The results are illustrated in Figure 6.12. The agreement with the beam theory is not exact because the theory makes assumptions about the stresses which are only approximations (see Appendix 1), and also the use of constant strain triangles is not conducive to accurate solutions of bending problems (Zienkiewicz, 1977). Nevertheless, the agreement is sufficiently close to suggest that altering the thickness would result in a different graben width, if the other parameters remained constant. Another possible reason for the poor agreement is the nature of the 'load' acting at a fault. The beam theory calculations assume a vertical downward force at the origin. However, the force applied along a fault is in the direction of the fault plane, which is not vertical, and also varies with depth. Clearly the true situation is much more complex than the theory assumes. The tentative conclusion that can be drawn from this is that, even in the situation where fault movement occurs throughout the elastic layer, the use of simple beam theory to predict the distance to the second fault is inadequate.

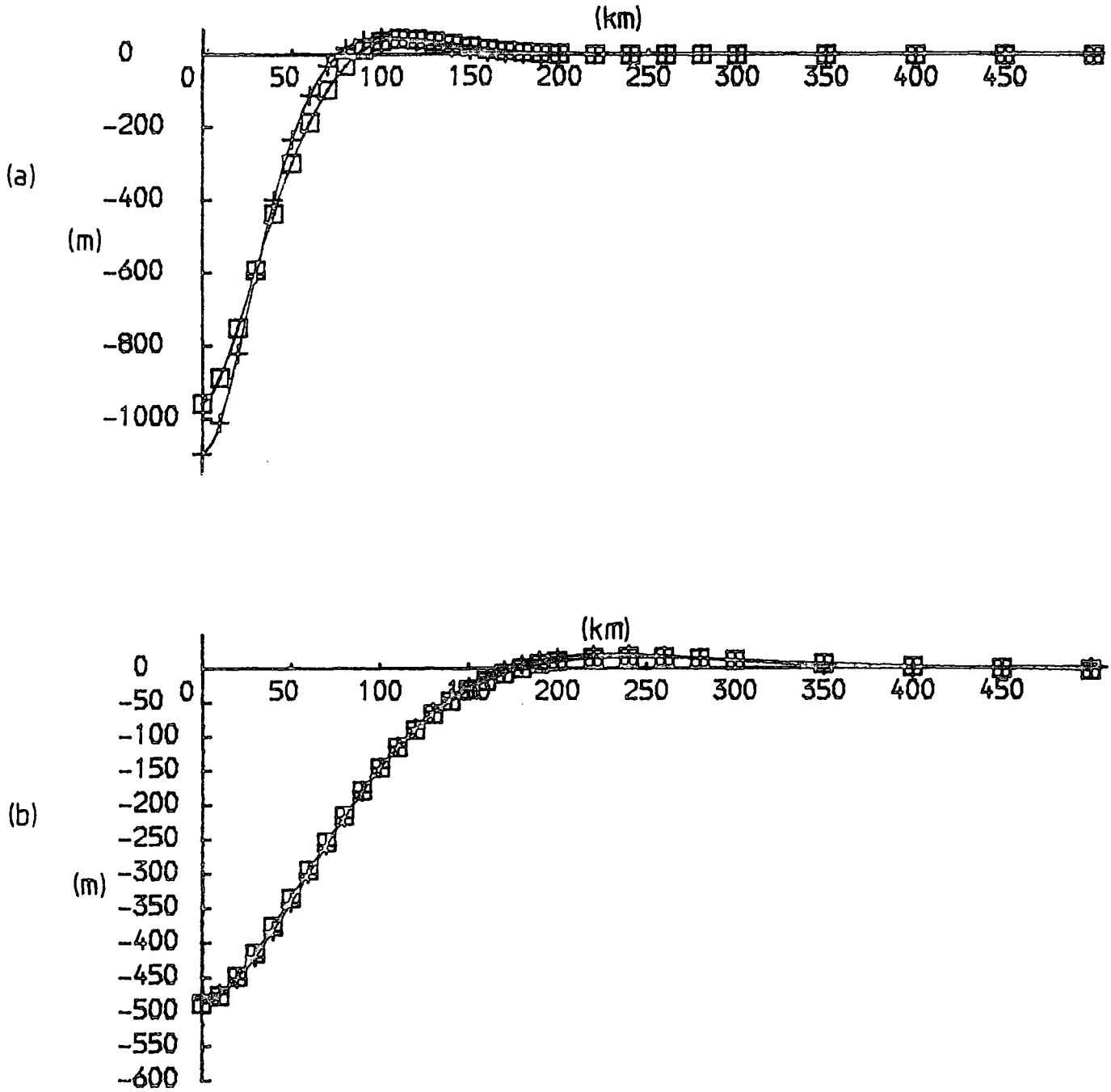

Fig. 6.12: Comparison of model bending with elastic beam theory for different thicknesses; elastic parameters as in Figure 6.1.

⊡ Plane strain finite element solution
\+ Solution from elastic beam theory
(a) 10 km thick layer
(b) 30 km thick layer

This may be due to the complex nature of the fault movement.

Of more interest, with regard to the rheology of the lithosphere, is the situation where elastic restoring forces are important. These will be discussed in the next section, where a more realistic model of the lithosphere will be considered.

6.3 Full lithosphere model

In this section the analysis on the full lithosphere model used earlier will be continued with a fault extending through the top 20 km of the model. The stress system existing at the time of failure, which was described in Chapter 4, will be re-applied to the model with a fault present and subsequent deformation will be investigated.

6.3.1 Model parameters

The elastic parameters, dimensions and rheology of the model are the same as those discussed in Chapter 2 and used in Chapter 4. The fault parameters are those that were used in the first part of this chapter: it dips at an angle of 63.43°, extends to a depth of 20 km, has normal and shear stiffnesses of 10^{15} and 5×10^{10} Nm^{-1} respectively, has a coefficient of friction of 0.1, and has a pore pressure equal to the overburden of water. The finite element grid is shown in Figure 6.13.

6.3.2 Stress system at the time of faulting

It was shown in Chapter 4 that if an applied stress of 20 MPa acted throughout the depth of the lithosphere, then relaxation of the stresses in the visco-elastic material of the lower part of the lithosphere would result in the amplification of stresses in the elastic layer and eventual faulting. After 1.19 M yrs, with a Newtonian visco-

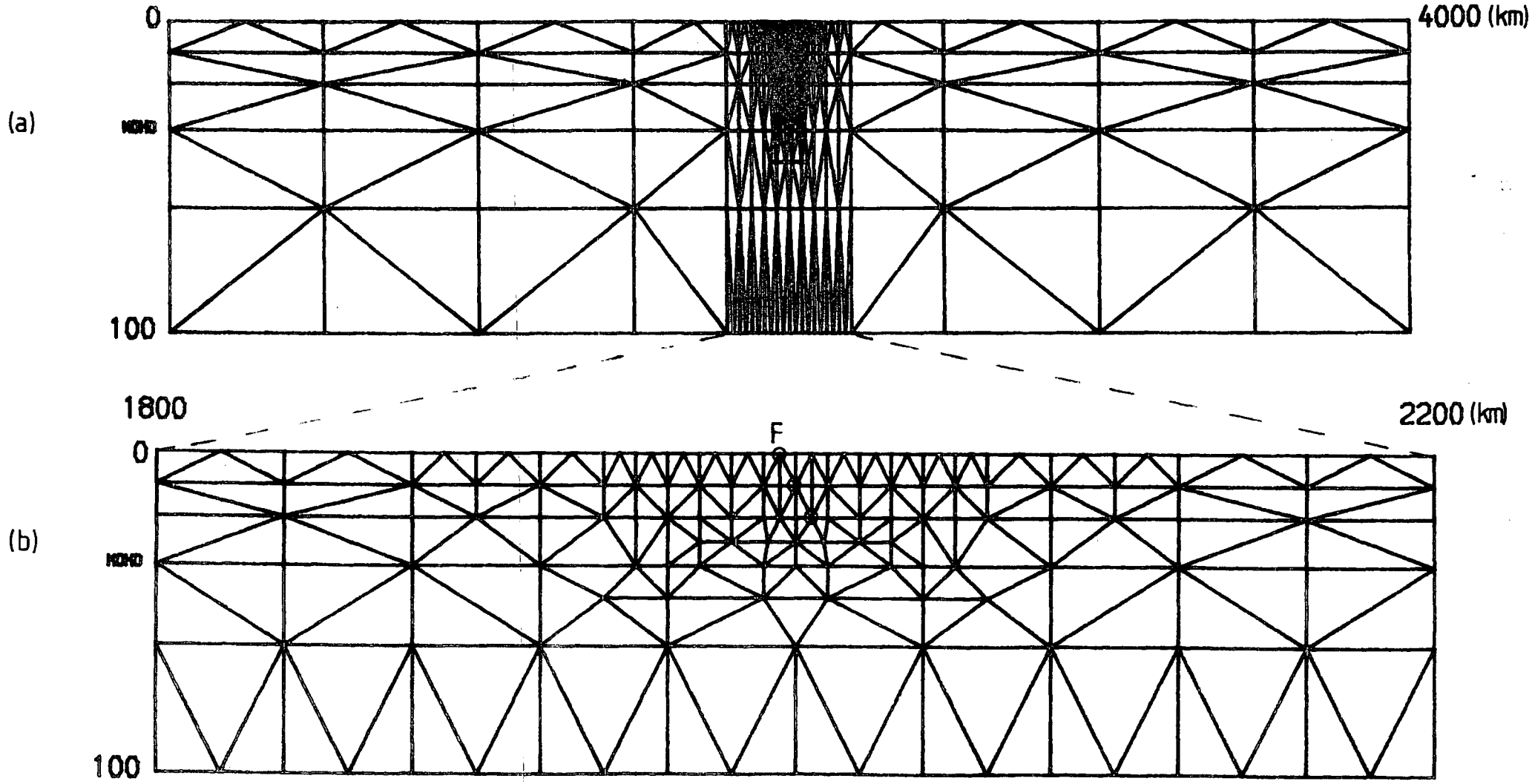

Fig. 6.13: Finite element grid for the lithosphere with a fault in the elastic layer.
(a) Full grid
(b) Central 400 km section of grid
F position of fault : ⊙ position of dual node

elastic rheology, faulting was predicted in the elastic layer. This situation was shown in Figure 4.9. To re-create this stress system, the method described in the final section of Chapter 3 was used. This involves applying the total forces that existed at the end of the time period of the earlier model to the nodes, and subtracting the creep strains from the total strains to give the elastic strains. Performing this operation with the grid used in Chapter 4 resulted in a stress system that agreed with that shown in Figure 4.9 to within 0.2 MPa. The introduction of the fault, however, necessitates some alteration of the grid. Three of the nodes in the elastic layer are replaced by dual nodes. To re-create the stress system of Figure 4.9 with this model, the forces that existed at the nodes which have become dual nodes were divided equally between the two node numbers. To verify that this stress system is indeed the same as that found earlier, the fault was 'sealed' by assigning high values of normal and shear stiffness (10^{15} Nm^{-1}) so that the model approximated to a continuum. The stress system obtained by doing this was the same as the re-created stress system for the continuum model of Chapter 4: in other words, it agreed with the stress system at the time of faulting (Figure 4.9) to within 0.2 MPa. Consequently, changes in the stresses and displacements given by the stress system at the time of faulting when applied to the model with the fault present will represent the changes in deformation caused by the faulting.

6.3.3 Fault deformation and subsequent failure

The immediate deformation pattern resulting from the faulting is shown in Figure 6.14. The fault has behaved as a normal fault with a throw of 53 m. The horizontal deviatoric tensions in the elastic layer, away from the immediate vicinity of the fault, have been reduced by this

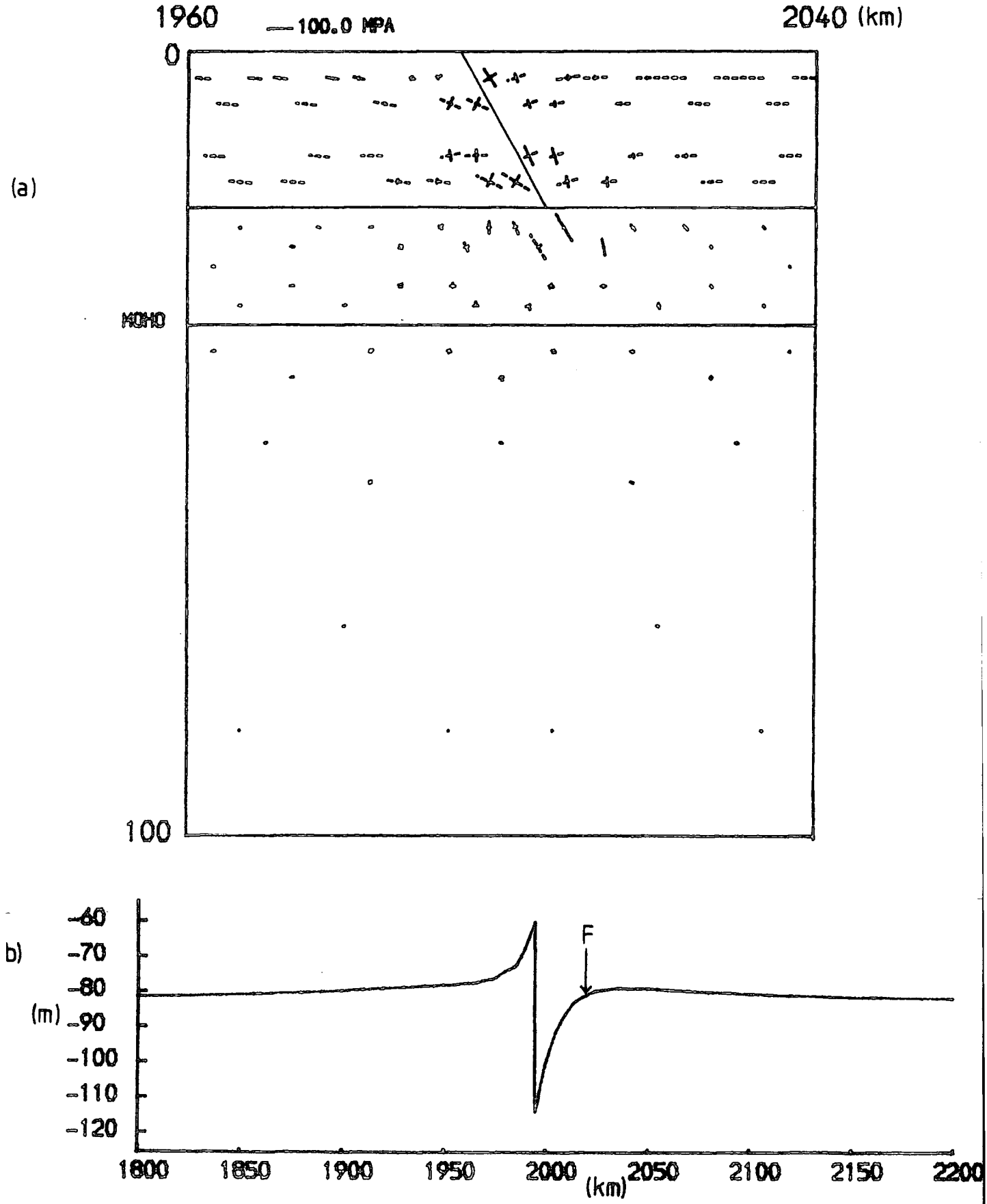

Fig. 6.14: Immediate deformation caused by faulting
(a) Principal stresses around the fault
(b) Surface displacement profile
F position of predicted failure for tensile strengths less than 16 MPa

fault movement. The principal stresses adjacent to the fault are aligned approximately parallel and perpendicular to the fault. Compression exists parallel to the fault on the downthrown side and tension on the upthrown side. A deviatoric compressive stress of 130 MPa develops parallel to the fault plane in the lower crustal material immediately beneath the downthrown side, and a deviatoric tensile stress of 115 MPa develops beneath the upthrown side. The relief of horizontal, deviatoric tensile strain in the elastic layer by the fault movement has resulted in a small increase in the horizontal, deviatoric tensile stresses in the underlying visco-elastic material.

For values of tensile strength between 10 and 15 MPa, failure is predicted immediately at a distance of about 20 km from the original fault. This is the position where the deviatoric tensile stresses have been most greatly increased by the bending. Immediately before faulting the horizontal deviatoric stress was 86.5 MPa. The fault movement has resulted in it increasing to about 97.0 MPa. Open crack shear failure is predicted with a fault plane dip of about 60°. If this new fault dips towards the original fault, a graben of width 20 km will be formed. For tensile strengths greater than 15 MPa, the model was allowed to relax through time until failure was predicted. A Newtonian visco-elastic rheology was used for the lower crust and lithospheric mantle with a viscosity of 10^{23} Pa s. The results for tensile strengths in the range 10 to 20 MPa are listed in Table 6.3. There is an increase in predicted graben width to 25 km for a tensile strength of 17 MPa. 70,000 yrs must elapse before this failure occurs. For higher tensile strengths, which require longer times, there is no change in the predicted width. To check that this result holds even for very long time periods, the model was run for a tensile strength of 30 MPa. A period of 430,000 yrs was

Tensile Strength (MPa)	Time to predicted faulting (x 10^3 yrs)	Throw of fault (m)	Distance of predicte fault from original fault (km)
10 - 15	0	53	20
16	30	58	20
17	70	63	25
18	100	68	25
19	120	70	25
20	150	73	25
30	430	102	25 - 30

Table 6.3: Predicted faulting for varying tensile strengths with a Newtonian visco-elastic rheology. Viscosity of lower crust and mantle is 10^{23} Pa s .

Tensile Strength (MPa)	Time to predicted faulting (x 10^3 yrs)	Throw of fault (m)	Distance of predicted fault from original fault (km)
10 - 15	0	53	20
16	6	58	25
17	12	61	25
18	18	64	25
19	28	66	25
20	40	69	25 - 30
30	630	98	25 - 30

Table 6.4: Predicted faulting for varying tensile strengths with a power law creep rheology for the lower crust and mantle.

necessary before faulting was predicted, but again this was at a distance of about 25 km from the original fault.

As the model is allowed to relax through time, there is an increase in fault throw which results from the amplification of stresses in the elastic layer caused by creep below.This can be seen by comparing Figure 6.14 with Figure 6.15, which shows the deformation at the time of subsequent failure for a tensile strength of 20 MPa (i.e. after 150,000 yrs). The fault throw has increased from 53 m to 73 m and the maximum horizontal deviatoric tensions near the top of the elastic layer, which are situated about 25 km from the original fault, have increased to 107 MPa. The stresses in the underlying material have become more nearly hydrostatic, although the magnitude of the stresses parallel to the fault plane remains about the same. The possible consequences of these stresses beneath the base of the fault are discussed in the next section.

The same models have been run for a power law creep rheology using the creep equations for the lower crust and mantle that were given in Chapter 2. The results are shown in Table 6.4. Again, even for high tensile strengths, the predicted graben width was 25 km. The only significant difference between these results and those obtained using a Newtonian visco-elastic rheology are in the times necessary for subsequent failure to occur. For tensile strengths up to 20 MPa, the power law creep rheology results in much shorter times. Figure 6.16 shows the situation at the time of failure for a tensile strength of 20 MPa (i.e. after 40,000 yrs). The stresses in the underlying material are closer to a hydrostatic state than in Figure 6.15. For a tensile strength of 30 MPa the time necessary is much longer. This is because the effective viscosity is stress dependent. When the deviatoric stresses are large the viscosity is low, but as the stresses are relaxed the viscosity

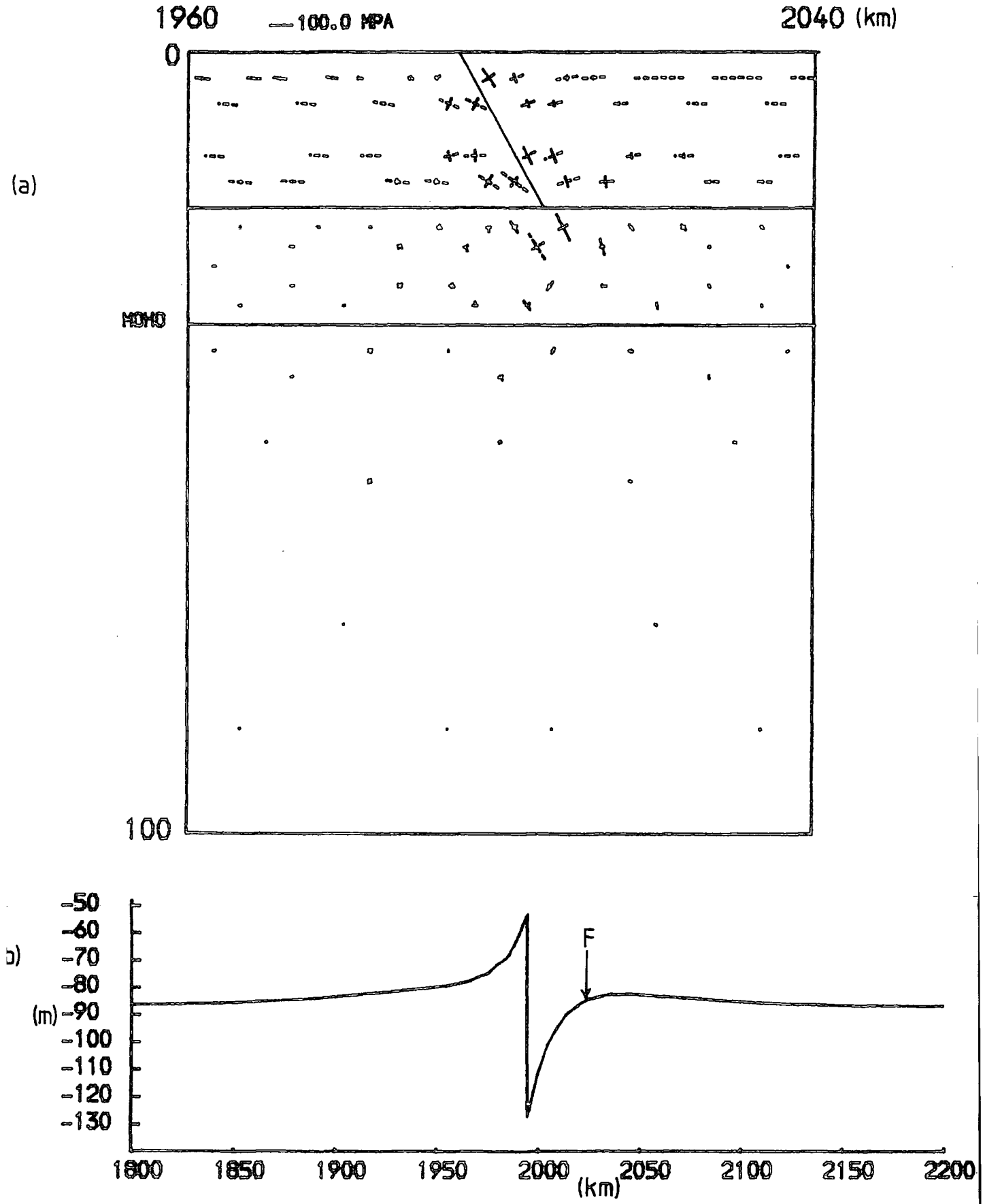

Fig. 6.15: Deformation caused by faulting after 150,000 yrs using a Newtonian visco-elastic rheology
(a) Principal stresses around the fault
(b) Surface displacement profile
F position of predicted failure for a tensile strength of 20 MPa

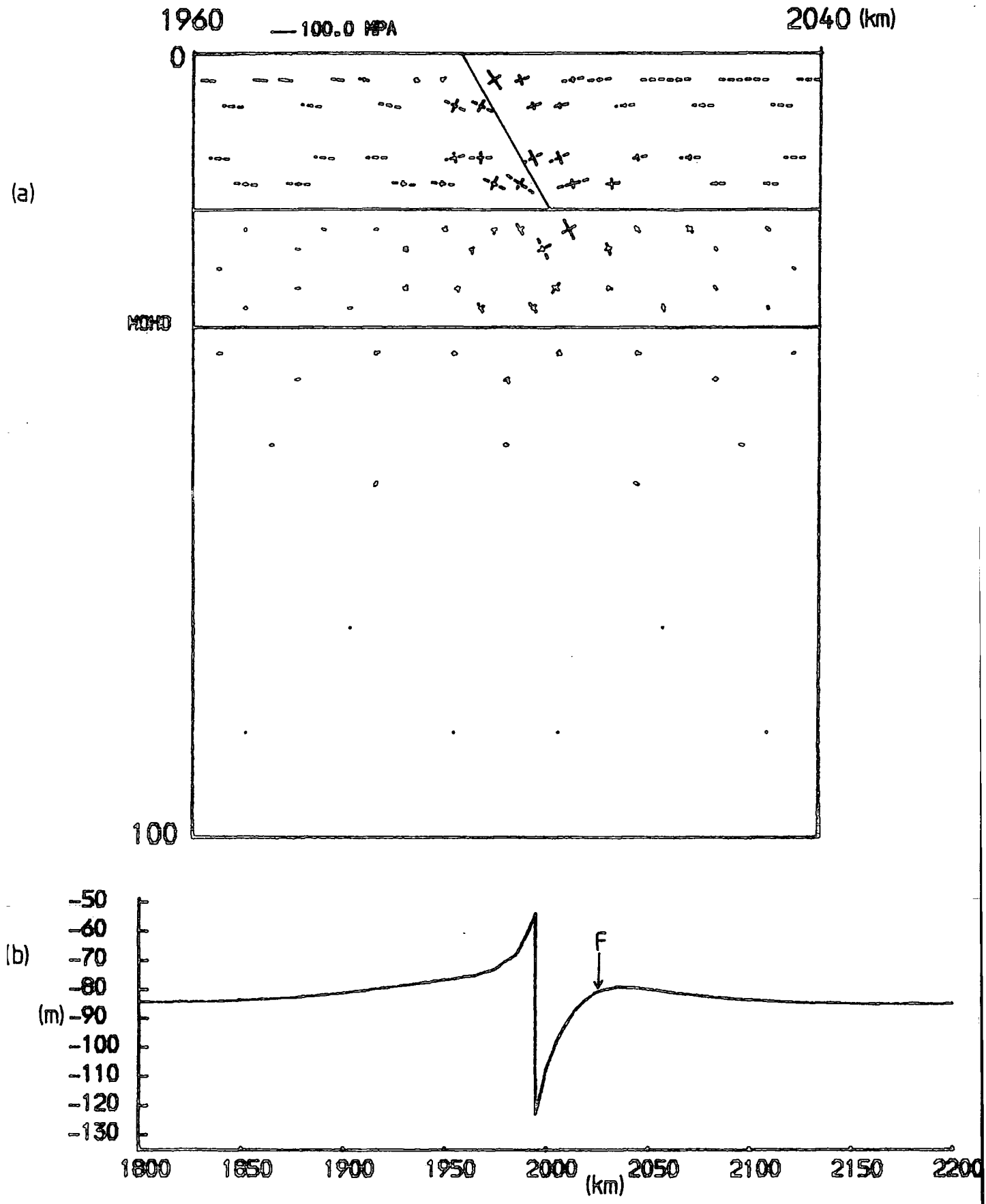

Fig. 6.16: Deformation caused by faulting after 40,000 yrs using a power law creep rheology
(a) Principal stresses around the fault
(b) Surface displacement profile
F position of predicted failure for a tensile strength of 20 MPa

is increased. Similar results on the differences between Newtonian visco-elastic and power law creep rheologies were shown and discussed in Chapter 4.

6.3.4 Discussion of results

The stress pattern in the elastic layer as a result of fault movement is the same as that seen in the first section of this chapter. The use of the full lithosphere model, however, allows the stresses in the material underlying the elastic layer to be investigated. It has been shown in Figures 6.14 to 6.16 that the material beneath the fault is subjected to large stresses parallel to the fault plane. It seems likely that this concentration of stress at the base of the fault will result in propagation of the fault plane. The mechanism of this propagation is not clear. Brittle failure seems unlikely because very large deviatoric stresses would be needed at these depths as a result of the overburden pressure. It is possible, however, that large, localised stresses concentrated at the fault tip will lead to dynamic recrystallisation and superplastic flow. Superplasticity involves grain-boundary sliding and requires reasonably high temperatures (greater than about half of the melting temperature) and very small grain sizes (Nicolas and Poirier, 1976). If the recrystallisation is to a sufficiently small grain size, then the temperature at depth is likely to be within the regime of superplasticity. Ball (1980) has shown that the onset of superplastic flow will result in a large increase in the shear strain rate. The resistance to shear will be small, and the recrystallisation to fine-grained material may result in fabrics similar to mylonites, which are associated with shear zones. The orientation of the principal stresses beneath the fault in Figures 6.14 to 6.16 suggests that the fault may not continue in the same

direction since the shear stresses will be concentrated on planes lying between the principal axes, and the principal axes are aligned with the fault. This may result in listric faulting, although this is highly speculative since it is the concentration of stresses around the crack tip that leads to fault propagation and this cannot be determined with the type of finite element analysis used here.

The results obtained in this section show that the deformation associated with a normal fault extending to a depth of 20 km results in the formation of a second normal fault at a distance of about 25 km form the original fault. The width of the graben seems to be relatively independent of the length of time for which the underlying visco-elastic material is allowed to relax. Consequently, it appears that the predicted graben width is mainly dependent on the depth of faulting. The results, however, are significantly different from those predicted by elastic beam theory. This is probably because of approximations made in beam theory calculations. Firstly, the underlying material is treated as a fluid which gives rise to an isostatic restoring force beneath the fault. A more realistic rheology for the lower lithosphere is visco-elasticity; indeed, whatever the true rheology, it must involve a component of elastic behaviour since both P and S waves are observed to propagate through the lower lithosphere with finite velocities. The elastic part of the rheology results in dilatational stresses which cannot be relaxed by creep (Chapter 3; Stocker and Ashby, 1973). The deformation of the visco-elastic material beneath the fault gives rise to elastic restoring forces rather than simple isostatic forces, and these seem to give a different bending profile. The second significant approximation used in predicting the range of graben widths by elastic beam theory is that the fault can be represented by a vertical load.

As was pointed out earlier in this chapter, the true situation is likely to be much more complex with forces acting in the direction of the fault plane. These forces will probably exist throughout the fault depth and will vary with depth because of the variation in frictional strength. In view of these observations, it does not seem so surprising that the predicted graben widths from the finite element analysis do not agree well with simple beam theory calculations.

The prediction of a 25 km wide graben seems to follow on from the results of the first section for the situations where fault movement occurred for depths less than 20 km. The predicted graben widths in those cases were from 5 to 15 km. This suggests that the development of wider graben may be a response to deeper faulting than has been considered here. This possibility will be investigated in the next chapter.

CHAPTER 7

PREDICTED GRABEN WIDTHS FOR VARIABLE DEPTH FAULTING

7.1 Introduction

In Chapters 4 and 6, the development of normal faulting and then of graben formation was investigated for a model with a 20 km thick elastic layer. The fault was considered to extend to 20 km only, and the predicted graben width was about 25 km. In this chapter a line of weakness will be assumed to be present and to extend to 50 km. Fault movement will not necessarily extend to 50 km, however, since the frictional strength must be exceeded for slip to occur. Tensile stresses will be applied to the edges of the model and the visco-elastic material of the lower lithosphere will be allowed to relax with time. This should result in fault movement to a maximum depth of 50 km. Instead of looking at failure for particular values of the tensile strength, as was done in the previous chapter, the position of the element closest to failure will be used to determine the predicted graben width for particular depths of fault movement.

7.2 Finite element model

The finite element grid used in this chapter is illustrated in Figures 7.1 and 7.2. It is necessary to use a very long grid, as discussed in Chapter 4, to avoid edge effects. The grid used here is 6,000 km long. The lithosphere is taken as being 100 km thick and is underlain by a fluid of density 3,300 kg m^{-3}. In this chapter, the possibility of fault movement extending down to 50 km will be investigated. For this to occur it will be necessary to have fairly large stresses at

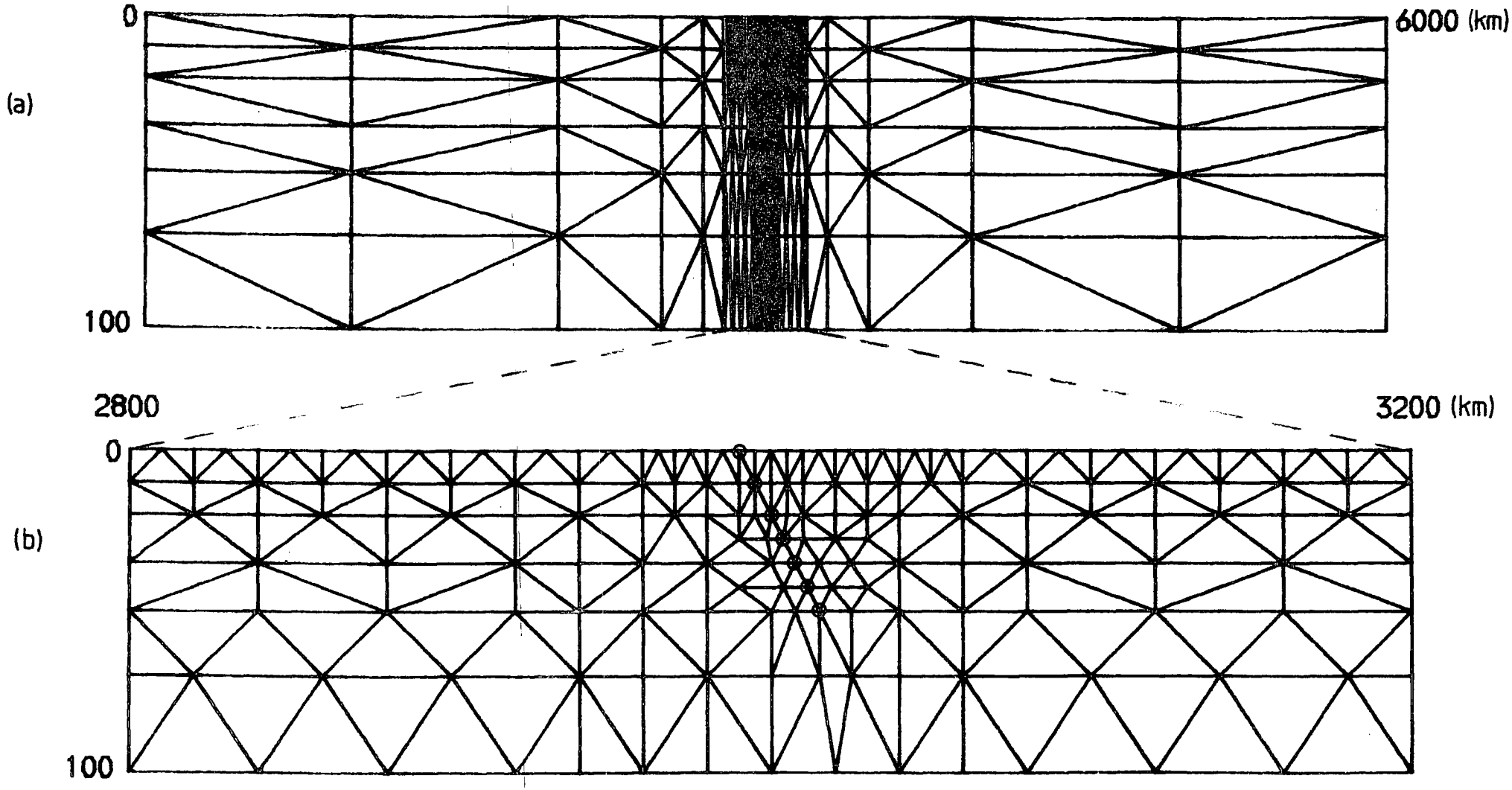

Fig. 7.1: Finite element grid for a fault extending to 50 km depth.
(a) Full grid
(b) Central 400 km section of grid
⊙ position of dual node

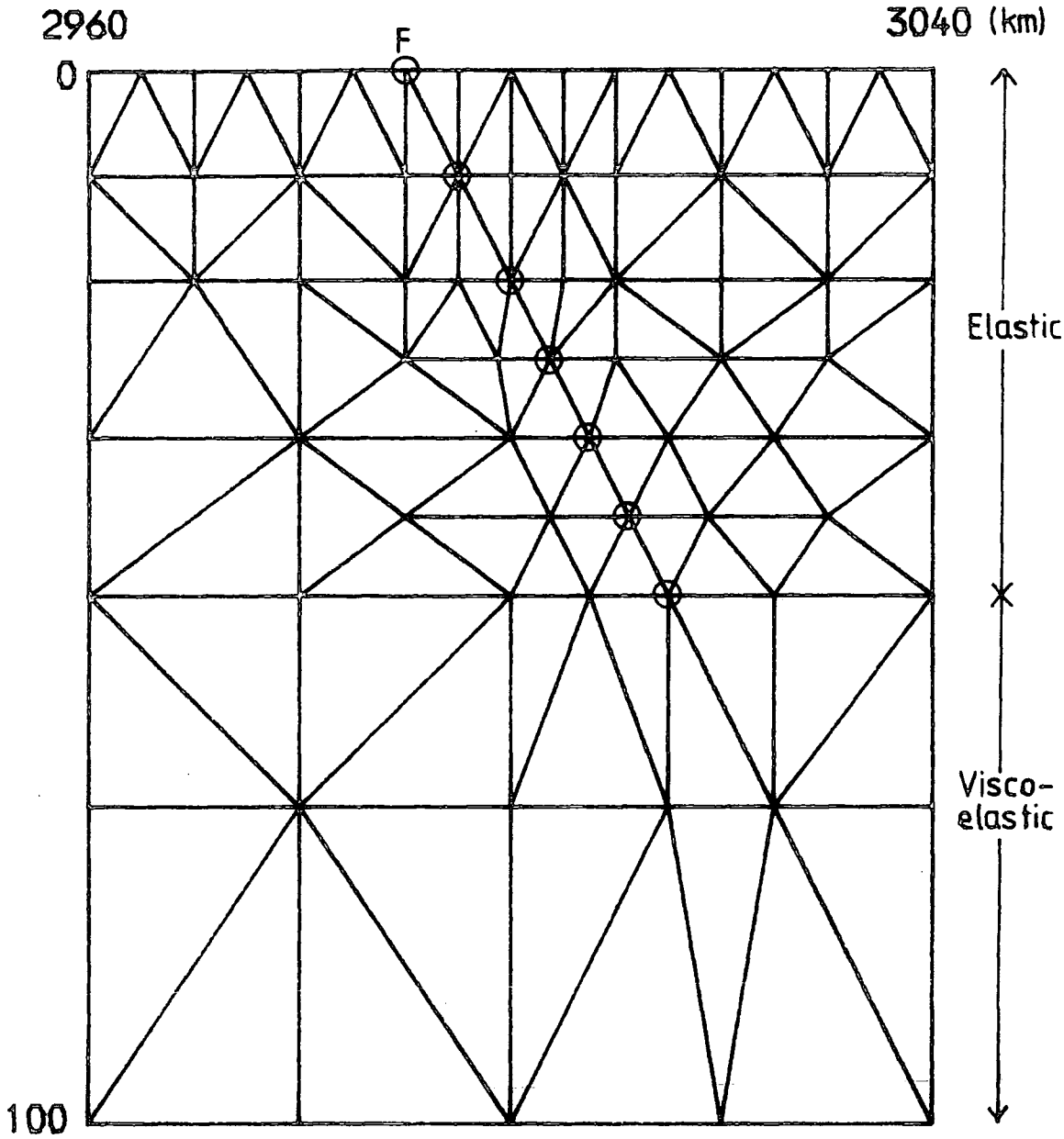

Fig. 7.2: Central 80 km of finite element grid

F position of fault

⊙ position of dual node

depth. Consequently, the model is defined in this chapter to consist of two layers: an elastic layer extending down to 50 km and a ductile layer from 50 to 100 km. The physical properties of these two layers are listed in Table 7.1.

The fault has a dip of 63.43° and has the potential to extend down to 50 km. It is divided into six sections. The normal and shear stiffnesses are taken to be $10^{15} Nm^{-1}$ and 5×10^{10} Nm^{-1}, as in Chapter 6. A pore pressure equal to the overburden pressure of water is assumed to exist on the fault.

	Depth Range(km)	E (Nm^{-2})	ν	ρ ($kg\ m^{-3}$)	Rheology
Elastic layer	0-50	1.0×10^{11}	0.25	2,900	Elastic
Ductile layer	50-100	1.8×10^{11}	0.25	3,300	Visco-elastic

Table 7.1: Properties of the finite element model

In order to satisfy the non-singularity of the stiffness matrix, the central node on the base is fixed in the x-direction. If the fault was not present, this node would lie on an axis of symmetry. There is no axis of symmetry in this model. However, it has been found that the fault is sufficiently far away from the fixed node for the results to be unaffected by this prescribed displacement. This can be seen in the stress diagrams shown later in this chapter, in which there are no anomalous stresses in the vicinity of the fixed node.

A tensile stress of 50 MPa is applied to the edges of the model. In the absence of the fault, this permits a maximum value of 100 MPa to develop in the elastic layer. The equations which govern this amplification have been discussed in Chapter 4.

7.3 Fault deformation

A value of 0.1 has been taken for the coefficient of friction on the fault. This value is representative of a fault containing a wet clay gouge (Wang and Mao, 1979) and was used in the previous chapter. A Newtonian visco-elastic rheology has been used for the ductile layer, with a viscosity of 10^{23} Pa s, and the stresses in the visco-elastic material have been allowed to relax with time. The results for this model are shown in Table 7.2 and in Figures 7.3 to 7.7. The depth of fault movement has been taken to be the depth of the base of the deepest fault section on which the frictional strength has been exceeded. In Table 7.2, the elements adjacent to the fault have not been considered from the point of view of being the closest to failure. This is because failure in these elements leads to secondary faulting which will intercept the original fault close to the surface. In fact, secondary faulting is predicted to be the first occurrence of failure for time periods up to 100,000 yrs. Beyond this time, failure will occur first in the elements where the deviatoric tensile stresses have been most greatly increased by the bending. These are given in Table 7.2.

Several points are apparent about the results. As the visco-elastic material relaxes, the stresses in the elastic layer are amplified which results in an increase in the shear stresses on the fault. As these exceed the frictional strength, fault movement propagates down the line of weakness. Associated with this propagation of fault movement is an increase in the throw of the fault. There is also an increase in the distance to the weakest element. Normal faulting will occur in the weakest element if the tensile strength is sufficiently small. If the new fault dips towards the original fault a graben will be formed. Consequently, the distance of the weakest element from the fault can

Time ($\times 10^3$ yrs)	Depth of fault movement (km)	Throw of fault (m)	Distance of weakest element from fault (km)
0	10.0	13	15 - 20
100	20.0	34	15 - 20
200	27.5	49	20
300	27.5	62	20
400	27.5	70	20 - 25
500	35.0	77	20 - 25
700	35.0	86	20 - 25
1000	35.0	95	25

Table 7.2: Fault deformation with time for an applied stress of 50 MPa, a coefficient of friction of 0.1, and a Newtonian visco-elastic rheology for the ductile material

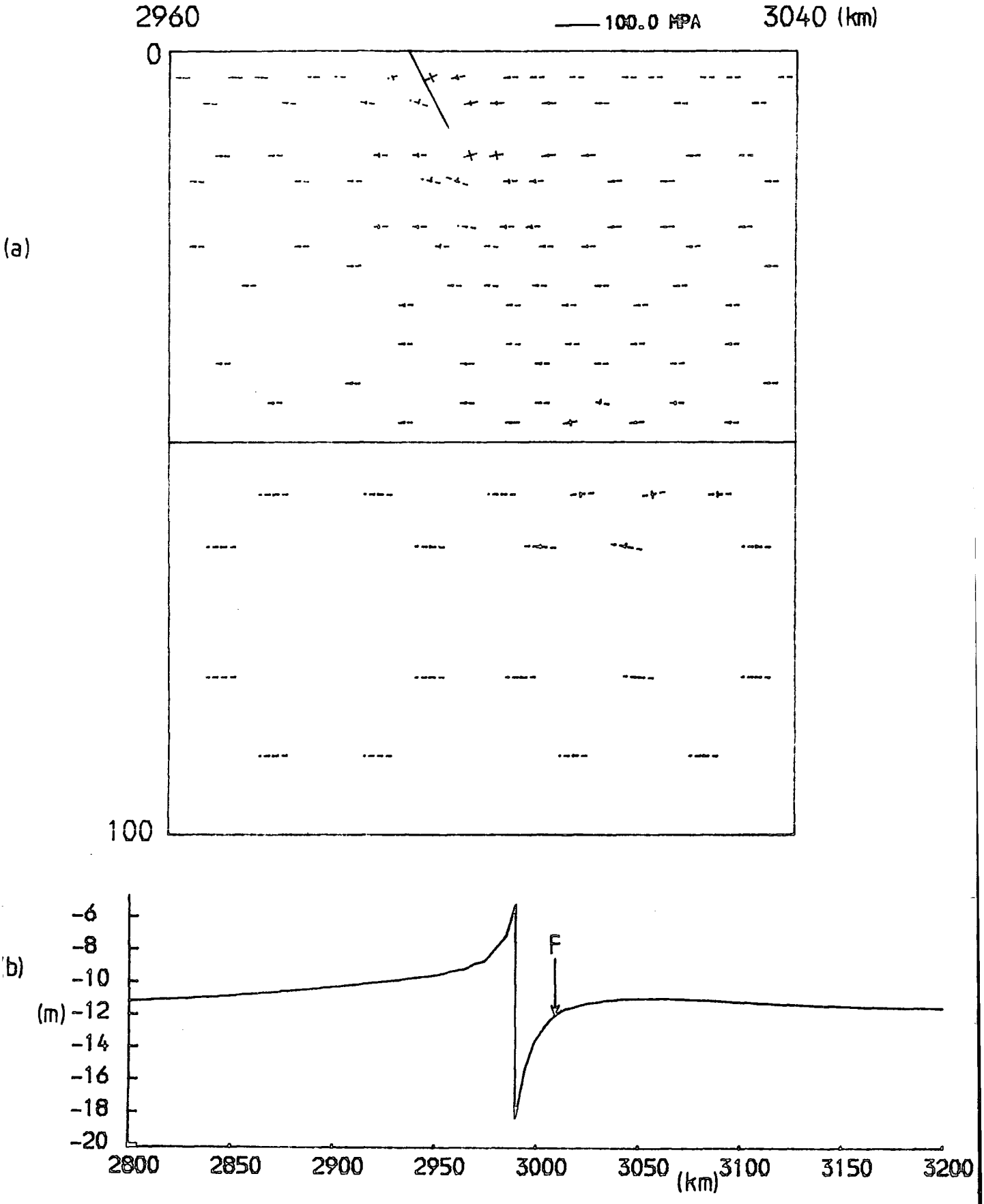

Fig. 7.3: Immediate fault deformation for an applied stress of 50 MPa and a coefficient of friction of 0.1
(a) Principal stresses around the fault
(b) Surface displacement profile
F position of weakest element

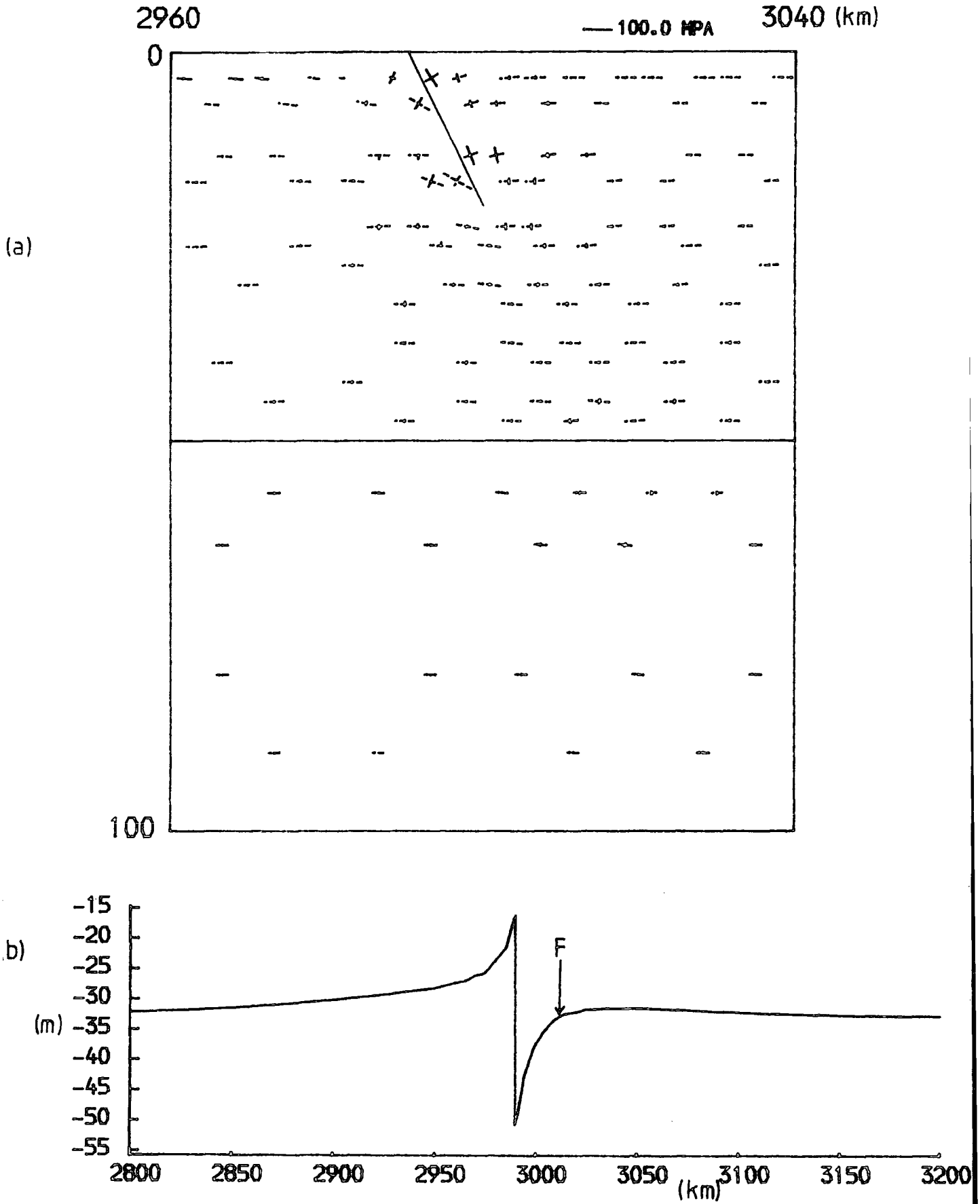

Fig. 7.4: Fault deformation after 100,000 yrs for a coefficient of friction of 0.1 and a Newtonian visco-elastic rheology
(a) Principal stresses around the fault
(b) Surface displacement profile
F position of weakest element

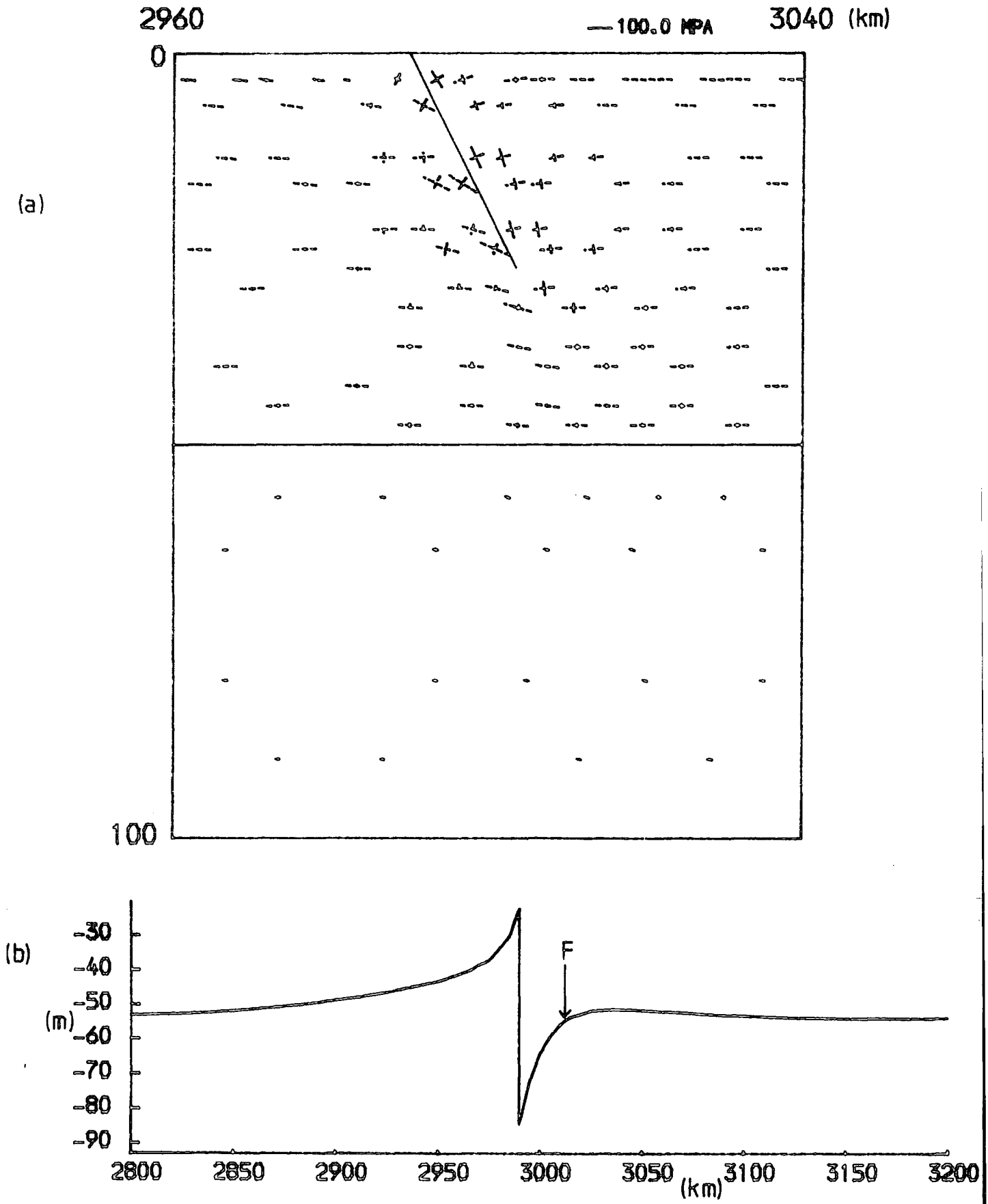

Fig. 7.5: Fault deformation after 300,000 yrs for a coefficient of friction of 0.1 and a Newtonian visco-elastic rheology
(a) Principal stresses around the fault
(b) Surface displacement profile
F position of weakest element

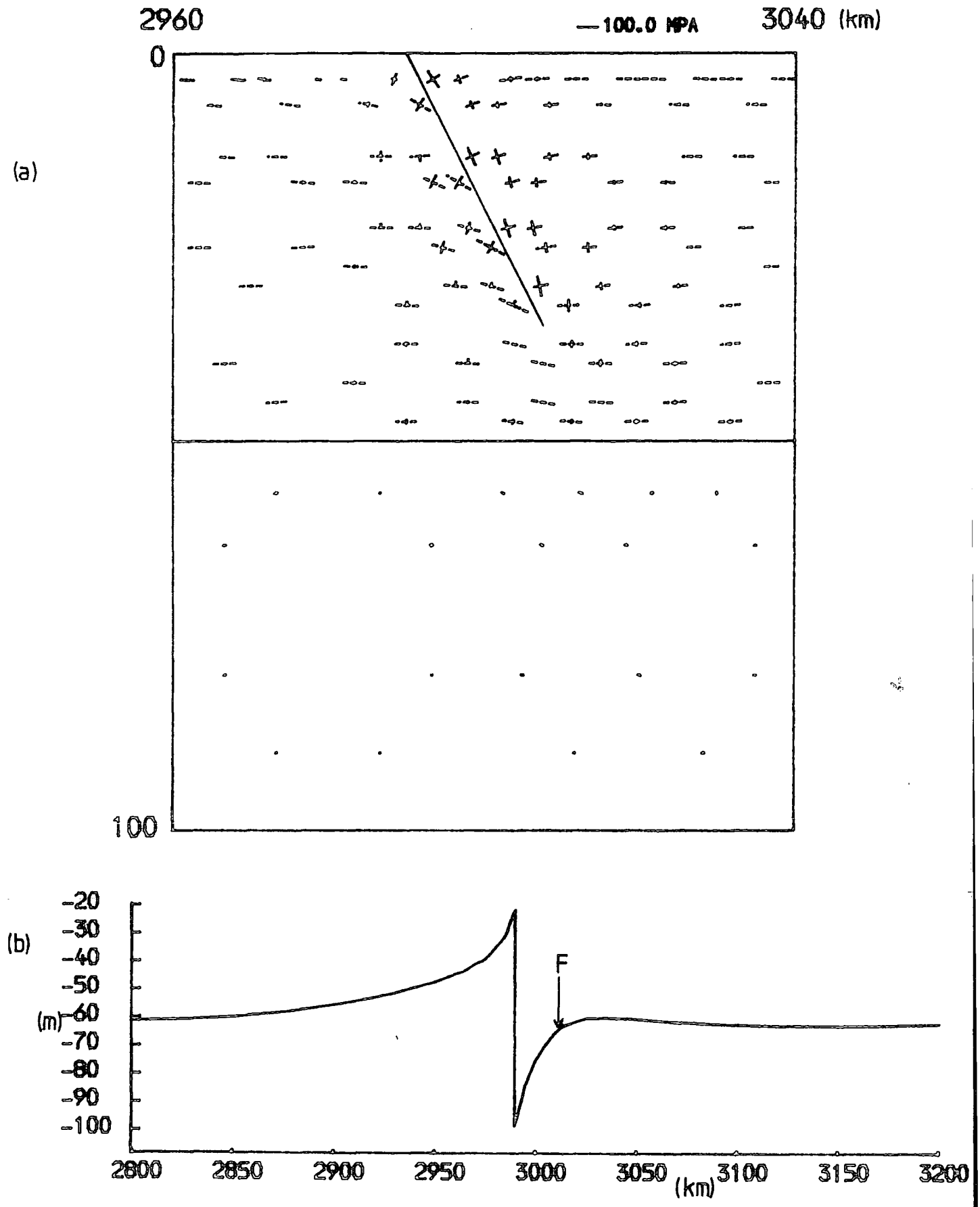

Fig. 7.6: Fault deformation after 500,000 yrs for a coefficient of friction of 0.1 and a Newtonian visco-elastic rheology
(a) Principal stresses around the fault
(b) Surface displacement profile
F position of weakest element

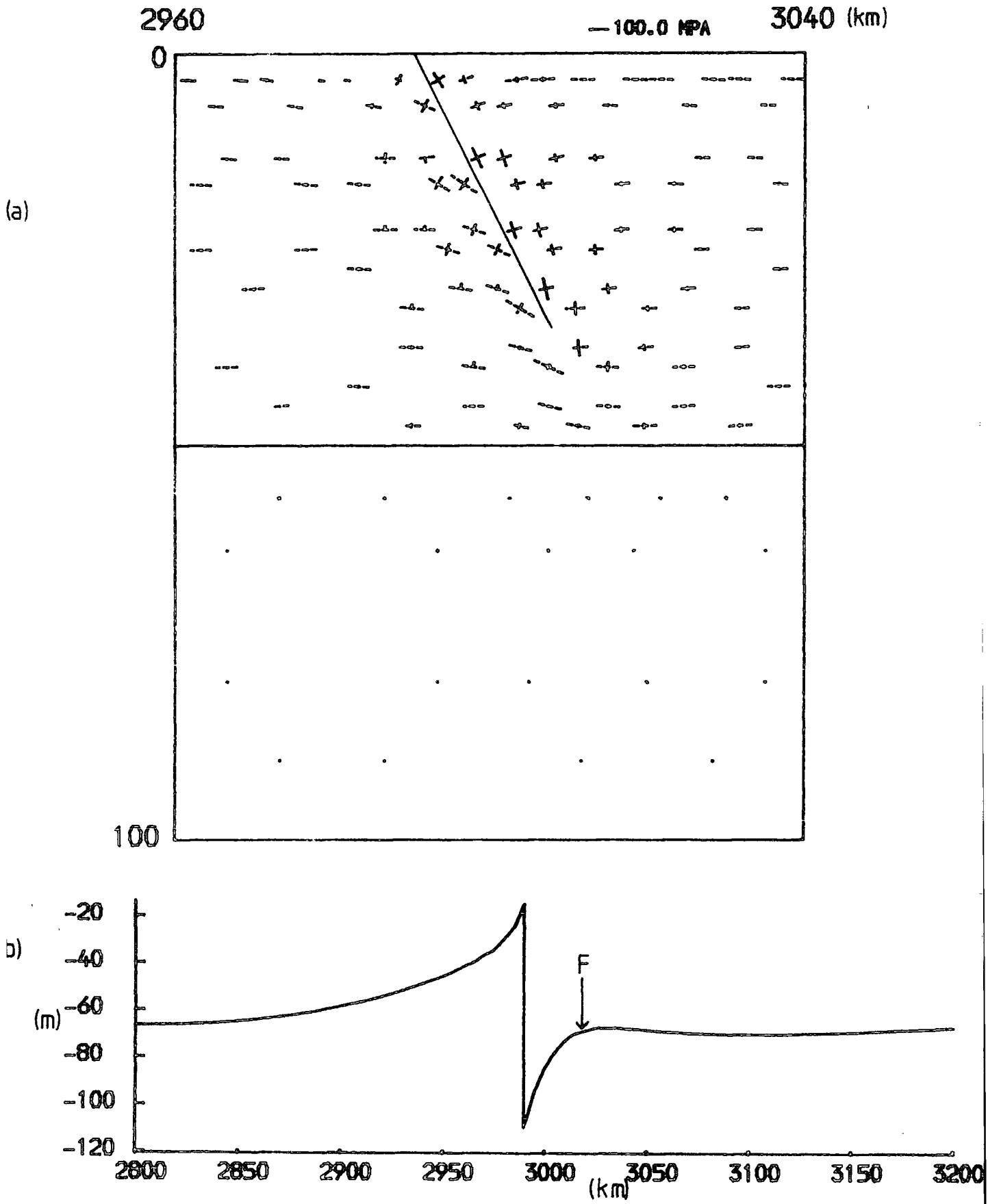

Fig. 7.7: Fault deformation after 1M yrs for a coefficient of friction of 0.1 and a Newtonian visco-elastic rheology
(a) Principal stresses around the fault
(b) Surface displacement profile
F position of weakest element

be regarded as the predicted graben width. The changes in the stresses around the fault and in the displacement profile can be seen in Figures 7.3 to 7.7. The extent of the fault on which slip has occurred is marked on the stress diagrams, and the position of the weakest element (ignoring possible secondary faulting) is marked on the displacement profiles. As was seen in the previous chapter, the principal stresses in the immediate vicinity of the fault are rotated so that their principal axes are approximately parallel and perpendicular to the fault. This is a consequence of the low frictional strength of the fault. Deviatoric compressive stresses exist on the downthrown side and deviatoric tensile stresses on the upthrown side. The increase in horizontal, near-surface, deviatoric tension on the downthrown side, and the decrease on the upthrown side, are apparent, particularly in Figures 7.6 and 7.7. This is a result of the bending, as described in Chapter 6. Stresses are developed beneath the base of the active part of the fault; compression on the downthrown side and tension on the upthrown side. These stresses, however, do not aid the propagation of the fault since they are aligned parallel to the fault. As was mentioned in the previous chapter, the orientation of these stresses may suggest listric faulting, although this is largely speculative since insufficient information is available about the concentrations of stress at the crack tip, and it is these that determine how the fault will propagate. It can be seen that, for this model, fault movement has only extended to a depth of 35 km. This is because the stresses in the elastic layer have not been large enough at lower depths to exceed the frictional strength, which increases with normal stress. Furthermore, it is apparent from Figure 7.7 that after 1M yrs the deviatoric stresses in the ductile material are very small (less than 2 MPa) and further amplification

of the stresses in the elastic layer will be insignificant. The maximum predicted graben width for this model is still only about 25 km.

In order to obtain fault movement down to greater depths, it is therefore necessary to do one of two things. Either the applied stresses on the edges of the model can be increased, or the frictional strength of the fault can be decreased by lowering the coefficient of friction. It is felt to be unlikely that stresses greater than 50 MPa are acting throughout the depth of the lithosphere. This leaves the second alternative. There is evidence that the frictional strength on the San Andreas fault may be extremely small. Brune et al. (1969) estimated a shear stress of no more than 20 MPa on the fault from a study of the heat flow anomaly. More recently Zoback and Roller (1979) have taken stress measurements, below the region of stress relief, at varying distances from the fault. Their results suggest that, even at depths of 15 to 20 km, the shear stresses on the fault reach only about 10 MPa. They suggest that high pore pressures may exist in the fault zone. To reduce the frictional strength on the fault to the very small value that they infer would require huge pore pressures. It is difficult to imagine pore pressures of this size. Another possible explanation for the low frictional strength may be in the mechanism of fault movement at depth. It may be that, at considerable depth, the nature of the fault is different from that nearer the surface. One possibility is that superplasticity controls the continuation of brittle fracture at depth. This idea has been discussed by Ball (1980). Superplastic flow may occur with very small resistance to shear (Ball, 1980) and consequently the apparent frictional strength would be very small and would presumably measure the resistance to grain-boundary sliding in the very fine grained material that would need to be present. Whatever the mechanism of fault movement at depth, it seems

likely that the effective frictional strength may be very small. The effect of this will now be investigated by decreasing the coefficient of friction.

7.4 Effect of reducing the frictional strength

The same model has been re-run, but with a coefficient of friction of 0.05. The results are shown in Table 7.3 and Figures 7.8 to 7.13. The same stress pattern is seen as before, but now the fault propagates to greater depth because of the reduction in the frictional strength. After 300,000 yrs fault movement has propagated to its maximum depth of 50 km. The increase in depth of fault movement is a result of the relaxation of the deviatoric stresses in the visco-elastic material, and consequent stress amplification in the elastic layer, and is well shown in Figures 7.8 to 7.13. The throw of the fault is greater than in the earlier model and after 1M yrs the throw is 236 m. The increased depth and throw of the fault has resulted in an increase in the predicted graben width to 30 km.

Although faulting has, in this case, reached a depth of 50 km it appears that the frictional strength on the lowest fault section has only just been exceeded. In Figure 7.12 it is apparent that relatively small stresses have developed in the visco-elastic material immediately beneath the fault, although the whole fault has moved. This suggests that the forces resulting from the shear stresses on the lowest fault section are small.

In order to determine whether there is any significant change in the deformation pattern when larger shear stresses act on the fault, the coefficient of friction has been reduced further to 0.01. The results, again using a Newtonian visco-elastic rheology with a viscosity of 10^{23} Pa s, are shown in Table 7.4 and Figures 7.14 to 7.17. The frictional strength

Time ($\times 10^3$ yrs)	Depth of fault movement (km)	Throw of fault (m)	Distance of weakest element from fault (km)
0	20.0	18	15 - 20
50	27.5	34	20
100	35.0	49	25 - 30
200	42.5	78	30
300	50.0	104	30
400	50.0	129	30
500	50.0	151	30
700	50.0	189	30
1000	50.0	236	30

Table 7.3: Fault deformation with time for an applied stress of 50 MPa, a coefficient of friction of 0.05, and a Newtonian visco-elastic rheology for the ductile material

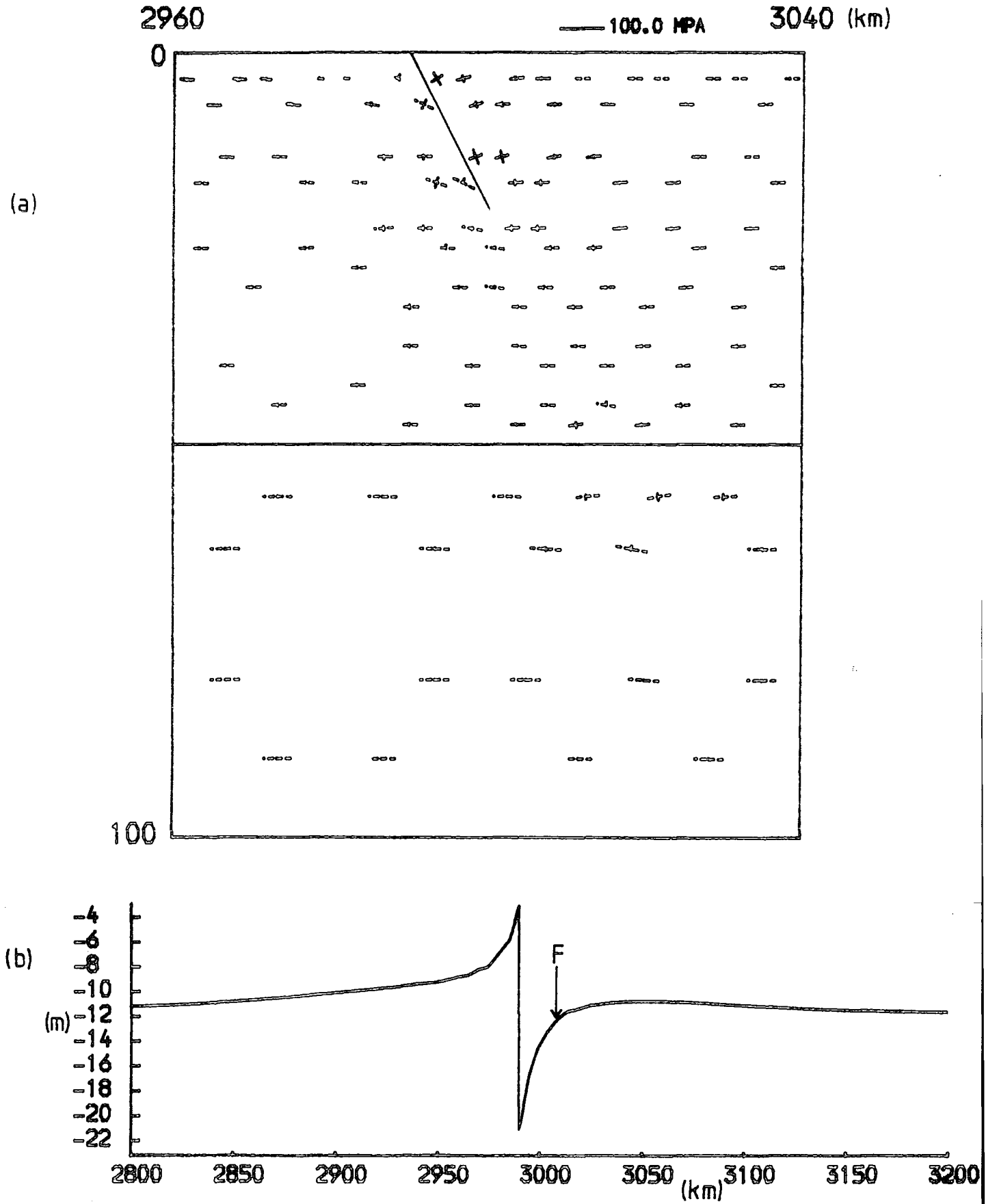

Fig. 7.8: Immediate fault deformation for an applied stress of 50 MPa and a coefficient of friction of 0.05
(a) Principal stresses around the fault
(b) Surface displacement profile
F position of weakest element

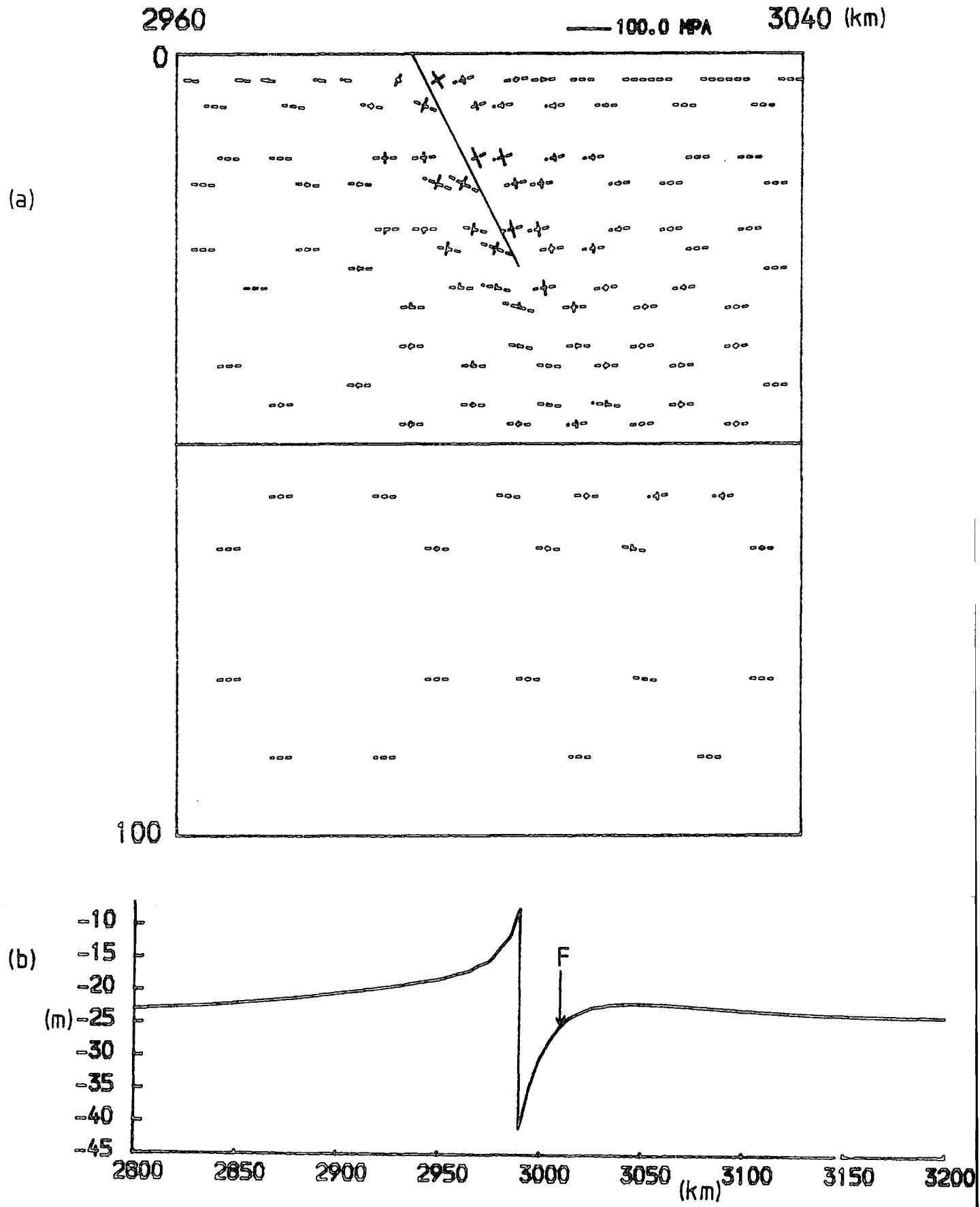

Fig. 7.9: Fault deformation after 50,000 yrs for a coefficient of friction of 0.05 and a Newtonian visco-elastic rheology
(a) Principal stresses around the fault
(b) Surface displacement profile
F position of weakest element

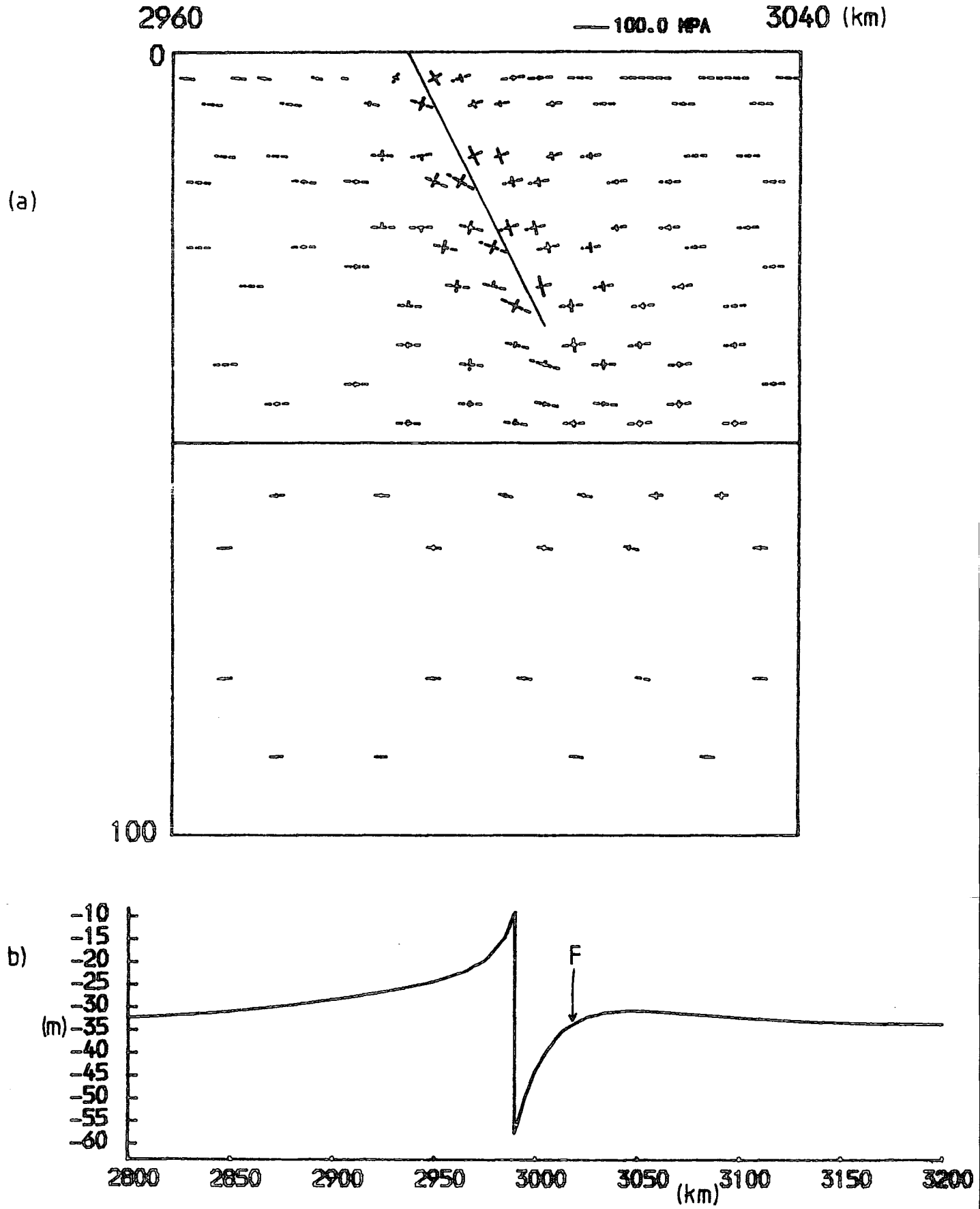

Fig. 7.10: Fault deformation after 100,000 yrs for a coefficient of friction of 0.05 and a Newtonian visco-elastic rheology
(a) Principal stresses around the fault
(b) Surface displacement profile
F position of weakest element

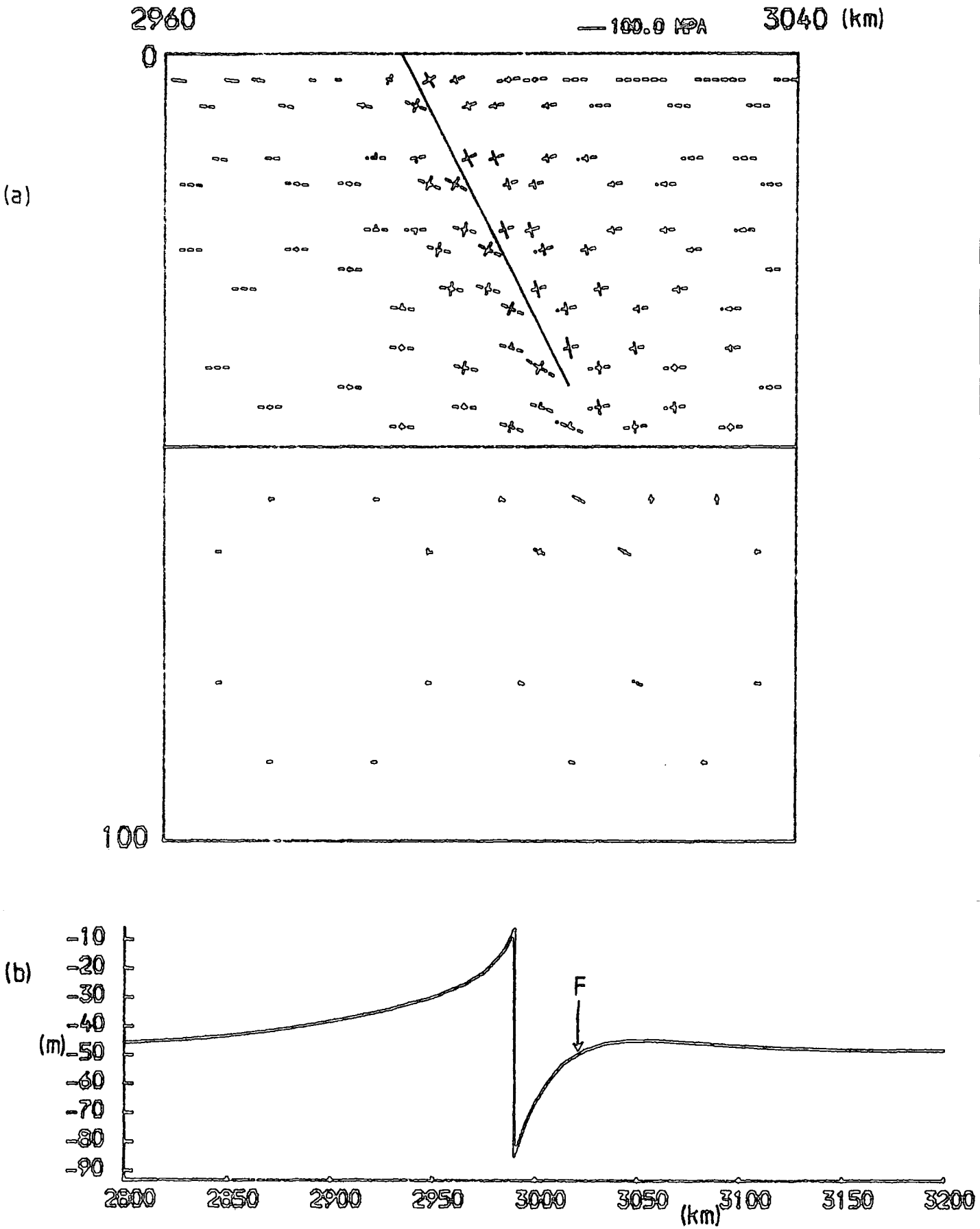

Fig. 7.11: Fault deformation after 200,000 yrs for a coefficient of friction of 0.05 and a Newtonian visco-elastic rheology
(a) Principal stresses around the fault
(b) Surface displacement profile
F position of weakest element

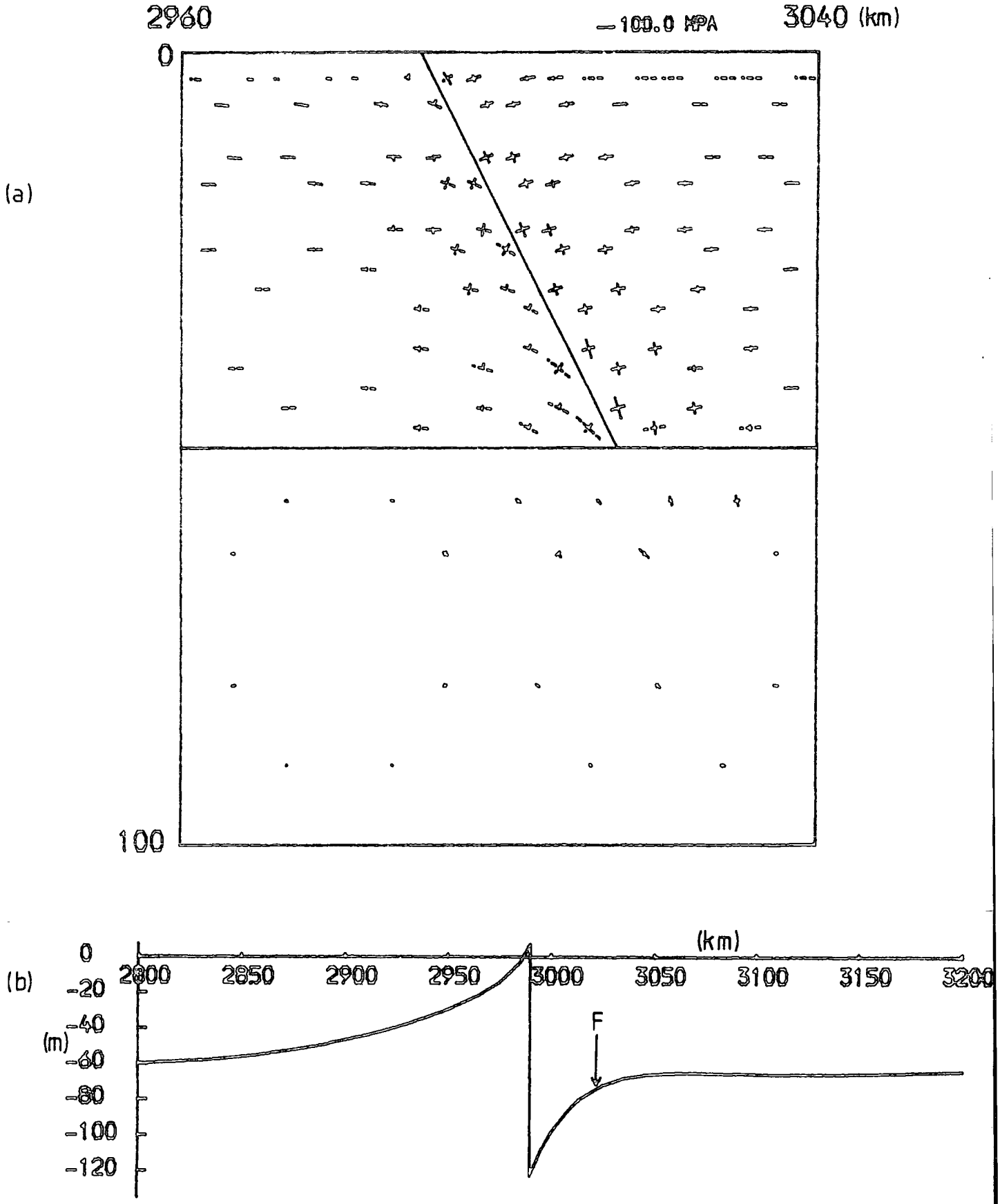

Fig. 7.12: Fault deformation after 400,000 yrs for a coefficient of friction of 0.05 and a Newtonian visco-elastic rheology
(a) Principal stresses around the fault
(b) Surface displacement profile
F position of weakest element

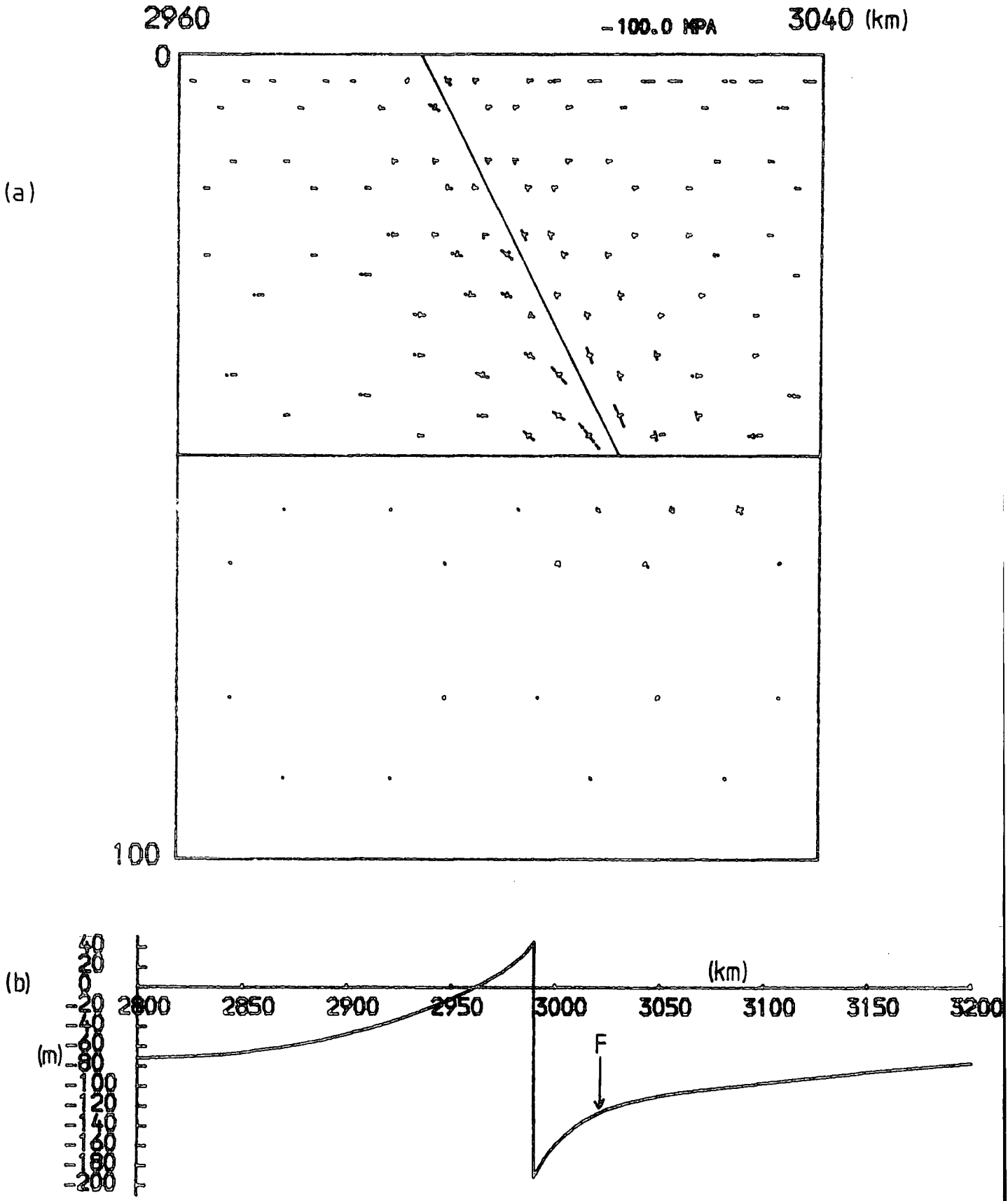

Fig. 7.13: Fault deformation after 1M yrs for a coefficient of friction of 0.05 and a Newtonian visco-elastic rheology
(a) Principal stresses around the fault
(b) Surface displacement profile
F position of weakest element

has been exceeded immediately on all sections of the fault, as can be seen from Figure 7.14. As the visco-elastic material relaxes and increases the deviatoric tension in the elastic layer, the fault throw increases until after 1M yrs the throw is 408 m. Because of this greater fault movement, larger stresses are generated in the underlying material. The deviatoric components of these stresses relax with time and cause stress amplification in the elastic layer, particularly in those stresses adjacent to the fault at the base of the elastic layer. These stresses become large, as can be seen in Figure 7.17, and attain values of several hundred MPa.

The predicted graben widths for these models, based on the distance from the original fault of the element closest to failure, shows a significant change from that of the previous models. As the time is increased the predicted width decreases. This is the opposite to the situation for the earlier models. For times up to 50,000 yrs the predicted graben width is between 40 and 45 km. As the model is run through time, the width decreases to between 30 and 35 km after 1M yrs. This is probably because of the low frictional strength of the fault. Fault movement occurs throughout the whole depth of the fault immediately, giving the sharp displacement profile seen in Figure 7.14. Now, as the visco-elastic material relaxes, the deviatoric stresses beneath the fault relax and cause a general 'smoothing-out' of the profile. This effect is well seen in the displacement diagrams of Figures 7.14 to 7.17. As the profile is smoothed out, so the element which is most affected by the bending (which is the weakest element) migrates slowly back towards the original fault. Clearly, if failure occurs fairly soon after the development of the first fault, then a graben of width 40 to 45 km will be formed.

So far in this chapter, the models have assumed a Newtonian visco-

Time (x 10^3 yrs)	Depth of fault movement (km)	Throw of fault (m)	Distance of weakest element from fault (km)
0	50	40	40 - 45
50	50	72	40 - 45
100	50	100	40
200	50	149	40
300	50	191	35 - 40
400	50	230	35
500	50	265	35
700	50	328	30 - 35
1000	50	408	30 - 35

Table 7.4: Fault deformation with time for an applied stress of 50 MPa, a coefficient of friction of 0.01, and a Newtonian visco-elastic rheology.

Time (x 10^3yrs)	Depth of fault movement (km)	Throw of fault (m)	Distance of weakest element from fault (km)
0	50	40	40 - 45
5	50	68	40 - 45
10	50	91	40
20	50	131	35 - 40
30	50	165	35
50	50	211	35
100	50	343	30 - 35

Table 7.5: Fault deformation with time for an applied stress of 50 MPa, a coefficient of friction of 0.01, and a power law creep rheology.

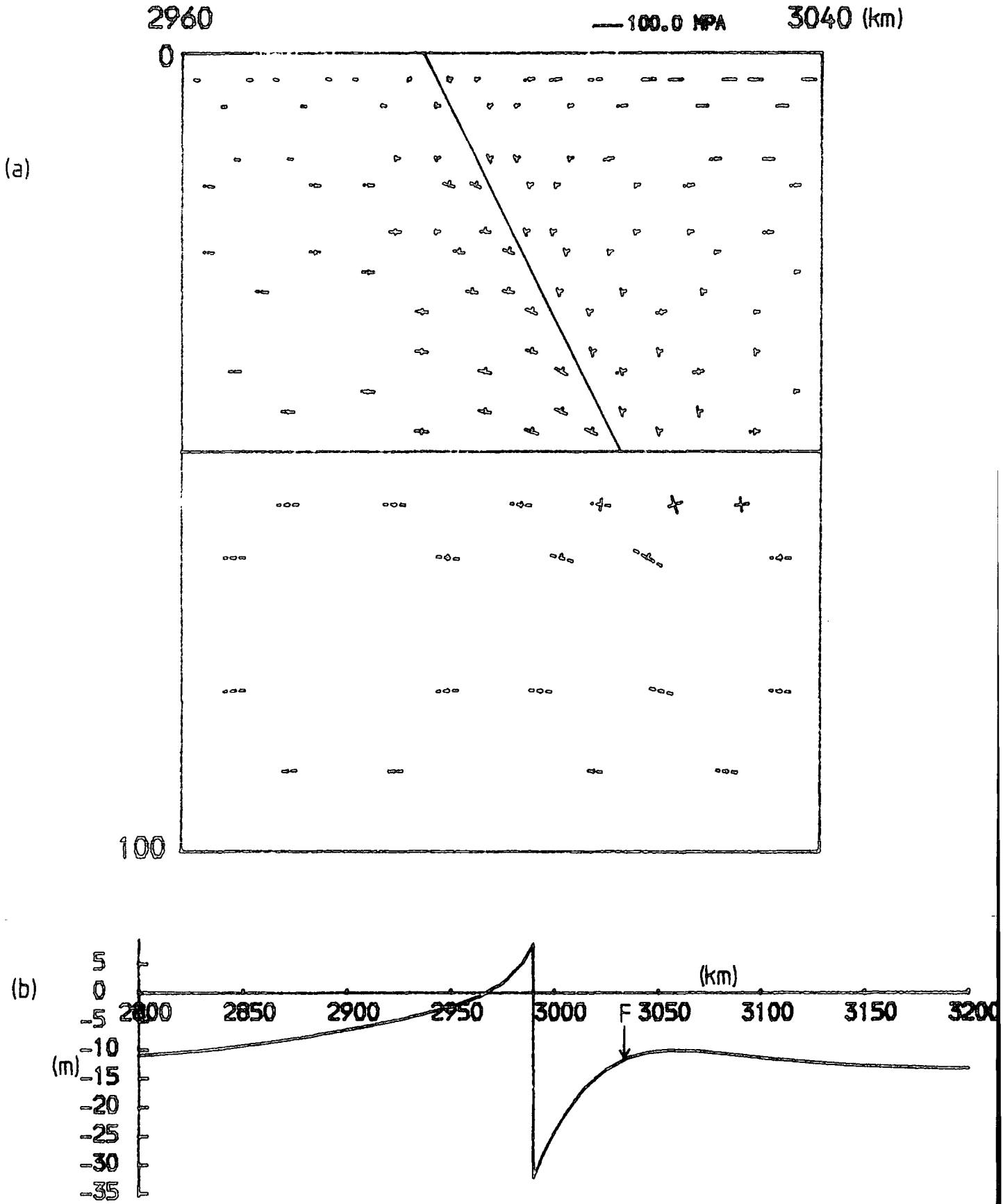

Fig. 7.14: Immediate fault deformation for an applied stress of 50 MPa and a coefficient of friction of 0.01
(a) Principal stresses around the fault
(b) Surface displacement profile
F position of weakest element

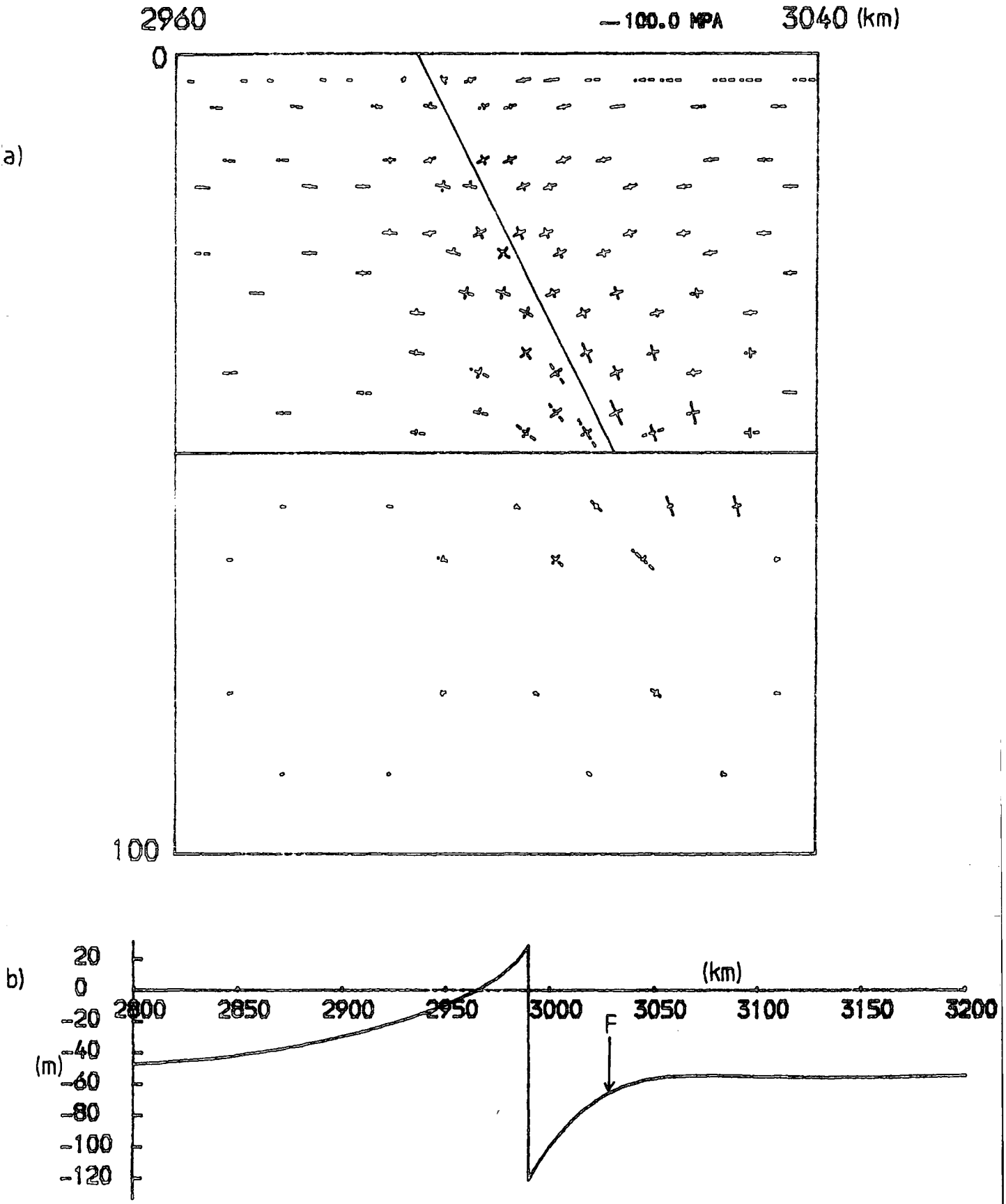

Fig. 7.15: Fault deformation after 200,000 yrs for a coefficient of friction of 0.01 and a Newtonian visco-elastic rheology
(a) Principal stresses around the fault
(b) Surface displacement profile
F position of weakest element

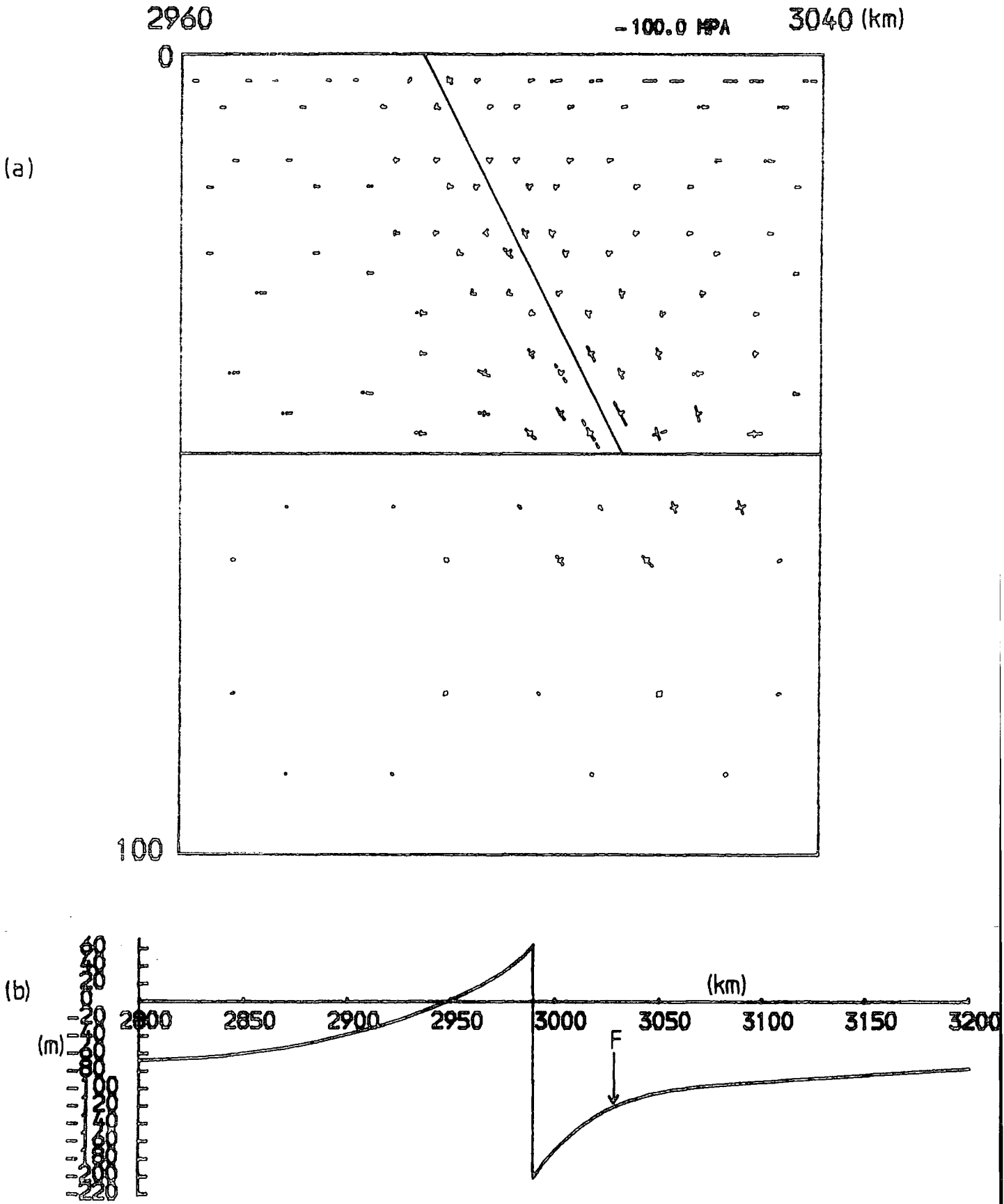

Fig. 7.16: Fault deformation after 500,000 yrs for a coefficient of friction of 0.01 and a Newtonian visco-elastic rheology
(a) Principal stresses around the fault
(b) Surface displacement profile
F position of weakest element

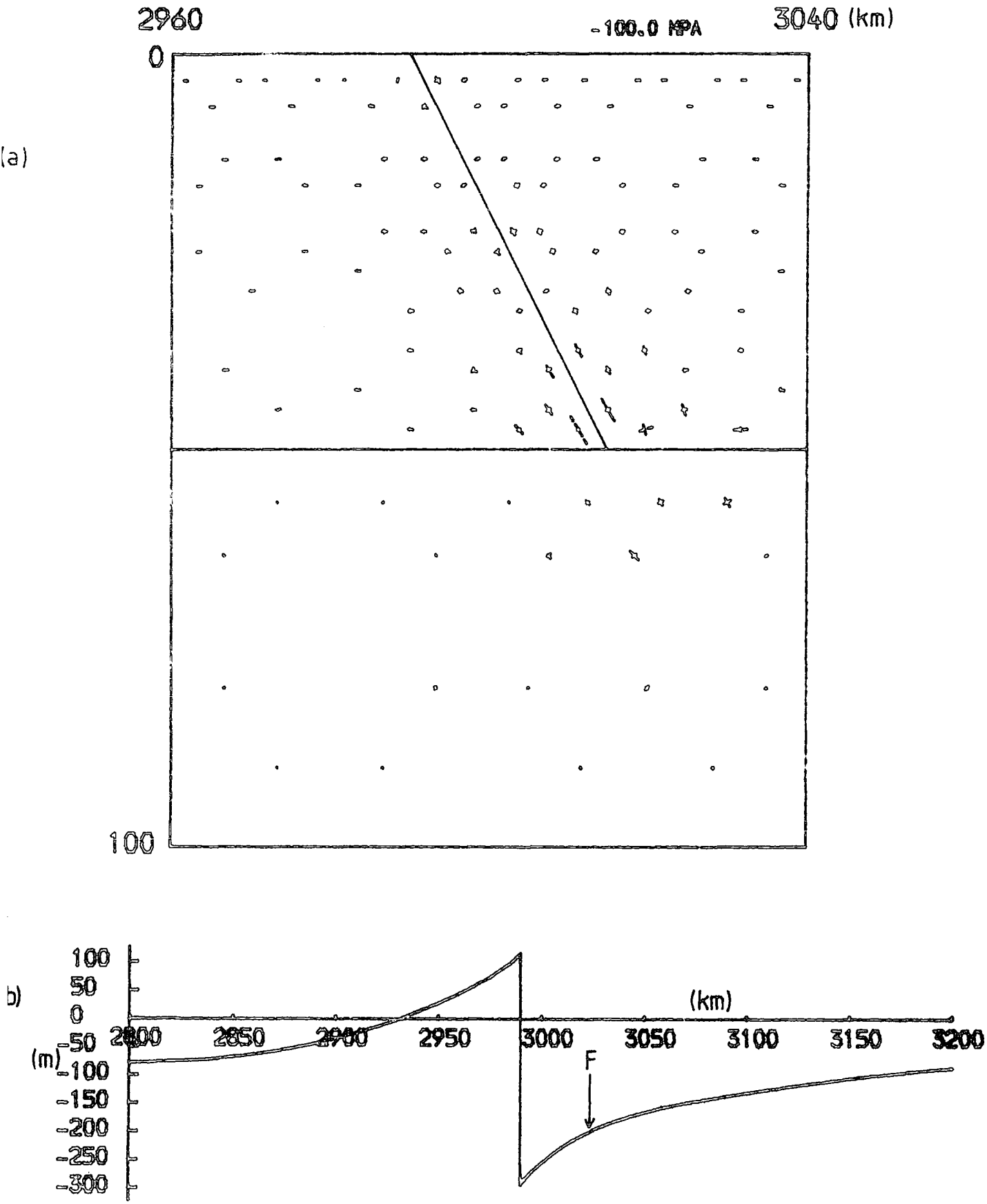

Fig. 7.17: Fault deformation after 1M yrs for a coefficient of friction of 0.01 and a Newtonian visco-elastic rheology
(a) Principal stresses around the fault
(b) Surface displacement profile
F position of weakest element

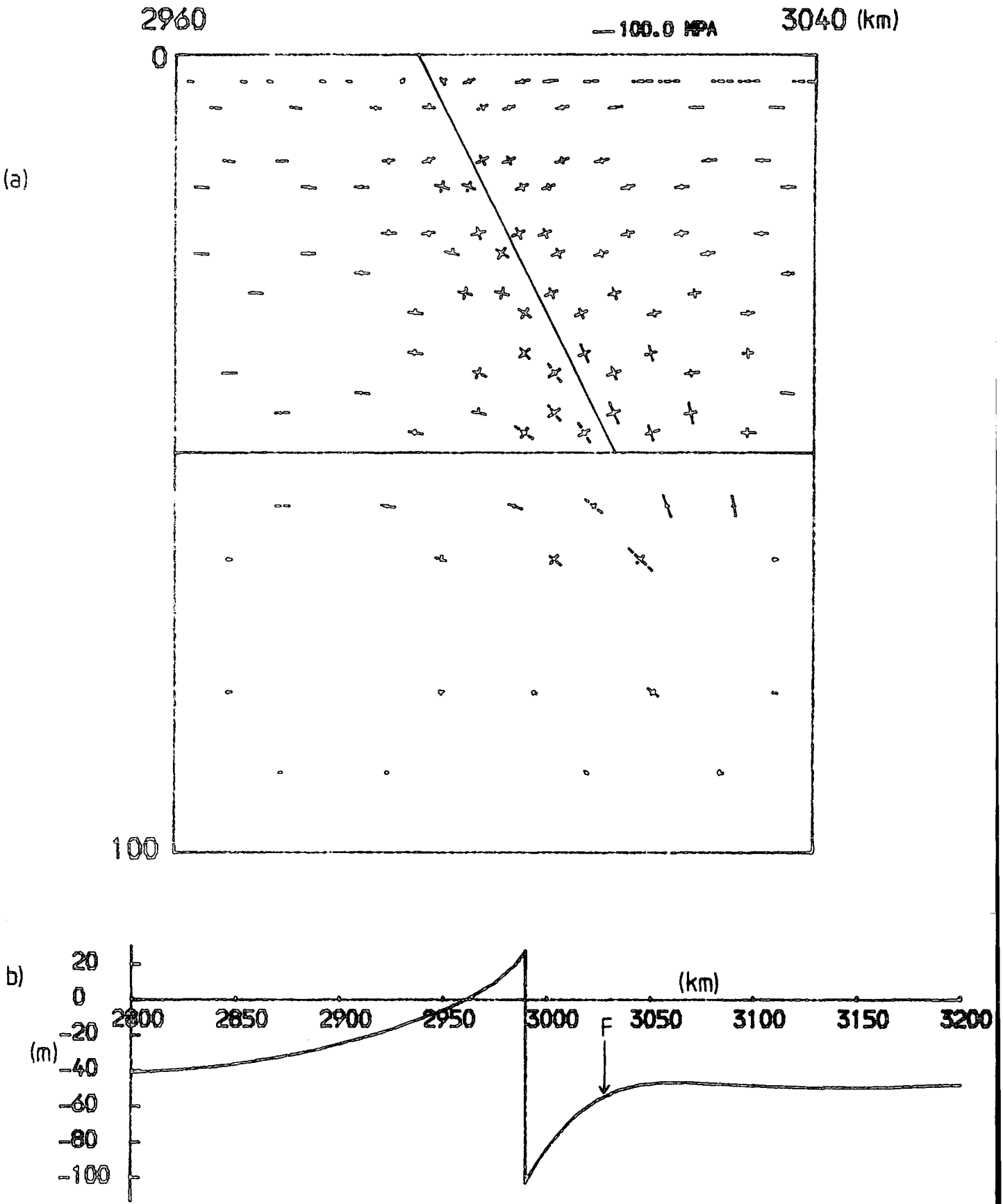

Fig. 7.18: Fault deformation after 20,000 yrs for a coefficient of friction of 0.01 and a power law creep rheology
(a) Principal stresses around the fault
(b) Surface displacement profile
F position of weakest element

elastic rheology for the lower lithosphere. It would be expected, from the results of earlier chapters, that a power law creep rheology would not significantly change the deformation pattern. To verify this, the last set of models, with a coefficient of friction of 0.01, have been re-run using a power law creep rheology for the ductile layer. The creep equation used was that for the lithospheric mantle, given in Chapter 2. The results are shown in Table 7.5. Once again, the only significant difference between these and the earlier results is in the times necessary to bring about a particular amount of deformation. It can be seen by comparing Table 7.5 with Table 7.4 that similar displacements require about one-tenth of the time for a power law creep rheology. This suggests that for the creep values used here, the state of stress in the lower lithosphere in these models results in an effective viscosity closer to 10^{22} Pa s than the value of 10^{23} Pa s used in the Newtonian visco-elastic rheology. Figure 7.18 shows the deformation using the power law creep rheology after 20,000 yrs. Comparing this with Figure 7.15 shows that the basic stress pattern and displacement profile are relatively unaffected by assuming a different rheology for the ductile layer.

7.5 Conclusions

The predicted graben width has been found to increase slightly with the depth of faulting, although this would not seem to be the only factor. The graben width from the first model used, with a coefficient of friction of 0.1 (Table 7.2), was the same as that of the last chapter. This was despite the fact that faulting extended to 35 km rather than 20 km. This may be because the throw of the fault was similar in both cases, up to about 100 m. If this is true, it would suggest that not only is the displacement profile dependent on the depth of faulting, but it is also

dependent on the throw of the fault. This conclusion has been supported, to some extent, by the results for the later models with lower coefficients of friction. Although faulting extended to 50 km in both cases (Tables 7.3 and 7.4), the predicted graben width was greater for the situation with lower frictional strength. The throw of the fault was also considerably greater in this case.

If the effective coefficient of friction is very low, it has been shown that a graben of width 40 to 45 km can be formed, providing that the second fault develops fairly soon after the first fault. Whether the coefficient of friction can be that small so soon after the fault has formed is debatable. It may be, however, that the laboratory experiments on frictional sliding discussed in Chapter 2 are not applicable to the mechanism of fault movement at any but shallow depths. It also seems somewhat unlikely that the brittle layer of the lithosphere can extend to a depth of 50 km in the typically warm regions of the lithosphere where major graben form.

CHAPTER 8

SUBSIDENCE OF A GRABEN WEDGE

8.1 Introduction

In the previous chapters of this thesis the formation of a typical graben wedge bounded by normal faults was investigated. It was found that if the second normal fault is dependent on the deformation caused by the first fault, then the development of wide graben of about 50 km is difficult to explain unless very weak faults extending to great depths are present, and these seem unlikely in the warm regions where wide graben generally form. A fuller discussion of these problems is reserved for the final chapter. Nevertheless, wide graben do exist, and in this chapter the subsidence of a 50 km wide graben wedge bounded by normal faults extending to 20 km depth will be investigated.

8.2 Finite element model

In this chapter the model of the continental lithosphere arrived at in Chapter 2 (Table 2.1, Figure 2.1) is used. The rheological division is a 20 km elastic layer overlying 80 km of visco-elastic material. The model is of a 4,000 km long section of the lithosphere with a 50 km wide graben at the centre. This model is symmetrical and, consequently, only one half of the model needs to be considered. The finite element grid is shown in Figures 8.1 and 8.2. The right-hand edge of the grid is constrained to have zero horizontal displacement, thus satisfying the symmetrical properties of the model. The model is considered to be underlain by a fluid of density 3,300 kg m^{-3} and the isostatic compensation routine described in Chapter 3 is used for the base. A fault which dips at 63.43°

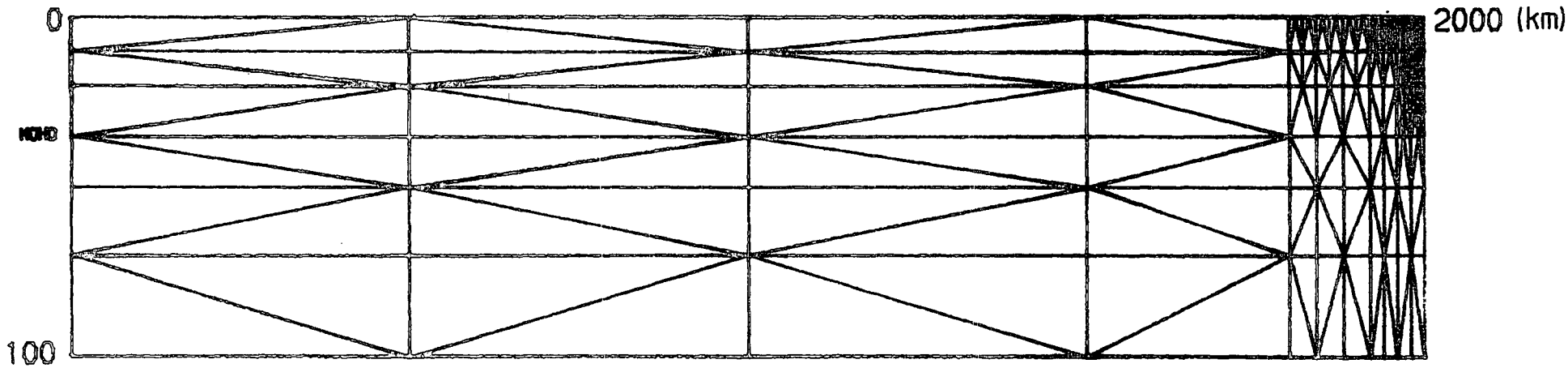

Fig. 8.1: Finite element grid for the model of a graben. Right-hand edge is an axis of symmetry.

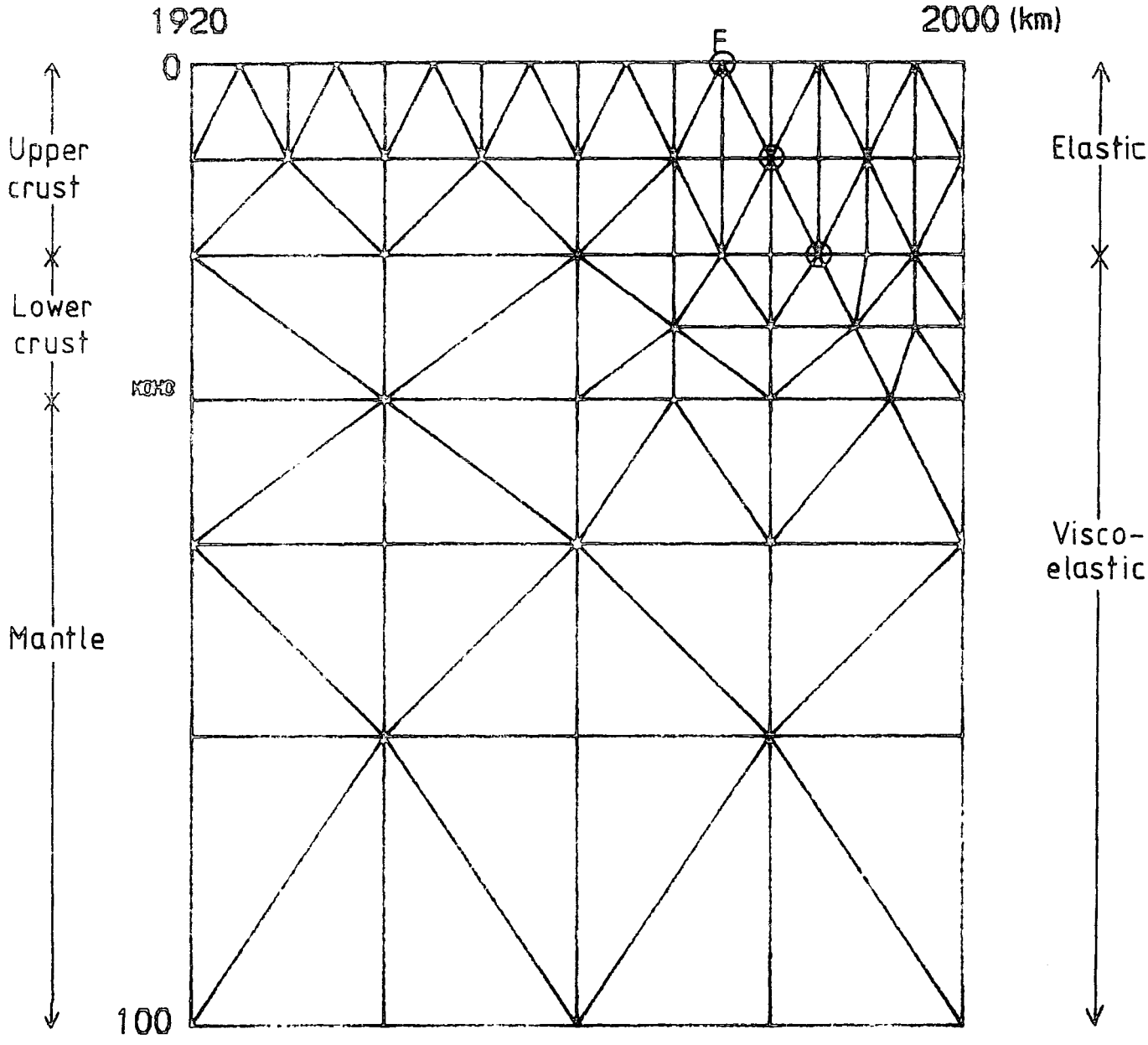

Fig. 8.2: Central section of finite element grid for the model of a graben. Right-hand edge is an axis of symmetry.

F position of fault

⊙ position of dual node

and extends to a depth of 20 km is present at 25 km from the right-hand end of the grid (thus giving a 50 km wide graben). The normal and shear stiffnesses of the fault are again taken to be 10^{15} and 5×10^{10} Nm^{-1}, respectively, and a pore pressure equal to the overburden pressure of water is assumed to exist on the fault. A tensile stress is applied to the left-hand edge of the model and the visco-elastic material allowed to relax with time.

8.3 Wedge subsidence

A tensile stress of 20 MPa was applied to the edge of the model. This is the same value that was used in Chapters 4 and 6, where the development and later deformation of normal faulting was investigated. A value of 0.1 was used for the coefficient of friction on the fault. This also is in line with the earlier work in this thesis and is representative of a fault containing a wet clay gouge (Wang and Mao, 1979). A Newtonian visco-elastic rheology was used for the lower crust and lithospheric mantle, with a viscosity of 10^{23} Pa s.

The results for this model are illustrated in Figures 8.3 to 8.7. These figures show the principal stresses around one half of the graben (not including the lithostatic stresses), and the surface displacements. For the stress plots, the scale is given in terms of both 100 MPa and the largest stress. This is useful in later diagrams where the stresses become very large. Once again dashed lines represent tensile stresses and full lines represent compressive stresses. Figure 8.3 shows the deformation for an instantaneous elastic solution. The stresses in the elastic layer are only about 11 MPa and are not sufficiently large to cause frictional sliding on the fault. The surface displacements across the fault are only 0.8 m and are due to elastic deformation of the fault resulting from its shear stiffness. The deformation pattern after 200,000 yrs is shown

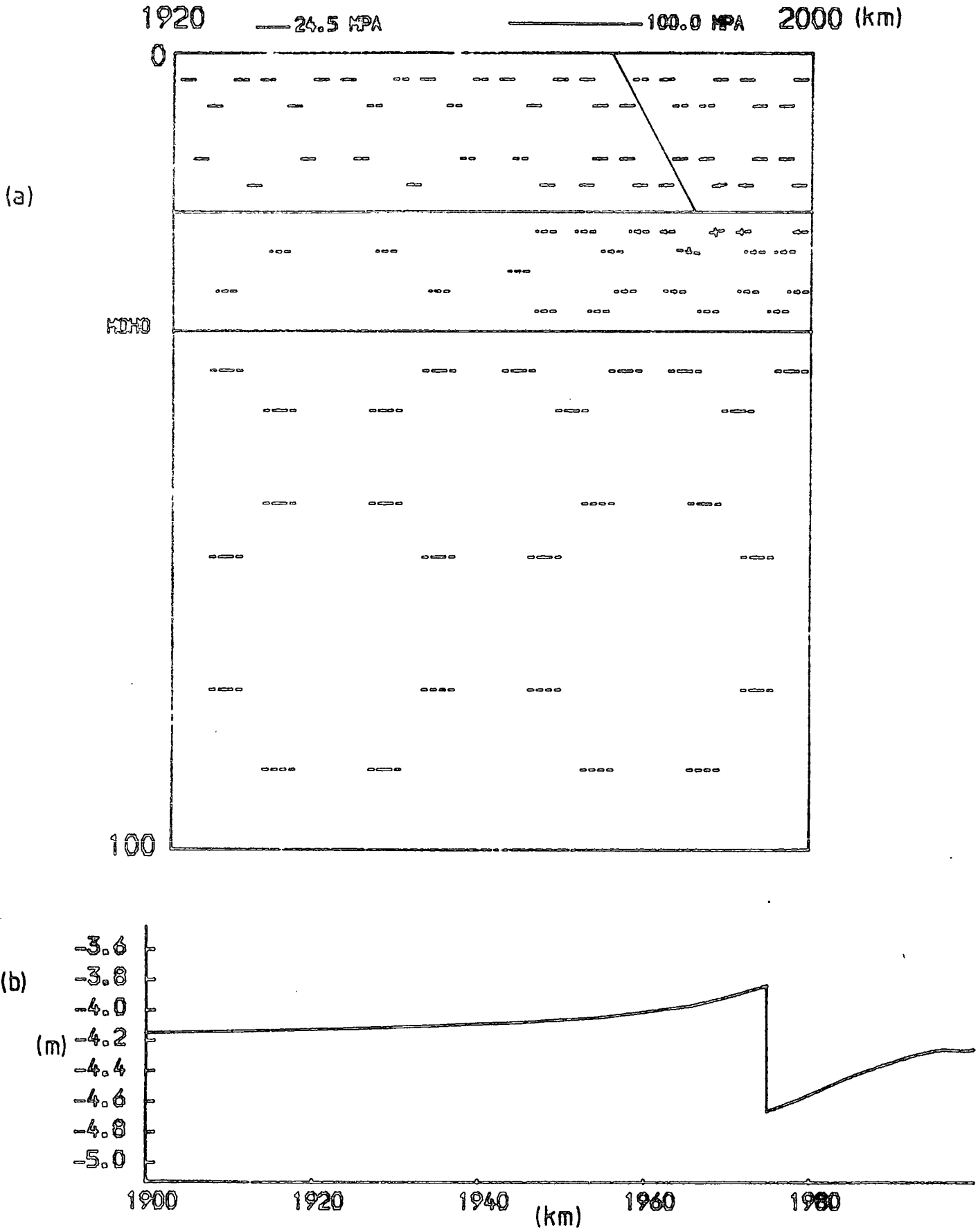

Fig. 8.3: Immediate deformation for an applied stress of 20 MPa and a coefficient of friction of 0.1
(a) Principal stresses around one half of the graben
(b) Surface displacement profile

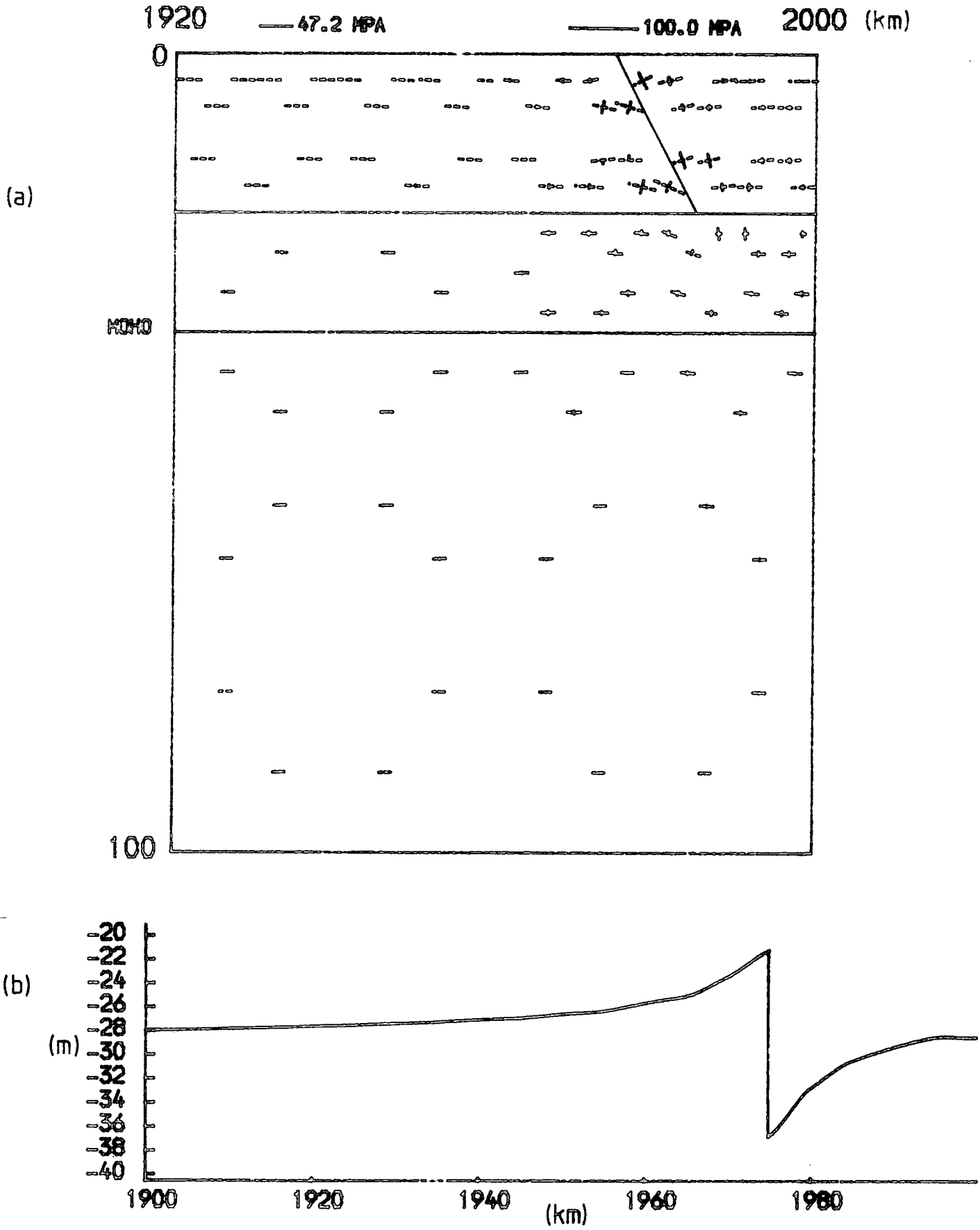

Fig. 8.4: Deformation after 200,000 yrs for an applied stress of 20 MPa and a coefficient of friction of 0.1
(a) Principal stresses around one half of the graben
(b) Surface displacement profile

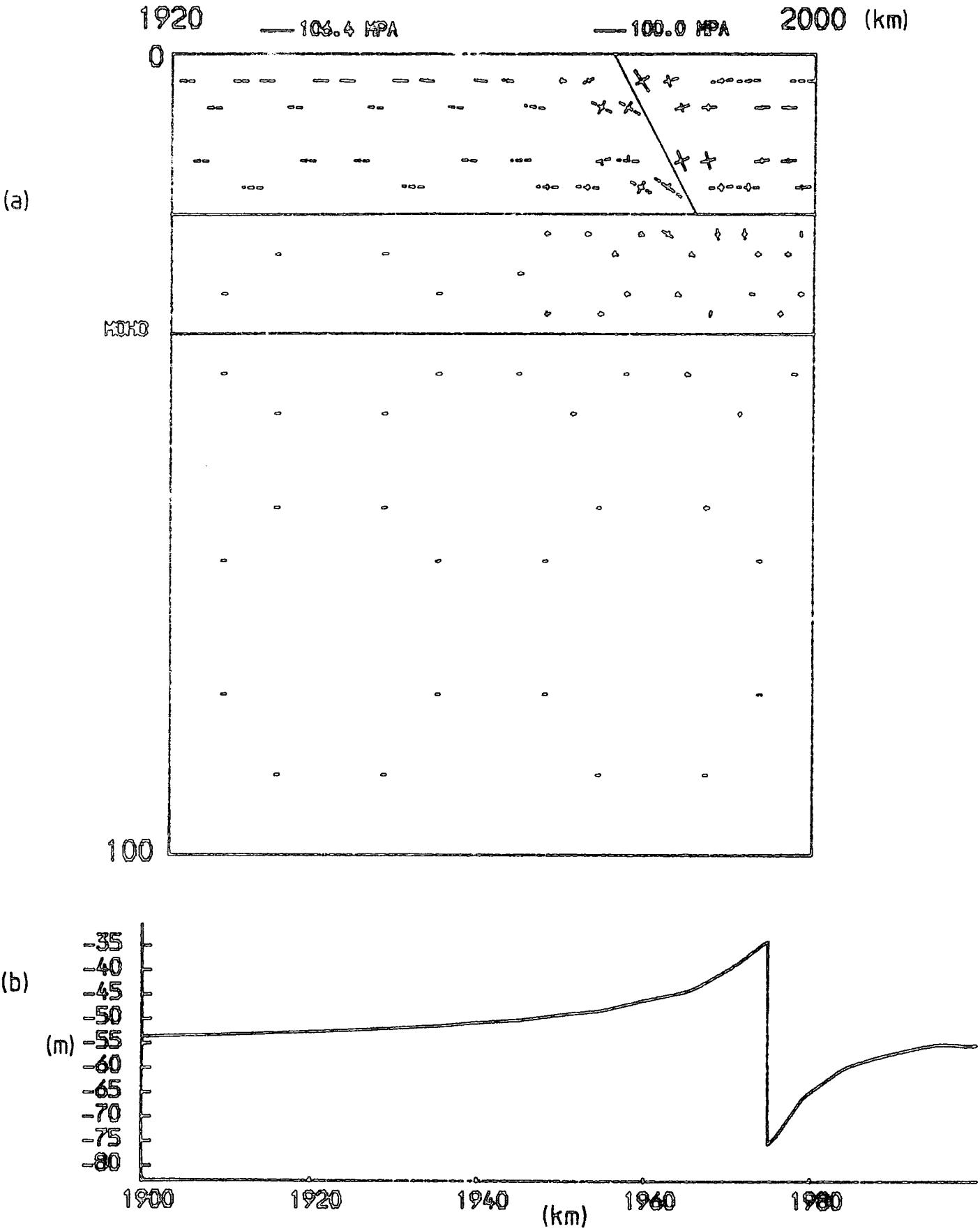

Fig. 8.5: Deformation after 500,000 yrs for an applied stress of 20 MPa and a coefficient of friction of 0.1
(a) Principal stresses around one half of the graben
(b) Surface displacement profile

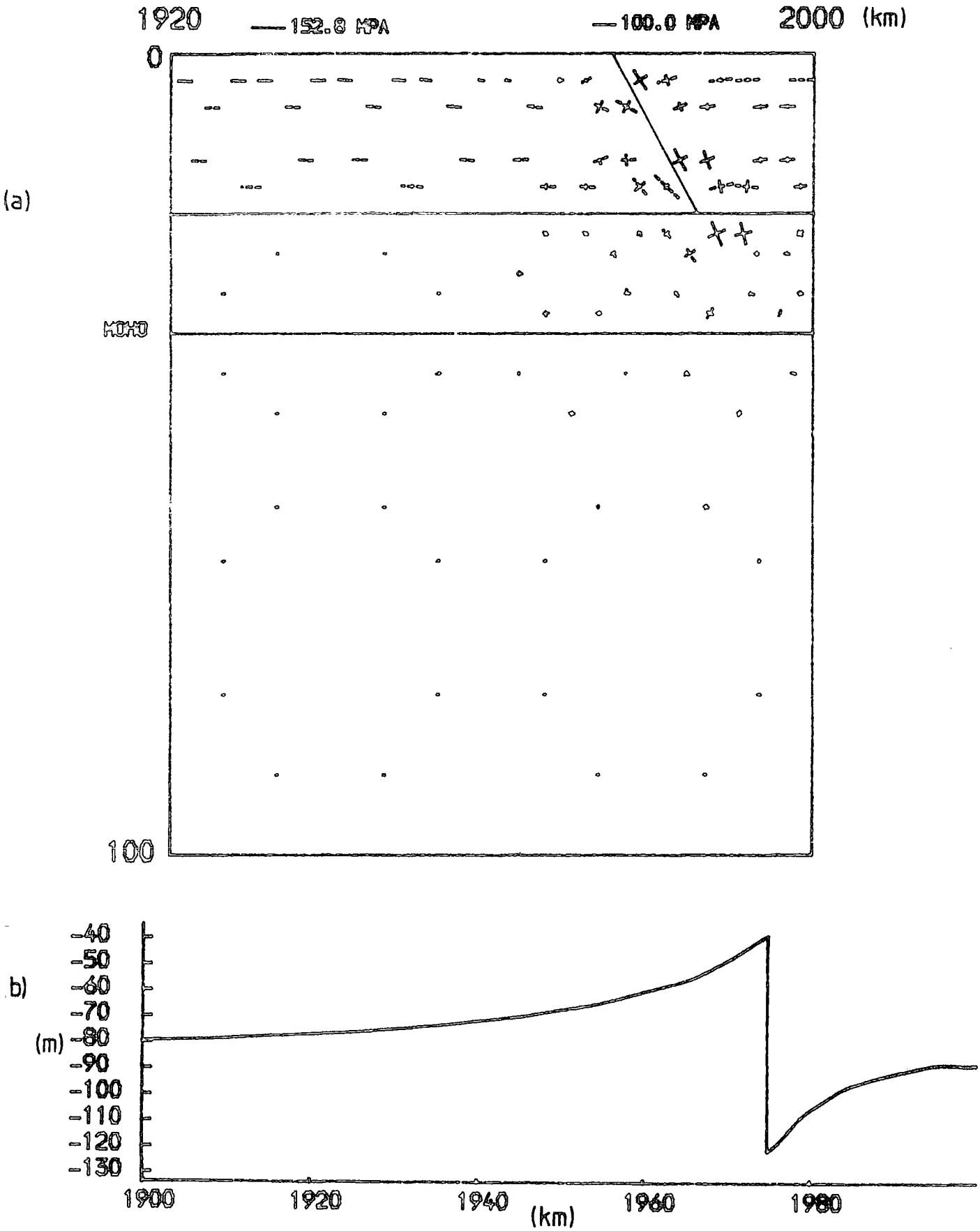

Fig. 8.6: Deformation after 1M yrs for an applied stress of 20 MPa and a coefficient of friction of 0.1
(a) Principal stresses around one half of the graben
(b) Surface displacement profile

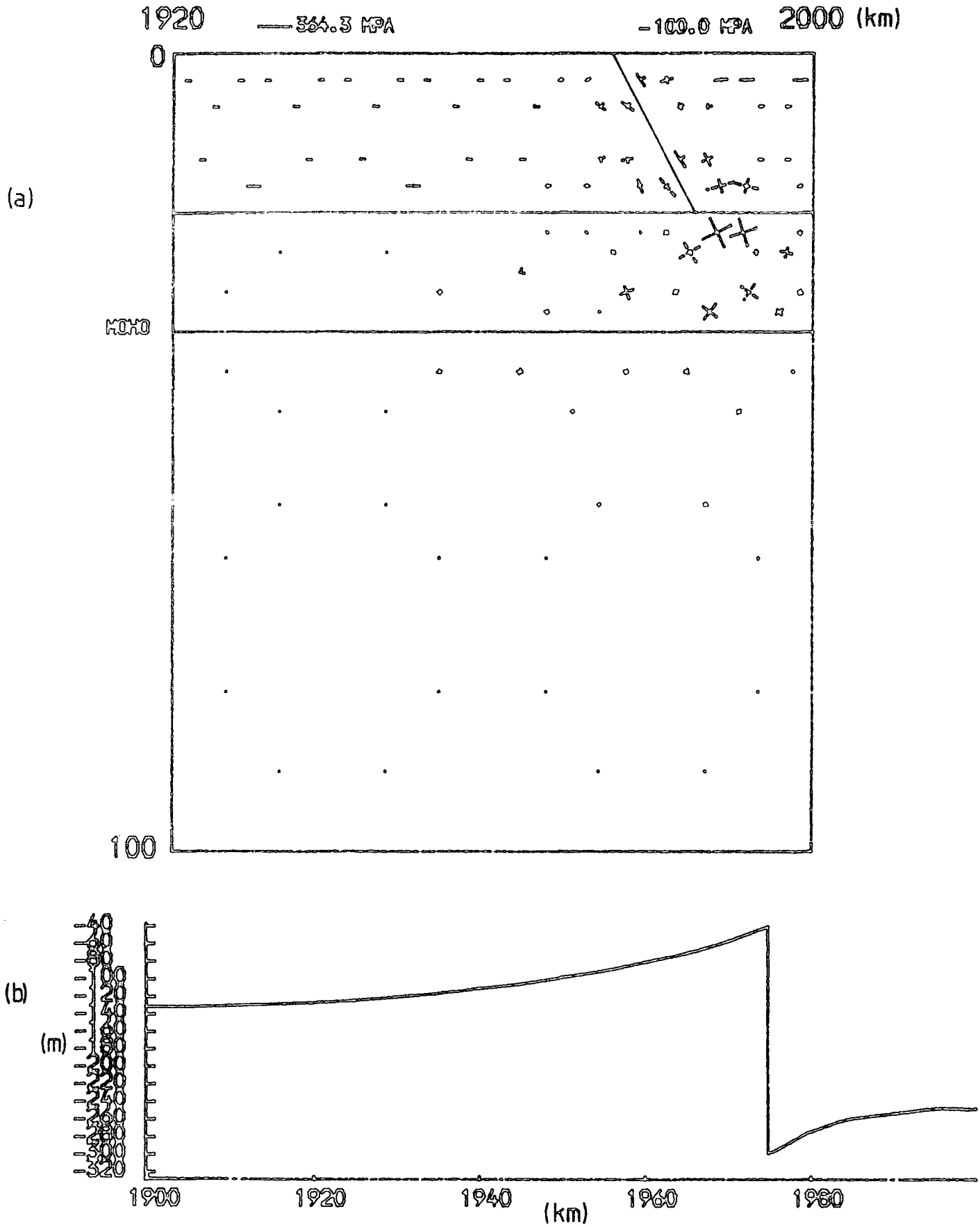

Fig. 8.7: Deformation after 5M yrs for an applied stress of 20 MPa and a coefficient of friction of 0.1
(a) Principal stresses around one half of the graben
(b) Surface displacement profile

in Figure 8.4. The amplification of the stresses in the elastic layer as a result of creep in the underlying visco-elastic material has resulted in the frictional strength being exceeded on the upper part of the fault, and the throw of the fault is now about 15 m.

The situation after 500,000 yrs is shown in Figure 8.5. The rim uplift which is characteristic of most graben (e.g. Illies, 1970) is apparent and is a result of the fault movement, which now extends throughout the depth of the fault and results in a throw of 40 m. The stresses in the visco-elastic material have relaxed to a large extent except beneath the wedge, where compression is produced as a result of subsidence of the wedge into the ductile material of the lower crust. It is very interesting that the wedge does not subside uniformly. This is because the subsidence is caused by frictional sliding on the faults, and it is the edges of the wedge that subside more than the centre. This causes bending and deformation within the wedge itself. The bending amplifies the deviatoric tensions in the uppermost part of the wedge and the elements there are much closer to failure than any others in the model. Failure adjacent to the fault is likely to result in secondary faulting, as discussed in Chapter 6. All the elements across the wedge are weak, however, so that faulting is also likely to occur further into the wedge. This may be the cause of the typical, heavy faulting, with antithetic fault blocks, seen in many graben (e.g. Illies, 1970). This prediction of faulting within the wedge is very interesting and contradicts the conclusions of Artemjev and Artyushkov (1971) that no large stresses or surface relief can exist in a wedge-shaped block after its formation. Their argument supposes that the block sinks uniformly. However, the subsidence of the block will be controlled by frictional sliding along its boundary faults. For a wide block, this will cause the type of

bending seen here. For narrower graben, it seems likely that the amount of bending will be less, because the boundary faults are closer together, and will probably result in less faulting within the wedge and , possibly, relatively undeformed graben blocks.

Figure 8.6 shows the deformation pattern after 1M yrs. The compressive stresses beneath the downthrown block have increased in magnitude as a result of the increased throw of the fault, which is now about 85 m, and these are the only large stresses remaining in the ductile material. The stresses in the wedge caused by the bending are larger than in Figure 8.5, as a result of the increased throw, and this supports the suggestion above that faulting will occur within the wedge. This faulting is likely to be confined to fairly shallow depths since the lower part of the wedge is subjected to compression due to the bending, and this will inhibit the development of faulting at depth within the block. These inferences on the nature of the faulting within the wedge agree well with observations (e.g. Illies, 1970), as can be seen in the diagram of the Rhinegraben shown in Figure 1.1.

After 5M yrs (Figure 8.7) the throw of the fault has increased to 250 m. The compressive stresses beneath the block have also increased and the largest has magnitude of about 364 MPa. Although these values are fairly large, it must be realised that they are not deviatoric stresses. The principal stresses are close to being hydrostatic, and the stress difference is only about 13 MPa .

The series of figures shown here demonstrates that the compressive stresses beneath the wedge increase as the wedge subsides, but they become closer to the hydrostatic state because of the creep in the lower crust which always tends to relax the deviatoric stresses. The surface displacements of Figures 8.3 to 8.7 show the increase in the subsidence of the wedge as the stresses in the visco-elastic material relax. The

flanks of the graben remain differentially upthrown throughout, and the downthrown block is deformed by bending even after very long periods of time. The total throw on the boundary faults was only about 250 m after 5M yrs. Furthermore, 85 m of this occurred in the first 1M yrs and only 165 m in the next 4M yrs. Therefore, it seems likely that even if the model was run over longer periods of time, the amount of subsidence would not reach the value of several kilometres that is observed in many of the large graben (Illies, 1970; Sherman, 1978; Baker and Wohlenberg, 1971). Sedimentary infilling of the depression would slightly increase the subsidence, but for a typical sediment density of about 2,000 kg m^{-3} and a depth of depression of only about 200 m, the additional subsidence is likely to be very small.

There are two possibilities for bringing about a larger amount of subsidence. The first is that the frictional strength of the fault is very small. This was discussed in the previous chapter with reference to the estimates of the shear stress on the San Andreas fault (Brune et al., 1969; Zoback and Roller, 1979). The second possibility is that stresses larger than 20 MPa are acting on the lithosphere. Bott (1976) has investigated wedge subsidence by a consideration of the energy budget, and his results suggest that an increase in stress will have a greater effect than a reduction in the frictional strength. The effect of these two parameters on the deformation pattern will now be examined.

8.4 Effect of decreasing the frictional strength

The frictional strength of the fault can be reduced throughout its depth by decreasing the coefficient of friction. The model has been re-run using a coefficient of friction of 0.01 and the results are shown in Figures 8.8 to 8.12. The frictional strength is now exceeded immediately

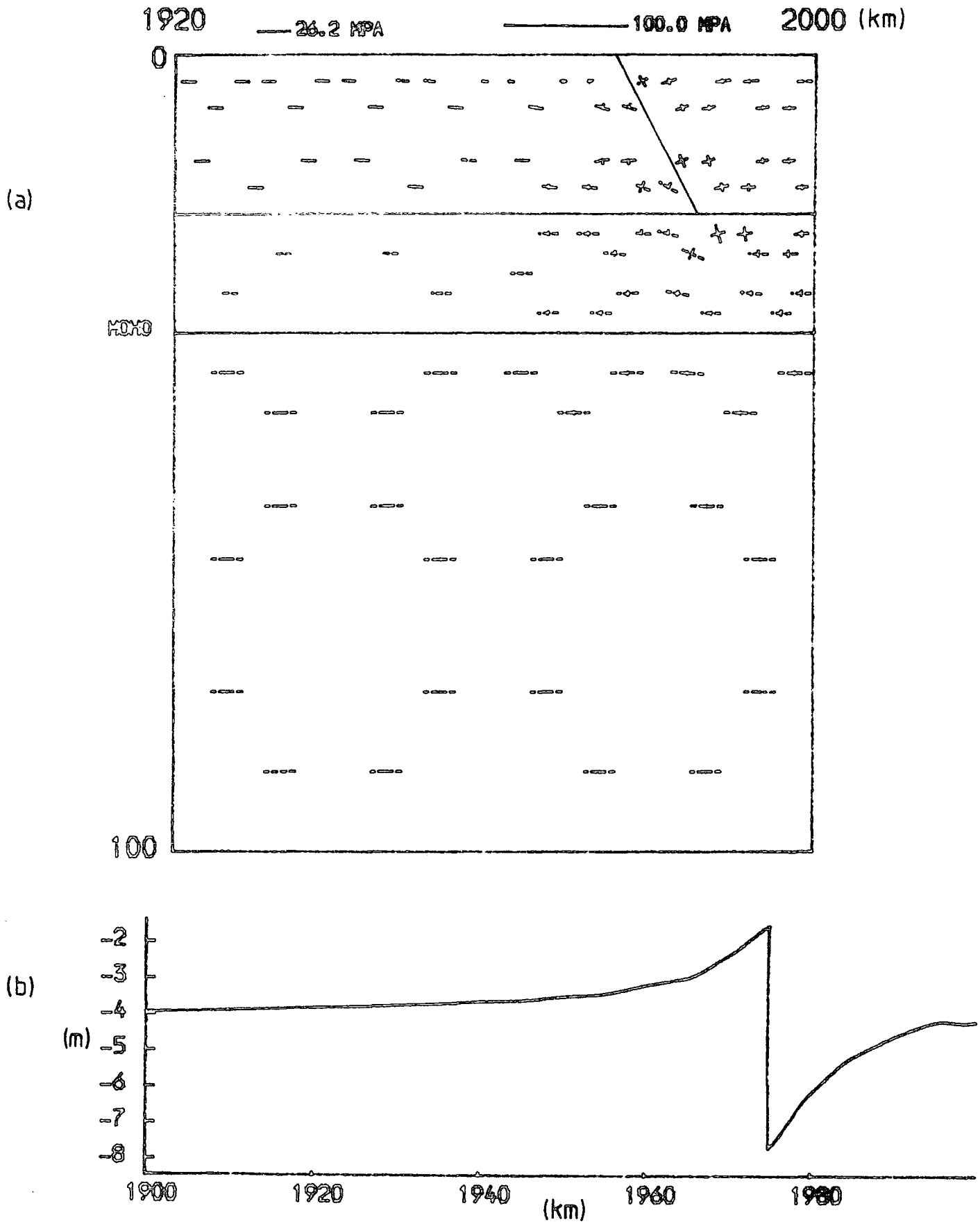

Fig. 8.8: Immediate deformation for an applied stress of 20 MPa and a coefficient of friction of 0.01
(a) Principal stresses around one half of the graben
(b) Surface displacement profile

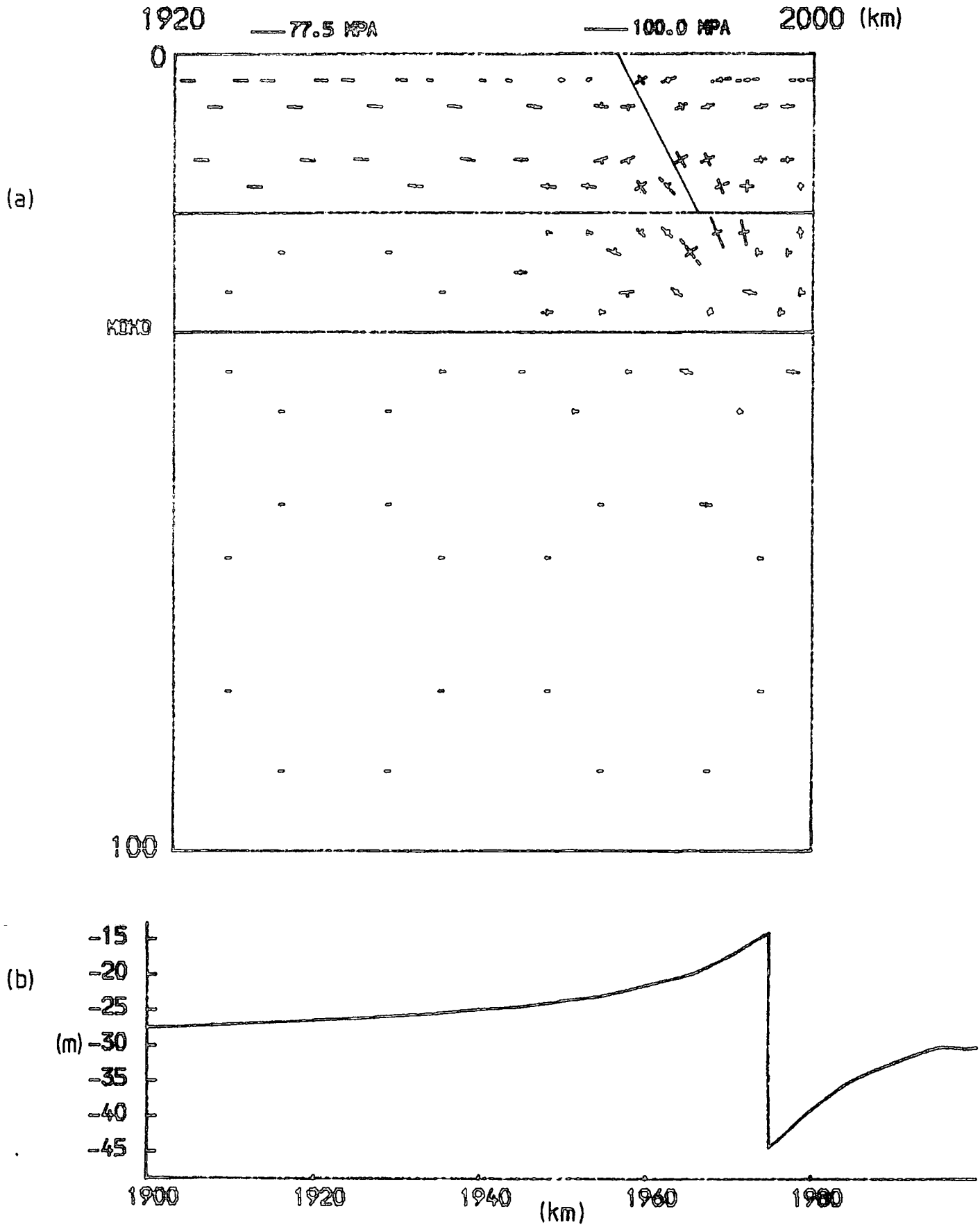

Fig. 8.9: Deformation after 200,000 yrs for an applied stress of 20 MPa and a coefficient of friction of 0.01
(a) Principal stresses around one half of the graben
(b) Surface displacement profile

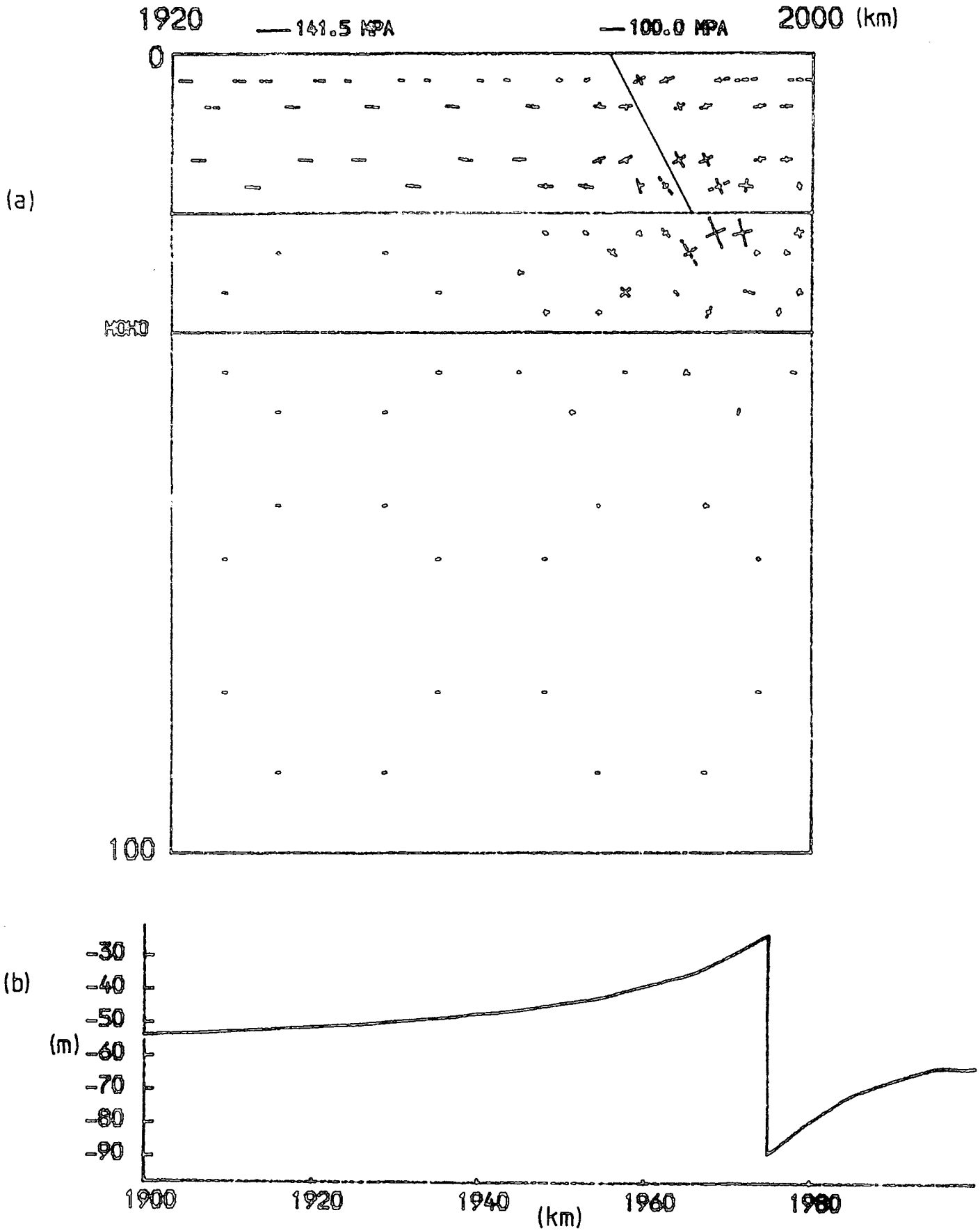

Fig. 8.10: Deformation after 500,000 yrs for an applied stress of 20 MPa and a coefficient of friction of 0.01
(a) Principal stresses around one half of the graben
(b) Surface displacement profile

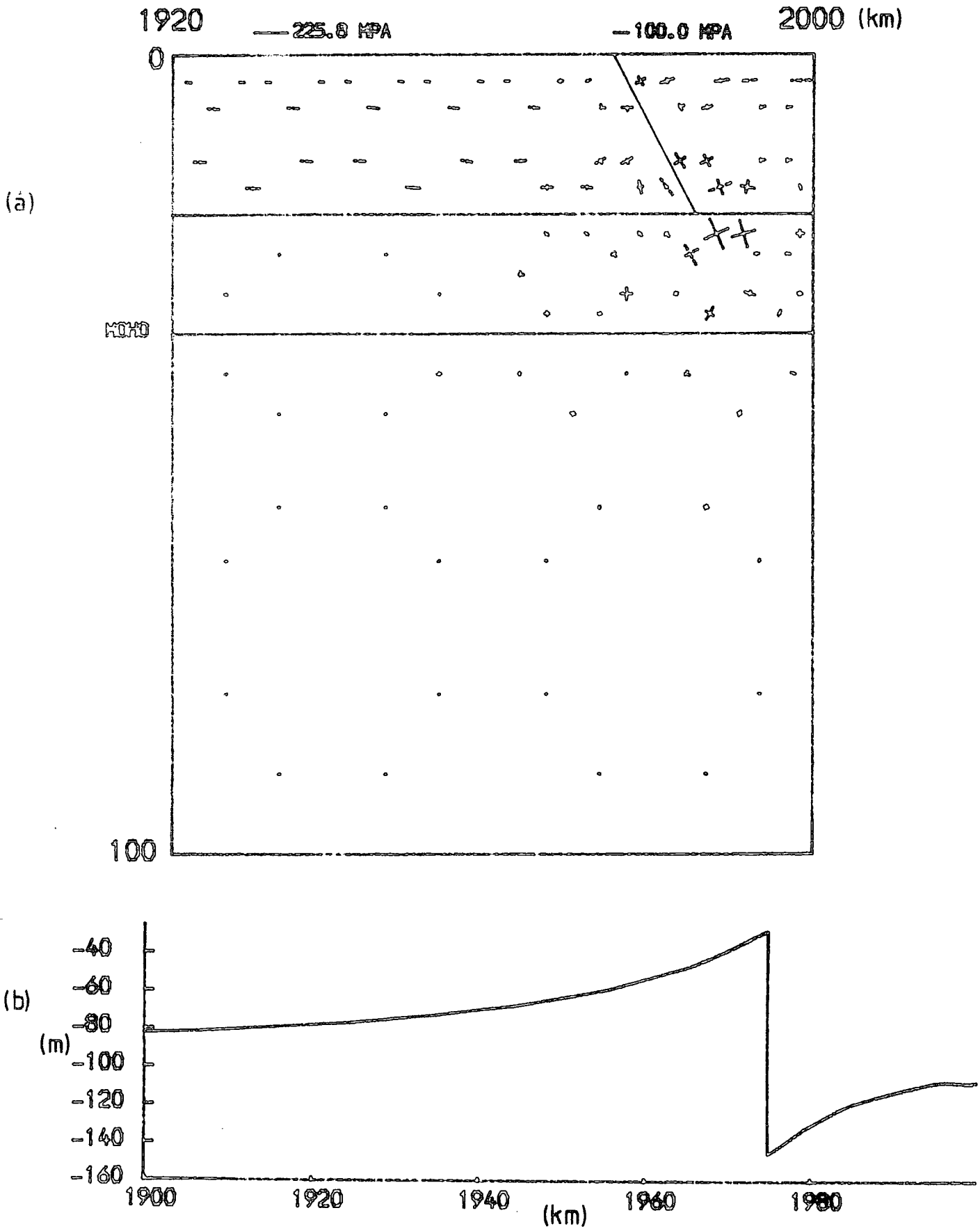

Fig. 8.11: Deformation after 1M yrs for an applied stress of 20 MPa and a coefficient of friction of 0.01
(a) Principal stresses around one half of the graben
(b) Surface displacement profile

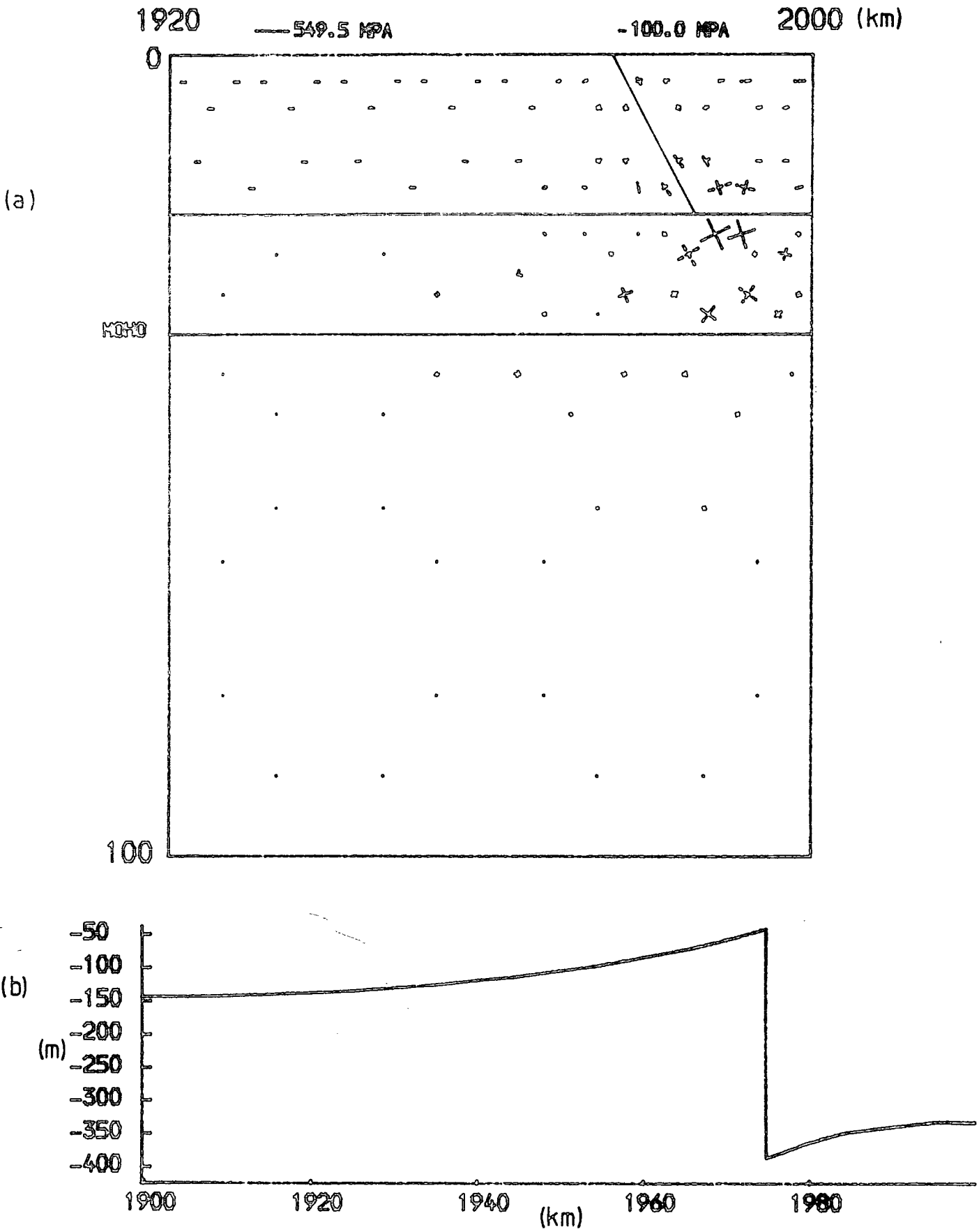

Fig. 8.12: Deformation after 5M yrs for an applied stress of 20 MPa and a coefficient of friction of 0.01
(a) Principal stresses around one half of the graben
(b) Surface displacement profile

for the entire depth of the fault, although the instantaneous fault throw is only about 6m (Figure 8.8). As the visco-elastic material is allowed to relax, the same pattern of deformation is seen as before. Both the rim uplift and the bending of the wedge are apparent in Figures 8.8 to 8.12. The basic difference between this model and the one described previously is in the amount of subsidence and, associated with this, the magnitude of the compressive stresses beneath the wedge. After 1M yrs (Figure 8.11) the throw is 115 m and this increases to 345 m after 5M yrs (Figure 8.12). This is greater than in the earlier model, although perhaps not significantly so. The compressive stresses beneath the wedge increase to about 550 MPa after 5M yrs, although they are again close to hydrostatic and the maximum stress difference between the principal stresses is only 20 MPa. In fact, the same pattern is seen as in the previous models: the hydrostatic component of the stress field beneath the wedge increases whilst the deviatoric components slowly decrease. It is not clear how long this situation will continue for, but the relatively small deviatoric stresses will result in low creep strain rates, and the large pressure differences are likely to exist for a long period of time after the applied stress has ceased to act. This is an important point as it highlights the difference between visco-elastic and viscous rheologies. For a purely viscous material these pressure differences could not exist, whereas for a visco-elastic material they are caused by volume changes and cannot be directly relaxed by creep.

8.5 Effect of increasing the applied stress

In order to investigate the effect of increasing the applied stress, the same model has been used as in the first section of this chapter, but the applied stress has been increased from 20 MPa to 50 MPa. The

coefficient of friction was taken to be 0.1. The results are shown in Figures 8.13 to 8.17. The instantaneous stresses (Figure 8.13) are only sufficient to cause sliding on the upper section of the fault. After 200,000 yrs the frictional strength has been exceeded throughout the depth of the fault and compressive stresses develop beneath the wedge. This situation is shown in Figure 8.14. As the visco-elastic material relaxes the same pattern is seen as before and the hydrostatic component of the compressive stress beneath the wedge increases. The large applied stress results in much greater subsidence than either of the previous models. This is in agreement with the work of Bott (1976). After 1M yrs the fault throw is about 275 m and after 5M yrs it has increased to 813 m. The compressive stresses beneath the fault have attained a value of nearly 1270 MPa, although the stress difference is only 50 MPa which is geologically reasonable (Murrell, 1977). The high pressures beneath the wedge may result in phase changes in the lower crust.

It seems likely that, for coefficients of friction less than about 0.1 and applied stresses close to 50 MPa, fault throws of greater than 1 km can occur. These may become considerably larger if the graben is filled with sediment. Bott (1976) has reached similar conclusions on the amount of subsidence that can occur by a consideration of the energy budget. He showed that the gravitational energy loss resulting from the subsiding wedge must exceed the gain in gravitational energy caused by rim uplifts, the gain in strain energy caused by normal faulting (providing absolute tension does not exist), and the energy dissipated by friction on the fault. The results presented here qualitatively support this energy budget since it is apparent from the displacement profiles (e.g. Figure 8.17) that the loss of gravitational energy resulting from the wedge subsidence considerably exceeds the gain in gravitational energy caused by the uplifted rims. This excess is

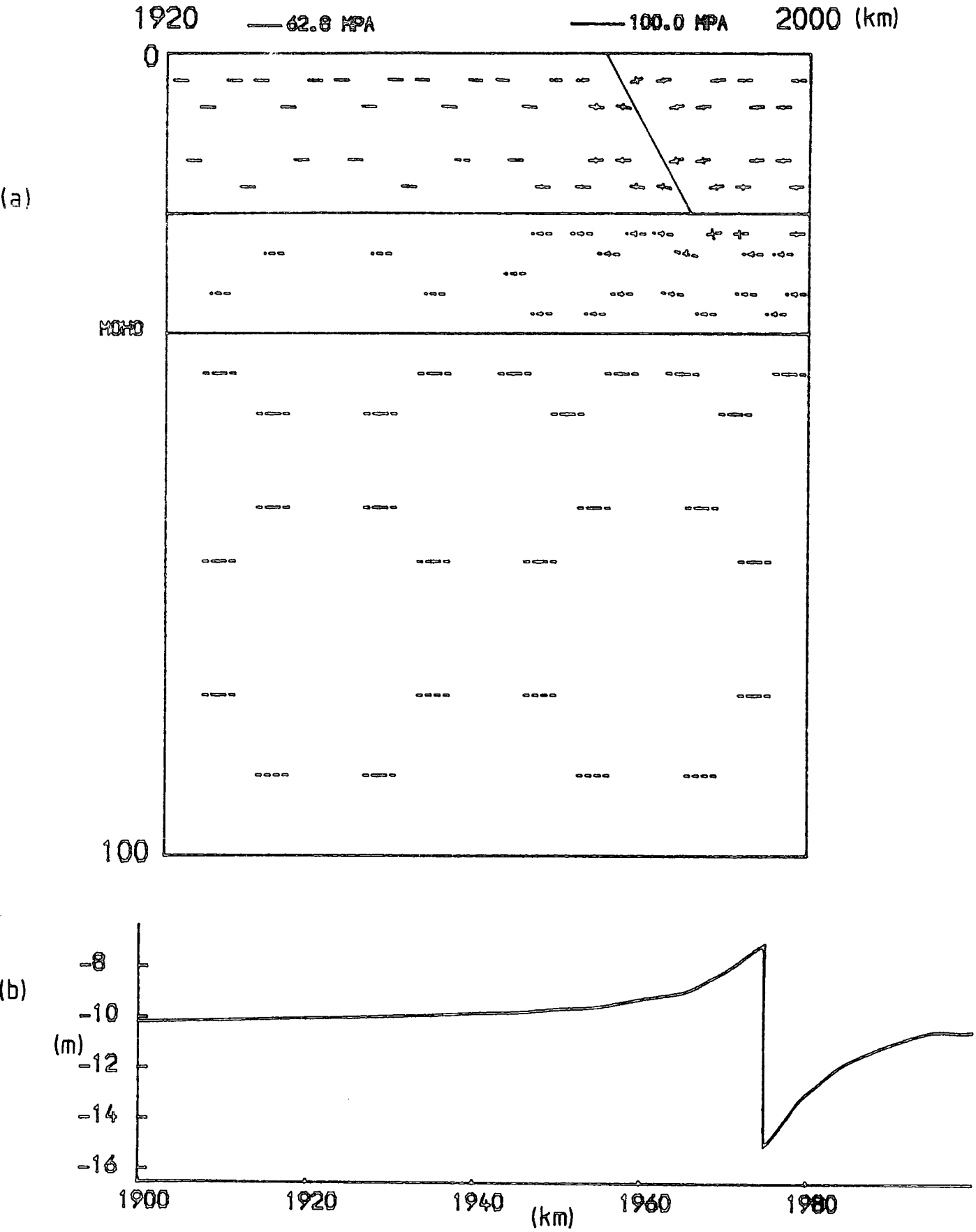

Fig. 8.13: Immediate deformation for an applied stress of 50 MPa and a coefficient of friction of 0.1
(a) Principal stresses around one half of the graben
(b) Surface displacement profile

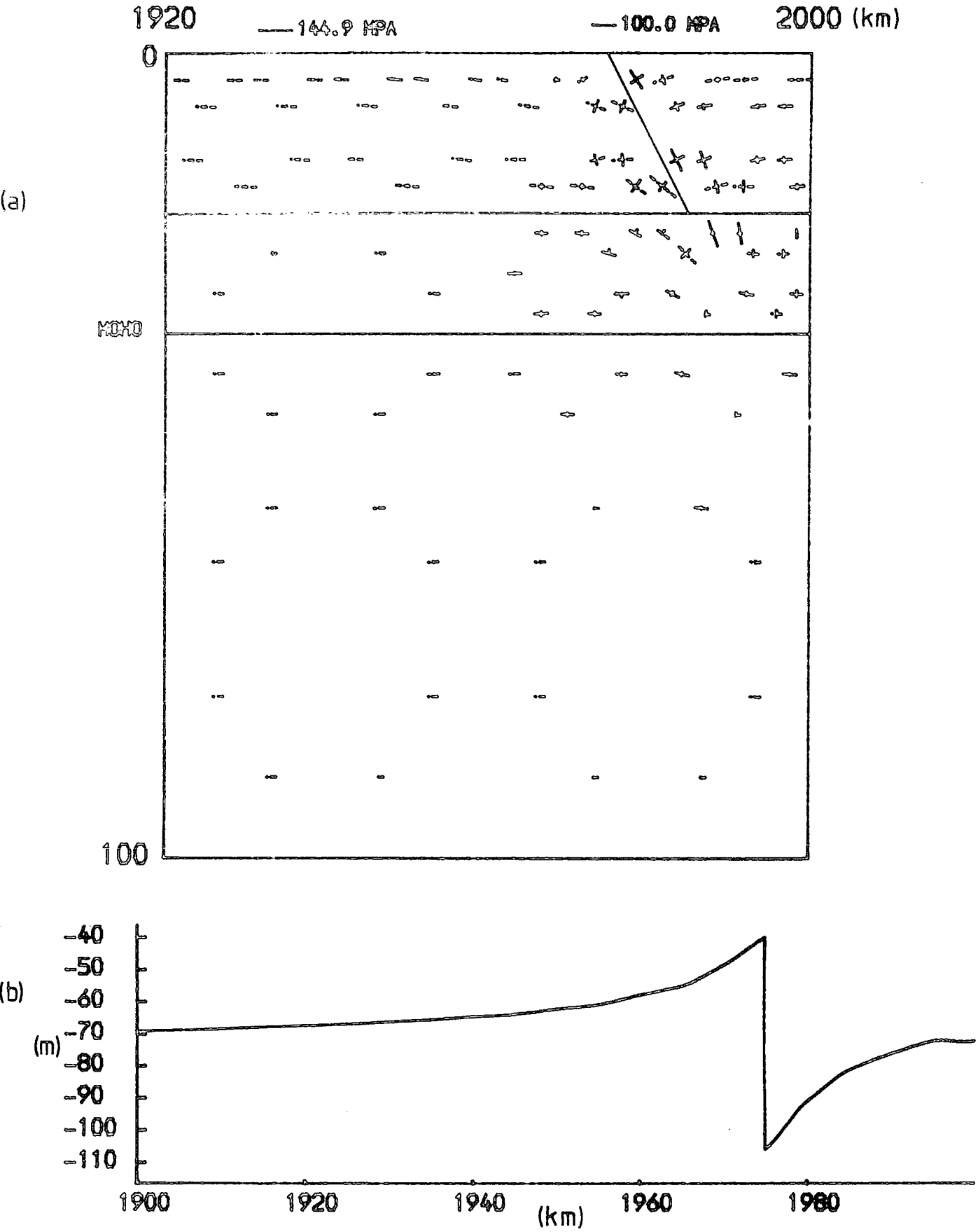

Fig. 8.14: Deformation after 200,000 yrs for an applied stress of 50 MPa and a coefficient of friction of 0.1
(a) Principal stresses around one half of the graben
(b) Surface displacement profile

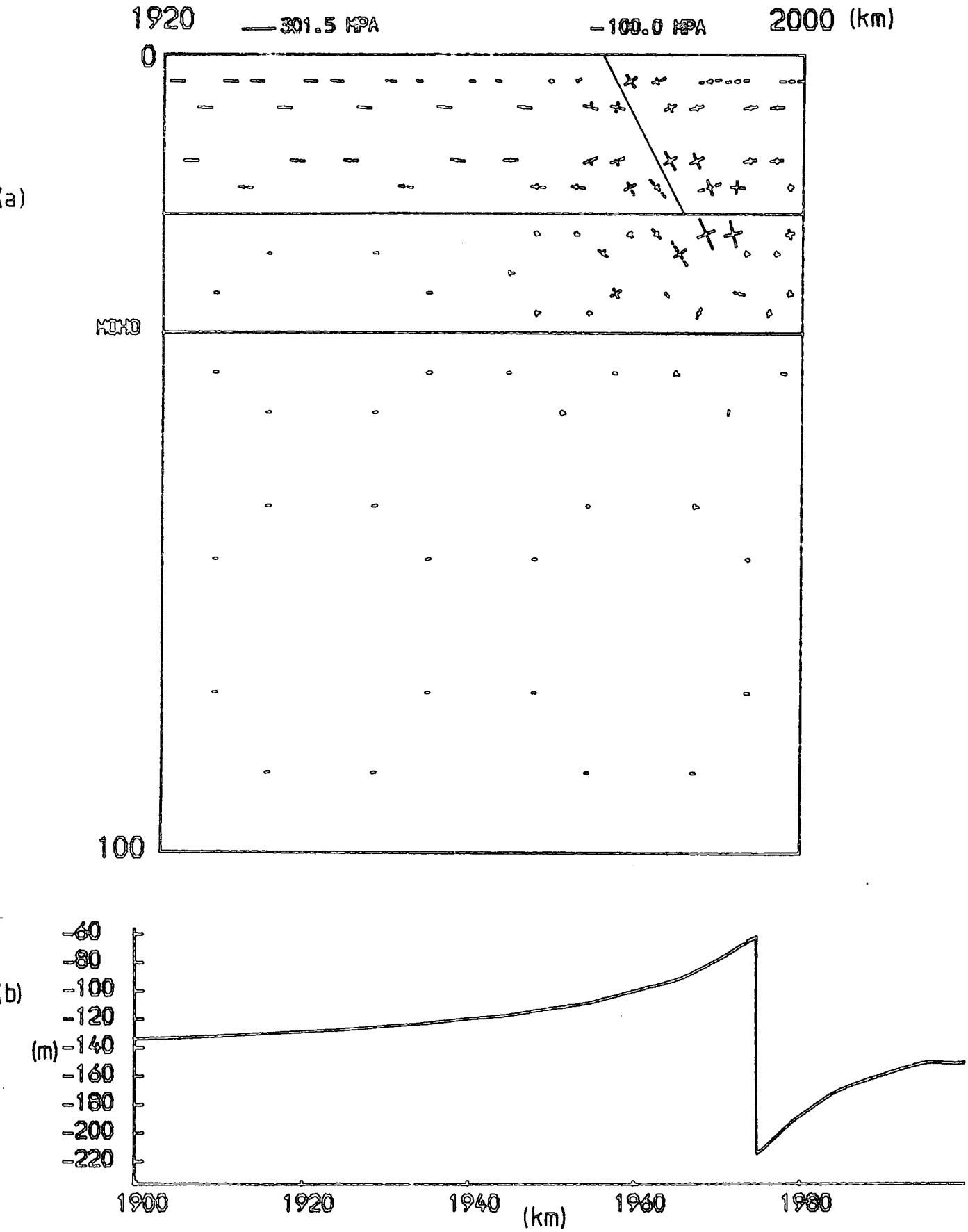

Fig. 8.15: Deformation after 500,000 yrs for an applied stress of 50 MPa and a coefficient of friction of 0.1
(a) Principal stresses around one half of the graben
(b) Surface displacement profile

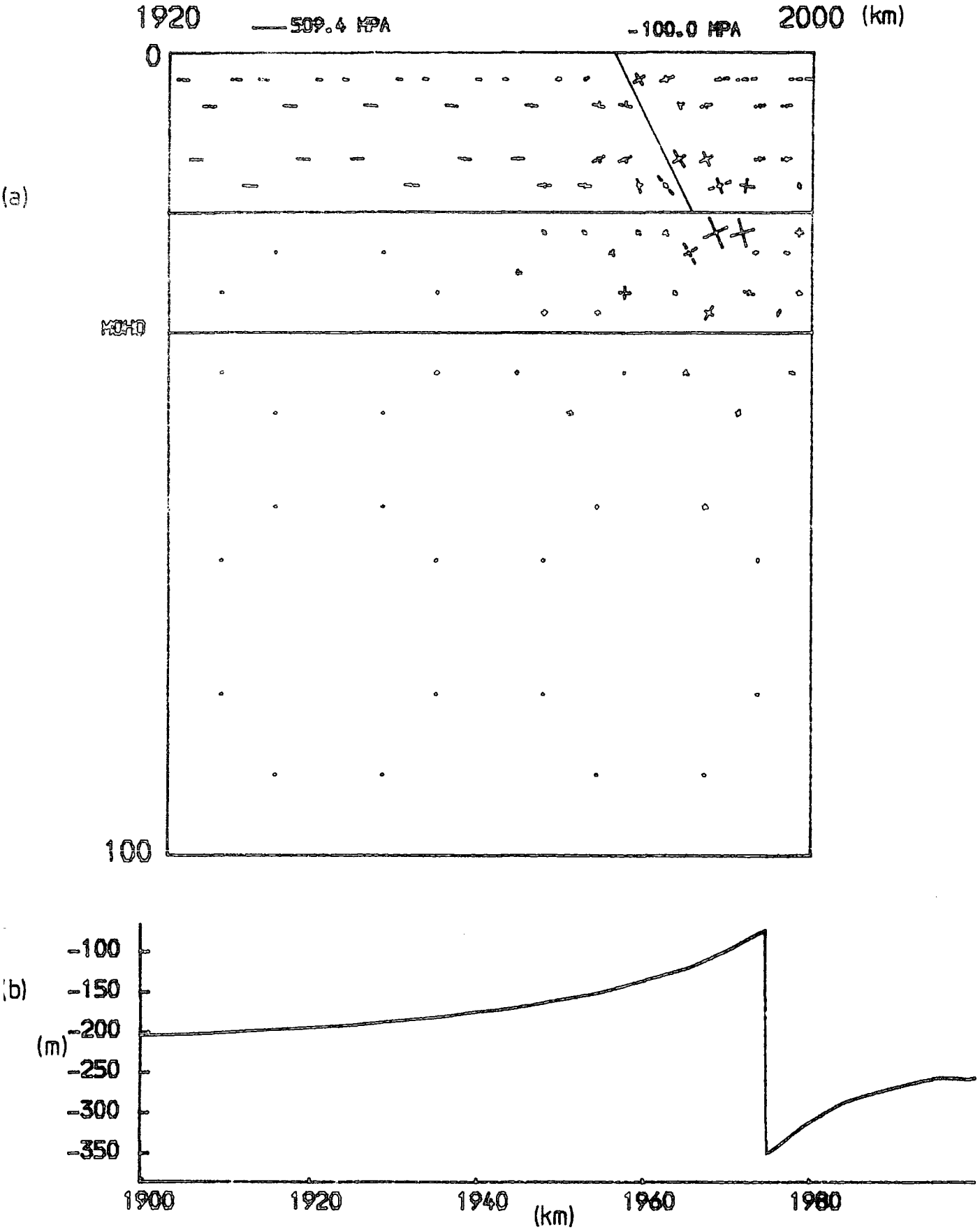

Fig. 8.16: Deformation after 1M yrs for an applied stress of 50 MPa and a coefficient of friction of 0.1
(a) Principal stresses around one half of the graben
(b) Surface displacement profile

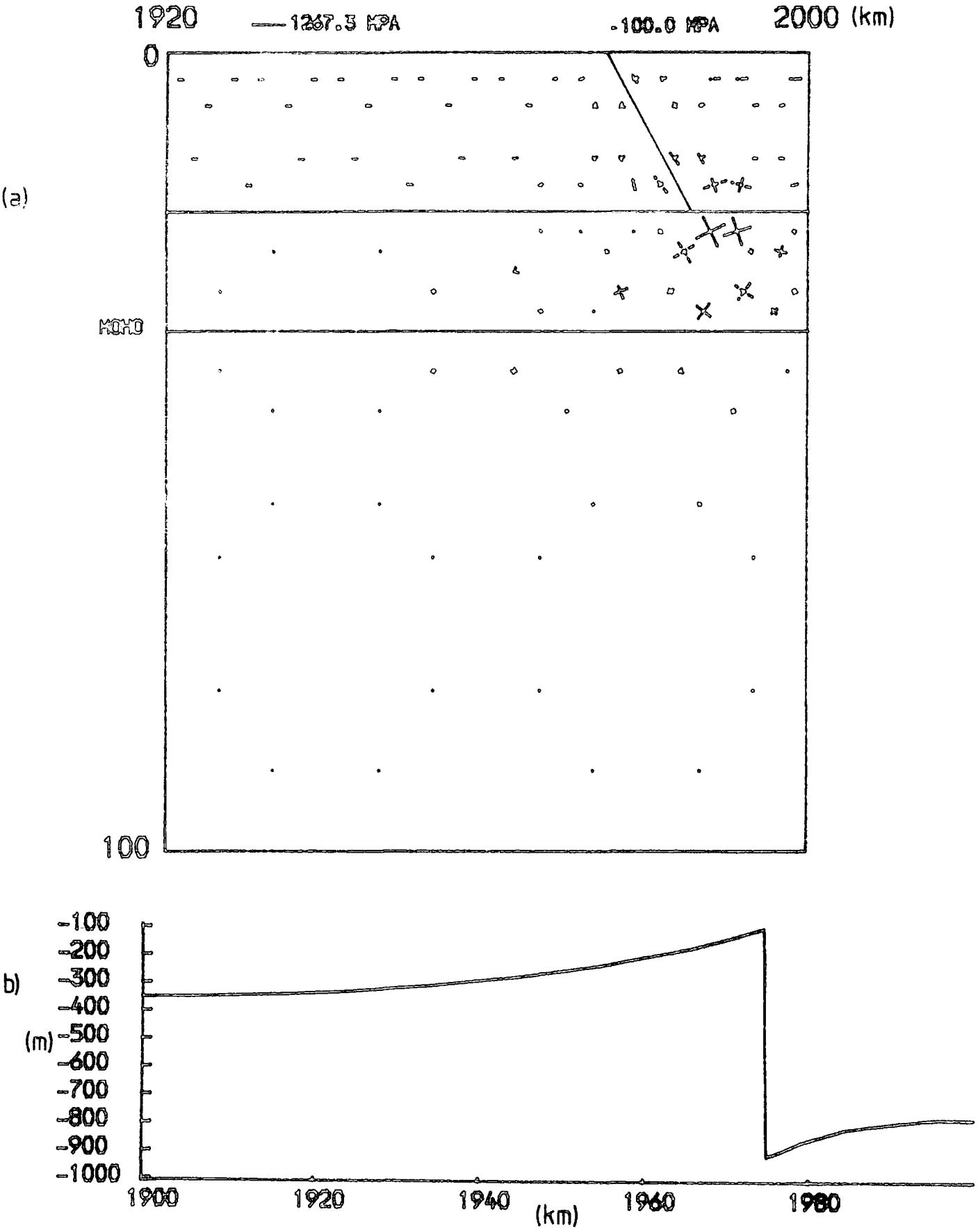

Fig. 8.17: Deformation after 5M yrs for an applied stress of 50 MPa and a coefficient of friction of 0.1
(a) Principal stresses around one half of the graben
(b) Surface displacement profile

available to overcome the dissipation of energy associated with the normal faulting.

8.6 Summary

The main conclusions reached in this chapter will be summarised in point form:

1) Subsidence of the graben block increases with time as the stresses in the visco-elastic material relax and amplify the stresses in the elastic layer. Associated with the subsiding wedge are rim uplifts at the flanks of the graben.
2) The process of wedge subsidence is stable from the energy viewpoint (Bott, 1976) since the loss in gravitational energy resulting from the downthrown block greatly exceeds the gain in gravitational energy caused by the rim uplifts.
3) Subsidence of the wedge results in the development of compressive stresses immediately beneath the wedge. The hydrostatic component increases as the block subsides, although the deviatoric components are relatively small. This may lead to significant pressure differences in the underlying, lower crustal material and the possibility of phase changes.
4) Decreasing the frictional strength of the fault or increasing the applied stress results in a greater amount of subsidence. The effect of a larger stress is much greater than the effect of a weak fault. For a coefficient of friction less than about 0.1 and an applied stress of about 50 MPa, subsidence of 1 km or greater seems likely, particularly if the graben is filled with sediment.
5) The wedge does not subside uniformly. This is because it is controlled by frictional sliding on the boundary faults. The greatest amount of

subsidence occurs near the faults and the wedge is subjected to bending stresses which increase the deviatoric tension near the top, but decrease it near the base. This is likely to result in shallow, normal faulting within the downthrown block, which is observed in many graben (e.g. Illies, 1970). A narrower graben would be expected to have smaller bending stresses and, consequently, less deformation within the block.

CHAPTER 9

DISCUSSION

9.1 Discussion of the results

In this thesis, the formation of graben structures has been divided into three stages. The first stage has been considered to be the development of normal faulting in the upper part of the lithosphere. The results from Chapter 4 show that this is possible when comparatively small stresses act throughout the depth of the lithosphere. If these stresses do not vary significantly with depth, then failure will probably occur near the top of the lithosphere where the overburden pressure is small. It will presumably not occur very close to the surface because of stress relief associated with joints and weathering (Zoback and Roller, 1979). The models used assumed that the shallowest depth for faulting to commence was 3.33 km (the centre of the shallowest elements). The models showed that an applied stress of 20 MPa was sufficient to cause faulting after suitable time periods. The mechanism by which this occurs is stress amplification, which has been investigated previously by Kusznir and Bott (1977). The results presented here agree well with their work. Of particular interest, with regard to the development of graben structures, is the conclusion that warm regions of the lithosphere are more susceptible to faulting. This is a result of localised thinning of the brittle layer and a decrease in the effective viscosity of the underlying material. A good example is the Basin and Range province. The tensile stresses which act on the lithosphere may be a result of the driving mechanism of plate tectonics, in particular, the effect of the downgoing slab at subduction zones.

Another important source of tensile stress is likely to be due to compensated plateau uplifts (Bott and Kusznir, 1979). In some areas this may be the principal source. It is significant that most regions where major graben have developed were subjected to doming and volcanism prior to the faulting episode (Kiselev et al., 1978; Davidson and Rex, 1980), which would give rise to these stresses. The position of the normal faulting in these regions was probably dependent on ancient lines of weakness (Illies, 1977; Logatchev and Florensov, 1978).

The hypothesis that the second normal fault develops as a result of the deformation caused by the first fault, which was first suggested by Vening Meinesz (1950), has been found to be feasible. The results presented in Chapters 6 and 7 show that a significant weakening near the top of the crust occurs where the stresses are most greatly modified by the bending profile of the first fault. In the event of a homogeneous upper crust, it seems probable that normal faulting will occur at this position of weakness. For situations where the fault movement occurs only in the upper part of the elastic layer, because of the frictional strength of the fault, graben of widths between 5 and 15 km were predicted. If the elastic layer is underlain by a fluid, then when fault movement extends through most of the elastic layer the predicted graben widths increase to between 50 and 55 km. A large increase in the fault throw also results. When fault movement extends throughout the elastic layer the throw increases further, although there is no change in the predicted graben width. These results are interesting when compared with elastic beam theory calculations (Heiskanen and Vening Meinesz, 1958; Bott, 1976), but are not considered significant with regard to the true nature of graben formation. This is because the assumption that the underlying material is a fluid is considered to be too unrealistic.

A much more realistic rheology for the lower part of the lithosphere is visco-elasticity. When faulting extends throughout a 20 km thick elastic layer overlying visco-elastic material, the predicted graben width is about 25 km. This seems to follow on from the 5 to 15 km widths which were predicted for shallower faulting. These conclusions are in good agreement with observed structures in several areas. The Basin and Range province is characterised by many graben with typical widths of between 10 and 20 km (Stewart, 1978), and faulting in this region may be confined to the uppermost 15 km of the lithosphere since focal depths of earthquakes are typically less than this (Smith and Sbar, 1974). Other narrow graben, such as the Levant graben which have widths of 5 to 10 km, may also be explained by this mechanism. The development of graben of widths of about 50 km, which are typically associated with rift valleys, can not be explained by the results in this thesis. The widest graben that has been predicted by this work is of 40 to 45 km. However, this requires a very weak fault and a brittle layer extending to 50 km depth, and this seems very unlikely since wide graben, such as Lake Baikal and those of East Africa, typically form in warm areas where the brittle layer would be expected to be fairly thin. One possible explanation of the development of these wide graben is that the second normal fault is also controlled by basement weaknesses. The South Baikal depression overlies an ancient suture (Logatchev and Florensov, 1978) and the Rhinegraben follows Hercynian and Caledonian basement faults (Illies, 1977). The asymmetry of the sediment fill and the gravity anomaly associated with the Rhinegraben (Mueller and Rybach, 1974) may suggest that the first fault to form changed from being the eastern boundary to being the western boundary, and this could indicate the possible importance of basement

control. Another possibility is that there is another mechanism acting in these areas which has not been considered in the models. It is possible that this could be connected with the deep structure beneath the rifts.

In this thesis, only a brief investigation of the subsidence of the graben wedge has been possible. The results, which were described in Chapter 8, suggest that subsidence of at least 1 km can occur if the applied stresses are about 50 MPa and the coefficient of friction on the fault is less than about 0.1. This is in agreement with calculations made by Bott (1976). In the time available for this research, it has not proved possible to include the effect of sedimentary infilling of the graben. This is likely to increase the amount of subsidence considerably (Bott, 1976). Two other interesting effects of the subsiding graben block were seen. Firstly, very large compressive stresses build up beneath the wedge. The deviatoric components associated with these stresses are relatively small and, consequently, these pressure differences are likely to exist for long periods of time. It is possible that these could cause phase changes in the lower crust. Secondly, the subsiding wedge is likely to be heavily deformed by faulting. This is because the wedge does not sink uniformly, as assumed by Artemjev and Artyushkov (1971), but is controlled by frictional sliding on the boundary faults. It seems likely that narrower graben will suffer less deformation because the amount of bending of the wedge will be smaller.

9.2 Limitations in the modelling

The limitations in the models presented in this thesis fall into two classes. The first of these are those resulting from the finite element method used here and can be summarised in a number of points:

1) Constant strain elements have been used in all of the models. These are not particularly suitable when large stress gradients exist. Higher order elements would be more useful, especially in the vicinity of the fault where stress concentrations are likely to occur. Nevertheless, it is felt that these elements do give a reasonable approximation to the stress system and, of course, are relatively simple to use.

2) The plane strain approximation is probably not a severe constraint on the models presented here, since they all represent sections through structures which are very long in the third dimension.

3) The application of body forces in finite element models is always a problem because of the boundary conditions (see Chapter 4). A lithostatic stress distribution has been assumed for all of the models in this thesis. This will not introduce significant errors when the differential surface displacements are small, which is the situation for most of the results presented here. It is only in the final model, when the graben wedge has subsided considerably, that the body forces may be important.

4) It is not clear how accurately the fault modelling technique which has been developed in this thesis reflects the true behaviour of a

fault. This is likely to be the case with any fault modelling procedure since the mechanism of fault movement, particularly at depth, is not well-known. The method developed here has the advantage that it is based on the concept of frictional sliding which is, probably, by far the most significant cause of fault movement, at least at shallow depths. This is supported by laboratory studies (Byerlee, 1978) and by investigations into the features of active faulting (Nur, 1978). It would be very interesting to use the fault modelling method developed in this thesis, together with higher order elements and variations in the frictional strength, for the purpose of investigating stick slip behaviour and the mechanism of earthquake generation.

When the fault modelling method is used with constant strain elements, as is the case here, it is only possible to model plane faults. Listric faults have been described in several areas (e.g. Proffett, 1977; Montadert et al., 1979) and may give rise to significant differences in the displacement profiles and stress distributions associated with movement on them. The method developed here could probably be adapted to model listric faults by using curved, isoparametric elements (Zienkiewicz, 1977).

Evidence that the method does give reasonable results is that certain effects, such as the re-distribution of stresses adjacent to the fault and the development of secondary faulting, which the model predicts, are observed on naturally occurring faults (Ramsay, 1967).

The second class of limitations that affects the model is concerned with the current state of knowledge about the lithosphere. Uncertainties

about the mechanism of fault behaviour have already been mentioned. The state of stress at depth is largely unknown, as is the rheology. The models that have been run in this thesis suggest that the deformation pattern is not significantly altered by the type of creep mechanism used, assuming it is uniform throughout the layer. Local variations in the stress system, however, may result in significant variations in the rheological behaviour. One example of this, which has been discussed earlier in this thesis, is the possibility of superplastic flow at the base of faults (Ball, 1980).

These problems are likely to confront research workers dealing with geodynamics problems for many years.

APPENDIX 1

ELASTIC BEAM THEORY

A brief explanation of elastic beam theory, with particular emphasis on its geophysical use, will be given here. For a more complete description the reader is referred to one of several texts on stress and deformation which cover this subject (e.g. Housner and Vreeland, 1966).

A1.1 The basic beam equation

Consider a beam in the x-y plane which is slender in the z-direction. The shearing strains will be very small. In the technical theory of bending, the shearing strains are assumed to be zero and deformation of the beam is considered to be a result only of the bending strains. This implies the following:

$$\varepsilon_y = 0$$

$$\gamma_{xy} = 0$$

$$\varepsilon_z = \gamma_{yz} = \gamma_{xz} = 0$$

The radius of curvature, r, is given by

$$\frac{1}{r} = \frac{M}{EI} \qquad \text{A1.1}$$

where M is the bending moment at the point where r is measured, E is Young's modulus, and I is the moment of inertia per unit width. If V is the vertical displacement (in the y-direction), then, provided the beam has small slopes,

$$EI \frac{d^2V}{dx^2} = M \qquad \text{A1.2}$$

Now, $\frac{dM}{dx} = \mathcal{V}$ where $\mathcal{V}$ is the shear force per unit width

and $\frac{d\mathcal{V}}{dx} = -q$ where q is the restoring stress per unit width

$$\therefore \quad EI \frac{d^4V}{dx^4} + q = 0 \qquad \text{A1.3}$$

This is the basic beam equation. It is often written as

$$\underline{D \frac{d^4V}{dx^4} + q = 0} \qquad \text{A1.4}$$

where D is the flexural rigidity, given by

$$D = EI = \frac{ET^3}{12} \qquad \text{A1.5}$$

where T is the thickness of the beam.

<u>Note</u>: For thin plate theory, the basic equation is

$$D'\nabla^4 V + q = 0$$

where D' is the flexural rigidity of the plate,

$$D' = \frac{EI}{1-\nu^2} \qquad \text{where } \nu \text{ is Poisson's ratio}$$

and

$$\nabla^4 = \frac{\partial^4}{\partial x^4} + \frac{2\partial^4}{\partial x^2 \partial z^2} + \frac{\partial^4}{\partial z^4}$$

The flexural rigidity for a thin plate is often used in bending problems pertaining to the earth.

A1.2 Flexure due to vertical loading

Consider the brittle, upper part of the lithosphere to be an elastic beam and the underlying, ductile material to be a fluid.

Then the restoring stress, q, is given by

$$q = \rho_m g V \qquad \text{A1.6}$$

where ρ_m is the density of the underlying fluid and g is the gravitational constant.

Then the basic equation becomes

$$D \frac{d^4V}{dx^4} + \rho_m g V = 0 \qquad \text{A1.7}$$

The solution of this equation is of the form

$$V = \exp(-\frac{x}{\alpha}) \ (A \cos \frac{x}{\alpha} + B \sin \frac{x}{\alpha}) + \exp(\frac{x}{\alpha})(C \cos \frac{x}{\alpha} + D \sin \frac{x}{\alpha}) \qquad \text{A1.8}$$

where α is the flexural parameter, given by

$$\alpha = \left(\frac{4D}{\rho_m g}\right)^{\frac{1}{4}} \qquad \text{A1.9}$$

At great distance from the applied load there will be zero displacement,

$$\therefore \ V \rightarrow 0 \ \text{ as } \ x \rightarrow \infty$$

$$\therefore \ C = D = 0$$

$$\therefore \ \underline{V = \exp(-\frac{x}{\alpha}) \ (A \cos \frac{x}{\alpha} + B \sin \frac{x}{\alpha})} \qquad \text{A1.10}$$

This equation can be differentiated to obtain the following useful equations:

$$\frac{dV}{dx} = \frac{\exp\left(-\frac{x}{\alpha}\right)}{\alpha}\left((B-A)\cos\frac{x}{\alpha} - (A+B)\sin\frac{x}{\alpha}\right) \qquad \text{A1.11}$$

$$\frac{d^2V}{dx^2} = \frac{2\exp\left(-\frac{x}{\alpha}\right)}{\alpha^2}\left(-B\cos\frac{x}{\alpha} + A\sin\frac{x}{\alpha}\right) \qquad \text{A1.12}$$

$$\frac{d^3V}{dx^3} = \frac{2\exp\left(-\frac{x}{\alpha}\right)}{\alpha^3}\left((A+B)\cos\frac{x}{\alpha} + (B-A)\sin\frac{x}{\alpha}\right) \qquad \text{A1.13}$$

Equation A1.10 can also be solved for two cases:

Case 1

Continuous beam with a downward force P applied at the origin.

Since the beam is horizontal at the origin the following boundary condition holds:

$$\frac{dV}{dx} = 0, \; x = 0$$

So from equation A1.11

$$B - A = 0$$

$$\therefore B = A \qquad \text{A1.14}$$

Now, the force P is carried by both the left and right sides of the beam.

$$\therefore \mathcal{V} = \frac{P}{2}, \quad x = 0 \quad \text{and} \quad \mathcal{V} = D\,\frac{d^3V}{dx^3}$$

$$\therefore \frac{d^3V}{dx^3} = \frac{P}{2D}, \; x = 0$$

So from equations A1.13 and A1.14,

$$\frac{4A}{\alpha^3} = \frac{P}{2D}$$

$$= \frac{2P}{\alpha^4 \rho_m g}$$

$$\therefore \quad A = \frac{P}{2\alpha\rho_m g} \qquad \text{A1.15}$$

$\therefore$ the displacement curve is given by

$$V = \frac{P}{2\alpha\rho_m g} \exp\left(-\frac{x}{\alpha}\right)\left(\cos\frac{x}{\alpha} + \sin\frac{x}{\alpha}\right) \qquad \text{A1.16}$$

Case 2

Vertically fractured beam with the origin at the fracture. Downward force P applied at the origin, working on one half of the beam.

The boundary condition is now that there is no moment acting at the origin.

$\therefore M = 0, x = 0$

$\therefore$ from equation A1.2

$$\frac{d^2V}{dx^2} = 0, \; x = 0$$

So from equation A1.12,

$$B = 0 \qquad \text{A1.17}$$

For this case, the force is carried all on one side of the crust,

$$\therefore \mathcal{V} = P, \; x = 0$$

and

$$\mathcal{V} = D\frac{d^3V}{dx^3}$$

$$\therefore \frac{d^3V}{dx^3} = \frac{P}{D}$$

$$= \frac{4P}{\alpha^4\rho_m g}$$

So from equations A1.13 and A1.17,

$$\frac{2A}{\alpha^3} = \frac{4P}{\alpha^4 \rho_m g}$$

$$\therefore A = \frac{2P}{\alpha \rho_m g} \qquad \text{A1.18}$$

$\therefore$ the displacement curve is given by

$$V = \frac{2P}{\alpha \rho_m g} \exp\left(-\frac{x}{\alpha}\right) \cos \frac{x}{\alpha} \qquad \text{A1.19}$$

A1.3 Predicted width of a graben

If a fault in the brittle layer of the lithosphere can be regarded as a vertical load, then equations A1.16 and A1.19 give the displacement profile for the situations of maximum constraint (continuous beam) and minimum constraint (vertically fractured beam).

If the second fault, on the downthrown side, is related to the deformation caused by the first fault, then it is likely to develop where the bending moment is a maximum,

i.e. where $\frac{d^3V}{dx^3} = 0.$

Using the above condition, the width of the graben, x_w, can be calculated for the two cases.

Case 1

Continuous beam.

From equations A1.13, A1.14 and A1.15,

$$\frac{2P}{\alpha \rho_m g} \exp\left(-\frac{x}{\alpha}\right) \cos \frac{x_w}{\alpha} = 0$$

$$\therefore \cos \frac{x_w}{\alpha} = 0$$

So taking the first value of x_w,

$$\underline{x_w = \frac{\pi\alpha}{2}} \qquad \text{A1.20}$$

Case 2

Vertically fractured beam.

From equations A1.13, A1.17 and A1.18,

$$\frac{4P}{\alpha\rho_m g} \exp\left(-\frac{x}{\alpha}\right) \left(\cos \frac{x_w}{\alpha} - \sin \frac{x_w}{\alpha}\right) = 0, \quad \therefore \cos \frac{x_w}{\alpha} = \sin \frac{x_w}{\alpha}$$

So taking the first value,

$$\underline{x_w = \frac{\pi\alpha}{4}} \qquad \text{A1.21}$$

Now, case 1 represents a situation of maximum constraint and case 2 represents a situation of minimum constraint. Therefore the predicted graben width can be considered to lie in the range

$$\underline{\frac{\pi\alpha}{2} \geqslant x_w \geqslant \frac{\pi\alpha}{4}}$$

and substitution of appropriate values of α allows limits to be placed on x_w.

APPENDIX 2

FINITE ELEMENT PROGRAM

A2.1 Program Structure

The finite element program described here has been written by the author in the form of a library of subroutines and a master calling program. The programs are written in FORTRAN IV and double precision is used for all real characters except those starting with X to Z. The calling program is stored in the file FEGEN and lists all the common blocks, which transfer data among the subroutines, together with calls to every subroutine in the library. Subroutine calls that are not required for a particular job are prefixed by a letter 'C' in the first column which results in the calls not being executed. The subroutines are stored in the file FELIB. The purpose and calling order of these subroutines are illustrated in the form of flow diagrams in Figures A2.1 and A2.2. Two additional libraries are necessary when the program is run. These are *HARWELL, which contains the subroutine MA07BD, and *GHOST, which contains plotting subroutines. These two libraries are available at most computing centres.

The data within the program is stored in eight common blocks. In general, each of the common blocks contains information relevant to a certain part of the program. Consequently, only the necessary common blocks need to be passed to each subroutine. The contents of the common blocks refer to the following:

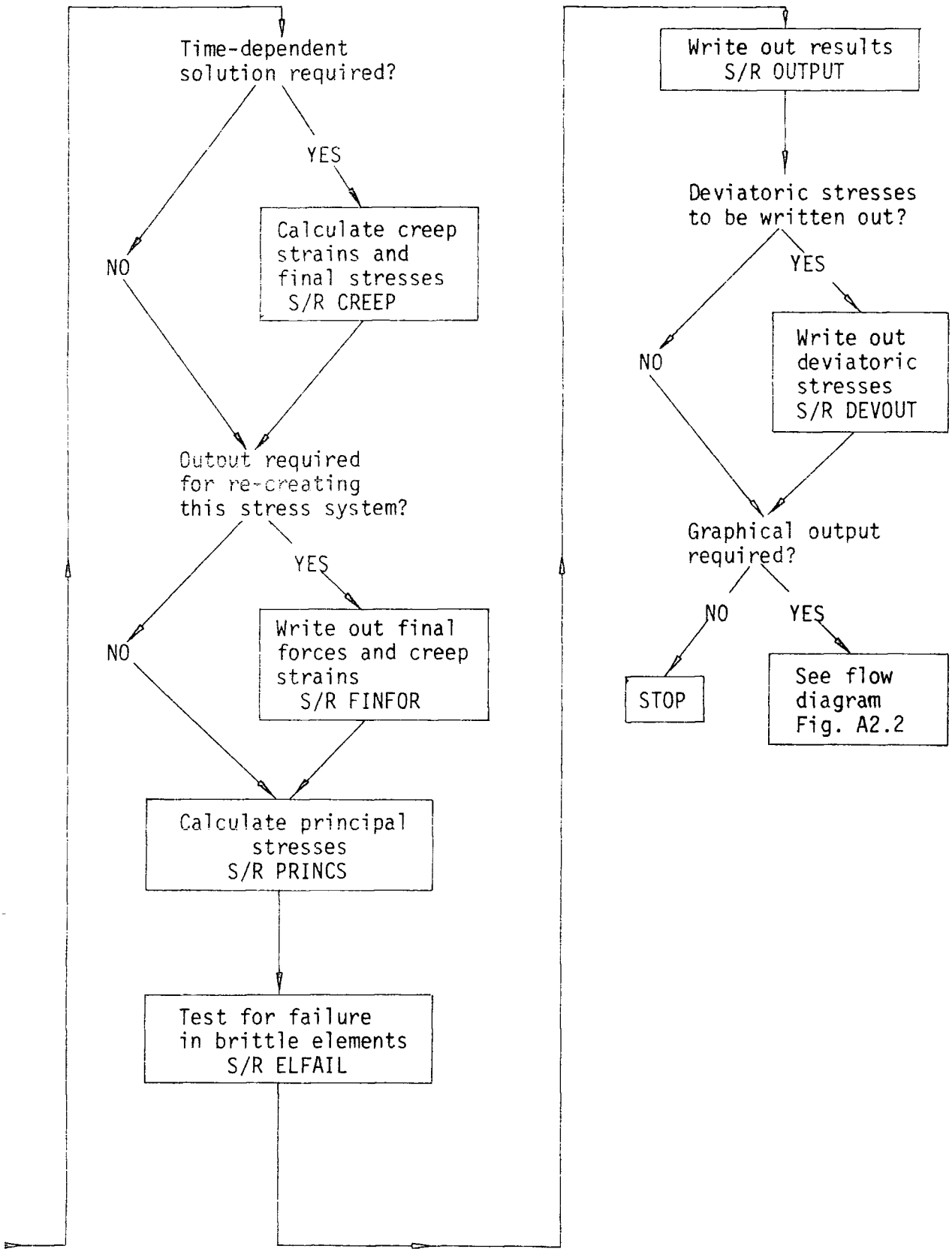

Fig. A2.1: Flow diagram for the main section of the finite element program.

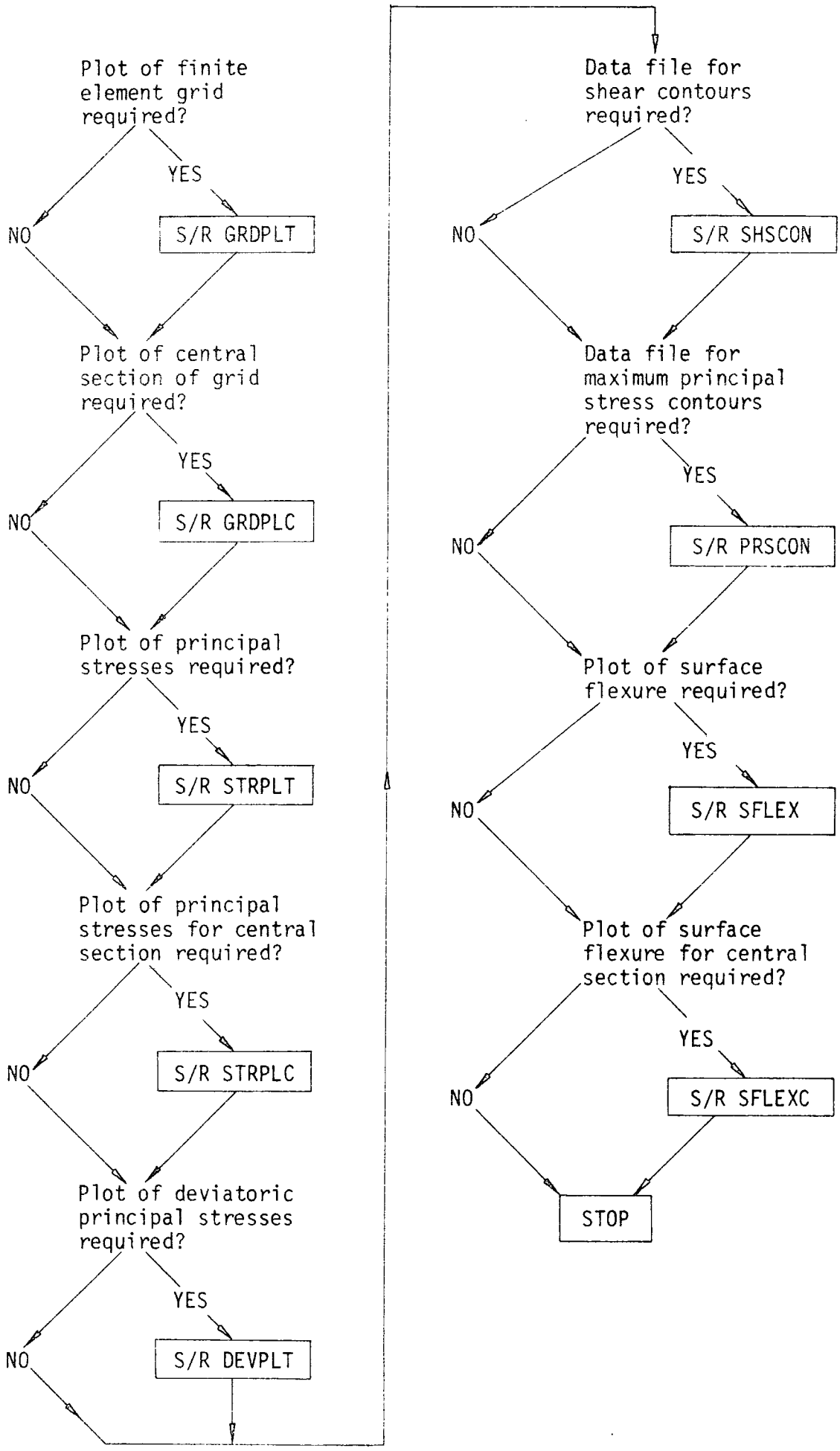

Fig. A2.2: Flow diagram for the graphics section of finite element program

COM 1 : element information

COM 2 : nodal information

COM 3 : forces and displacements

COM 4 : stiffness matrix

COM 5 : strains and stresses

COM 6 : principal stresses and failure information

COM 7 : creep information

COM 8 : fault information

The calling program and the subroutine library are listed at the end of this appendix. It is not felt to be necessary to describe each subroutine in detail here since the programs contain comment cards which adequately describe the operations being performed.

A2.2 Description of input

The input data is read into the program via three channels. These are attached to the following device numbers:

device number 1 : data on the elements, nodes and physical properties

device number 4 : data on the fault (if present)

device number 5 : title of the job

The input data will now be described in detail. The formats are given in brackets.

Device number 1

NNOD (I1Ø) : number of nodes.

I, X(I), Y(I) (I1Ø, 2E2Ø·6) : node number, x and y co-ordinates (m).

One card for each node.

NEL (I1Ø) : number of elements.

I, (NELTOP (I,J), J=1,3) (4I1Ø) : element number, element topology (numbers of the three nodes defining the element). One card for each element.

EUCRU, NUUCRU, ROUCRU (E1Ø·3, F1Ø·3, E1Ø·3) : Young's modulus (Nm^{-2}), Poisson's ratio, and density (kg m^{-3}) of the upper crust.

ELCRU, NULCRU, ROLCRU (E1Ø·3, F1Ø·3, E1Ø·3) : Young's modulus (Nm^{-2}), Poisson's ratio, and density (kg m^{-3}) of the lower crust.

EMANT, NUMANT, ROMANT (E1Ø·3, F1Ø·3, E1Ø·3) : Young's modulus (Nm^{-2}), Poisson's ratio, and density (kg m^{-3}) of the lithospheric mantle.

VISCR, VISMAN (2E1Ø·3) : viscosities of the lower crust and mantle (Pa s).

NBF (I1Ø) : number of nodes at which forces are applied.

I, FORCE (2*I-1), FORCE (2*I) (I1Ø, 2E25·15) : node number, x and y components of applied force (N). One for each node which has an applied force.

NPDX,NPDY (2I1Ø) : number of nodes with prescribed x displacements, number of nodes with prescribed y displacements.

I, DISP (2*I-1) (I1Ø, E1Ø·3) : node number, prescribed x displacement (m). One for each node fixed in x direction.

I, DISP (2*I) (I1Ø, E1Ø·3) : node number, prescribed y displacement (m). One for each node fixed in y direction.

MAXIT, MAXINC, TINC (2I1Ø, F1Ø·4) : maximum number of iterations per time increment, maximum number of time increments, length of each time increment (secs).

T, COEFF (E1Ø·3, F4·2) : tensile strength of brittle material (Nm^{-2}), coefficient of friction on closed Griffith cracks.

IBF (I1Ø) : body force marker.

IBF = 0 body forces not included

IBF $\neq$ 0 body forces included

IPS (I1Ø) : plane stress marker.

IPS = 1 plane stress

IPS ≠ 1 plane strain

ICR (I1Ø) : creep marker.

ICR = 0 Newtonian visco-elastic rheology

ICR = 1 Power law creep rheology

CLC, QLC (E1Ø·3, F1Ø·3) : pre-exponential constant and activation energy for lower crust. Only necessary if ICR = 1.

CM, QM (E1Ø·3, F1Ø·3) : pre-exponential constant and activation energy for lithospheric mantle. Only necessary if ICR = 1.

ITEM (I1Ø) : temperature anomaly marker.

ITEM = Ø no anomaly

ITEM ≠ Ø anomaly

Only necessary if ICR = 1.

NTEM (I1Ø) : number of elements with anomalous temperature. Only necessary if ICR = 1 and ITEM ≠ Ø.

NELTEM (I) (I3) : element number. One for each element with an anomalous temperature. Only necessary if ICR = 1 and ITEM ≠ Ø.

ANTEMP (F5·1) : magnitude of temperature anomaly (°C). Only necessary if ICR = 1 and ITEM ≠ Ø.

Device number 4

THETA (F1Ø·3) : hade of fault (measured anti-clockwise from positive y axis).

KN, KS (2E1Ø ·3) : normal and shear stiffnesses for the fault (Nm^{-1}).

NFS (I1Ø) : number of fault sections.

NUP (I,J), NDN (I,J) (2I1Ø) : node number on upthrown side, node number on downthrown side. Two cards for each fault section: first is for

dual node at the top of the section, second is for dual node at the base of the section. One set of two cards for each fault section.

NELF (I,1), NELF (I,2) (2I1Ø) : numbers of the two elements adjacent to the fault section. One card for each fault section.

NUMIT (I,1Ø) : maximum number of iterations allowed in subroutine FSHEAR.

FMU (F1Ø·3) : coefficient of friction on the fault.

FAC (F1Ø·3) : convergence factor.

Device number 5

TITLE (5A4) : title of job. Device number 5 defaults to *SOURCE* and program prompts for input of title.

A2.3 Description of output

Output from the program is possible via four channels. These are attached to the following device numbers:

device number 6 : this informs the user of the state of the program by writing a message when each subroutine has finished, together with the amount of CPU time currently used by the program. Device number 6 defaults to *SINK* and need not be assigned.

device number 7 : written results.

device number 9 : graphical results.

device number 2 : a data file for use with the CALCOMP package GPCP to produce a contour map of the maximum shear stress.

device number 3 : a data file for use with the CALCOMP package GPCP to produce a contour map of the maximum principal stress.

The written results are presented in the following form:

A. Echoed input data:

1. Nodal co-ordinates, applied forces and prescribed displacements.
2. Element topologies and physical properties.
3. Creep data.
4. Failure criteria data.
5. Fault data (if fault present).

B. Results:

1. Information on which fault sections have had the frictional strength exceeded (if fault present).
2. Time through which the solution has been run.
3. Nodal displacements.
4. Element stresses and failure information.
5. Deviatoric stresses (if subroutine DEVOUT was called).

The graphical output that can be generated is apparent from Figure A2.2. These subroutines are not general and it may be necessary to adjust the annotation for different models.

A2.4 Additional input/output for re-created stress systems

If a long job is run and it may be helpful to be able to re-create the results at a later time by an elastic solution, then additional output is written out via the following device numbers:

device number 8 : the node numbers and total x and y components of the forces at the end of the solution are written in format I1Ø, 2E25·15.

device number 0 : final creep strains for each element are written unformatted.

These operations are performed in subroutine FINFOR.

When the stress system is re-created, the output from device number 8 is incorporated into the data file attached to device number 1. The final creep strains are read in as input, again via device number 0, for use in subroutine CRSMIN.

A2.5 Program Test

The visco-elastic finite element program has been tested against an analytical solution for the time-dependent, visco-elastic deformation of a hollow cylinder of visco-elastic material subjected to applied internal pressure and enclosed within an elastic, steel casing. The analytical solution is given by Lee et al. (1959). The finite element model used is shown in Figure A2.3. It is only necessary to model one quarter of the cylinder because of the axes of symmetry, which are constrained for zero tangential displacement. The material properties of the model are listed in Table A2.1.

	Young's Modulus, E	Poisson's Ratio, ν	Viscosity η
Visco-elastic material	10^5	1/3	$3/8 \times 10^5$
Steel	3×10^7	$1/\sqrt{11}$	∞

Table A2.1: Material properties of the test model

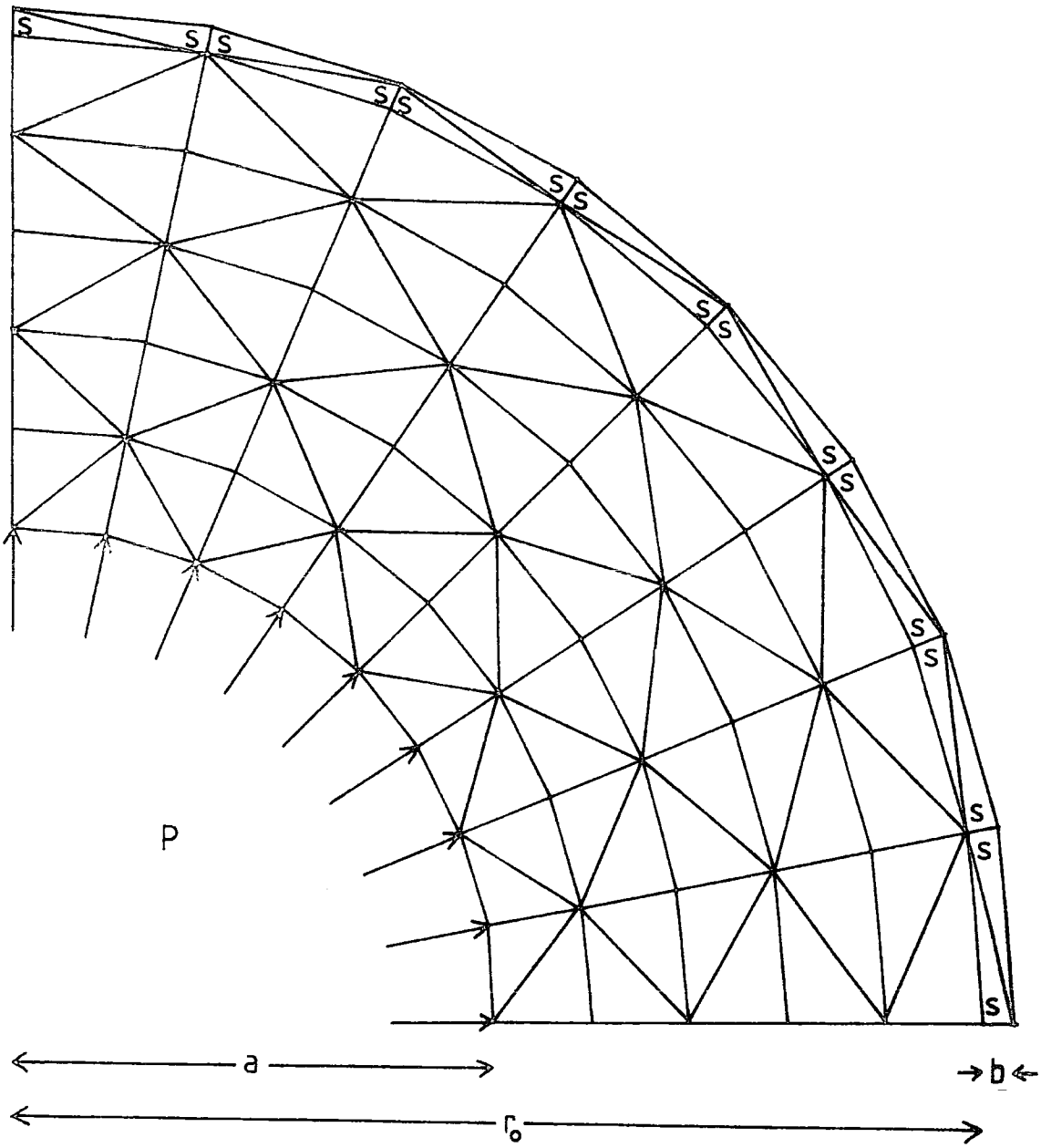

Fig. A2.3: Finite element model used for testing the program.

S steel casing

Dimensions are:

$a = 2$

$b = 3/8$

$r_0 = 4$

The tangential and radial stresses from the finite element solution (normalised with respect to the applied pressure) are plotted against the analytical solution in Figures A2.4 and A2.5 for varying time periods. The times have been normalised with respect to the relaxation time constant, which is $\frac{2(1+\nu)\eta}{E}$.

It is clear from these diagrams that the finite element results agree well with the analytical solution.

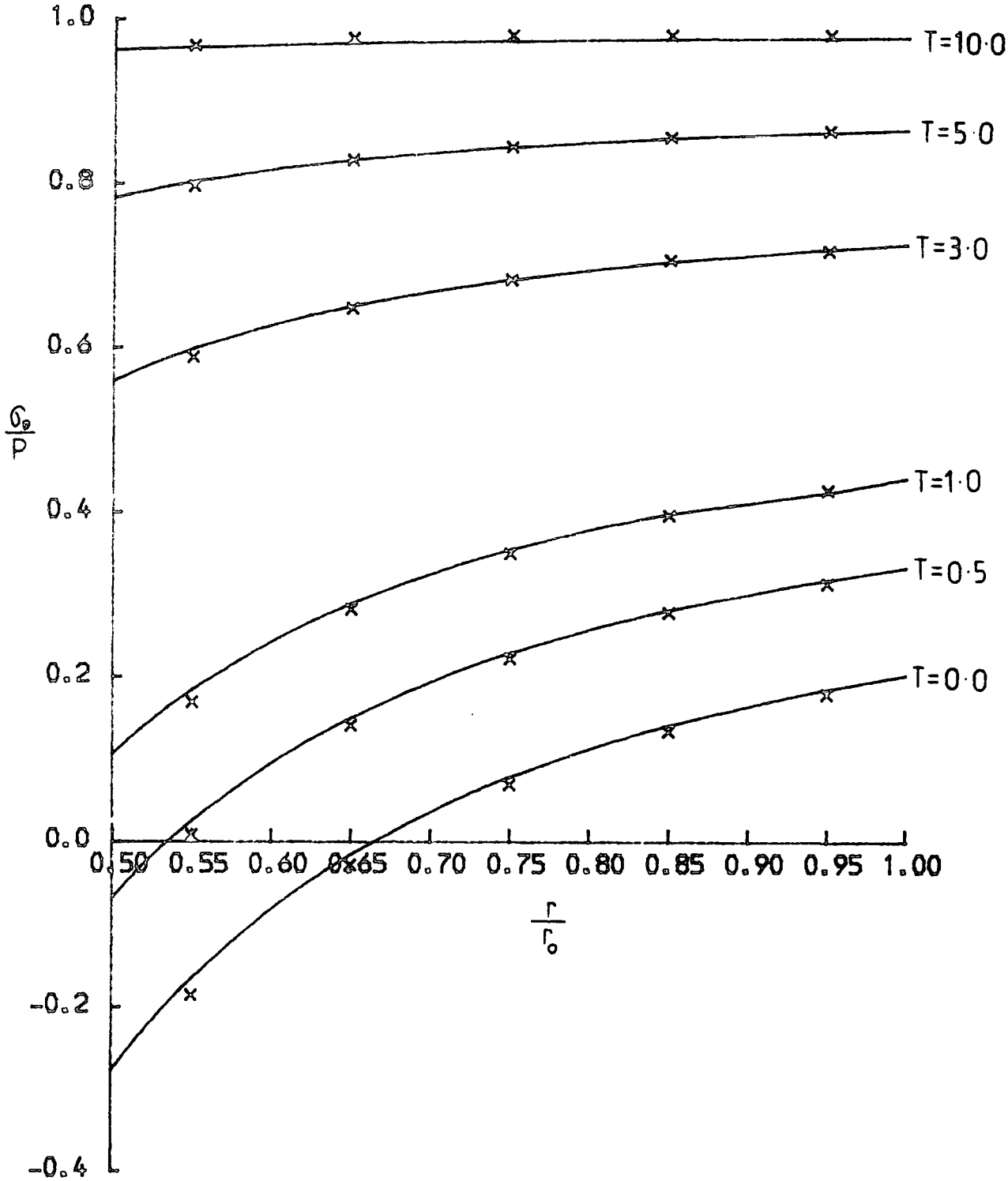

Fig. A2.4: Comparison of the analytical solutions and the finite element results for the tangential stresses.

——— analytical solutions
x finite element results
T normalised times

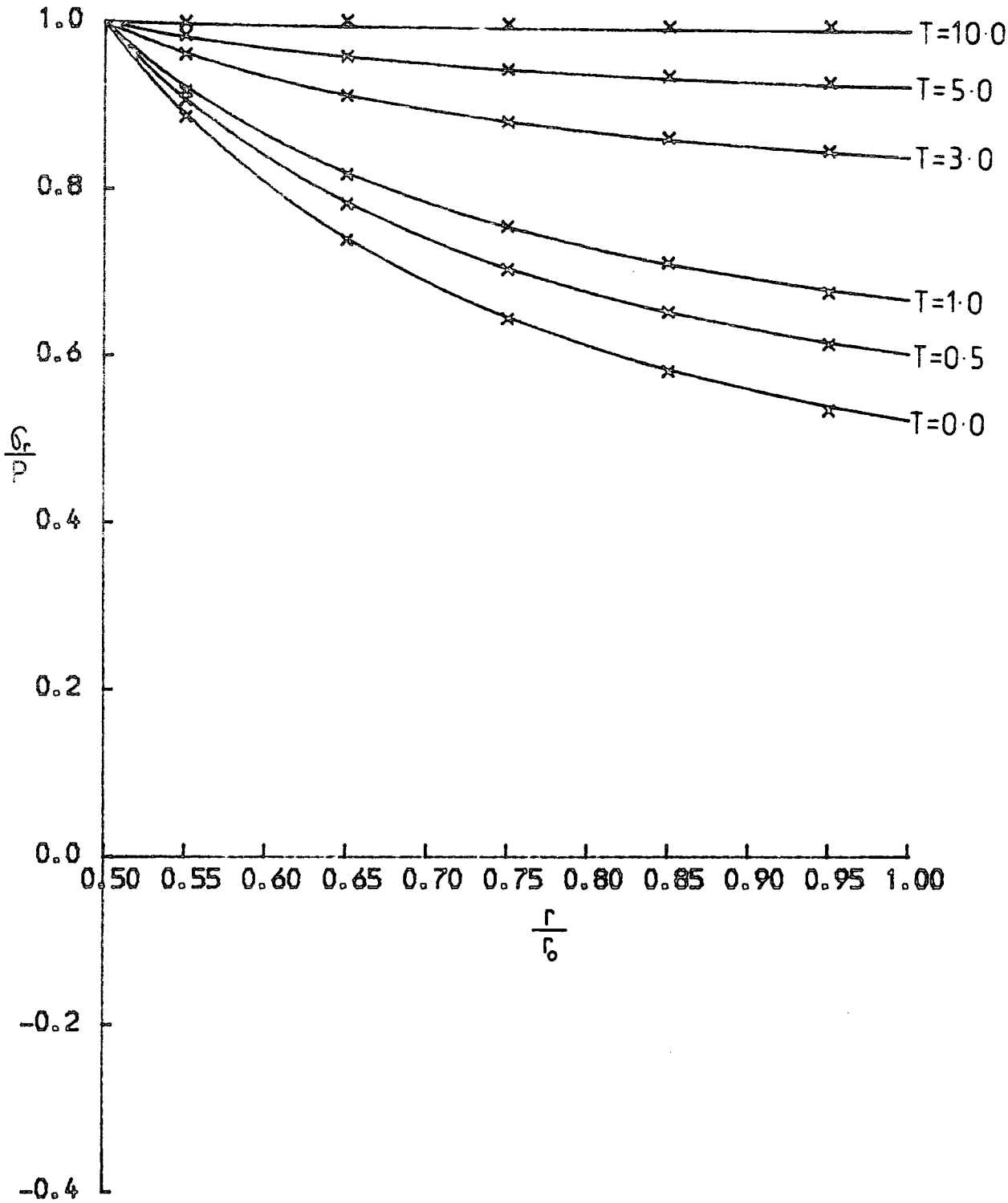

Fig. A2.5: Comparison of the analytical solutions and the finite element results for the radial stresses.

——— analytical solutions
x finite element results
T normalised times

```
C                    FEGEN
C                    =====
C
C
C*********************************************************************
C
C     THIS PROGRAM WAS WRITTEN BY D.P.MITHEN  , 1978-1980
C     THE SUBROUTINES REFERRED TO ARE CONTAINED IN FELIB
C
C*********************************************************************
C
C
C
      IMPLICIT REAL *8(A-H,O-W)
      REAL *8NU(510),NUF,K(600,200),KEL(6,6),NUCRUS,NUMANT,KF(8,8),KN,KS
      COMMON/COM1/E(510),NU,RO(510),TITLE(5),VIS(510),TIM,T,COEFF,CLC,
     1            QLC,CM,QM,ANTEMP,NEL,NELTOP(510,3),IRHEO(510),IBF,
     2            ICALL,INS,IFS,ICR,ITEM,NTEM,NELTEM(100)
      COMMON/COM2/X(300),Y(300),XPL(3),YPL(3),XS(300),YS(300),NNOD,NNOD2
      COMMON/COM3/FORCE(600),FORCE1(600),DISP(600),STORD(600),A,AA,TINC,
     1            DISP1(600),NBF,NPDX,NPDY,MAXIT,MAXINC,IFA,IFDM(6)
      COMMON/COM4/K,KEL,BT(6,3),DB(3,6),
     1            DELLIB(510),FISOS(100),ISNOD(100),KBW,KSBW
      COMMON/COM5/D(3,3),B(3,6),DLIB(3,3,510),BLIB(3,6,510),DISPEL(6),
     1            STRAIN(510,4),STRESS(510,4),STRIN(510,3),BTS(6)
      COMMON/COM6/PRINST(510,3),DEVPR(510,3),ALPHA(510),FAIL(510),
     1            FVAL(510),PHI(510),F1,F2,ITYPE(510)
      COMMON/COM7/STRBEG(510,4),STREND(510,4),STRAV(510,4),
     1            CREEPS(510,4),D1(3,4),D1C(3),FISTEL(6),PRESTR(510,4),
     2            FIST(600),DEV(4),CRSTR(510,4),CRSTR1(510,4),
     3            DEVEND(510,4),DEVBEG(510,4),PREDEV(510,4),
     4            CRIST(510,4),EFFDEV(510),TEMP(510)
      COMMON/COM8/SNORM(6,2),SHEAR(6,2),SHAV(6),SNAV(6),SHAVXS(6),THETA,
     1            FMU,FAC,R(8,8),RT(8,8),KF,RKF(8,8),RKFRT(8,8),NN(8),
     2            NELF(6,2),NUF(6,2),NDN(6,2),NUMIT,NFS,IIT(6)
C
C
      CALL TIME(0,1)
      CALL INPUT
      CALL ECHO
      CALL FORMK
C     CALL BODYF
      CALL ISOS
      CALL PDISP
      CALL FORMKF
      CALL SOLN
      CALL STRES
C     CALL CRSMIN
      CALL FSHEAR
C     CALL CREEP
C     CALL FINFOR
      CALL PRINCS
      CALL ELFAIL
      CALL OUTPUT
C     CALL DEVOUT
C
      CALL PAPER(1)
C     CALL GRDPLT
C     CALL FRAME
C     CALL GRDPLC
```

```
C       CALL FRAME
C       CALL STRPLT
C       CALL FRAME
        CALL STRPLC
        CALL FRAME
C       CALL DEVPLT
C       CALL FRAME
C       CALL SHSCON
C       CALL PRSCON
C       CALL SFLEX(0.0)
C       CALL FRAME
        CALL SFLEXC(0.0)
        CALL GREND
        STOP
        END
C
C
C
        BLOCK DATA
        IMPLICIT REAL *8(A-H,O-W)
        COMMON/COM3/FORCE(600),FORCE1(600),DISP(600),STORD(600),A,AA,TINC,
       1            DISP1(600),NBF,NPDX,NPDY,MAXIT,MAXINC,IFA,IFDM(6)
        COMMON/COM6/PRINST(510,3),DEVPR(510,3),ALPHA(510),FAIL(510),
       1            FVAL(510),PHI(510),F1,F2,ITYPE(510)
        DATA A/'FREE'/,F1/'NO'/,F2/'YES'/,AA/'NO'/
C
C
C
C
C
C
C
C
        END
C                       FELIB
C                       =====
C
C
C*********************************************************************
C
C       THIS PROGRAM WAS WRITTEN BY D.P.MITHEN , 1978-1980
C       THIS PROGRAM CONTAINS SUBROUTINES TO PERFORM PLANE STRAIN FINITE
C       ELEMENT ANALYSIS
C       THERE IS ALSO THE FACILITY TO PERFORM PLANE STRESS ELASTIC
C       SOLUTIONS
C       THESE ROUTINES WORK IN S.I. UNITS AND ARE FOR TRIANGULAR 3-NODED
C       ELEMENTS
C       X-AXIS IS FROM LEFT TO RIGHT
C       Y-AXIS IS VERTICALLY UPWARDS
C       MAX. NO. OF ELEMENTS = 510
C       MAX. NO. OF NODES = 300
C          -THESE CAN BE VARIED BY ALTERING THE ARRAY DIMENSIONS
C
C*********************************************************************
C
C
C
C       DESCRIPTION OF SUBROUTINES:
C       ---------------------------
C           INPUT  - READS IN DATA FROM CHANNEL 1
```

```
C          ECHO    - ECHOES INPUT DATA TO CHANNEL 7
C          FORMK   - FORMS THE GLOBAL STIFFNESS MATRIX,K, VIA THE
C                    ELASTICITY MATRICES,D, THE STRAIN MATRICES,B, AND
C                    THE ELEMENT STIFFNESS MATRICES,KEL
C          BODYF   - INCORPORATES BODY FORCES INTO FORCE VECTOR
C          ISOS    - COMPENSATES FOR FLUID UNDERLYING THE MODEL BY
C                    DAMPING THE DISPLACEMENTS AT THE BASE
C          PDISP   - INTRODUCES PRESCRIBED DISPLACEMENTS BY MODIFYING
C                    THE FORCE VECTOR AND THE STIFFNESS MATRIX
C          FORMKF  - FORMS THE STIFFNESS MATRICES FOR THE FAULT SECTIONS
C                    AND ADDS THEM INTO THE GLOBAL STIFFNESS MATRIX.
C                    FAULT DATA IS READ IN FROM CHANNEL 4
C          SOLN    - SOLVES FOR THE DISPLACEMENTS FOR A STATIC SOLUTION
C                    USING THE *HARWELL SUBROUTINE MA07BD
C          STRES   - CALCULATES THE STRESSES FROM THE DISPLACEMENTS VIA
C                    THE STRAINS
C          CRSMIN  - SUTRACTS INITIAL CREEP STRAINS FROM TOTAL STRAINS.
C                    INITIAL CREEP STRAINS ARE READ IN FROM CHANNEL 0
C          FSHEAR  - REMOVES EXCESS SHEAR STRESS ON THE FAULT BY
C                    ITERATIVELY MODIFYING THE FORCE APPLIED ON THE
C                    FAULT NODES
C          CREEP   - INCORPORATES THE EFFECT OF  VISCO-ELASTIC STRESS
C                    RELAXATION IN THE LOWER CRUST AND MANTLE USING
C                    EITHER NEWTONIAN VISCO-ELASTIC OR POWER LAW
C                    CREEP RHEOLOGIES
C          FINFOR  - WRITES OUT FINAL FORCE VECTOR TO CHANNEL 8 AND
C                    FINAL CREEP STRAINS TO CHANNEL 0
C          PRINCS  - CALCULATES THE PRINCIPAL STRESSES
C          ELFAIL  - TESTS FOR FAILURE USING THE MODIFIED GRIFFITH CRITERI
C          OUTPUT  - WRITES RESULTS TO CHANNEL 7
C          DEVOUT  - WRITES DEVIATORIC STRESSES TO CHANNEL 7
C          GRDPLT  - PLOTS GRID USING *GHOST GRAPHICAL SUBROUTINES
C          STRPLT  - PLOTS PRINCIPAL STRESS VECTORS AT ELEMENT CENTRES
C                    USING *GHOST GRAPHICAL SUBROUTINES
C          DEVPLT  - PLOTS DEVIATORIC STRESS VECTORS AT ELEMENT CENTRES
C                    USING *GHOST GRAPHICAL SUBROUTINES
C          SHSCON  - GENERATES A FILE FOR PLOTTING MAX. SHEAR STRESS
C                    CONTOURS USING *GPCP. FILE IS ATTACHED TO CHANNEL 2
C          PRSCON  - GENERATES A FILE FOR PLOTTING MAX. (MOST POSITIVE)
C                    PRINCIPAL STRESS CONTOURS USING *GPCP. FILE IS
C                    ATTACHED TO CHANNEL 3
C          SFLEX   - PLOTS SHAPE OF SURFACE FLEXURE USING *GHOST
C                    GRAPHICAL SUBROUTINES
C
C*********************************************************************
C
C
C
C
C
C
      SUBROUTINE INPUT
C     ----------------
C
      IMPLICIT REAL *8(A-H,O-W)
      REAL *8 NU(510),NUUCRU,NULCRU,NUMANT
      COMMON/COM1/E(510),NU,RO(510),TITLE(5),VIS(510),TIM,T,COEFF,CLC,
     1            QLC,CM,QM,ANTEMP,NEL,NELTOP(510,3),IRHEO(510),IBF,
     2            ICALL,INS,IPS,ICR,ITEM,NTEM,NELTEM(100)
      COMMON/COM2/X(300),Y(300),XPL(3),YPL(3),XS(300),YS(300),NNOD,NNOD2
```

```
      COMMON/COM3/FORCE(600),FORCE1(600),DISP(600),STORD(600),A,AA,TINC,
     1            DISP1(600),NBF,NPDX,NPDY,MAXIT,MAXINC,IFA,IFDM(6)
C
C**** READ IN TITLE OF JOB ***************************************
C
      WRITE(6,99)
   99 FORMAT(/,'READ IN TITLE OF JOB (UP TO 30 CHARACTERS)')
      READ(5,98)TITLE
   98 FORMAT(5A8)
C
C**** READ IN NODE INFORMATION ***********************************
C
      READ(1,97)NNOD
   97 FORMAT(I10)
      DO 49 N1=1,NNOD
   49 READ(1,96)I,X(I),Y(I)
   96 FORMAT(I10,2E20.6)
C
C**** READ IN ELEMENT INFORMATION ********************************
C
      READ(1,97)NEL
      DO 48 N2=1,NEL
   48 READ(1,95)I,(NELTOP(I,J),J=1,3)
   95 FORMAT(4I10)
      READ(1,94)EUCRU,NUUCRU,ROUCRU
      READ(1,94)ELCRU,NULCRU,ROLCRU
      READ(1,94)EMANT,NUMANT,ROMANT
   94 FORMAT(E10.3,F10.3,E10.3)
      DO 47 N3=1,NEL
      I1=NELTOP(N3,1)
      I2=NELTOP(N3,2)
      I3=NELTOP(N3,3)
C
C**** ASSUMES MODEL HAS THREE LAYERS;0 TO -20,-20 TO -35,-35 TO -100KM
C**** AND THESE REPRESENT UPPER CRUST(BRITTLE),LOWER CRUST AND MANTLE
C
      YCON=-20.0E3
      YMOHO=-35.0E3
C     YELAS=-50.0E3
      DEPTH=(Y(I1)+Y(I2)+Y(I3))/3.0
      IF (DEPTH.GT.YCON) IRHEO(N3)=0
      IF (DEPTH.LT.YCON.AND.DEPTH.GT.YMOHO) IRHEO(N3)=1
      IF (DEPTH.LT.YMOHO) IRHEO(N3)=2
      IF (IRHEO(N3).NE.2) GO TO 100
      E(N3)=EMANT
      NU(N3)=NUMANT
      RO(N3)=ROMANT
      GO TO 47
  100 IF (IRHEO(N3).NE.1) GO TO 104
      E(N3)=ELCRU
      NU(N3)=NULCRU
      RO(N3)=ROLCRU
      GO TO 47
  104 E(N3)=EUCRU
      NU(N3)=NUUCRU
      RO(N3)=ROUCRU
   47 CONTINUE
      READ(1,88)VISCR,VISMAN
   88 FORMAT(2E10.3)
      DO 38 N9=1,NEL
```

```
      IF (IRHEO(N9).EQ.0) VIS(N9)=AA
      IF (IRHEO(N9).EQ.1) VIS(N9)=VISCR
      IF (IRHEO(N9).EQ.2) VIS(N9)=VISMAN
   38 CONTINUE
C
C**** READ IN BOUNDARY FORCE INFORMATION ********************************
C
      NNOD2=NNOD*2
      DO 46 N4=1,600
   46 FORCE(N4)=0.0
      READ(1,97)NBF
      IF (NBF.EQ.0) GO TO 101
      DO 45 N5=1,NBF
   45 READ(1,87)I,FORCE(2*I-1),FORCE(2*I)
   87 FORMAT(I10,2E25.15)
  101 CONTINUE
      DO 37 NN=1,NNOD2
   37 FORCE1(NN)=FORCE(NN)
C
C**** READ IN PRESCRIBED DISPLACEMENTS ***********************************
C
      READ(1,92)NPDX,NPDY
   92 FORMAT(2I10)
      DO 44 N5=1,NNOD2
   44 DISP(N5)=A
      IF (NPDX.EQ.0) GO TO 102
      DO 43 N6=1,NPDX
   43 READ(1,91)I,DISP(2*I-1)
   91 FORMAT(I10,E10.3)
  102 IF (NPDY.EQ.0) GO TO 103
      DO 42 N7=1,NPDY
   42 READ(1,91)I,DISP(2*I)
  103 DO 40 N9=1,NNOD2
   40 DISP1(N9)=DISP(N9)
C
C**** READ IN CREEP ITERATION DATA ***************************************
C
      READ(1,90)MAXIT,MAXINC,TINC
   90 FORMAT(2I10,F10.4)
C
C**** READ IN FAILURE DATA ***********************************************
C
      READ(1,85)T,COEFF
   85 FORMAT(E10.3,F4.2)
C
C**** READ IN BODY FORCE MARKER ******************************************
C**** IF IBF=0 BODY FORCES NOT INCLUDED
C
      READ(1,97)IBF
C
C**** READ IN PLANE STRESS MARKER IF REQUIRED ****************************
C**** IF IPS=1 PLANE STRESS , OTHERWISE PLANE STRAIN
C
      READ(1,97)IPS
C
C**** READ IN CREEP MARKER ***********************************************
C**** IF ICR=0 NEWTONIAN , IF ICR=1 POWER LAW
C
      READ(1,97)ICR
C
```

```
C**** IF POWER LAW READ IN CONSTANT AND ACTIVATION ENERGY ********* ****
C**** UNITS ARE /CU.KB/S AND KCAL/MOL
C
      IF (ICR.EQ.0) GO TO 105
C
C**** LOWER CRUST VALUES
C
      READ(1,84)CLC,QLC
   84 FORMAT(E10.3,F10.3)
C
C**** MANTLE VALUES
C
      READ(1,84)CM,QM
C
C**** READ IN TEMPERATURE ANOMALY MARKER ******************************
C**** IF ITEM=0 , NO ANOMALY
C
      READ(1,97)ITEM
      IF (ITEM.EQ.0) GO TO 105
C
C**** READ ELEMENT NUMBERS ****************************************
C
      READ(1,97)NTEM
      DO 36 I=1,NTEM
   36 READ(1,83)NELTEM(I)
   83 FORMAT(I3)
C
C**** READ VALUE OF ANOMALY (DEGREES C) ******************************
C
      READ(1,82)ANTEMP
   82 FORMAT(F5.1)
C
  105 ICALL=0
      IFA=0
      INS=0
      TIM=0.0
      TIM=0.0
      WRITE(6,93)
   93 FORMAT(/,'SUBROUTINE INPUT COMPLETED')
      CALL TIME(1,1)
      RETURN
      END
C
C
C
C
C
      SUBROUTINE ECHO
C     ---------------
C
      IMPLICIT REAL *8(A-H,O-W)
      REAL *8 NU(510)
      COMMON/COM1/E(510),NU,RO(510),TITLE(5),VIS(510),TIM,T,COEFF,CLC,
     1            QLC,CM,QM,ANTEMP,NEL,NELTOP(510,3),IRHEO(510),IBF,
     2            ICALL,INS,IPS,ICR,ITEM,NTEM,NELTEM(100)
      COMMON/COM2/X(300),Y(300),XPL(3),YPL(3),XS(300),YS(300),NNOD,NNOD2
      COMMON/COM3/FORCE(600),FORCE1(600),DISP(600),STORD(600),A,AA,TINC,
     1            DISP1(600),NBF,NPDX,NPDY,MAXIT,MAXINC,IFA,IFDM(6)
C
C**** WRITE OUT TITLE OF JOB ******************************************
```

```
C
      WRITE(7,99)TITLE
   99 FORMAT(1H ,5A8)
      WRITE(7,98)
   98 FORMAT(1H0,'*****INPUT DATA IS:')
C
C**** WRITE OUT NODE INFORMATION ************************************
C
      WRITE(7,97)NNOD
   97 FORMAT(1H-,'NUMBER OF NODES = ',I3)
      WRITE(7,96)
   96 FORMAT(1H0,'NODE NO.',5X,'X CO-ORD.',5X,'Y CO-ORD.',5X,'X FORCE',
     1        5X,'Y FORCE',5X,'X DISP.',5X,'Y DISP.')
      DO 49 I=1,NNOD
      IF (DISP(2*I-1).EQ.A.AND.DISP(2*I).EQ.A) WRITE(7,95)I,X(I),Y(I),
     1   FORCE(2*I-1),FORCE(2*I),DISP(2*I-1),DISP(2*I)
      IF (DISP(2*I-1).EQ.A.AND.DISP(2*I).NE.A) WRITE(7,94)I,X(I),Y(I),
     1   FORCE(2*I-1),FORCE(2*I),DISP(2*I-1),DISP(2*I)
      IF (DISP(2*I-1).NE.A.AND.DISP(2*I).EQ.A) WRITE(7,93)I,X(I),Y(I),
     1   FORCE(2*I-1),FORCE(2*I),DISP(2*I-1),DISP(2*I)
   49 IF (DISP(2*I-1).NE.A.AND.DISP(2*I).NE.A) WRITE(7,92)I,X(I),Y(I),
     1   FORCE(2*I-1),FORCE(2*I),DISP(2*I-1),DISP(2*I)
   95 FORMAT(1H ,2X,I3,7X,E10.3,3X,E10.3,2(2X,E10.3),5X,A4,8X,A4)
   94 FORMAT(1H ,2X,I3,7X,E10.3,3X,E10.3,2(2X,E10.3),5X,A4,6X,E10.3)
   93 FORMAT(1H ,2X,I3,7X,E10.3,3X,E10.3,2(2X,E10.3),4X,E10.3,3X,A4)
   92 FORMAT(1H ,2X,I3,7X,E10.3,3X,E10.3,2(2X,E10.3),2X,2(2X,E10.3))
C
C**** WRITE OUT ELEMENT INFORMATION *********************************
C
      WRITE(7,91)NEL
   91 FORMAT(1H-,'NUMBER OF ELEMENTS = ',I3)
      WRITE(7,90)
   90 FORMAT(1H0,'ELEMENT NO.',5X,'ELEMENT TOPOLOGY',5X,'YOUNGS MOD.',
     1        5X,'POISSONS RATIO',5X,'DENSITY',5X,'IRHEO',5X,
     2        'VISCOSITY')
      DO 48 I=1,NEL
      IF (VIS(I).EQ.AA) WRITE(7,84)I,(NELTOP(I,J),J=1,3),E(I),NU(I),
     1   RO(I),IRHEO(I),VIS(I)
   48 IF (VIS(I).NE.AA) WRITE(7,89)I,(NELTOP(I,J),J=1,3),E(I),NU(I),
     1   RO(I),IRHEO(I),VIS(I)
   84 FORMAT(1H ,4X,I3,9X,3(I3,3X),1X,E10.3,8X,F10.3,7X,E10.3,6X,I1,
     1        10X,A4)
   89 FORMAT(1H ,4X,I3,9X,3(I3,3X),1X,E10.3,8X,F10.3,7X,E10.3,6X,I1,
     1        8X,E10.3)
C
C**** WRITE OUT CREEP ITERATION DATA ********************************
C
      IF (ICR.EQ.0) GO TO 100
      WRITE(7,79)
   79 FORMAT(1H-,'POWER LAW CREEP RHEOLOGY')
      IF (ITEM.EQ.0)  GO TO 101
      WRITE(7,78)ANTEMP
   78 FORMAT(1H0,'TEMPERATURE ANOMALY (HIGH) OF ',F5.1,'DEGREES C.')
      WRITE(7,77)
   77 FORMAT(1H ,'IN ELEMENT NUMBERS:')
      WRITE(7,76)(NELTEM(I),I=1,NTEM)
   76 FORMAT(1H ,20I5)
      GO TO 101
  100 WRITE(7,80)
   80 FORMAT(1H-,'NEWTONIAN VISCO-ELASTIC RHEOLOGY')
```

```
  101 WRITE(7,87)MAXIT
   87 FORMAT(1H-,'MAX. NO. OF ITERATIONS PER. TIME INCREMENT = ',I2)
      WRITE(7,86)MAXINC
   86 FORMAT(1H0,'NO. OF TIME INCREMENTS = ',I4)
      WRITE(7,85)TINC
   85 FORMAT(1H0,'VALUE OF EACH TIME INCREMENT = ',E11.4,'SECS.')
C
C**** WRITE OUT FAILURE INFORMATION ***********************************
C
      WRITE(7,82)T
   82 FORMAT(1H-,'TENSILE STRENGTH OF UPPER CRUST =',E10.3,'N/SQ.M')
      WRITE(7,81)COEFF
   81 FORMAT(1H0,'COEFFICIENT OF INTERNAL FRICTION = ',F4.2)
      WRITE(6,88)
   88 FORMAT(/,'SUBROUTINE ECHO COMPLETED')
      CALL TIME(1,1)
      RETURN
      END
C
C
C
C
C
      SUBROUTINE FORMK
C     ----------------
C
      IMPLICIT REAL *8(A-H,O-W)
      REAL *8 NU(510),NUF,K(600,200),KEL(6,6)
      COMMON/COM1/E(510),NU,RO(510),TITLE(5),VIS(510),TIM,T,COEFF,CLC,
     1            QLC,CM,QM,ANTEMP,NEL,NELTOP(510,3),IRHEO(510),IBF,
     2            ICALL,INS,IPS,ICR,ITEM,NTEM,NELTEM(100)
      COMMON/COM2/X(300),Y(300),XPL(3),YPL(3),XS(300),YS(300),NNOD,NNOD2
      COMMON/COM4/K,KEL,BT(6,3),DB(3,6),
     1        DELLIB(510),FISOS(100),ISNOD(100),KBW,KSBW
      COMMON/COM5/D(3,3),B(3,6),DLIB(3,3,510),BLIB(3,6,510),DISPEL(6),
     1            STRAIN(510,4),STRESS(510,4),STRIN(510,3),BTS(6)
C
C**** TO CALCULATE THE BAND-WIDTH OF THE GLOBAL STIFFNESS MATRIX *******
C
      MAXND=0
      DO 1 J=1,NEL
      ND1=IABS(NELTOP(J,1)-NELTOP(J,2))
      ND2=IABS(NELTOP(J,2)-NELTOP(J,3))
      ND3=IABS(NELTOP(J,3)-NELTOP(J,1))
    1 MAXND=MAX0(ND1,ND2,ND3,MAXND)
      KSBW=(2*MAXND)+2
      KBW=(2*KSBW)-1
      IF (IPS.EQ.1) WRITE(7,502)
  502 FORMAT(1H-,'PLANE STRESS')
      WRITE(7,98)KBW
   98 FORMAT(1H-,'BAND-WIDTH OF STIFFNESS MATRIX =',I3)
C
C**** TO INITIALISE THE GLOBAL STIFFNESS MATRIX ************************
C
      DO 2 J1=1,NNOD2
      DO 2 J2=1,KBW
    2 K(J1,J2)=0.0
      DO 3 I=1,NEL
      IF (IPS.EQ.1) GO TO 500
C
```

```
C**** TO FORM THE ELASTICITY MATRIX ,D, FOR PLANE STRAIN ***************
C
      CONST1=E(I)*(1.0-NU(I))/((1.0+NU(I))*(1.0-2*NU(I)))
      CONST2=NU(I)/(1.0-NU(I))
      D(1,1)=CONST1
      D(1,2)=CONST1*CONST2
      D(1,3)=0.0
      D(2,1)=CONST1*CONST2
      D(2,2)=CONST1
      D(2,3)=0.0
      D(3,1)=0.0
      D(3,2)=0.0
      D(3,3)=CONST1*(1.0-CONST2)/2.0
      GO TO 501
C
C**** TO FORM THE ELASTICITY MATRIX ,D, FOR PLANE STRESS ***************
C
  500 CONST3=E(I)/(1.0-(NU(I)*NU(I)))
      D(1,1)=CONST3
      D(1,2)=NU(I)*CONST3
      D(1,3)=0.0
      D(2,1)=NU(I)*CONST3
      D(2,2)=CONST3
      D(2,3)=0.0
      D(3,1)=0.0
      D(3,2)=0.0
      D(3,3)=((1.0-NU(I))*CONST3)/2.0
C
C**** TO FORM THE STRAIN MATRIX ,B ************************************
C
  501 DX1=X(NELTOP(I,1))
      DX2=X(NELTOP(I,2))
      DX3=X(NELTOP(I,3))
      DY1=Y(NELTOP(I,1))
      DY2=Y(NELTOP(I,2))
      DY3=Y(NELTOP(I,3))
      DELTA2=(DX1*DY2)+(DX2*DY3)+(DX3*DY1)-(DY1*DX2)-(DY2*DX3)-(DY3*DX1)
C
C**** DELTA2 IS TWICE THE AREA OF THE ELEMENT *************************
C
      B1=(DY2-DY3)/DELTA2
      B2=(DY3-DY1)/DELTA2
      B3=(DY1-DY2)/DELTA2
      C1=(DX3-DX2)/DELTA2
      C2=(DX1-DX3)/DELTA2
      C3=(DX2-DX1)/DELTA2
      B(1,1)=B1
      B(1,2)=0.0
      B(1,3)=B2
      B(1,4)=0.0
      B(1,5)=B3
      B(1,6)=0.0
      B(2,1)=0.0
      B(2,2)=C1
      B(2,3)=0.0
      B(2,4)=C2
      B(2,5)=0.0
      B(2,6)=C3
      B(3,1)=C1
      B(3,2)=B1
```

```
      B(3,3)=C2
      B(3,4)=B2
      B(3,5)=C3
      B(3,6)=B3
C
C**** STORE DELTA2 , D , B FOR EACH ELEMENT IN LIBRARIES ***************)
C
      DELTA2=DABS(DELTA2)
      DELLIB(I)=DELTA2
      DO 49 N1=1,3
      DO 49 N2=1,3
   49 DLIB(N1,N2,I)=D(N1,N2)
      DO 48 N3=1,3
      DO 48 N4=1,6
   48 BLIB(N3,N4,I)=B(N3,N4)
C
C**** TRANSPOSE B TO BT ***********************************************)
C
      DO 47 M1=1,3
      DO 47 M2=1,6
   47 BT(M2,M1)=B(M1,M2)
C
C**** MULTIPLY D BY B TO GIVE DB **************************************)
C
      DO 46 K1=1,3
      DO 46 K2=1,6
   46 DB(K1,K2)=(D(K1,1)*B(1,K2))+(D(K1,2)*B(2,K2))+(D(K1,3)*B(3,K2))
C
C**** MULTIPLY BT BY DB TO GIVE KEL ***********************************)
C
      DO 45 K3=1,6
      DO 45 K4=1,6
      KEL(K3,K4)=(BT(K3,1)*DB(1,K4))+(BT(K3,2)*DB(2,K4))+
     1           (BT(K3,3)*DB(3,K4))
C
C**** MULTIPLY KEL BY ELEMENT AREA TO GIVE ELEMENT STIFFNESS MATRIX
C
   45 KEL(K3,K4)=KEL(K3,K4)*DELTA2/2.0
C
C**** TO FORM THE GLOBAL STIFFNESS MATRIX *****************************)
C
      L2=-2
      DO 44 NN1=1,3
      L2=L2+2
      DO 44 NN2=1,2
      L1=-2
      DO 44 NN3=1,3
      L1=L1+2
      DO 44 NN4=1,2
      NX=NELTOP(I,NN1)
      NX=2*NX-2+NN2
      NY=NELTOP(I,NN3)
      NY=2*NY-2+NN4
      NXNEW=NX-NY+KSBW
      IF (NXNEW.LT.1.OR.NXNEW.GT.KBW) GO TO 100
      M1=L1+NN4
      M2=L2+NN2
   44 K(NY,NXNEW)=K(NY,NXNEW)+KEL(M1,M2)
    3 CONTINUE
      GO TO 101
```

```
  100 WRITE(6,97)
   97 FORMAT(1H0,'*ERROR* A COMPONENT OF THE GLOBAL STIFFNESS MATRIX
     1        LIES OUTSIDE THE BAND-WIDTH (<1 OR >KBW)')
      STOP
  101 WRITE(6,96)
   96 FORMAT(/,'SUBROUTINE FORMK COMPLETED')
      CALL TIME(1,1)
      RETURN
      END
C
C
C
C
C
      SUBROUTINE BODYF
C     ----------------
C
      IMPLICIT REAL *8(A-H,O-W)
      REAL *8 NU(510),K(600,200),KEL(6,6)
      COMMON/COM1/E(510),NU,RO(510),TITLE(5),VIS(510),TIM,T,COEFF,CLC,
     1            QLC,CM,QM,ANTEMP,NEL,NELTOP(510,3),IRHEO(510),IBF,
     2            ICALL,INS,IPS,ICR,ITEM,NTEM,NELTEM(100)
      COMMON/COM2/X(300),Y(300),XPL(3),YPL(3),XS(300),YS(300),NNOD,NNOD2
      COMMON/COM3/FORCE(600),FORCE1(600),DISP(600),STORD(600),A,AA,TINC,
     1            DISP1(600),NBF,NPDX,NPDY,MAXIT,MAXINC,IFA,IFDM(6)
      COMMON/COM4/K,KEL,BT(6,3),DB(3,6),
     1            DELLIB(510),FISOS(100),ISNOD(100),KBW,KSBW
      DO 1 I=1,NEL
C
C**** CALCULATE THE TOTAL BODY FORCE DUE TO ELEMENT I ******************
C
      DELTA2=DELLIB(I)
      BF=-(DELTA2/2.0)*RO(I)*9.81
C
C**** ADD 1/3 OF THE BODY FORCE TO EACH NODE OF ELEMENT I ***************
C
      N1Y=NELTOP(I,1)*2
      N2Y=NELTOP(I,2)*2
      N3Y=NELTOP(I,3)*2
      FORCE(N1Y)=FORCE(N1Y)+(BF/3.0)
      FORCE(N2Y)=FORCE(N2Y)+(BF/3.0)
    1 FORCE(N3Y)=FORCE(N3Y)+(BF/3.0)
      DO 2 J=1,NNOD2
    2 FORCE1(J)=FORCE(J)
      IBF=1
      WRITE(6,99)
   99 FORMAT(/,'SUBROUTINE BODYF COMPLETED')
      CALL TIME(1,1)
      RETURN
      END
C
C
C
C
C
      SUBROUTINE ISOS
C     ---------------
C
      IMPLICIT REAL *8(A-H,O-W)
      REAL *8 K(600,200),KEL(6,6)
```

```
      COMMON/COM2/X(300),Y(300),XPL(3),YPL(3),XS(300),YS(300),NNOD,NNOD2
      COMMON/COM4/K,KEL,BT(6,3),DB(3,6),
     1            DELLIB(510),FISOS(100),ISNOD(100),KBW,KSBW
C
C**** ASSUMES NODE NUMBERING INCREASES FROM LEFT TO RIGHT  **************
C**** DENSITY OF UNDERLYING MANTLE = 3.3E3 KG./CU.M.       *************
C
C**** TO FIND THE BASE NODES ****************************************
C
      YMIN=0.0
      DO 49 I=1,NNOD
   49 YMIN=AMIN1(Y(I),YMIN)
      NODCNT=0
      DO 48 I=1,NNOD
      IF (Y(I).NE.YMIN) GO TO 48
      NODCNT=NODCNT+1
      ISNOD(NODCNT)=I
   48 CONTINUE
C
C**** TO CALCULATE FISOS FOR END NODES ********************************
C
      N1=ISNOD(1)
      N2=ISNOD(2)
      FISOS(1)=((X(N2)-X(N1))/2.0)*3.3E3*9.81
      NM=NODCNT-1
      N3=ISNOD(NM)
      N4=ISNOD(NODCNT)
      FISOS(NODCNT)=((X(N4)-X(N3))/2.0)*3.3E3*9.81
C
C**** TO CALCULATE FISOS FOR OTHER BASE NODES *************************
C
      DO 47 I1=2,NM
      NMN=I1-1
      NPL=I1+1
      N5=ISNOD(NMN)
      N6=ISNOD(NPL)
   47 FISOS(I1)=((X(N6)-X(N5))/2.0)*3.3E3*9.81
C
C**** TO INCORPORATE FISOS INTO K *************************************
C
      DO 46 I2=1,NODCNT
      NY=2*ISNOD(I2)
   46 K(NY,KSBW)=K(NY,KSBW)+FISOS(I2)
      WRITE(6,99)
   99 FORMAT(/,'SUBROUTINE ISOS COMPLETED')
      CALL TIME(1,1)
      RETURN
      END
C
C
C
C
C
      SUBROUTINE FDISP
C     ----------------
C
      IMPLICIT REAL *8(A-H,O-W)
      REAL *8 K(600,200),KEL(6,6)
      COMMON/COM2/X(300),Y(300),XPL(3),YPL(3),XS(300),YS(300),NNOD,NNOD2
      COMMON/COM3/FORCE(600),FORCE1(600),DISP(600),STORD(600),A,AA,TINC,
```

```
     1              DISP1(600),NBF,NPDX,NPDY,MAXIT,MAXINC,IFA,IFDM(6)
      COMMON/COM4/K,KEL,BT(6,3),DB(3,6),
     1              DELLIB(510),FISOS(100),ISNOD(100),KBW,KSBW
C
C**** FIND THE PRESCRIBED DISPLACEMENTS ******************************
C
      DO 49 I=1,NNOD
      IX=2*I-1
      IY=2*I
      DO 48 J=IX,IY
      IF (DISP1(J).EQ.A) GO TO 48
C
C**** FIND AND ADJUST ELEMENTS IN THE SAME ROW OF K ******************
C
      DO 45 N=1,KBW
   45 K(J,N)=0.0
C
C**** ADJUST THE DIAGONAL ELEMENTS AND THE FORCE VECTOR ***************
C
      FORCE(J)=DISP1(J)*1.0E11
      K(J,KSBW)=1.0E11
      FORCE1(J)=FORCE(J)
   48 CONTINUE
   49 CONTINUE
      IF (ICALL.EQ.1) RETURN
      WRITE(6,99)
   99 FORMAT(/,'SUBROUTINE PDISP COMPLETED')
      CALL TIME(1,1)
      RETURN
      END
C
C
C
C
C
      SUBROUTINE FORMKF
C     ------------------------
C
      IMPLICIT REAL *8(A-H,O-W)
      REAL *8K(600,200),KEL(6,6),KF(8,8),KN,KS
      COMMON/COM2/X(300),Y(300),XPL(3),YPL(3),XS(300),YS(300),NNOD,NNOD2,
      COMMON/COM4/K,KEL,BT(6,3),DB(3,6),
     1              DELLIB(510),FISOS(100),ISNOD(100),KBW,KSBW
      COMMON/COM8/SNORM(6,2),SHEAR(6,2),SHAV(6),SNAV(6),SHAVXS(6),THETA,
     1              FMU,FAC,R(8,8),RT(8,8),KF,RKF(8,8),RKFRT(8,8),NN(8),
     2              NELF(6,2),NUF(6,2),NDN(6,2),NUMIT,NFS,IIT(6)
C
      PI=4.0*ATAN(1.0)
C
C**** READ IN HADE OF FAULT (MEASURED ANTICLOCKWISE FROM +VE. Y-AXIS ***
C
      READ(4,96)THETA
   96 FORMAT(F10.3)
      RTHETA=THETA*(PI/180.0)
      A1=DCOS(RTHETA)
      A2=DSIN(RTHETA)
C
C**** FORM ROTATION MATRIX , R , AND TRANSPOSE , RT ******************
C
      DO 46 K5=1,8
```

```
      DO 46 K6=1,8
   46 R(K5,K6)=0.0
      DO 45 K7=1,8
   45 R(K7,K7)=A1
      DO 44 K8=1,7,2
   44 R(K8,K8+1)=-A2
      DO 43 K9=2,8,2
   43 R(K9,K9-1)=A2
      DO 42 K10=1,8
      DO 42 K11=1,8
   42 RT(K10,K11)=R(K11,K10)
C
C**** READ IN NORMAL AND SHEAR STIFFNESSES ******************************
C
      READ(4,99)KN,KS
   99 FORMAT(2E10.3)
C
C**** READ IN NUMBER OF FAULT SECTIONS ******************************
C
      READ(4,98)NFS
   98 FORMAT(I10)
C
C**** READ IN NODE NUMBERS FOR EACH FAULT SECTION ************************
C**** NUP ARE NODES ON UPTHROWN SIDE ; NDN ARE NODES ON DOWNTHROWN SIDE
C
      DO 1 I=1,NFS
      DO 49 J=1,2
   49 READ(4,97)NUP(I,J),NDN(I,J)
   97 FORMAT(2I10)
C
C**** FORM FAULT SECTION STIFFNESS MATRIX , KF ***************************
C
      DO 48 K1=1,8
      DO 48 K2=1,8
   48 KF(K1,K2)=0.0
      KF(1,1)=2.0*KN
      KF(1,3)=KN
      KF(1,5)=-KN
      KF(1,7)=-2.0*KN
      KF(2,2)=2.0*KS
      KF(2,4)=KS
      KF(2,6)=-KS
      KF(2,8)=-2.0*KS
      KF(3,1)=KN
      KF(3,3)=2.0*KN
      KF(3,5)=-2.0*KN
      KF(3,7)=-KN
      KF(4,2)=KS
      KF(4,4)=2.0*KS
      KF(4,6)=-2.0*KS
      KF(4,8)=-KS
      KF(5,1)=-KN
      KF(5,3)=-2.0*KN
      KF(5,5)=2.0*KN
      KF(5,7)=KN
      KF(6,2)=-KS
      KF(6,4)=-2.0*KS
      KF(6,6)=2.0*KS
      KF(6,8)=KS
      KF(7,1)=-2.0*KN
```

```
      KF(7,3)=-KN
      KF(7,5)=KN
      KF(7,7)=2.0*KN
      KF(8,2)=-2.0*KS
      KF(8,4)=-KS
      KF(8,6)=KS
      KF(8,8)=2.0*KS
      DO 47 K3=1,8
      DO 47 K4=1,8
   47 KF(K3,K4)=KF(K3,K4)/6.0
C
C**** ROTATE KF TO GLOBAL CO-ORDINATES ********************************
C
      DO 41 L1=1,8
      DO 41 L2=1,8
      RKF(L1,L2)=0.0
   41 RKFRT(L1,L2)=0.0
      DO 40 L3=1,8
      DO 39 L4=1,8
      DO 38 LL1=1,8
   38 RKF(L3,L4)=RKF(L3,L4)+(R(L3,LL1)*KF(LL1,L4))
   39 CONTINUE
   40 CONTINUE
      DO 37 L5=1,8
      DO 36 L6=1,8
      DO 35 LL2=1,8
   35 RKFRT(L5,L6)=RKFRT(L5,L6)+(RKF(L5,LL2)*RT(LL2,L6))
   36 CONTINUE
   37 CONTINUE
C
C**** ADD RKFRT INTO GLOBAL STIFFNESS MATRIX ****************************
C
      NN(1)=2*NUP(I,1)-1
      NN(2)=2*NUP(I,1)
      NN(3)=2*NUP(I,2)-1
      NN(4)=2*NUP(I,2)
      NN(5)=2*NDN(I,2)-1
      NN(6)=2*NDN(I,2)
      NN(7)=2*NDN(I,1)-1
      NN(8)=2*NDN(I,1)
      DO 34 J1=1,8
      DO 34 J2=1,8
      JJ=NN(J1)-NN(J2)
   34 K(NN(J1),KSBW-JJ)=K(NN(J1),KSBW-JJ)+RKFRT(J1,J2)
    1 CONTINUE
C
C**** THE FOLLOWING DATA IS FOR USE IN SUBROUTINE FSHEAR ***************
C
C**** READ IN ELEMENT NUMBERS ADJACENT TO THE FAULT ********************
C
      DO 2 I=1,NFS
    2 READ(4,97)NELF(I,1),NELF(I,2)
C
C**** READ IN MAXIMUM NUMBER OF ITERATIONS *****************************
C
      READ(4,98)NUMIT
C
C**** READ IN COEFFICIENT OF FRICTION FOR THE FAULT ********************
C
      READ(4,96)FMU
```

```
C
C**** READ IN CONVERGENCE FACTOR ***************************************
C
      READ(4,96)FAC
C
C**** WRITE OUT RELEVANT FAULT DATA ************************************
C
      WRITE(7,90)THETA
   90 FORMAT(1H-,'HADE OF FAULT= ',F6.2)
      WRITE(7,89)FMU
   89 FORMAT(1H0,'COEFFICIENT OF FRICTION= ',F4.2)
      WRITE(7,88)KN,KS
   88 FORMAT(1H0,'NORMAL STIFFNESS=',E10.3,' ; SHEAR STIFFNESS=',E10.3)
      WRITE(7,87)FAC
   87 FORMAT(1H0,'CONVERGENCE FACTOR= ',F10.3)
C
      WRITE(6,95)
   95 FORMAT(/,'SUBROUTINE FORMKF COMPLETED')
      CALL TIME(1,1)
      RETURN
      END
C
C
C
C
C
      SUBROUTINE SOLN
C     ---------------
C
      IMPLICIT REAL *8(A-H,O-W)
      REAL *8 K(600,200),KEL(6,6),NU(510)
      COMMON/COM1/E(510),NU,RO(510),TITLE(5),VIS(510),TIM,T,COEFF,CLC,
     1            QLC,CM,QM,ANTEMP,NEL,NELTOP(510,3),IRHEO(510),IBF,
     2            ICALL,INS,IPS,ICR,ITEM,NTEM,NELTEM(100)
      COMMON/COM2/X(300),Y(300),XPL(3),YPL(3),XS(300),YS(300),NNOD,NNOD2
      COMMON/COM3/FORCE(600),FORCE1(600),DISP(600),STORD(600),A,AA,TINC,
     1            DISP1(600),NBF,NPDX,NPDY,MAXIT,MAXINC,IFA,IFDM(6)
      COMMON/COM4/K,KEL,BT(6,3),DB(3,6),
     1            DELLIB(510),FISOS(100),ISNOD(100),KBW,KSBW
C
C**** THE EQN. K*DISP=FORCE IS SOLVED USING HARWELL ROUTINE MA07BD  ****)
C**** 1ST. DIMENSION OF K IS NUM (>NNOD2 OR =NNOD2)                 ****)
C**** 2ND. DIMENSION OF K MUST BE > OR = ((3*KBW)+1)/2              ****)
C
   70 FORMAT(E10.3)
      PT=1.0
      IF (IFA.EQ.1) PT=0.0
      IF (ICALL.EQ.1) PT=0.0
      NUM=600
      CALL MA07BD(K,FORCE,NUM,NNOD2,KBW,PT)
      DO 49 I=1,NNOD2
   49 DISP(I)=FORCE(I)
      IF (IFA.EQ.1) RETURN
      IF (ICALL.EQ.1) RETURN
      WRITE(7,99)PT
   99 FORMAT(1H-,'EQUATION SOLVED BY GAUSSIAN ELIMINATION;SMALLEST PIVOT
     1AL VALUE USED = ',E10.3)
      WRITE(6,98)
   98 FORMAT(/,'SUBROUTINE SOLN COMPLETED')
      CALL TIME(1,1)
```

```
      RETURN
      END
C
C
C
C
C
      SUBROUTINE STRES
C     ----------------
C
      IMPLICIT REAL *8(A-H,O-W)
      REAL *8 NU(510)
      COMMON/COM1/E(510),NU,RO(510),TITLE(5),VIS(510),TIM,T,COEFF,CLC,
     1            QLC,CM,QM,ANTEMP,NEL,NELTOP(510,3),IRHEO(510),IBF,
     2            ICALL,INS,IPS,ICR,ITEM,NTEM,NELTEM(100)
      COMMON/COM3/FORCE(600),FORCE1(600),DISP(600),STORD(600),A,AA,TINC,
     1            DISP1(600),NBF,NPDX,NPDY,MAXIT,MAXINC,IFA,IFDM(6)
      COMMON/COM5/D(3,3),B(3,6),DLIB(3,3,510),BLIB(3,6,510),DISPEL(6),
     1            STRAIN(510,4),STRESS(510,4),STRIN(510,3),BTS(6)
      DO 1 I=1,NEL
C
C**** UNLOAD D AND B MATRICES FROM LIBRARIES ****************************
C
      DO 49 N1=1,3
      DO 49 N2=1,3
   49 D(N1,N2)=DLIB(N1,N2,I)
      DO 48 N3=1,3
      DO 48 N4=1,6
   48 B(N3,N4)=BLIB(N3,N4,I)
C
C**** FIND DISPLACEMENTS FOR ELEMENT I ******************************
C
      JY1=2*NELTOP(I,1)
      JX1=JY1-1
      JY2=2*NELTOP(I,2)
      JX2=JY2-1
      JY3=2*NELTOP(I,3)
      JX3=JY3-1
      DISPEL(1)=DISP(JX1)
      DISPEL(2)=DISP(JY1)
      DISPEL(3)=DISP(JX2)
      DISPEL(4)=DISP(JY2)
      DISPEL(5)=DISP(JX3)
      DISPEL(6)=DISP(JY3)
      DO 47 L=1,4
      STRAIN(I,L)=0.0
   47 STRESS(I,L)=0.0
C
C**** CALCULATE STRAINS FROM DISPLACEMENTS ****************************
C
      DO 46 L1=1,3
      DO 46 L2=1,6
   46 STRAIN(I,L1)=STRAIN(I,L1)+(B(L1,L2)*DISPEL(L2))
C
C**** CALCULATE STRESSES FROM STRAINS *******************************
C
      DO 45 M1=1,3
      DO 45 M2=1,3
   45 STRESS(I,M1)=STRESS(I,M1)+(D(M1,M2)*STRAIN(I,M2))
      STRESS(I,4)=STRESS(I,3)
```

```
      STRESS(I,3)=NU(I)*(STRESS(I,1)+STRESS(I,2))
      IF (IPS.EQ.1) STRESS(I,3)=0.0
      STRAIN(I,4)=STRAIN(I,3)
      STRAIN(I,3)=0.0
    1 CONTINUE
      IF (IFA.EQ.1) RETURN
      IF (ICALL.EQ.1) RETURN
      WRITE(6,99)
   99 FORMAT(/,'SUBROUTINE STRES COMPLETED')
      CALL TIME(1,1)
      RETURN
      END
C
C
C
C
C
      SUBROUTINE CRSMIN
C     ------------------------
C
      IMPLICIT REAL *8(A-H,O-W)
      REAL *8NU(510)
      COMMON/COM1/E(510),NU,RO(510),TITLE(5),VIS(510),TIM,T,COEFF,CLC,
     1            QLC,CM,QM,ANTEMP,NEL,NELTOP(510,3),IRHEO(510),IBF,
     2            ICALL,INS,IPS,ICR,ITEM,NTEM,NELTEM(100)
      COMMON/COM3/FORCE(600),FORCE1(600),DISP(600),STORD(600),A,AA,TINC,
     1            DISP1(600),NBF,NPDX,NPDY,MAXIT,MAXINC,IFA,IFDM(6)
      COMMON/COM5/D(3,3),B(3,6),DLIB(3,3,510),BLIB(3,6,510),DISPEL(6),
     1            STRAIN(510,4),STRESS(510,4),STRIN(510,3),BTS(6)
      COMMON/COM7/STRBEG(510,4),STREND(510,4),STRAV(510,4),
     1            CREEPS(510,4),D1(3,4),D1C(3),FISTEL(6),PRESTR(510,4),
     2            FIST(600),DEV(4),CRSTR(510,4),CRSTR1(510,4),
     3            DEVEND(510,4),DEVBEG(510,4),PREDEV(510,4),
     4            CRIST(510,4),EFFDEV(510),TEMP(510)
C
      INS=1
      IF (ICALL.EQ.1) GO TO 100
      IF (IFA.EQ.1) GO TO 100
C
C**** READ IN INITIAL CREEP STRAINS FROM CHANNEL 0 ********************
C
      DO 1 N=1,NEL
    1 READ(0)(CRIST(N,J),J=1,4)
  100 DO 2 I=1,NEL
C
C**** SUBTRACT CREEP STRAINS FROM ELASTIC STRAINS *********************
C
      DO 49 J1=1,4
   49 STRAIN(I,J1)=STRAIN(I,J1)-CRIST(I,J1)
C
C**** FORM D1 MATRIX ***************************************************
C
      DO 48 N1=1,3
      DO 48 N2=1,3
   48 D(N1,N2)=DLIB(N1,N2,I)
      DO 47 N3=1,3
      DO 47 N4=1,2
   47 D1(N3,N4)=D(N3,N4)
      DO 46 N5=1,3
   46 D1(N5,4)=D(N5,3)
```

```
      D1(1,3)=D1(1,2)
      D1(2,3)=D1(1,2)
      D1(3,3)=0.0
      DO 45 NN=1,4
   45 STRESS(I,NN)=0.0
C
C**** CALCULATE REMNANT ELASTIC STRESS ********************************
C
      DO 44 M1=1,3
      DO 44 M2=1,4
   44 STRESS(I,M1)=STRESS(I,M1)+(D1(M1,M2)*STRAIN(I,M2))
      STRESS(I,4)=STRESS(I,3)
      STRESS(I,3)=E(I)*NU(I)*(STRAIN(I,1)+STRAIN(I,2)+((1.0-NU(I))
     1              *STRAIN(I,3)/NU(I)))/((1.0+NU(I))*(1.0-(2.0*NU(I)
     2              )))
    2 CONTINUE
      IF (IFA.EQ.1) RETURN
      IF (ICALL.EQ.1) RETURN
      WRITE(6,99)
   99 FORMAT(/,'SUBROUTINE CRSMIN COMPLETED')
      CALL TIME(1,1)
      RETURN
      END
C
C
C
C
C
C
      SUBROUTINE FSHEAR
C     ------------------------
C
      IMPLICIT REAL *8(A-H,O-W)
      REAL *8NU(510),KF(8,8)
      COMMON/COM1/E(510),NU,RO(510),TITLE(5),VIS(510),TIM,T,COEFF,CLC,
     1              QLC,CM,QM,ANTEMP,NEL,NELTOF(510,3),IRHEO(510),IBF,
     2              ICALL,INS,IPS,ICR,ITEM,NTEM,NELTEM(100)
      COMMON/COM2/X(300),Y(300),XPL(3),YPL(3),XS(300),YS(300),NNOD,NNOD2
      COMMON/COM3/FORCE(600),FORCE1(600),DISP(600),STORD(600),A,AA,TINC,
     1              DISP1(600),NBF,NPDX,NPDY,MAXIT,MAXINC,IFA,IFDM(6)
      COMMON/COM5/D(3,3),B(3,6),DLIB(3,3,510),BLIB(3,6,510),DISPEL(6),
     1              STRAIN(510,4),STRESS(510,4),STRIN(510,3),BTS(6)
      COMMON/COM7/STRBEG(510,4),STREND(510,4),STRAV(510,4),
     1              CREEPS(510,4),D1(3,4),D1C(3),FISTEL(6),PRESTR(510,4),
     2              FIST(600),DEV(4),CRSTR(510,4),CRSTR1(510,4),
     3              DEVEND(510,4),DEVBEG(510,4),PREDEV(510,4),
     4              CRIST(510,4),EFFDEV(510),TEMP(510)
      COMMON/COM8/SNORM(6,2),SHEAR(6,2),SHAV(6),SNAV(6),SHAVXS(6),THETA,
     1              FMU,FAC,R(8,8),RT(8,8),KF,RKF(8,8),RKFRT(8,8),NN(8),
     2              NELF(6,2),NUP(6,2),NDN(6,2),NUMIT,NFS,IIT(6)
C
      PI=4.0*ATAN(1.0)
      IFA=1
      IT=1
      RTHETA=THETA*(PI/180.0)
      A1=DCOS(RTHETA)**2
      A2=DSIN(RTHETA)**2
      A3=DCOS(RTHETA)*DSIN(RTHETA)
C
C**** INITIALISE IFDM AND IIT ***************************************
```

```
C
      DO 49 J=1,NFS
      IFDM(J)=0
   49 IIT(J)=0
  106 DO 1 I=1,NFS
      DO 2 J=1,2
C
C**** CALCULATE NORMAL STRESS IN ADJACENT ELEMENTS ********************
C
      SNORM(I,J)=(STRESS(NELF(I,J),1)*A1)+(STRESS(NELF(I,J),2)*A2)+
     1           (2.0*STRESS(NELF(I,J),4)*A3)
C
C**** ADD IN LITHOSTATIC PRESSURE IF NECESSARY ************************
C
      IF (IBF.NE.0) GO TO 100
      I1=NELTOP(NELF(I,J),1)
      I2=NELTOP(NELF(I,J),2)
      I3=NELTOP(NELF(I,J),3)
      DEPTH=(Y(I1)+Y(I2)+Y(I3))/3.0
      SLITH=DEPTH*RO(NELF(I,1))*9.81
      SNORM(I,J)=SNORM(I,J)+SLITH
C
C**** CALCULATE SHEAR STRESS IN ADJACENT ELEMENTS *********************
C
  100 SHEAR(I,J)=((-STRESS(NELF(I,J),1)+STRESS(NELF(I,J),2))*A3)+
     1           (STRESS(NELF(I,J),4)*(A1-A2))
    2 CONTINUE
C
C**** AVERAGE EACH PAIR OF ELEMENTS ACROSS THE FAULT ******************
C
      SHAV(I)=(SHEAR(I,1)+SHEAR(I,2))/2.0
      SNAV(I)=(SNORM(I,1)+SNORM(I,2))/2.0
C
C**** CALCULATE PORE PRESSURE ON FAULT SECTION ************************
C**** BASED ON OVERBURDEN PRESSURE OF WATER
C
      FDEPTH=(Y(NUP(I,1))+Y(NUP(I,2)))/2.0
      POREP=FDEPTH*1.0E3*9.81
C
C**** SUBTRACT PORE PRESSURE FROM NORMAL STRESS ***********************
C
      SNAV(I)=SNAV(I)-POREP
C
C**** CALCULATE FRICTIONAL STRENGTH OF FAULT SECTION ******************
C
      IF (SNAV(I).GT.0.0) SNAV(I)=0.0
      FRS=FMU*DABS(SNAV(I))
C
C**** CALCULATE EXCESS SHEAR STRESS ON FAULT SECTION ******************
C
      IF (FRS.GE.DABS(SHAV(I))) GO TO 101
  103 IF (SHAV(I).LT.0.0) GO TO 102
      SHAVXS(I)=SHAV(I)-FRS
      GO TO 107
  102 SHAVXS(I)=SHAV(I)+FRS
      GO TO 107
  101 IF (IT.EQ.1) IIT(I)=1
      IF (IIT(I).EQ.0) GO TO 103
      SHAVXS(I)=0.0
  107 IF (IT.NE.1) GO TO 1
```

```
      IF (SHAVXS(I).NE.0.0) IFDM(I)=1
    1 CONTINUE
C
C**** NEGATIVE SHEAR IS DEXTRAL SHEAR ********************************
C**** POSITIVE SHEAR IS SINISTRAL SHEAR ******************************
C
C**** CHECK CONVERGENCE OF EXCESS SHEAR STRESS TO ZERO ****************
C
      DO 48 K=1,NFS
      IF (DABS(SHAVXS(K)).GT.1.0E5) GO TO 104
   48 CONTINUE
      IF (ICALL.EQ.1) RETURN
      WRITE(6,99)
   99 FORMAT(/,'SUBROUTINE FSHEAR COMPLETED')
      CALL TIME(1,1)
      RETURN
C
C**** CALCULATE SHEAR FORCE ON FAULT BETWEEN NODES ********************
C
  104 DO 3 I=1,NFS
      FDIST=SQRT(((X(NUP(I,1))-X(NUP(I,2)))**2)+((Y(NUP(I,1))-
     1       Y(NUP(I,2)))**2))
      SFORCE=SHAVXS(I)*FDIST
C
C**** DIVIDE FORCE BETWEEN NODES AND MULTIPLY BY CONVERGENCE FACTOR ****
C
      SFORCE=(SFORCE/2.0)*FAC
C
C**** ROTATE FORCE TO GLOBAL CO-ORDINATE COMPONENTS *******************
C
      FORCEX=SFORCE*(-DSIN(RTHETA))
      FORCEY=SFORCE*DCOS(RTHETA)
C
C**** ADD FORCES INTO GLOBAL FORCE VECTOR *****************************
C
      FORCE1(NUP(I,1)*2-1)=FORCE1(NUP(I,1)*2-1)-FORCEX
      FORCE1(NUP(I,1)*2)=FORCE1(NUP(I,1)*2)-FORCEY
      FORCE1(NUP(I,2)*2-1)=FORCE1(NUP(I,2)*2-1)-FORCEX
      FORCE1(NUP(I,2)*2)=FORCE1(NUP(I,2)*2)-FORCEY
      FORCE1(NDN(I,1)*2-1)=FORCE1(NDN(I,1)*2-1)+FORCEX
      FORCE1(NDN(I,1)*2)=FORCE1(NDN(I,1)*2)+FORCEY
      FORCE1(NDN(I,2)*2-1)=FORCE1(NDN(I,2)*2-1)+FORCEX
      FORCE1(NDN(I,2)*2)=FORCE1(NDN(I,2)*2)+FORCEY
    3 CONTINUE
      DO 4 K=1,NNOD2
    4 FORCE(K)=FORCE1(K)
C
C**** RESOLVE EQN. AND CALCULATE STRESSES *****************************
C
      CALL SOLN
      CALL STRES
      IF (INS.EQ.1) CALL CRSMIN
      IF (TIM.EQ.0.0) GO TO 108
C
C**** SUBTRACT CREEP STRAINS FROM TOTAL STRAINS ***********************
C
      DO 5 II=1,NEL
      DO 47 J=1,4
   47 STRAIN(II,J)=STRAIN(II,J)-CRSTR(II,J)
C
```

```
C**** FORM D1 MATRIX ***********************************************
C
      DO 46 N1=1,3
      DO 46 N2=1,3
   46 D(N1,N2)=DLIB(N1,N2,II)
      DO 45 N3=1,3
      DO 45 N4=1,2
   45 D1(N3,N4)=D(N3,N4)
      DO 44 N5=1,3
   44 D1(N5,4)=D(N5,3)
      D1(1,3)=D1(1,2)
      D1(2,3)=D1(1,2)
      D1(3,3)=0.0
      DO 43 N6=1,4
   43 STRESS(II,N6)=0.0
C
C**** CALCULATE ELASTIC STRESSES ***********************************
C
      DO 42 M1=1,3
      DO 42 M2=1,4
   42 STRESS(II,M1)=STRESS(II,M1)+(D1(M1,M2)*STRAIN(II,M2))
      STRESS(II,4)=STRESS(II,3)
      STRESS(II,3)=E(II)*NU(II)*(STRAIN(II,1)+STRAIN(II,2)+
     1              ((1.0-NU(II))*STRAIN(II,3)/NU(II)))/((1.0+
     2              NU(II))*(1.0-(2.0*NU(II))))
    5 CONTINUE
C
C**** CHECK NUMBER OF ITERATIONS DONE ******************************
C
  108 IF (IT.EQ.NUMIT) GO TO 105
      IT=IT+1
      GO TO 106
  105 WRITE(6,98)
   98 FORMAT(/,'EXCESS SHEAR STRESSES ON FAULT TOO LARGE')
      STOP
      END
C
C
C
C
C
      SUBROUTINE CREEP
C     ----------------
C
      IMPLICIT REAL *8(A-H,O-W)
      REAL *8K(600,200),KEL(6,6),NU(510)
      COMMON/COM1/E(510),NU,RO(510),TITLE(5),VIS(510),TIM,T,COEFF,CLC,
     1            QLC,CM,QM,ANTEMP,NEL,NELTOP(510,3),IRHEO(510),IBF,
     2            ICALL,INS,IPS,ICR,ITEM,NTEM,NELTEM(100)
      COMMON/COM2/X(300),Y(300),XPL(3),YPL(3),XS(300),YS(300),NNOD,NNOD2
      COMMON/COM3/FORCE(600),FORCE1(600),DISP(600),STORD(600),A,AA,TINC,
     1            DISP1(600),NBF,NPDX,NPDY,MAXIT,MAXINC,IFA,IFDM(6)
      COMMON/COM4/K,KEL,BT(6,3),DB(3,6),DELLIB(510),FISOS(100),
     1            ISNOD(100),KBW,KSBW
      COMMON/COM5/D(3,3),B(3,6),DLIB(3,3,510),BLIB(3,6,510),DISPEL(6),
     1            STRAIN(510,4),STRESS(510,4),STRIN(510,3),BTS(6)
      COMMON/COM7/STRBEG(510,4),STREND(510,4),STRAV(510,4),
     1            CREEPS(510,4),D1(3,4),D1C(3),FISTEL(6),PRESTR(510,4),
     2            FIST(600),DEV(4),CRSTR(510,4),CRSTR1(510,4),
     3            DEVEND(510,4),DEVBEG(510,4),PREDEV(510,4),
```

```
     4              CRIST(510,4),EFFDEV(510),TEMP(510)
      COMMON/COM6/PRINST(510,3),DEVPR(510,3),ALPHA(510),FAIL(510),
     1              FVAL(510),PHI(510),F1,F2,ITYPE(510)
C
      TIM=0.0
      NINC=1
      IT=0
      DO 999 I=1,NEL
      DO 999 J=1,4
      CRSTR(I,J)=0.0
  999 CRSTR1(I,J)=0.0
C
C**** STORE STRESSES AT BEGINNING OF INCREMENT IN STRBEG ***************
C
      DO 1 I=1,NEL
      DO 49 J=1,4
      STRBEG(I,J)=STRESS(I,J)
   49 STRAV(I,J)=STRBEG(I,J)
      SIGMA=(STRBEG(I,1)+STRBEG(I,2)+STRBEG(I,3))/3.0
      DO 46 JJ=1,3
   46 DEVBEG(I,JJ)=STRBEG(I,JJ)-SIGMA
      DEVBEG(I,4)=STRBEG(I,4)
    1 CONTINUE
C
C**** CALCULATE CREEP STRAINS ****************************************
C
  119 DO 997 N=1,NNOD2
  997 FIST(N)=0.0
      DO 2 I1=1,NEL
      IF (IRHEO(I1).EQ.0) GO TO 101
C
C**** CALCULATE DEVIATORIC STRESSES
C
      SIGMA=(STRAV(I1,1)+STRAV(I1,2)+STRAV(I1,3))/3.0
      DO 48 N1=1,3
   48 DEV(N1)=STRAV(I1,N1)-SIGMA
      DEV(4)=STRAV(I1,4)
C
C**** DETERMINE CREEP MECHANISM TO BE USED ****************************
C
      IF (ICR.EQ.0) GO TO 133
C
C**** ASSIGN TEMPERATURE OF ELEMENTS ***************************
C**** BASED ON LOW TEMP. OCEANIC GEOTHERM OF MERCIER AND CARTER(1975)
C
C**** ASSUMES MANTLE HAS TWO LAYERS;-35 TO -60,AND -60 TO -100KM ********
C
      IF (IRHEO(I1).EQ.1) GO TO 134
      DEPTH=(Y(NELTOP(I1,1))+Y(NELTOP(I1,2))+Y(NELTOP(I1,3)))/3.0
      IF (DEPTH.GT.-60.0E3) TEMP(I1)=906.0
      IF (DEPTH.LT.-60.0E3) TEMP(I1)=1122.0
      GO TO 135
  134 TEMP(I1)=676.0
C
C**** ADJUST FOR TEMPERATURE ANOMALY IF PRESENT ************************
C
  135 IF (ITEM.EQ.0) GO TO 136
      DO 3 KK=1,NTEM
      IF (I1.NE.NELTEM(KK)) GO TO 3
      TEMP(I1)=TEMP(I1)+ANTEMP
```

```
    3 CONTINUE
C
C**** CALCULATE EFFECTIVE DEVIATORIC STRESS ***************************
C
  136 EFFDEV(I1)=DSQRT((0.5*((DEV(1)**2)+(DEV(2)**2)+(DEV(3)**2)))
     1                  +(DEV(4)**2))
C
C**** CALCULATE EFFECTIVE VISCOSITY ***********************************
C
      IF (IRHEO(I1).EQ.2) GO TO 137
      AC=CLC
      Q=QLC
      GO TO 138
  137 AC=CM
      Q=QM
  138 VIS(I1)=(1.0/(2.0*AC))*DEXP((Q*4186.0)/(8.31*(TEMP(I1)+273.0)))
     1         *(1.0/(EFFDEV(I1)**2))*1.0E24
      IF (VIS(I1).LT.1.0E22) VIS(I1)=1.0E22
      IF (VIS(I1).GT.1.0E24) VIS(I1)=1.0E24
  133 DO 47 N2=1,4
   47 CREEPS(I1,N2)=(DEV(N2)/(2.0*VIS(I1)))*TINC
      CREEPS(I1,4)=2.0*CREEPS(I1,4)
C
C**** CALCULATE FISTEL ************************************************
C**** FORM D1 MATRIX (3*4)
C
      DO 36 L1=1,3
      DO 36 L2=1,3
   36 D(L1,L2)=DLIB(L1,L2,I1)
      DO 35 L3=1,3
      DO 35 L4=1,2
   35 D1(L3,L4)=D(L3,L4)
      DO 34 L5=1,3
   34 D1(L5,4)=D(L5,3)
      D1(1,3)=D1(1,2)
      D1(2,3)=D1(1,2)
      D1(3,3)=0.0
C
C**** FORM BT MATRIX
C
      DO 33 L6=1,3
      DO 33 L7=1,6
   33 B(L6,L7)=BLIB(L6,L7,I1)
      DO 32 L8=1,3
      DO 32 L9=1,6
   32 BT(L9,L8)=B(L8,L9)
C
C**** MULTIPLY D1 BY CREEPS TO GIVE D1C
C
      DO 31 M1=1,3
   31 D1C(M1)=D1(M1,1)*CREEPS(I1,1)+D1(M1,2)*CREEPS(I1,2)+D1(M1,3)*
     1         CREEPS(I1,3)+D1(M1,4)*CREEPS(I1,4)
C
C**** MULTIPLY BT BY D1C AND MULTIPLY BY ELEMENT AREA TO GIVE FISTEL
C
      DO 30 M2=1,6
      FISTEL(M2)=BT(M2,1)*D1C(1)+BT(M2,2)*D1C(2)+BT(M2,3)*D1C(3)
   30 FISTEL(M2)=FISTEL(M2)*(DELLIB(I1)/2.0)
C
C**** ADD ELEMENTS OF FISTEL INTO FIST ********************************
```

```
C
      FIST((NELTOP(I1,1)*2)-1)=FIST((NELTOP(I1,1)*2)-1)+FISTEL(1)
      FIST(NELTOP(I1,1)*2)=FIST(NELTOP(I1,1)*2)+FISTEL(2)
      FIST((NELTOP(I1,2)*2)-1)=FIST((NELTOP(I1,2)*2)-1)+FISTEL(3)
      FIST(NELTOP(I1,2)*2)=FIST(NELTOP(I1,2)*2)+FISTEL(4)
      FIST((NELTOP(I1,3)*2)-1)=FIST((NELTOP(I1,3)*2)-1)+FISTEL(5)
      FIST(NELTOP(I1,3)*2)=FIST(NELTOP(I1,3)*2)+FISTEL(6)
      GO TO 130
  101 DO 22 IJ=1,4
   22 CREEPS(I1,IJ)=0.0
C
C**** UPDATE TOTAL CREEP STRAIN ************************************
C
  130 DO 998 J=1,4
  998 CRSTR(I1,J)=CRSTR1(I1,J)+CREEPS(I1,J)
    2 CONTINUE
C
C**** MODIFY FORCE VECTOR ******************************************
C
C**** ADJUST FIST FOR PRESCRIBED GLOBAL DISPLACEMENTS
C
      DO 15 MM=1,NNOD2
   15 IF (DISP1(MM).NE.A) FIST(MM)=0.0
      DO 29 N=1,NNOD2
   29 FORCE(N)=FORCE1(N)+FIST(N)
C
C**** RESOLVE EQN. AND CALCULATE NEW STRAINS ***************************
C
  500 ICALL=1
      CALL SOLN
  131 CALL STRES
      IF (INS.EQ.1) CALL CRSMIN
C
C**** CALCULATE STRESS AT END OF TIME INC. *****************************
C
      DO 5 I4=1,NEL
C
C**** MODIFY STRAIN VECTOR
C
      DO 28 N1=1,4
   28 STRAIN(I4,N1)=STRAIN(I4,N1)-CRSTR(I4,N1)
C
C**** FORM D1 MATRIX (3*4)
C
      DO 27 N3=1,3
      DO 27 N2=1,3
   27 D(N2,N3)=DLIB(N2,N3,I4)
      DO 26 N4=1,3
      DO 26 N5=1,2
   26 D1(N4,N5)=D(N4,N5)
      DO 25 N6=1,3
   25 D1(N6,4)=D(N6,3)
      D1(1,3)=D1(1,2)
      D1(2,3)=D1(1,2)
      D1(3,3)=0.0
      DO 21 NNN=1,4
   21 STREND(I4,NNN)=0.0
C
C**** CALCULATE STREND
C
```

```
      DO 24 N7=1,3
      DO 24 N9=1,4
   24 STREND(I4,N7)=STREND(I4,N7)+(D1(N7,N9)*STRAIN(I4,N9))
      STREND(I4,4)=STREND(I4,3)
      STREND(I4,3)=E(I4)*NU(I4)*(STRAIN(I4,1)+STRAIN(I4,2)+((1.0-NU(I4))
     1              *STRAIN(I4,3)/NU(I4)))/((1.0+NU(I4))*(1.0-(2.0*NU(I4)
     2              )))
      SIGMA=(STREND(I4,1)+STREND(I4,2)+STREND(I4,3))/3.0
      DO 20 JJ=1,3
   20 DEVEND(I4,JJ)=STREND(I4,JJ)-SIGMA
      DEVEND(I4,4)=STREND(I4,4)
C
C**** CALCULATE MEAN STRESS ****************************************
C
      DO 23 N8=1,4
   23 STRAV(I4,N8)=(STRBEG(I4,N8)+STREND(I4,N8))/2.0
    5 CONTINUE
  124 IT=IT+1
      IF (IT.EQ.1) GO TO 116
C
C**** CHECK CONVERGENCE ********************************************
C
      DO 6 I5=1,NEL
      IF (IRHEO(I5).EQ.0) GO TO 6
      DO 17 J5=1,4
      IF (DABS(DEVEND(I5,J5)-PREDEV(I5,J5)).LE.1.0E5)
     1  GO TO 17
      GO TO 117
   17 CONTINUE
    6 CONTINUE
  120 TIM=TIM+TINC
C
C**** UPDATE FORCE1 AND CRSTR1 *************************************
C
      DO 995 II1=1,NNOD2
  995 FORCE1(II1)=FORCE1(II1)+FIST(II1)
      DO 994 II2=1,NEL
      DO 994 JJ=1,4
  994 CRSTR1(II2,JJ)=CRSTR(II2,JJ)
      DO 8 I7=1,NEL
      DO 8 J2=1,4
    8 STRESS(I7,J2)=STREND(I7,J2)
      IF (IFA.NE.1) GO TO 132
C
C**** ITERATE TO REMOVE EXCESS SHEAR STRESS ON FAULT ******************
C
      CALL FSHEAR
C
C**** CHECK IF THERE HAS BEEN FAILURE AND STOP S/R IF THERE HAS ********
C
  132 CALL PRINCS
      CALL ELFAIL
      DO 14 I=1,NEL
      IF (I.LE.44.OR.I.GE.283) GO TO 14
      IF (IRHEO(I).NE.0) GO TO 14
      IF (FAIL(I).EQ.F2) GO TO 118
   14 CONTINUE
C
C**** CHECK NUMBER OF TIME INCREMENTS DONE ****************************
C
```

```
      IF (NINC.EQ.MAXINC) GO TO 118
      NINC=NINC+1
      DO 7 I6=1,NEL
      DO 12 J1=1,4
      STRBEG(I6,J1)=STREND(I6,J1)
   12 STRAV(I6,J1)=STRBEG(I6,J1)
      SIGMA=(STRBEG(I6,1)+STRBEG(I6,2)+STRBEG(I6,3))/3.0
      DO 13 JJ=1,3
   13 DEVBEG(I6,JJ)=STRBEG(I6,JJ)-SIGMA
    7 DEVBEG(I6,4)=STRBEG(I6,4)
      IT=0
      GO TO 119
  118 ICALL=0
      WRITE(6,99)
   99 FORMAT(/,'SUBROUTINE CREEP COMPLETED')
      CALL TIME(1,1)
      RETURN
  116 DO 9 I8=1,NEL
      DO 9 J3=1,4
      IF (DABS(DEVEND(I8,J3)-DEVBEG(I8,J3)).LE.1.0E5)
     1  GO TO 9
      GO TO 121
    9 CONTINUE
      GO TO 120
  121 DO 11 I9=1,NEL
      DO 11 J4=1,4
   11 PREDEV(I9,J4)=DEVEND(I9,J4)
      GO TO 119
  117 IF (IT.LT.MAXIT) GO TO 121
      WRITE(6,98)
   98 FORMAT(/,'STRESSES HAVE NOT CONVERGED WITHIN 1 BAR')
      STOP
      END
C
C
C
C
C
      SUBROUTINE FINFOR
C     ------------------
C
      IMPLICIT REAL *8(A-H,O-W)
      REAL *8NU(510)
      COMMON/COM1/E(510),NU,RO(510),TITLE(5),VIS(510),TIM,T,COEFF,CLC,
     1            QLC,CM,QM,ANTEMP,NEL,NELTOP(510,3),IRHEO(510),IBF,
     2            ICALL,INS,IPS,ICR,ITEM,NTEM,NELTEM(100)
      COMMON/COM2/X(300),Y(300),XPL(3),YPL(3),XS(300),YS(300),NNOD,NNOD2
      COMMON/COM3/FORCE(600),FORCE1(600),DISP(600),STORD(600),A,AA,TINC,
     1            DISP1(600),NBF,NPDX,NPDY,MAXIT,MAXINC,IFA,IFDM(6)
      COMMON/COM7/STRBEG(510,4),STREND(510,4),STRAV(510,4),
     1            CREEPS(510,4),D1(3,4),D1C(3),FISTEL(6),PRESTR(510,4),
     2            FIST(600),DEV(4),CRSTR(510,4),CRSTR1(510,4),
     3            DEVEND(510,4),DEVBEG(510,4),PREDEV(510,4),
     4            CRIST(510,4),EFFDEV(510),TEMP(510)
C
C**** WRITE OUT FINAL FORCES TO CHANNEL 8 ****************************
C
      DO 1 I=1,NNOD
      F1=FORCE1(2*I-1)+FIST(2*I-1)
      F2=FORCE1(2*I)+FIST(2*I)
```

```
    1 WRITE(8,99)I,F1,F2
   99 FORMAT(I10,2E25.15)
      DO 2 N=1,NEL
C
C**** WRITE OUT FINAL CREEP STRAINS TO CHANNEL 0 ***********************
C
    2 WRITE(0)(CRSTR(N,J),J=1,4)
      WRITE(6,98)
   98 FORMAT(/,'SUBROUTINE FINFOR COMPLETED')
      CALL TIME(1,1)
      RETURN
      END
C
C
C
C
C
      SUBROUTINE PRINCS
C     ------------------------------
C
      IMPLICIT REAL *8(A-H,O-W)
      REAL *8 NU(510)
      COMMON/COM1/E(510),NU,RO(510),TITLE(5),VIS(510),TIM,T,COEFF,CLC,
     1            QLC,CM,QM,ANTEMP,NEL,NELTOP(510,3),IRHEO(510),IBF,
     2            ICALL,INS,IPS,ICR,ITEM,NTEM,NELTEM(100)
      COMMON/COM5/D(3,3),B(3,6),DLIB(3,3,510),BLIB(3,6,510),DISPEL(6),
     1            STRAIN(510,4),STRESS(510,4),STRIN(510,3),BTS(6)
      COMMON/COM6/PRINST(510,3),DEVPR(510,3),ALPHA(510),FAIL(510),
     1            FVAL(510),PHI(510),F1,F2,ITYPE(510)
C
      PI=4.0*ATAN(1.0)
      DO 1 I=1,NEL
C
C**** CALCULATE THE ANGLE OF ROTATION ******************************
C
      IF (STRESS(I,1).EQ.STRESS(I,2)) GO TO 100
      ALPHA(I)=(2.0*STRESS(I,4))/(STRESS(I,1)-STRESS(I,2))
      ALPHA(I)=0.5*(360.0/(2*PI))*DATAN(ALPHA(I))
      IF (ALPHA(I).LT.0.0) ALPHA(I)=ALPHA(I)+90.0
      BETA=ALPHA(I)*(2.0*PI)/360.0
      GO TO 101
  100 ALPHA(I)=45
      BETA=0.7854
C
C**** CALCULATE THE PRINCIPAL STRESSES *****************************
C
  101 A1=DCOS(BETA)**2
      A2=DSIN(BETA)**2
      A3=DSIN(2.0*BETA)
      PRINST(I,1)=(STRESS(I,1)*A1)+(STRESS(I,2)*A2)+(STRESS(I,4)*A3)
      PRINST(I,2)=(STRESS(I,1)*A2)+(STRESS(I,2)*A1)-(STRESS(I,4)*A3)
      PRINST(I,3)=STRESS(I,3)
    1 CONTINUE
      IF (ICALL.EQ.1) RETURN
      WRITE(6,99)
   99 FORMAT(/,'SUBROUTINE PRINCS COMPLETED')
      CALL TIME(1,1)
      RETURN
      END
C
```

```
C
C
C
C
      SUBROUTINE ELFAIL
C     ------------------
C
      IMPLICIT REAL *8(A-H,O-W)
      REAL *8 NU(510)
      COMMON/COM1/E(510),NU,RO(510),TITLE(5),VIS(510),TIM,T,COEFF,CLC,
     1            QLC,CM,QM,ANTEMP,NEL,NELTOP(510,3),IRHEO(510),IBF,
     2            ICALL,INS,IFS,ICR,ITEM,NTEM,NELTEM(100)
      COMMON/COM2/X(300),Y(300),XPL(3),YPL(3),XS(300),YS(300),NNOD,NNOD2
      COMMON/COM6/PRINST(510,3),DEVPR(510,3),ALPHA(510),FAIL(510),
     1            FVAL(510),PHI(510),F1,F2,ITYPE(510)
C
      PI=4.0*ATAN(1.0)
       STCRIT=-10.0*T
      RAD=PI/180.0
      DO 1 I=1,NEL
      IF (IRHEO(I).NE.0) GO TO 1
C
C**** ADD ON LITHOSTATIC STRESS FIELD IF BODY FORCES NOT INCLUDED ******
C**** LITHOSTATIC STRESSES ARE HYDROSTATIC, =RO*9.81*DEPTH
C
      IF (IBF.EQ.1) GO TO 100
      I1=NELTOP(I,1)
      I2=NELTOP(I,2)
      I3=NELTOP(I,3)
      DEPTH=(Y(I1)+Y(I2)+Y(I3))/3.0
      HYD=RO(1)*9.81*DEPTH
      PST1=PRINST(I,1)+HYD
      PST2=PRINST(I,2)+HYD
      GO TO 101
  100 PST1=PRINST(I,1)
      PST2=PRINST(I,2)
C
C**** CALCULATE MEAN STRESS AND MAX. SHEAR STRESS ********************
C
  101 PMAX=DMAX1(PST1,PST2)
      PMIN=DMIN1(PST1,PST2)
      STMEAN=(PMAX+PMIN)/2.0
      TORMAX=(PMAX-PMIN)/2.0
      FAIL(I)=F1
      PHI(I)=F1
C
C**** TEST FOR TENSIONAL FAILURE ************************************
C
      IF (((2.0*STMEAN)+TORMAX).LT.0.0) GO TO 102
      FVAL(I)=1.0-(TORMAX/(T-STMEAN))
      ITYPE(I)=1
      IF (FVAL(I).GT.0.0) GO TO 1
      FAIL(I)=F2
      PHI(I)=90.0
      GO TO 1
C
C**** TEST FOR OPEN CRACK FAILURE ***********************************
C
  102 IF (STMEAN.LT.(STCRIT-(2.0*T))) GO TO 103
      FVAL(I)=1.0-(TORMAX/(2.0*DSQRT(-STMEAN*T)))
```

```
      ITYPE(I)=2
      IF (FVAL(I).GT.0.0) GO TO 1
      FAIL(I)=F2
      PHI(I)=0.5*DARCOS((2.0*DSQRT(-STMEAN*T))/(2.0*STMEAN))/RAD
      GO TO 1
C
C**** TEST FOR TRANSITION REGION FAILURE ****************************
C
  103 C=2.0*T*DSQRT(1.0-(STCRIT/T))
      IF (STMEAN.LT.(STCRIT-(COEFF*C))) GO TO 104
      FVAL(I)=1.0-(TORMAX/DSQRT((C**2)+((STCRIT-STMEAN)**2)))
      ITYPE(I)=3
      IF (FVAL(I).GT.0.0) GO TO 1
      FAIL(I)=F2
      PHI(I)=0.5*DATAN(C/(STCRIT-STMEAN))/RAD
      PHI(I)=90.0-PHI(I)
      GO TO 1
C
C**** TEST FOR CLOSED CRACK FAILURE ********************************
C
  104 IF (STMEAN.GE.(STCRIT-(COEFF*C))) GO TO 105
      FVAL(I)=1.0-((TORMAX*DSQRT((COEFF**2)+1.0))/(C+(COEFF*(STCRIT-
     1         STMEAN))))
      ITYPE(I)=4
      IF (FVAL(I).GT.0.0) GO TO 1
      FAIL(I)=F2
      PHI(I)=0.5*DATAN(1.0/COEFF)/RAD
      PHI(I)=90.0-PHI(I)
    1 CONTINUE
      IF (ICALL.EQ.1) RETURN
      WRITE(6,99)
   99 FORMAT(/,'SUBROUTINE ELFAIL COMPLETED')
      CALL TIME(1,1)
      RETURN
  105 WRITE(6,98)I
   98 FORMAT(/,'ERROR: STRESSES FOR ELEMENT',I3,'ARE NOT CLASSIFIED')
      STOP
      END
C
C
C
C
C
      SUBROUTINE OUTPUT
C     ------------------------
C
      IMPLICIT REAL *8(A-H,O-W)
      REAL *8 NU(510)
      COMMON/COM1/E(510),NU,RO(510),TITLE(5),VIS(510),TIM,T,COEFF,CLC,
     1            QLC,CM,QM,ANTEMP,NEL,NELTOP(510,3),IRHEO(510),IBF,
     2            ICALL,INS,IPS,ICR,ITEM,NTEM,NELTEM(100)
      COMMON/COM2/X(300),Y(300),XPL(3),YPL(3),XS(300),YS(300),NNOD,NNOD2
      COMMON/COM3/FORCE(600),FORCE1(600),DISP(600),STORD(600),A,AA,TINC,
     1            DISP1(600),NBF,NPDX,NPDY,MAXIT,MAXINC,IFA,IFDM(6)
      COMMON/COM6/PRINST(510,3),DEVPR(510,3),ALPHA(510),FAIL(510),
     1            FVAL(510),PHI(510),F1,F2,ITYPE(510)
      WRITE(7,74)
   74 FORMAT(1H1,'*****RESULTS ARE:')
C
C**** WRITE OUT DEPTH OF FAULT MOVEMENT IF RELEVANT ******************
```

```
C
      IF (IFA.NE.1) GO TO 103
      WRITE(7,73)
   73 FORMAT(1H-,'FAULT MOVEMENT HAS OCCURRED ON:')
      DO 47 J=1,6
      IF (IFDM(J).EQ.0) WRITE(7,72)J
      IF (IFDM(J).EQ.1) WRITE(7,71)J
   72 FORMAT(1H ,'SECTION ',I1,'    NO')
   71 FORMAT(1H ,'SECTION ',I1,'    YES')
   47 CONTINUE
C
C**** WRITE TOTAL TIME USED FOR SOLUTION ******************************
C
  103 TIMY=TIM/(3.156*1.0E7)
      WRITE(7,100)TIMY
  100 FORMAT(1H-,'*SOLUTION HAS BEEN GENERATED THROUGH ',E11.4,' YEARS')
C
C**** WRITE NODAL DISPLACEMENTS ***************************************
C
  102 WRITE(7,99)
   99 FORMAT(1H-,'*NODAL DISPLACEMENTS IN METRES*')
      WRITE(7,98)
   98 FORMAT(1H0,' X-AXIS IS FROM LEFT TO RIGHT')
      WRITE(7,97)
   97 FORMAT(1H ,' Y-AXIS IS VERTICALLY UPWARDS')
      WRITE(7,96)
   96 FORMAT(1H-,18X,'NODE NO.',9X,'X-DISP.',13X,'Y-DISP.')
      DO 49 J=1,NNOD
      JX=2*J-1
      JY=2*J
   49 WRITE(7,95)J,DISP(JX),DISP(JY)
   95 FORMAT(1H0,20X,I3,2(10X,E10.3))
C
C**** WRITE ELEMENT STRESSES AND FAILURE MARKERS **********************
C
      WRITE(7,94)
   94 FORMAT(1H1,'*ELEMENT STRESSES IN N/SQ.M AND FAILURE INFORMATION*')
      WRITE(7,93)
   93 FORMAT(1H-,' 1ST. STRESS,2ND. STRESS ARE THE IN-PLANE PRINCIPAL ST
     1RESSES AT THE CENTRE OF THE ELEMENT')
      WRITE(7,78)
   78 FORMAT(1H0,' Z STRESS IS THE STRESS NECESSARY TO SATISFY PLANE
     1 STRAIN')
      WRITE(7,92)
   92 FORMAT(1H0,' ALPHA IS THE ANGLE OF THE 1ST. STRESS MEASURED FROM T
     1HE +VE X-AXIS TO THE +VE Y-AXIS')
      WRITE(7,91)
   91 FORMAT(1H0,' FAIL SHOWS WHETHER OR NOT THE ELEMENT HAS FAILED')
      WRITE(7,90)
   90 FORMAT(1H0,' AMOUNT IS A DIMENSIONLESS VARIABLE INDICATING:')
      WRITE(7,89)
   89 FORMAT(1H ,'          -HOW NEAR THE ELEMENT IS TO FAILURE (IF -VE)')
      WRITE(7,88)
   88 FORMAT(1H ,'          -HOW MUCH IT HAS FAILED BY (IF +VE)')
      WRITE(7,86)
   86 FORMAT(1H0,' TYPE INDICATES THE TYPE OF FAILURE:')
      WRITE(7,85)
   85 FORMAT(1H ,'          1=TENSIONAL FAILURE')
      WRITE(7,84)
   84 FORMAT(1H ,'          2=OPEN CRACK COMPRESSIONAL (SHEAR) FAILURE')
```

```
      WRITE(7,83)
   83 FORMAT(1H ,'          3=TRANSITIONAL COMPRESSIONAL (SHEAR) FAILURE')
      WRITE(7,75)
   75 FORMAT(1H ,'          4=CLOSED CRACK COMPRESSIONAL (SHEAR) FAILURE')
      WRITE(7,82)
   82 FORMAT(1H0,' PHI IS THE ANGLE BETWEEN THE FRACTURE PLANE AND THE
     1 LARGER STRESS')
      WRITE(7,81)
   81 FORMAT(1H-,'ELEMENT NO.',6X,'1ST. STRESS',9X,'2ND. STRESS',10X,
     1'Z STRESS',11X,'ALPHA',8X,'FAIL',7X,'AMOUNT',5X,'TYPE',3X,'PHI')
      DO 48 I=1,NEL
      IF (IRHEO(I).EQ.0) GO TO 101
      WRITE(7,76)I,PRINST(I,1),PRINST(I,2),PRINST(I,3),ALPHA(I)
   76 FORMAT(1H0,4X,I3,3(10X,E10.3),10X,F5.2)
      GO TO 48
  101 IF (PHI(I).EQ.F1) WRITE(7,77)I,PRINST(I,1),PRINST(I,2),
     1PRINST(I,3),ALPHA(I),FAIL(I),FVAL(I),ITYPE(I),PHI(I)
   77 FORMAT(1H0,4X,I3,3(10X,E10.3),10X,F5.2,8X,A4,5X,E9.3,5X,I1,5X,
     1A4)
      IF (PHI(I).NE.F1) WRITE(7,80)I,PRINST(I,1),PRINST(I,2),
     1PRINST(I,3),ALPHA(I),FAIL(I),FVAL(I),ITYPE(I),PHI(I)
   80 FORMAT(1H0,4X,I3,3(10X,E10.3),10X,F5.2,8X,A4,5X,E9.3,5X,I1,5X,
     1F5.2)
   48 CONTINUE
      WRITE(6,79)
   79 FORMAT(/,'SUBROUTINE OUTPUT COMPLETED')
      CALL TIME(1,1)
      RETURN
      END
C
C
C
C
C
      SUBROUTINE DEVOUT
C     ------------------
C
      IMPLICIT REAL *8(A-H,O-W)
      REAL *8 NU(510)
      COMMON/COM1/E(510),NU,RO(510),TITLE(5),VIS(510),TIM,T,COEFF,CLC,
     1            QLC,CM,QM,ANTEMP,NEL,NELTOP(510,3),IRHEO(510),IBF,
     2            ICALL,INS,IPS,ICR,ITEM,NTEM,NELTEM(100)
      COMMON/COM6/PRINST(510,3),DEVPR(510,3),ALPHA(510),FAIL(510),
     1            FVAL(510),PHI(510),F1,F2,ITYPE(510)
C
C**** WRITE OUT DEVIATORIC STRESSES ********************************
C
      WRITE(7,99)
   99 FORMAT(1H1,'*DEVIATORIC STRESSES IN N/SQ.M*')
      WRITE(7,98)
   98 FORMAT(1H-,'ELEMENT NO.',6X,'1ST. STRESS',9X,'2ND. STRESS',10X,
     1'Z STRESS',11X,'ALPHA')
      DO 1 I=1,NEL
      HYD=(PRINST(I,1)+PRINST(I,2)+PRINST(I,3))/3.0
      DO 2 J=1,3
    2 DEVPR(I,J)=PRINST(I,J)-HYD
    1 WRITE(7,97)I,(DEVPR(I,K),K=1,3),ALPHA(I)
   97 FORMAT(1H0,4X,I3,3(10X,E10.3),10X,F5.2)
      WRITE(6,96)
   96 FORMAT(/,'SUBROUTINE DEVOUT COMPLETED')
```

```
      CALL TIME(1,1)
      RETURN
      END
C
C
C
C
C
      SUBROUTINE GRIDPLT
C     ------------------
C
      IMPLICIT REAL *8(A-H,O-W)
      REAL *8 NU(510)
      COMMON/COM1/E(510),NU,RO(510),TITLE(5),VIS(510),TIM,T,COEFF,CLC,
     1            QLC,CM,QM,ANTEMP,NEL,NELTOP(510,3),IRHEO(510),IBF,
     2            ICALL,INS,IPS,ICR,ITEM,NTEM,NELTEM(100)
      COMMON/COM2/X(300),Y(300),XPL(3),YPL(3),XS(300),YS(300),NNOD,NNOD2
C
C**** DRAW THE GRID ***************************************************
C
      CALL PSPACE(0.075,1.075,0.325,0.575)
      CALL MAP(0.000,2.0E6,-1.0E5,0.0)
C     CALL MAP(2.8E6,3.2E6,-1.0E5,0.0)
      DO 49 I=1,NEL
      I1=NELTOP(I,1)
      I2=NELTOP(I,2)
      I3=NELTOP(I,3)
      XPL(1)=X(I1)
      XPL(2)=X(I2)
      XPL(3)=X(I3)
      YPL(1)=Y(I1)
      YPL(2)=Y(I2)
      YPL(3)=Y(I3)
   49 CALL PTPLOT(XPL,YPL,1,3,-1)
C
C**** ASSIGN ELEMENT NUMBERS ******************************************
C
C     XC=(X(I1)+X(I2)+X(I3))/3.0+2.0E3
C     YC=(Y(I1)+Y(I2)+Y(I3))/3.0
C     CALL CTRMAG(7)
C     CALL ITALIC(1)
C     CALL PLOTNI(XC,YC,I)
C  49 CALL ITALIC(0)
C
C**** ASSIGN NODE NUMBERS *********************************************
C
      CALL PSPACE(0.025,1.21,0.05,0.75)
      CALL CSPACE(0.025,1.21,0.05,0.75)
C     CALL MAP(-0.05E5,10.05E5,-0.55E5,0.05E5)
C     DO 48 J=1,NNOD
C     XP=X(J)+3.0E3
C     YP=Y(J)+1.0E3
C     CALL CTRMAG(5)
C  48 CALL PLOTNI(XP,YP,J)
C
C**** ASSIGN DIMENSIONS OF GRID IN KMS. *******************************
C
      CALL MAP(0.025,1.21,0.05,0.75)
      CALL CTRMAG(15)
      CALL PLOTNI(0.075,0.570,0)
```

```
C       CALL PLOTNI(0.105,0.605,460)
C       CALL PLOTNI(1.105,0.605,540)
        CALL PLOTNI(1.14,0.570,2000)
        CALL PLOTNI(0.075,0.325,100)
        CALL CTRMAG(8)
        CALL PLOTCS(0.04,0.4875,'MOHO',4)
C
C**** WRITE TITLES ***********************************************
C
        CALL CTRMAG(15)
        CALL PLOTCS(0.075,0.675,TITLE,40)
        CALL CTRMAG(10)
        CALL PLOTCS(0.075,0.65,'DIMENSIONS OF GRID ARE IN KMS.',30)
C       CALL PLOTCS(0.15,0.77,'NODES AND ELEMENTS NUMBERED',27)
C       CALL BORDER
        WRITE(6,99)
   99   FORMAT(/,'SUBROUTINE GRDPLT COMPLETED')
        CALL TIME(1,1)
        RETURN
        END
C
C
C
C
C
        SUBROUTINE GRDPLC
C       ------------------------
C
        IMPLICIT REAL *8(A-H,O-W)
        REAL *8 NU(510)
        COMMON/COM1/E(510),NU,RO(510),TITLE(5),VIS(510),TIM,T,COEFF,CLC,
     1              QLC,CM,QM,ANTEMP,NEL,NELTOP(510,3),IRHEO(510),IBF,
     2              ICALL,INS,IPS,ICR,ITEM,NTEM,NELTEM(100)
        COMMON/COM2/X(300),Y(300),XPL(3),YPL(3),XS(300),YS(300),NNOD,NNOD2
C
C**** DRAW THE GRID ***********************************************
C
        CALL PSPACE(0.075,0.575,0.075,0.700)
        CALL MAP(1.92E6,2.00E6,-1.0E5,0.0)
C       CALL MAP(1.8E6,2.2E6,-1.0E5,0.0)
        DO 49 I=1,NEL
        I1=NELTOP(I,1)
        I2=NELTOP(I,2)
        I3=NELTOP(I,3)
        XPL(1)=X(I1)
        XPL(2)=X(I2)
        XPL(3)=X(I3)
        YPL(1)=Y(I1)
        YPL(2)=Y(I2)
        YPL(3)=Y(I3)
   49   CALL PTPLOT(XPL,YPL,1,3,-1)
C
C**** ASSIGN ELEMENT NUMBERS ***************************************
C
C       XC=(X(I1)+X(I2)+X(I3))/3.0+2.0E3
C       YC=(Y(I1)+Y(I2)+Y(I3))/3.0
C       CALL CTRMAG(7)
C       CALL ITALIC(1)
C       CALL PLOTNI(XC,YC,I)
C  49   CALL ITALIC(0)
```

```
C
C**** ASSIGN NODE NUMBERS ***********************************************
C
C       CALL PSPACE(0.025,1.21,0.05,0.75)
C       CALL CSPACE(0.025,1.21,0.05,0.75)
C       CALL MAP(-0.05E5,10.05E5,-0.55E5,0.05E5)
C       DO 48 J=1,NNOD
C       XP=X(J)+3.0E3
C       YP=Y(J)+1.0E3
C       CALL CTRMAG(5)
C   48  CALL PLOTNI(XP,YP,J)
C
C**** ASSIGN DIMENSIONS OF GRID IN KMS. *******************************
C
        CALL PSPACE(0.025,0.700,0.025,0.85)
        CALL CSPACE(0.025,0.700,0.025,0.85)
        CALL MAP(0.025,0.700,0.025,0.85)
        CALL CTRMAG(15)
        CALL PLOTNI(0.075,0.695,0)
        CALL PLOTNI(0.105,0.725,1920)
        CALL PLOTNI(0.605,0.725,2000)
        CALL PLOTNI(0.075,0.075,100)
        CALL CTRMAG(8)
        CALL PLOTCS(0.04,0.4875,'MOHO',4)
C
C**** WRITE TITLES ****************************************************
C
        CALL CTRMAG(15)
        CALL PLOTCS(0.075,0.825,TITLE,40)
        CALL CTRMAG(10)
        CALL PLOTCS(0.075,0.8,'DIMENSIONS OF GRID ARE IN KMS.',30)
C       CALL PLOTCS(0.15,0.77,'NODES AND ELEMENTS NUMBERED',27)
C       CALL BORDER
        WRITE(6,99)
   99   FORMAT(/,'SUBROUTINE GRDPLC COMPLETED')
        CALL TIME(1,1)
        RETURN
        END
C
C
C
C
C
        SUBROUTINE STRPLT
C       ---------------------
C
        IMPLICIT REAL *8(A-H,O-W)
        REAL *8 NU(510)
        COMMON/COM1/E(510),NU,RO(510),TITLE(5),VIS(510),TIM,T,COEFF,CLC,
       1            QLC,CM,QM,ANTEMP,NEL,NELTOP(510,3),IRHEO(510),IBF,
       2            ICALL,INS,IPS,ICR,ITEM,NTEM,NELTEM(100)
        COMMON/COM2/X(300),Y(300),XPL(3),YPL(3),XS(300),YS(300),NNOD,NNOD2
        COMMON/COM6/PRINST(510,3),DEVPR(510,3),ALPHA(510),FAIL(510),
       1            FVAL(510),PHI(510),F1,F2,ITYPE(510)
C
        PI=4.0*ATAN(1.0)
        CALL PSPACE(0.075,1.075,0.325,0.575)
        CALL MAP(4.6E5,5.4E5,-2.0E4,0.0)
C
C**** CALCULATE MAXIMUM STRESS ****************************************
```

```
C
      YVEX=2.0
      STMAX=0.0
      DO 49 J=1,NEL
      PR1=DABS(PRINST(J,1))
      PR2=DABS(PRINST(J,2))
      STMAX=DMAX1(PR1,STMAX)
      STMAX=DMAX1(PR2,STMAX)
   49 CONTINUE
C
C**** PLOT PRINCIPAL STRESSES AT ELEMENT CENTRES ***********************
C
      DO 48 I=1,NEL
      I1=NELTOP(I,1)
      I2=NELTOP(I,2)
      I3=NELTOP(I,3)
      XC=(X(I1)+X(I2)+X(I3))/3.0
      YC=(Y(I1)+Y(I2)+Y(I3))/3.0
      IF1=0
      IF2=0
      IF (PRINST(I,1).LT.0.0) IF1=1
      IF (PRINST(I,2).LT.0.0) IF2=1
      IF (IF1.EQ.1) PRINST(I,1)=-PRINST(I,1)
      IF (IF2.EQ.1) PRINST(I,2)=-PRINST(I,2)
      XP1=PRINST(I,1)*DCOS(ALPHA(I)*(2.0*PI/360.0))*2.0E3/STMAX
      YP1=PRINST(I,1)*DSIN(ALPHA(I)*(2.0*PI/360.0))*2.0E3/STMAX
      XP2=PRINST(I,2)*DSIN(ALPHA(I)*(2.0*PI/360.0))*2.0E3/STMAX
      YP2=PRINST(I,2)*DCOS(ALPHA(I)*(2.0*PI/360.0))*2.0E3/STMAX
      XP1A=XC+XP1
      XP1S=XC-XP1
      YP1A=YC+YP1
      YP1S=YC-YP1
      XP2A=XC+XP2
      XP2S=XC-XP2
      YP2A=YC+YP2
      YP2S=YC-YP2
      CALL POSITN(XP1A,YP1A)
      IF (IF1.EQ.0) CALL BROKEN(3,4,3,4)
      CALL JOIN(XP1S,YP1S)
      CALL POSITN(XP2A,YP2S)
      IF (IF1.EQ.0) CALL FULL
      IF (IF2.EQ.0) CALL BROKEN(3,4,3,4)
      CALL JOIN(XP2S,YP2A)
      IF (IF2.EQ.0) CALL FULL
   48 CONTINUE
      CALL BORDER
C     CALL POSITN(1.8E6,-20.0E3)
C     CALL JOIN(2.2E6,-20.0E3)
C     CALL POSITN(2.2E6,-35.0E3)
C     CALL JOIN(1.8E6,-35.0E3)
C
C**** WRITE TITLES *****************************************************
C
      CALL PSPACE(0.025,1.125,0.05,0.75)
      CALL CSPACE(0.025,1.125,0.05,0.75)
      CALL MAP(0.025,1.125,0.05,0.75)
C
C**** ASSIGN MODEL DIMENSIONS
C
      CALL CTRMAG(15)
```

```
      CALL PLOTNI(0.075,0.570,0)
      CALL PLOTNI(0.105,0.605,460)
      CALL PLOTNI(1.105,0.605,540)
      CALL PLOTNI(0.075,0.325,20)
      CALL CTRMAG(8)
C     CALL PLOTCS(0.04,0.4875,'MOHO',4)
C
      CALL CTRMAG(15)
      CALL POSITN(0.075,0.7)
      CALL TYPECS('VECTOR PLOT OF PRINCIPAL STRESSES:',34)
      CALL TYPECS(TITLE,40)
      CALL POSITN(0.075,0.675)
      CALL CTRMAG(10)
      CALL TYPECS('BROKEN LINES = TENSILE STRESSES ; FULL LINES = COMPRE
     1SSIVE STRESSES',67)
      CALL POSITN(0.075,0.65)
      CALL JOIN(0.125,0.65)
      STMAX=STMAX/1.0D6
      CALL TYPENF(STMAX,1)
      CALL TYPECS(' MPA',4)
      R=100.0
      XX=0.05*(R/STMAX)
      XX1=0.3+XX
      CALL POSITN(0.3,0.65)
      CALL JOIN(XX1,0.65)
      CALL TYPENF(R,1)
      CALL TYPECS(' MPA',4)
C     CALL BORDER
      WRITE(6,99)
   99 FORMAT(/,'SUBROUTINE STRPLT COMPLETED')
      CALL TIME (1,1)
      RETURN
      END
C
C
C
C
C
      SUBROUTINE STRPLC
C     ------------------------
C
      IMPLICIT REAL *8(A-H,O-W)
      REAL *8 NU(510)
      COMMON/COM1/E(510),NU,RO(510),TITLE(5),VIS(510),TIM,T,COEFF,CLC,
     1            QLC,CM,QM,ANTEMP,NEL,NELTOP(510,3),IRHEO(510),IBF,
     2            ICALL,INS,IPS,ICR,ITEM,NTEM,NELTEM(100)
      COMMON/COM2/X(300),Y(300),XPL(3),YPL(3),XS(300),YS(300),NNOD,NNOD2
      COMMON/COM6/PRINST(510,3),DEVPR(510,3),ALPHA(510),FAIL(510),
     1            FVAL(510),PHI(510),F1,F2,ITYPE(510)
C
      PI=4.0*ATAN(1.0)
      CALL PSPACE(0.075,0.575,0.075,0.700)
      CALL MAP(1.92E6,2.00E6,-1.0E5,0.0)
C
C**** CALCULATE MAXIMUM STRESS ***************************************
C
      YVEX=2.0
      STMAX=0.0
      DO 49 J=1,NEL
      PR1=DABS(PRINST(J,1))
```

```
      PR2=DABS(PRINST(J,2))
      STMAX=DMAX1(PR1,STMAX)
      STMAX=DMAX1(PR2,STMAX)
   49 CONTINUE
C
C**** PLOT PRINCIPAL STRESSES AT ELEMENT CENTRES ***********************
C
      DO 48 I=1,NEL
      I1=NELTOP(I,1)
      I2=NELTOP(I,2)
      I3=NELTOP(I,3)
      XC=(X(I1)+X(I2)+X(I3))/3.0
      YC=(Y(I1)+Y(I2)+Y(I3))/3.0
      IF1=0
      IF2=0
      IF (PRINST(I,1).LT.0.0) IF1=1
      IF (PRINST(I,2).LT.0.0) IF2=1
      IF (IF1.EQ.1) PRINST(I,1)=-PRINST(I,1)
      IF (IF2.EQ.1) PRINST(I,2)=-PRINST(I,2)
      XP1=PRINST(I,1)*DCOS(ALPHA(I)*(2.0*PI/360.0))*2.0E3/STMAX
      YP1=PRINST(I,1)*DSIN(ALPHA(I)*(2.0*PI/360.0))*2.0E3/STMAX
      XP2=PRINST(I,2)*DSIN(ALPHA(I)*(2.0*PI/360.0))*2.0E3/STMAX
      YP2=PRINST(I,2)*DCOS(ALPHA(I)*(2.0*PI/360.0))*2.0E3/STMAX
      XP1A=XC+XP1
      XP1S=XC-XP1
      YP1A=YC+YP1
      YP1S=YC-YP1
      XP2A=XC+XP2
      XP2S=XC-XP2
      YP2A=YC+YP2
      YP2S=YC-YP2
      CALL POSITN(XP1A,YP1A)
      IF (IF1.EQ.0) CALL BROKEN(3,4,3,4)
      CALL JOIN(XP1S,YP1S)
      CALL POSITN(XP2A,YP2S)
      IF (IF1.EQ.0) CALL FULL
      IF (IF2.EQ.0) CALL BROKEN(3,4,3,4)
      CALL JOIN(XP2S,YP2A)
      IF (IF2.EQ.0) CALL FULL
   48 CONTINUE
      CALL BORDER
      CALL POSITN(1.92E6,-20.0E3)
      CALL JOIN(2.00E6,-20.0E3)
      CALL POSITN(2.00E6,-35.0E3)
      CALL JOIN(1.92E6,-35.0E3)
C
C**** WRITE TITLES ******************************************************
C
      CALL PSPACE(0.025,0.700,0.025,0.85)
      CALL CSPACE(0.025,0.700,0.025,0.85)
      CALL MAP(0.025,0.700,0.025,0.85)
C
C**** ASSIGN MODEL DIMENSIONS
C
      CALL CTRMAG(15)
      CALL PLOTNI(0.075,0.695,0)
      CALL PLOTNI(0.105,0.725,1920)
      CALL PLOTNI(0.605,0.725,2000)
      CALL PLOTNI(0.075,0.075,100)
      CALL CTRMAG(10)
```

```
      CALL PLOTCS(0.027,0.48325,'MOHO',4)
C
      CALL CTRMAG(15)
      CALL POSITN(0.075,0.825)
      CALL TYPECS('VECTOR PLOT OF PRINCIPAL STRESSES:',34)
      CALL TYPECS(TITLE,40)
      CALL POSITN(0.075,0.8)
      CALL CTRMAG(10)
      CALL TYPECS('BROKEN LINES = TENSILE STRESSES ; FULL LINES = COMPRE
     1SSIVE STRESSES',67)
      CALL POSITN(0.075,0.775)
      CALL JOIN(0.1,0.775)
      STMAX=STMAX/1.0D6
      CALL TYPENF(STMAX,1)
      CALL TYPECS(' MPA',4)
      R=100.0
      XX=0.025*(R/STMAX)
      XX1=0.3+XX
      CALL POSITN(0.3,0.775)
      CALL JOIN(XX1,0.775)
      CALL TYPENF(R,1)
      CALL TYPECS(' MPA',4)
C     CALL BORDER
      WRITE(6,99)
   99 FORMAT(/,'SUBROUTINE STRPLC COMPLETED')
      CALL TIME (1,1)
      RETURN
      END
C
C
C
C
C
      SUBROUTINE DEVPLT
C     ------------------
C
      IMPLICIT REAL *8(A-H,O-W)
      REAL *8 NU(510)
      COMMON/COM1/E(510),NU,RO(510),TITLE(5),VIS(510),TIM,T,COEFF,CLC,
     1            QLC,CM,QM,ANTEMP,NEL,NELTOP(510,3),IRHEO(510),IBF,
     2            ICALL,INS,IPS,ICR,ITEM,NTEM,NELTEM(100)
      COMMON/COM2/X(300),Y(300),XPL(3),YPL(3),XS(300),YS(300),NNOD,NNOD2
      COMMON/COM6/PRINST(510,3),DEVPR(510,3),ALPHA(510),FAIL(510),
     1            FVAL(510),PHI(510),F1,F2,ITYPE(510)
C
      PI=4.0*ATAN(1.0)
      CALL PSPACE(0.075,1.075,0.325,0.575)
      CALL MAP(1.6E5,2.4E5,-2.0E4,0.0)
C
C**** CALCULATE MAXIMUM STRESS ****************************************
C
      YVEX=2.0
      STMAX=0.0
      DO 49 J=1,NEL
      IF (J.LE.44.OR.J.GE.283) GO TO 49
      PR1=DABS(DEVPR(J,1))
      PR2=DABS(DEVPR(J,2))
      STMAX=DMAX1(PR1,STMAX)
      STMAX=DMAX1(PR2,STMAX)
   49 CONTINUE
```

```
C
C**** PLOT PRINCIPAL STRESSES AT ELEMENT CENTRES ***********************
C
      DO 48 I=1,NEL
      IF (I.LE.44.OR.I.GE.283) GO TO 48
      I1=NELTOP(I,1)
      I2=NELTOP(I,2)
      I3=NELTOP(I,3)
      XC=(X(I1)+X(I2)+X(I3))/3.0
      YC=(Y(I1)+Y(I2)+Y(I3))/3.0
      IF1=0
      IF2=0
      IF (DEVPR(I,1).LT.0.0) IF1=1
      IF (DEVPR(I,2).LT.0.0) IF2=1
      IF (IF1.EQ.1) DEVPR(I,1)=-DEVPR(I,1)
      IF (IF2.EQ.1) DEVPR(I,2)=-DEVPR(I,2)
      XP1=DEVPR(I,1)*DCOS(ALPHA(I)*(2.0*PI/360.0))*2.0E3/STMAX
      YP1=DEVPR(I,1)*DSIN(ALPHA(I)*(2.0*PI/360.0))*2.0E3/STMAX
      XP2=DEVPR(I,2)*DSIN(ALPHA(I)*(2.0*PI/360.0))*2.0E3/STMAX
      YP2=DEVPR(I,2)*DCOS(ALPHA(I)*(2.0*PI/360.0))*2.0E3/STMAX
      XP1A=XC+XP1
      XP1S=XC-XP1
      YP1A=YC+YP1
      YP1S=YC-YP1
      XP2A=XC+XP2
      XP2S=XC-XP2
      YP2A=YC+YP2
      YP2S=YC-YP2
      CALL POSITN(XP1A,YP1A)
      IF (IF1.EQ.0) CALL BROKEN(3,4,3,4)
      CALL JOIN(XP1S,YP1S)
      CALL POSITN(XP2A,YP2S)
      IF (IF1.EQ.0) CALL FULL
      IF (IF2.EQ.0) CALL BROKEN(3,4,3,4)
      CALL JOIN(XP2S,YP2A)
      IF (IF2.EQ.0) CALL FULL
   48 CONTINUE
      CALL BORDER
      CALL POSITN(1.8E6,-20.0E3)
      CALL JOIN(2.2E6,-20.0E3)
      CALL POSITN(2.2E6,-35.0E3)
      CALL JOIN(1.8E6,-35.0E3)
C
C**** WRITE TITLES ******************************************************
C
      CALL PSPACE(0.025,1.125,0.05,0.75)
      CALL CSPACE(0.025,1.125,0.05,0.75)
      CALL MAP(0.025,1.125,0.05,0.75)
C
C**** ASSIGN MODEL DIMENSIONS
C
      CALL CTRMAG(15)
      CALL PLOTNI(0.075,0.570,0)
      CALL PLOTNI(0.105,0.605,160)
      CALL PLOTNI(1.105,0.605,240)
      CALL PLOTNI(0.075,0.325,20)
      CALL CTRMAG(8)
C     CALL PLOTCS(0.04,0.4875,'MOHO',4)
C
      CALL CTRMAG(15)
```

```
      CALL POSITN(0.075,0.7)
      CALL TYPECS('VECTOR PLOT OF DEVIATORIC STRESSES:',35)
      CALL TYPECS(TITLE,40)
      CALL POSITN(0.075,0.675)
      CALL CTRMAG(10)
      CALL TYPECS('BROKEN LINES = TENSILE STRESSES ; FULL LINES = COMPRE
     1SSIVE STRESSES',67)
      CALL POSITN(0.075,0.65)
      CALL JOIN(0.085,0.65)
      STMAX=STMAX/1.0D6
      CALL TYPENF(STMAX,1)
      CALL TYPECS(' MPA',4)
C     CALL BORDER
      WRITE(6,99)
   99 FORMAT(/,'SUBROUTINE DEVPLT COMPLETED')
      CALL TIME (1,1)
      RETURN
      END
C
C
C
C
C
      SUBROUTINE SHSCON
C     ------------------------
C
      IMPLICIT REAL *8(A-H,O-W)
      REAL *8 NU(510)
      COMMON/COM1/E(510),NU,RO(510),TITLE(5),VIS(510),TIM,T,COEFF,CLC,
     1            QLC,CM,QM,ANTEMP,NEL,NELTOP(510,3),IRHEO(510),IBF,
     2            ICALL,INS,IPS,ICR,ITEM,NTEM,NELTEM(100)
      COMMON/COM2/X(300),Y(300),XPL(3),YPL(3),XS(300),YS(300),NNOD,NNOD2
      COMMON/COM6/PRINST(510,3),DEVPR(510,3),ALPHA(510),FAIL(510),
     1            FVAL(510),PHI(510),F1,F2,ITYPE(510)
C
C**** FORMS A DATA FILE FOR USE WITH *GPCP TO PLOT 10 CONTOURS *********
C
      WRITE(2,99)
   99 FORMAT('JOB  SHEAR STRESS CONTOURS')
      WRITE(2,98)
   98 FORMAT('SIZE 20.0 20.0 0.0  0.0  0.0',7X,' 5.0 400.0',5X,'-100.0',
     14X,' 5.0 0.0')
      WRITE(2,97)
   97 FORMAT('CNTL 0.00 0.00',5X,'0',4X,'2')
      SHMAX=-1.0D20
      SHMIN=1.0D20
      DO 49 I=1,NEL
      PMAX=DMAX1(PRINST(I,1),PRINST(I,2))
      PMIN=DMIN1(PRINST(I,1),PRINST(I,2))
      SHEAR=(PMAX-PMIN)/2.0D6
      SHMAX=DMAX1(SHEAR,SHMAX)
      SHMIN=DMIN1(SHEAR,SHMIN)
      I1=NELTOP(I,1)
      I2=NELTOP(I,2)
      I3=NELTOP(I,3)
      XC=(X(I1)+X(I2)+X(I3))/3.0E3
      YC=(Y(I1)+Y(I2)+Y(I3))/3.0E3
   49 WRITE(2,96)XC,YC,SHEAR
   96 FORMAT('CNTL ',3F10.3)
      WRITE(2,95)
```

```
   95 FORMAT('BEND')
      WRITE(2,89)
   89 FORMAT('BOLD      2')
      CONSPA=(SHMAX-SHMIN)/10.0
      WRITE(2,94)CONSPA
   94 FORMAT('BLEV ',F5.1)
      WRITE(2,93)
   93 FORMAT('BRDR')
      WRITE(2,86)TITLE
   86 FORMAT('SYMB',5X,'0  0.0  6.5  0.0 0.25 30.0',15X,5A8)
      WRITE(2,88)
   88 FORMAT('SYMB',5X,'0  0.0  6.0  0.0 0.20 30.0',15X,'CONTOURS OF MAX
     1. SHEAR STRESS')
      WRITE(2,87)
   87 FORMAT('SYMB ',5X,'0  6.0  6.0  0.0 0.20 10.0',15X,'(IN MPA)')
      WRITE(2,92)
   92 FORMAT('END')
      WRITE(6,91)
   91 FORMAT(5X,'DATA FILE FOR SHEAR STRESS CONTOURING HAS BEEN FORMED
     1(-SHSCONDATA)')
      WRITE(6,90)
   90 FORMAT(/,'SUBROUTINE SHSCON COMPLETED')
      CALL TIME(1,1)
      RETURN
      END
C
C
C
C
C
      SUBROUTINE PRSCON
C     ------------------------
C
      IMPLICIT REAL *8(A-H,O-W)
      REAL *8 NU(510)
      COMMON/COM1/E(510),NU,RO(510),TITLE(5),VIS(510),TIM,T,COEFF,CLC,
     1            QLC,CM,QM,ANTEMP,NEL,NELTOP(510,3),IRHEO(510),IBF,
     2            ICALL,INS,IFS,ICR,ITEM,NTEM,NELTEM(100)
      COMMON/COM2/X(300),Y(300),XPL(3),YPL(3),XS(300),YS(300),NNOD,NNOD2
      COMMON/COM6/PRINST(510,3),DEVPR(510,3),ALPHA(510),FAIL(510),
     1            FVAL(510),PHI(510),F1,F2,ITYPE(510)
C
C**** FORMS A DATA FILE FOR USE WITH *GPCP TO PLOT 10 CONTOURS *********
C
      WRITE(3,99)
   99 FORMAT('JOB  PRINC. STRESS CONTOURS')
      WRITE(3,98)
   98 FORMAT('SIZE 20.0 20.0 0.0  0.0  0.0',7X,'10.0 400.0',5X,'-100.0',
     14X,'10.0 0.0')
      WRITE(3,97)
   97 FORMAT('CNTL 0.03 0.06',5X,'1',4X,'3')
      PSMAX=-1.0D4
      PSMIN=1.0D4
      DO 49 I=1,NEL
      PMAX=DMAX1(PRINST(I,1),PRINST(I,2))/1.0D5
      I1=NELTOP(I,1)
      I2=NELTOP(I,2)
      I3=NELTOP(I,3)
      PSMAX=DMAX1(PSMAX,PMAX)
      PSMIN=DMIN1(PSMIN,PMAX)
```

```
      XC=(X(I1)+X(I2)+X(I3))/3.0E3
      YC=(Y(I1)+Y(I2)+Y(I3))/3.0E3
   49 WRITE(3,96)XC,YC,PMAX
   96 FORMAT('CNTL ',3F10.3)
      WRITE(3,95)
   95 FORMAT('BEND')
      CONSPA=(PSMAX-PSMIN)/10.0
      WRITE(3,94)CONSPA
   94 FORMAT('BLEV ',F5.2)
      WRITE(3,93)
   93 FORMAT('BRDR')
      WRITE(3,89)TITLE
   89 FORMAT('SYMB',5X,'0  0.0  6.5  0.0 0.25 30.0',15X,5A8)
      WRITE(3,88)
   88 FORMAT('SYMB',5X,'0  0.0  6.0  0.0 0.20 27.0',15X,'CONTOURS OF MAX
     1. (MOST +VE)')
      WRITE(3,87)
   87 FORMAT('SYMB',5X,'0  5.6  6.0  0.0 0.20 27.0',15X,'PRINCIPAL STRES
     1S (IN BARS)')
      WRITE(3,92)
   92 FORMAT('END')
      WRITE(6,91)
   91 FORMAT(5X,'DATA FILE FOR PRINCIPAL STRESS CONTOURING HAS BEEN FORM
     1ED (-PRSCONDATA)')
      WRITE(6,90)
   90 FORMAT(/,'SUBROUTINE PRSCON COMPLETED')
      CALL TIME(1,1)
      RETURN
      END
C
C
C
C
C
      SUBROUTINE SFLEX(YDATUM)
C     ------------------------
C
      IMPLICIT REAL *8(A-H,O-W)
      REAL *8 NU(510)
      COMMON/COM1/E(510),NU,RO(510),TITLE(5),VIS(510),TIM,T,COEFF,CLC,
     1            QLC,CM,QM,ANTEMP,NEL,NELTOP(510,3),IRHEO(510),IBF,
     2            ICALL,INS,IPS,ICR,ITEM,NTEM,NELTEM(100)
      COMMON/COM2/X(300),Y(300),XPL(3),YPL(3),XS(300),YS(300),NNOD,NNOD2
      COMMON/COM3/FORCE(600),FORCE1(600),DISP(600),STORD(600),A,AA,TINC,
     1            DISP1(600),NBF,NPDX,NPDY,MAXIT,MAXINC,IFA,IFDM(6)
      YD=YDATUM*1.0E3
C
C**** PLOT SHAPE OF FLEXURE ****************************************
C
      CALL PSPACE(0.175,1.025,0.075,0.325)
      CALL CSPACE(0.025,1.125,0.025,0.7)
      ICOUNT=0
      XMIN=10.0E5
      XMAX=0.0
      YMIN=0.0
      YMAX=-1.0E5
      DO 49 I=1,NNOD
      IF (I.LE.30.OR.I.GT.180) GO TO 49
      IF (Y(I).NE.YDATUM) GO TO 49
      IX=2*I-1
```

```
      IY=2*I
      ICOUNT=ICOUNT+1
      XS(ICOUNT)=(X(I)+DISP(IX))/1.0E3
      YS(ICOUNT)=((Y(I)+DISP(IY))-YDATUM)
      XMIN=AMIN1(XS(ICOUNT),XMIN)
      XMAX=AMAX1(XS(ICOUNT),XMAX)
      YMIN=AMIN1(YS(ICOUNT),YMIN)
      YMAX=AMAX1(YS(ICOUNT),YMAX)
   49 CONTINUE
      IF (YMAX.LT.0.0) YMAX=0.9*YMAX
      IF (YMAX.GE.0.0) YMAX=1.1*YMAX
      IF (YMIN.LE.0.0) YMIN=1.1*YMIN
      IF (YMIN.GT.0.0) YMIN=0.9*YMIN
      CALL MAP(XMIN,XMAX,YMIN,YMAX)
      CALL NSCURV(XS,YS,1,ICOUNT)
      CALL AXES
C
C**** WRITE TITLES ***********************************************
C
      CALL PSPACE(0.025,1.125,0.025,0.5)
      CALL CSPACE(0.025,1.125,0.025,0.5)
      CALL MAP(0.025,1.125,0.025,0.5)
      CALL CTRMAG(15)
      CALL POSITN(0.175,0.45)
      IF (YD.EQ.0.0) CALL TYPECS('SHAPE OF SURFACE FLEXURE:',25)
      IF (YD.EQ.-35.0E3) CALL TYPECS('SHAPE OF MOHO FLEXURE:',22)
      CALL TYPECS(TITLE,40)
      CALL POSITN(0.175,0.4)
      CALL CTRMAG(10)
C     CALL TYPECS('DIMENSIONS OF BOTH AXES ARE IN KMS.',35)
C     CALL BORDER
      WRITE(6,99)
   99 FORMAT(/,'SUBROUTINE SFLEX COMPLETED')
      CALL TIME(1,1)
      RETURN
      END
C
C
C
C
C
      SUBROUTINE SFLEXC(YDATUM)
C     ------------------------
C
      IMPLICIT REAL *8(A-H,O-W)
      REAL *8 NU(510)
      COMMON/COM1/E(510),NU,RO(510),TITLE(5),VIS(510),TIM,T,COEFF,CLC,
     1            QLC,CM,QM,ANTEMP,NEL,NELTOP(510,3),IRHEO(510),IBF,
     2            ICALL,INS,IPS,ICR,ITEM,NTEM,NELTEM(100)
      COMMON/COM2/X(300),Y(300),XPL(3),YPL(3),XS(300),YS(300),NNOD,NNOD2
      COMMON/COM3/FORCE(600),FORCE1(600),DISP(600),STORD(600),A,AA,TINC,
     1            DISP1(600),NBF,NPDX,NPDY,MAXIT,MAXINC,IFA,IFDM(6)
      YD=YDATUM*1.0E3
C
C**** PLOT SHAPE OF FLEXURE ***************************************
C
      CALL PSPACE(0.175,0.825,0.075,0.275)
      CALL CSPACE(0.025,1.125,0.025,0.7)
      ICOUNT=0
      XMIN=10.0E5
```

```
      XMAX=0.0
      YMIN=0.0
      YMAX=-1.0E5
      DO 49 I=1,NNOD
      IF (I.LT.61.OR.I.GT.133) GO TO 49
      IF (Y(I).NE.YDATUM) GO TO 49
      IX=2*I-1
      IY=2*I
      ICOUNT=ICOUNT+1
      XS(ICOUNT)=(X(I)+DISP(IX))/1.0E3
      YS(ICOUNT)=((Y(I)+DISP(IY))-YDATUM)
      XMIN=AMIN1(XS(ICOUNT),XMIN)
      XMAX=AMAX1(XS(ICOUNT),XMAX)
      YMIN=AMIN1(YS(ICOUNT),YMIN)
      YMAX=AMAX1(YS(ICOUNT),YMAX)
   49 CONTINUE
      IF (YMAX.LT.0.0) YMAX=0.9*YMAX
      IF (YMAX.GE.0.0) YMAX=1.1*YMAX
      IF (YMIN.LE.0.0) YMIN=1.1*YMIN
      IF (YMIN.GT.0.0) YMIN=0.9*YMIN
      CALL MAP(XMIN,XMAX,YMIN,YMAX)
      CALL NSCURV(XS,YS,1,ICOUNT)
      CALL AXES
C
C**** WRITE TITLES ***********************************************
C
      CALL PSPACE(0.025,1.125,0.025,0.5)
      CALL CSPACE(0.025,1.125,0.025,0.5)
      CALL MAP(0.025,1.125,0.025,0.5)
      CALL CTRMAG(15)
      CALL POSITN(0.175,0.45)
      IF (YD.EQ.0.0) CALL TYPECS('SHAPE OF SURFACE FLEXURE:',25)
      IF (YD.EQ.-35.0E3) CALL TYPECS('SHAPE OF MOHO FLEXURE:',22)
      CALL TYPECS(TITLE,40)
      CALL POSITN(0.175,0.4)
      CALL CTRMAG(10)
C     CALL TYPECS('DIMENSIONS OF BOTH AXES ARE IN KMS.',35)
C     CALL BORDER
      WRITE(6,99)
   99 FORMAT(/,'SUBROUTINE SFLEXC COMPLETED')
      CALL TIME(1,1)
      RETURN
      END
```

BIBLIOGRAPHY

Anderson, E.M., 1951. The dynamics of faulting and dyke formation with applications to Britain. Second edition, Oliver and Boyd, Edinburgh and London, 206 pp.

Anderson, H.W. and Dodd, J.S., 1966. Finite element method applied to rock mechanics. First Int. Congr. on Rock Mechanics, 2, 317-322.

Ansorge, J., Emter, D., Fuchs, K., Lauer, J.P., Mueller, St. and Peterschmitt, E., 1970. Structure of the crust and upper mantle in the rift system around the Rhinegraben. In: Graben problems, pp. 190-197, edited by Illies, J.H. and Mueller, St., E. Schweizerbart'sche Verlagsbuchhandlung, Stuttgart.

Artemjev, M.E. and Artyushkov, E.V., 1971. Structure and isostasy of the Baikal rift and the mechanism of rifting. J. geophys. Res., 76, 1197-1211.

Artyushkov, E.V., 1973. Stresses in the lithosphere caused by crustal thickness inhomogeneities. J. geophys. Res., 78, 7675-7708.

Ashby, M.F. and Verrall, R.A., 1978. Micromechanisms of flow and fracture, and their relevance to the rheology of the upper mantle. Phil. Trans. R. Soc., A, 288, 59-95.

Baker, B.H. and Wohlenberg, J., 1971. Structure and evolution of the Kenya rift valley. Nature, 229, 538-542.

Ball, A., 1980. A theory of geological faults and shear zones. Tectonophysics, 61, T1-T5.

Barton, N.R., 1972. A model study of rock-joint deformation. Int. J. Rock Mech. Min. Sci., 9, 579-602.

Beaumont, C., 1978. The evolution of sedimentary basins in a viscoelastic lithosphere: theory and examples. Geophys. J.R. astr. Soc., 55, 471-498.

Beaumont, C. and Sweeney, J.F., 1978. Graben generation of major sedimentary basins. Tectonophysics, 50, T19-T23.

Bird, P., 1978. Finite element modelling of lithosphere deformation: the Zagros collision orogeny. Tectonophysics, 50, 307-336.

Bischke, R.E., 1974. A model of convergent plate margins based on the recent tectonics of Shikoku, Japan. J. geophys. Res., 79, 4845-4857.

Bombolakis, E.G. and Brace, W.F., 1963. A note on brittle crack growth in compression. J.geophys. Res., 68, 3709-3713.

Bott, M.H.P., 1971. The interior of the Earth. Edward Arnold, London, 316 pp.

Bott, M.H.P., 1971. Evolution of young continental margins and formation of shelf basins. Tectonophysics, 11, 319-327.

Bott, M.H.P., 1976. Formation of sedimentary basins of graben type by extension of the continental crust. Tectonophysics, 36, 77-86.

Bott, M.H.P. and Dean, D.S., 1972. Stress systems at young continental margins. Nature Phys. Sci., 235, 23-25.

Bott, M.H.P. and Kusznir, N.J., 1979. Stress distributions associated with compensated plateau uplift structures with application to the continental splitting mechanism. Geophys. J.R. astr. Soc., 56, 451-459.

Brace, W.F., 1964. Brittle fracture of rocks. In: State of stress in the Earth's crust, pp. 111-174, edited by Judd, W.R., American Elsevier, New York.

Brace, W.F. and Byerlee, J.D., 1967. Recent experimental studies of brittle fracture of rocks. In: Failure and breakage of rock, pp. 58-81, edited by Fairhurst, C., Am. Inst. Min. Mett. and Pet. Engrs., New York.

Brune, J.N., Henyey, T.L. and Roy, R.F., 1969. Heat flow and rate of slip along the San Andreas fault, California. J. geophys. Res., 14, 3821-3827.

Bufe, C.G., Harsh, P.W. and Burford, R.O., 1977. Steady-state seismic slip - a precise recurrence model. Geophys. Res. Lett., 4, 91-94.

Bullard, E.C., 1936. Gravity measurements in East Africa. Phil. Trans. R. Soc., A, 235, 445 - 531.

Burke, K., 1976a. Development of graben associated with the initial ruptures of the Atlantic ocean. Tectonophysics, 36, 93 - 112.

Burke, K., 1976b. The Chad basin: an active intracontinental basin. Tectonophysics, 36, 197 - 206.

Burke, K. and Wilson, J. Tuzo, 1972. Is the African plate stationary ? Nature, 239, 387 - 390.

Burke, K. and Whiteman, A.J., 1973. Uplift rifting and the break-up of Africa. In: Implications of continental drift to the earth sciences, pp. 735 - 755, edited by Tarling, D.H. and Runcorn, S.K., Academic Press, London.

Byerlee, J.D., 1967. Frictional characteristics of granite under high confining pressure. J. geophys. Res., 72, 3639-3648.

Byerlee, J.D., 1978. Friction of rocks. Geofis. pura appl., 116, 615-626.

Carter, N.L., 1976. Steady state flow of rocks. Rev. Geophys. Space Phys. 14, 301-353.

Carter, N.L. and Ave'Lallemant, H.G., 1970. High temperature flow in dunite and peridotite. Bull. geol. Soc. Am., 81, 2181-2202.

Carter, N.L. and Kirby, S.H., 1978. Transient creep and semibrittle behaviour of crystalline rocks. Geofis. pura appl., 116, 807 - 839.

Cathles, L.M. III, 1975. The viscosity of the Earth's mantle. Princeton University Press, 386 pp.

Chinnery, M.A., 1966. Secondary faulting. Can. J. Earth Sci., 3, 163 - 190.

Clark, S.P. Jnr., and Ringwood, A.E., 1964. Density distribution and constitution of the mantle. Rev. Geophys., 2, 35 - 88.

Collette, B.J., 1976. Normal state of stress in the lithosphere. Geofis. pura appl., 114, 285 - 286.

Davidson, A. and Rex, D.C., 1980. Age of volcanism and rifting in southwestern Ethiopia. Nature, 283, 657 - 658.

Dean, D.S., 1973. Stress analysis of the lithosphere. Unpublished Ph.D. Thesis, University of Durham, 289 pp.

Digby, P.G. and Murrell, S.A.F., 1976. The deformation of flat ellipsoidal cavities under large confining pressures. Bull. seism. Soc. Am., 66, 425 - 432.

Durham, W.B. and Goetze, C., 1977. Plastic flow of oriented single crystals of olivine: 1. Mechanical data. J. geophys. Res., 82, 5737-5753.

Durham, W.B., Froidevaux, C. and Jaoul, O., 1979. Transient and steady-state creep of pure forsterite at low stress. Phys. Earth Planet. Inter., 19, 263-274.

Edel, J.B., Fuchs, K., Gelbke, C. and Prodehl, C., 1975. Deep structure of the southern Rhinegraben from seismic refraction investigations. J. geophys., 41, 333-356.

Fairhead, J.D. and Girdler, R.W., 1972. The seismicity of the East African rift system, Tectonophysics, 15, 115-122.

Forth, P.A., 1975. The structure of the upper mantle beneath East Africa. Unpublished Ph. D. thesis, University of Durham, 136 pp.

Fuchs, K., 1974. Geophysical contributions to taphrogenesis. In: Approaches to taphrogenesis, pp. 420-432, edited by Illies, J.H. and Fuchs, K., E. Schweizerbart'sche, Stuttgart.

Girdler, R.W., 1964. Geophysical studies of rift valleys. Physics Chem. Earth, 5, 121-156.

Girdler, R.W., Fairhead, J.D., Searle, R.C. and Sowerbutts, W.T.C., 1969. The evolution of rifting in Africa. Nature, 224, 1178-1182.

Goetze, C., 1971. High temperature rheology of Westerly granite. J. geophys. Res., 76, 1223-1230.

Goetze, C., 1978. The mechanisms of creep in olivine. Phil. Trans. R. Soc., A, 288, 99 - 119.

Goetze, C. and Brace, W.F., 1972. Laboratory observations of high-temperature rheology of rocks. Tectonophysics, 13, 583 - 600.

Goetze, C. and Kohlstedt, D.L., 1973. Laboratory study of dislocation climb and diffusion in olivine. J. geophys. Res., 78, 5961 - 5971.

Goldsmith, W., Sackman, J.L. and Ewert, C., 1976. Static and dynamic fracture strength of Barre granite. Int. J. Rock Mech. Min. Sci., 13, 303 - 309.

Golonetsky, S.I. and Misharina, L.A., 1978. Seismicity and earthquake focal mechanisms in the Baikal rift zone. Tectonophysics, 45, 71 - 85.

Goodman, R.E., 1976. Methods of geological engineering in discontinuous rocks. West Publishing Co., St. Paul.

Goodman, R.E., Taylor, R.L. and Brekke, T.L., 1968. A model for the mechanics of jointed rock. J. Soil Mech. Fdns Div. Am. Soc. civ. Engrs., 94, 637 - 659.

Green, D.H. and Ringwood, A.E., 1963. Mineral assemblages in a model mantle composition. J. geophys. Res., 68, 937 - 945.

Green, D.H. and Ringwood, A.E., 1967. An experimental investigation of the gabbro to eclogite transformation and its petrological applications. Geochim. cosmochim. Acta, 31, 767-833.

Griffith, A.A., 1921. The phenomena of rupture and flow in solids. Phil. Trans. R. Soc., A, 221, 163-198.

Griffiths, D.H., King, R.F., Khan, M.A. and Blundell, D.J., 1971. Seismic refraction line in the Gregory rift. Nature Phys. Sci., 229, 69-75.

Griggs, D.T. and Handin, J., 1960. Observations on fracture and a hypothesis of earthquakes. In: Rock deformation (a symposium), pp. 347-364, edited by Griggs, D. and Handin, J., Mem. geol. Soc. Am., 79.

Griggs, D.T., Turner, F.J. and Heard, H.C., 1960. Deformation of rocks at 500° to 800°C. In: Rock deformation (a symposium), pp. 39-104, edited by Griggs, D. and Handin, J., Mem. geol. Soc. Am., 79.

Haenel, R., 1970. Interpretation of the terrestrial heat flow in the Rhinegraben. In: Graben problems, pp.116-120, edited by Illies, J.H. and Mueller, St., E. Schweizerbart'sche Verlagsbuchhandlung, Stuttgart.

Handin, J., 1969. On the Coulomb-Mohr failure criterion. J. geophys. Res., 74, 5343-5350.

Heard, H.C. and Carter, N.L., 1968. Experimentally induced 'natural' intragranular flow in quartz and quartzite. Am.J. Sci., 266, 1-42.

Heiskanen, W.A. and Vening Meinesz, F.A., 1958. The Earth and its gravity field. McGraw-Hill Book Company, New York, Toronto and London, 470 pp.

Herrin, 1972. A comparative study of upper mantle models: Canadian shield and Basin and Range provinces. In: The nature of the solid Earth, pp. 216-231, edited by Robertson, E.C., McGraw-Hill Book Company, New York.

Hinton, E. and Campbell, J.S., 1974. Local and global smoothing of discontinuous finite element functions using a least squares method. Int. J. Num. Meth. Eng., 8, 461-480.

Hinton, E. and Owen, D.R.J., 1977. Finite element programming. Academic Press, London, 305 pp.

Hopper, M.J., 1973. Harwell subroutine library. H.M.S.O.

Housner, G.W. and Vreeland, T., Jr., 1966. The analysis of stress and deformation. The Macmillan Company, New York, 434 pp.

Hubbert, M.K. and Rubey, W.W., 1959. Role of fluid pressure in mechanics of overthrust faulting: I. Mechanics of fluid-filled porous solids and its application to overthrust faulting. Bull. geol. Soc. Am., 70, 115-166.

Illies, J.H., 1970. Graben tectonics as related to crust-mantle interaction. In: Graben problems, pp. 4-27, edited by Illies, J.H. and Mueller, St., E. Schweizerbart'sche Verlagsbuchhandlung, Stuttgart.

Illies, J.H., 1975. Recent and palaeo—intraplate tectonics in stable Europe and the Rhinegraben rift system. Tectonophysics, 29, 251-264.

Illies, J.H., 1977. Ancient and recent rifting in the Rhinegraben. Geologie Mijnb., 56, 329-350.

Jaeger, J.C., 1969. Elasticity, fracture and flow. Third edition, Science Paperbacks.

Jaeger, J.C. and Cook, N.G.W., 1976. Fundamentals of rock mechanics. Second edition, Science Paperbacks, 585 pp.

Jaeger, J.C. and Hoskins, E.R., 1966. Rock failure under the confined Brazilian test. J. geophys. Res., 71, 2651-2659.

Johnson, T.L., 1975. A comparison of frictional sliding on granite and dunite surfaces. J. geophys. Res., 80, 2600-2605.

Kahle, H-G. and Werner, D., 1980. A geophysical study of the Rhinegraben - II. Gravity anomalies and geothermal implications. Geophys. J.R. astr. Soc., 62, 631-647.

Kent, P.E., 1975. Review of North Sea basin development. J. geol. Soc. Lond., 131, 435-468.

King, G.C.P., 1978. Geological faults: fracture, creep and strain. Phil. Trans. R. Soc., A, 288, 197-212.

Kirby, S.H., and Raleigh, C.B., 1973. Mechanisms of high-temperature, solid-state flow in minerals and ceramics and their bearing on

the creep behaviour of the mantle. Tectonophysics, 19, 165-194.

Kiselev, A.T., Golovko, H.A. and Medvedev, M.E., 1978. Petrochemistry of Cenozoic basalts and associated rocks in the Baikal rift zone. Tectonophysics, 45, 49-59.

Kohlstedt, D.L. and Goetze, C., 1974. Low stress, high temperature creep in olivine single crystals. J. geophys. Res., 79, 2045-2051.

Kohlstedt, D.L., Goetze. C. and Durham, W.B., 1976. Experimental deformation of single crystal olivine with application to flow in the mantle. In: The physics and chemistry of minerals and rocks, pp. 35-50, edited by Strens, R.G.J, John Wiley and Sons, London, New York, Sydney and Toronto.

Kolmogorov, V.G. and Kolmogorova, P.P., 1978. Some results from studying recent crustal movements in the Baikal rift zone. Tectonophysics, 45, 101-105.

Kreyszig, E., 1972. Advanced engineering mathematics. John Wiley and Sons, New York, London, Sydney and Toronto, 865 pp.

Kusznir, N.J., 1976. Theoretical studies of the geodynamics of accretion boundaries in plate tectonics. Unpublished Ph.D. thesis, University of Durham, 145 pp.

Kusznir, N.J. and Bott, M.H.P., 1977. Stress concentration in the upper lithosphere caused by underlying visco-elastic creep. Tectonophysics, 43, 247-256.

Lanczos, C., 1949. The variational principles of mechanics. University of Toronto Press, 307 pp.

Lee, E.H., Radok, J.R.M. and Woodward, W.B., 1959. Stress analysis for linear viscoelastic materials. Trans. Soc. Rheology, 3, 41-59.

Logatchev, N.A., Beloussov, V.V. and Milanovsky, E.E., 1972. East African rift development. Tectonophysics, 15, 71-81.

Long, R.E. and Backhouse, R.W., 1976. The structure of the western flank of the Gregory rift. Part II. The mantle. Geophys. J.R. astr. Soc., 44, 677-688.

Long, R.E., Sundaralingam, K. and Maguire, P.K.H., 1973. Crustal structure of the East African rift zone. Tectonophysics, 20, 269-281.

McGill, G.E. and Stromquist, A.W., 1979. The grabens of Canyonlands National Park, Utah: geometry, mechanics and kinematics. J. geophys. Res., 84, 4547-4563.

McKinstry, H.E., 1953. Shears of the second order. Am. J. Sci., 251, 401-414.

McLintock, F.A. and Walsh, J.B., 1962. Friction of Griffith cracks under pressure. Proc. U.S. natn. Congr. appl. Mech., 4, 1015-1021.

Meissner, R., Berckhemer, H., Wilde, R. and Poursadeg, M., 1970. Interpretation of seismic refraction measurements in the northern part of the Rhinegraben. In: Graben problems, pp. 184-189, edited by Illies, J.H. and Mueller, St., E. Schweizerbart'sche Verlagsbuchhandlung, Stuttgart.

Mercier, J-C and Carter, N.L., 1975. Pyroxene geotherms. J. geophys. Res., 80, 3349-3362.

Misra, A.K. and Murrell, S.A.F., 1965. An experimental study of the effect of temperature and stress on the creep of rocks. Geophys. J.R. astr. Soc., 9, 509-535.

Mogi, K., 1974. On the pressure dependence of strength of rocks and the Coulomb fracture criterion. Tectonophysics, 21, 273-285.

Molnar, P. and Tapponier, P., 1975. Cenozoic tectonics of Asia: effects of a continental collision. Science, 189, 419-426.

Montadert, L., Roberts, D.G., De Charpal, O. and Guennoc, P., 1979. Rifting and subsidence of the northern continental margin of the Bay of Biscay. Initial Reports of the Deep Sea Drilling Projects v. 48:

Washington (U.S. Government Printing Office), 1025-1060.

Moody, J.D. and Hill, M.J., 1956. Wrench fault tectonics. Bull. geol. Soc. Am., 67, 1207 - 1246.

Mueller, St., 1970. Geophysical aspects of graben formation in continental rift systems. In: Graben problems, pp. 27 - 37, edited by Illies, J.H. and Mueller, St., E. Schweizerbart'sche Verlagsbuchhandlung, Stuttgart.

Mueller, St., and Rybach, L., 1974. Crustal dynamics in the central part of the Rhinegraben. In: Approaches to taphrogenesis, pp. 379 - 388, edited by Illies, J.H. and Fuchs, K., E. Schweizerbart'sche Verlagsbuchhandlung, Stuttgart.

Murrell, S.A.F., 1964a. The theory of the propagation of elliptical Griffith cracks under various conditions of plane strain or plane stress: Part I. Br. J. appl. Phys., 15, 1195 - 1210.

Murrell, S.A.F., 1964b. The theory of the propagation of elliptical Griffith cracks under various conditions of plane strain or plane stress: Parts II and III. Br. J. appl. Phys., 15, 1211 - 1223.

Murrell, S.A.F., 1965. The effect of triaxial stress systems on the strength of rocks at atmospheric temperatures. Geophys. J.R. astr. Soc., 10, 231 - 281.

Murrell, S.A.F., 1976. Rheology of the lithosphere - experimental indications. Tectonophysics, 36, 5 - 24.

Murrell, S.A.F., 1977. Natural faulting and the mechanics of brittle shear failure. J. geol. Soc. Lond., 133, 175 - 189.

Murrell, S.A.F. and Chakravarty, S., 1973. Some new rheological experiments on igneous rocks at temperatures up to 1120°C. Geophys. J.R. astr. Soc., 34, 211 - 250.

Neugebauer, H.J., 1978. Crustal doming and the mechanism of rifting. Part I: rift formation. Tectonophysics, 45, 159 - 186.

Neugebauer, H.J. and Braner, B., 1978. Crustal doming and the mechanism of rifting. Part II: rift development of the upper

Rhinegraben. Tectonophysics, 46, 1 - 20.

Neugebauer, H.J. and Spohn, T., 1978. Late stage development of mature Atlantic-type continental margins. Tectonophysics, 50, 275 - 305.

Nicolas, A. and Poirier, J.P., 1976. Crystalline plasticity and solid state flow in metamorphic rocks. John Wiley and Sons, London, New York, Sydney and Toronto, 444 pp.

Nur, A., 1978. Nonuniform friction as a physical basis for earthquake mechanics. Geofis. pura appl., 116, 964 - 988.

Oxburgh, E.R. and Turcotte, D.L., 1974. Membrane tectonics and the East African rift. Earth Planet. Sci. Lett., 22, 133 - 140.

Parrish, D.K., Krivz, A.L. and Carter, N.L., 1976. Finite element folds of similar geometry. Tectonophysics, 32, 183 - 207.

Post, R.L. and Griggs, D.T., 1973. The Earth's mantle: evidence of non-Newtonian flow. Science, 181, 1242 - 1244.

Profett, J.M., 1977. Cenozoic geology of the Yerington district, Nevada and implications for the nature and origin of Basin and Range faulting. Bull. geol. Soc. Am., 88, 247 - 266.

Puzyrev, N.N., Mandelbaum, M.M., Krylov, S.V., Mishenkin, B.P., Petrik, G.V. and Krupskaya, G.V., 1978. Deep structure of the Baikal and other continental rift zones from seismic data. Tectonophysics, 45, 15 - 22.

Ramberg, I., 1972. Crustal structure across the Permian Oslo graben from gravity measurements. Nature Phys. Sci., 240, 149 - 153.

Ramsay, J.G., 1967. Folding and fracturing of rocks. McGraw-Hill Book Company, New York, Toronto and London, 568 pp.

Ranalli, G. and Chandler, T.E., 1975. The stress field in the upper crust as determined from in-situ measurements. Geol. Rdsch., 64, 653 - 674.

Rhinegraben Research Group for Explosion Seismology, 1974. The 1972 seismic refraction experiment in the Rhinegraben - first

results. In: Approaches to taphrogenesis, pp. 122 - 137, edited by Illies, J.H. and Fuchs, K., E. Schweizerbart'sche Verlagsbuchhandlung, Stuttgart.

Ringwood, A.E. and Green, D.H., 1966. Petrological nature of the stable continental crust. In: The Earth beneath the continents, pp. 611 - 619, edited by Steinhart, J.S. and Smith, T.J., Geophys. Monogr. No. 10, American Geophysical Union, Washington D.C.

Sellevol, M.A. and Warrick, R.E., 1970. A refraction study of the crustal structure in southern Norway. Bull. seism. Soc. Am., 61, 457 - 471.

Service, K.G. and Douglas, A., 1973. Boundaries and fractures in finite element models of geological structures. Geophys. J.R. astr. Soc., 32, 1 - 14.

Sheridan, R.E., 1976. Sedimentary basins of the Atlantic margin of North America. Tectonophysics, 36, 113 - 132.

Sherman, S.I., 1978. Faults of the Baikal rift zone. Tectonophysics, 45, 31 - 39.

Sleep, N.H. and Snell, N.S., 1976. Thermal contraction and flexure of mid-continent and Atlantic marginal basins. Geophys. J.R. astr. Soc., 45, 125 - 154.

Smith, R.B. and Sbar, M.L., 1974. Contemporary tectonics and seismicity of the Western United States with emphasis on the Intermountain seismic belt. Bull. geol. Soc. Am., 85, 1205 - 1218.

Solonenko, V.P., 1978. Seismotectonics of the Baikal rift zone. Tectonophysics, 45, 61 - 69.

Stesky, R.M., 1978. Rock friction - effect of confining pressure, temperature, and pore pressure. Geofis. pura appl., 116, 690 - 704.

Stewart, J.H., 1978. Basin-range structure in western North America: A review. In: Cenozoic tectonics and regional geophysics of the Western Cordillera, pp. 1 - 32, edited by Smith, R.B. and Eaton, G.P., Mem. geol. Soc. Am., 152.

Stocker, R.L. and Ashby, M.F., 1973. On the rheology of the upper mantle. Rev. Geophys. Space Phys., 11, 391 - 426.

Strobach, K., 1974. Model of crustal stresses in the region of the Rhinegraben and southwestern Germany. In: Approaches to taphrogenesis, pp. 389 - 394, edited by Illies, J.H. and Fuchs, K., E. Schweizerbart'sche Verlagsbuchhandlung, Stuttgart.

Summers, R. and Byerlee, J.D., 1977. A note on the effect of fault gouge composition on the stability of frictional sliding. Int. J. Rock Mech. Min. Sci., 14, 155.

Tapponier, P. and Molnar, P., 1979. Active faulting and Cenozoic tectonics of the Tien Shan, Mongolia, and Baikal regions. J. geophys. Res., 84, 3425 - 3459.

Turcotte, D.L., 1974. Membrane tectonics. Geophys. J.R. astr. Soc., 36, 33 - 42.

Turcotte, D.L. and Oxburgh, E.R., 1973. Mid-plate tectonics. Nature, 224, 337 - 339.

Turcotte, D.L. and Oxburgh, E.R., 1976. Stress accumulation in the lithosphere. Tectonophysics, 35, 183 - 199.

Vening Meinesz, F.A., 1950. Les graben africains, resultat de compression ou de tension dans la croute terrestre ? Bull. Inst. R. Colon. Belge, 21, 539 - 552.

Vetter, U.R., and Meissner, R.O., 1979. Rheologic properties of the lithosphere and applications to passive continental margins. Tectonophysics, 59, 367 - 380.

Voight, B., 1974. Thin-skinned graben, plastic wedges, and deformable-plate tectonics. In: Approaches to taphrogenesis, pp. 395 - 419, edited by Illies, J.H. and Fuchs, K., E. Schweizerbart'sche Verlagsbuchhandlung, Stuttgart.

Walcott, R.I., 1970. Flexural rigidity, thickness and viscosity of the lithosphere. J. geophys. Res., 75, 3941 - 3954.

Wang, C-Y. and Mao, N.-H., 1979. Shearing of saturated clays in rock joints at high confining pressures. Geophys. Res. Lett., 6, 825 - 828.

Wang, C-Y., Lin, W. and Wu, F.T., 1978. Constitution of the San Andreas fault zone at depth. Geophys. Res. Lett., 5, 741.

Wang, H.F. and Simmons, G., 1978. Microcracks in crystalline rock from 5.3 km depth in the Michigan basin. J. geophys. Res., 83, 5849 - 5856.

Watts, A.B., 1978. An analysis of isostasy in the world's oceans. 1. Hawaiian - Emperor seamount chain. J. geophys. Res., 83, 5989 - 6004.

Weertman, J., 1970. The creep strength of the Earth's mantle. Rev. Geophys. Space Phys., 8, 145 - 168.

Weertman, J., 1978. Creep laws for the mantle of the Earth. Phil. Trans. R. Soc., A, 288, 9 - 26.

Weertman, J. and Weertman, J.R., 1975. High temperature creep of rock and mantle viscosity. Annu. Rev. Earth Planet Sci., 3, 293 - 315.

Whiteman, A., Naylor, D., Pegrum, R. and Rees, G., 1975. North Sea troughs and plate tectonics. Tectonophysics, 26, 39 - 54.

Woodward, D.J., 1976. Visco-elastic finite element analysis of subduction zones. Unpublished Ph.D. Thesis, University of Durham, 215 pp.

Wright, L.A. and Troxel, B.W., 1973. Shallow fault interpretation of basin and range structure, southwestern Great Basin. In: Gravity and tectonics, pp. 397 - 408, edited by De Jong, K.A. and Scholten, R., John Wiley and Sons, New York, Toronto.

Wu, F.T., 1978. Mineralogy and physical nature of clay gouge. Geofis. pura appl., 116, 655.

Wyllie, P.J., 1971. The dynamic Earth : textbook in geosciences. John Wiley and Sons, New York, 415pp.

Zamarayev, S.M. and Ruzhich, V.V., 1978. On relationships between the Baikal rift and ancient structures. Tectonophysics, 45, 41 - 47.

Ziegler, W.H., 1975. Outline of the geological history of the North Sea. In: Petroleum and the continental shelf of N.W. Europe, I. Geology, pp.165 - 190, edited by Woodland, A.W., John Wiley and Sons, New York.

Zienkiewicz, O.C., 1977. The finite element method in engineering science. Third edition, McGraw-Hill Book Company, London, 787 pp.

Zienkiewicz, O.C., Watson, M. and King, I.P., 1968. A numerical method of visco-elastic stress analysis. Int. J. Mech. Sci., 10, 807 - 827.

Zoback, M.D. and Roller, J.C., 1979. Magnitude of shear stress on the San Andreas fault: implications of a stress measurement profile at shallow depth. Science, 206, 445 - 447.

Zorin, Yu.A. and Rogozhina, V.A., 1978. Mechanism of rifting and some features of the deep-seated structure of the Baikal rift zone. Techtonophysics, 45, 23 - 30.